Study of CP-Violating Asymmetries in $B^0 \to K_S\,\pi^0$ Decay

Tatsunobu Shibata

Doctoral Program in Fundamental Science and Energy Techology

Graduate School of Science and Technology

Niigata University

January 28, 2005

Acknowledgment

I would like to thank the Belle collaboration of specially to all member of CP-fit and SVD group members, and residents of Tsukuda Experimental Hall: Prof. M.Hazumi, Prof. Y.Sakai, Prof. T.Browder, Prof. T.Higichi, Dr. K.Hara, Mr. K.F.Chen, Mr. Y.Chao, Dr. K.Sumisawa, Prof. Y.Ushiroda, Mr. A.Kusaka, Prof. O.Tajima, Pfor. F.Fang, Dr. S.Uchida.Kataoka, Prof. H.Kakuno, Prof. H.Ishino, Prof. K.Trabelsi, Prof. T.Hara, Prof. A.Kibayashi, Prof. S.Nishida, Prof. T.Tsukamoto, and Prof. I.Adachi for their kind advice and continuous support in this analysis.

I also appreciate all member in our group at Niigata University and other University: Mr. Y.Onuki, Mr. H.Matsumoto, Miss. M.Watanabe, Mr. T.Mori, and Dr. N.Abe for their several friendly help.

I am most indebted to my supervisors, Prof. N.Tamura, Prof. T.Kawasaki, and Prof. H.Miyata throughout their continual support and guidance for my reserch activity.

Abstract

$B^0 \to K_S\pi^0$ is $b \to s$ transition of penguin decay process, that is called flavor changing neutral current. The tree-level contribution is much smaller than penguin contribution. If the penguin deacay includes the intermadiate state of beyond Standard Model, for example SUSY particle, it is possible to search the new physics effect by comparing the sin$2\phi_1$ which is measured by $B^0 \to J/\psi K_S$ decay mode. We measured indirect CP-asymmetry, effective sin$2\phi_1$, and direct CP-asymmetry by $B^0 \to K_S\pi^0$ decay with $253fb^{-1}$ data sample, corresponding to 275×10^6 $B\bar{B}$ pairs, accumulated from Jan.2001 to Jun.2004 at the KEKB factory. In this analysis, we used two new analysis methods. One is vertex reconstruction with only K_S particle and constrained by interaction point. We developed new vertex reconsruction method and modified vertex resolution for $B^0 \to K_S\pi^0$. Another is measurement of direct CP-asymmetry methos. In basically, we use proper time difference and flavor information, but we can do it from only flavor information. To reduce statistical error of direct CP-asymmetry parameter, we used events which does not have proper time difference information but has flavor information. We reconstructed $B^0 \to K_S\pi^0$ events and obtained 71 candidates, which have proper time difference and flavor information, and 176 candidates, which have only flavor information. We measured CP-asymmetry parameters by un-binned maximum likelihood fit. We got direct CP-asymmetry parameter as -0.11±0.20(stat)±0.09(syst), and indirect CP-asymmetry parameter as +0.32±0.61(stat)±0.13(syst). These results are consistent with Standard Model expectation within error. Since the statistic error are larger than systematic error, we need more statistics to conclude that CP-Violation of $B^0 \to K_S\pi^0$ resides within or beyond the Standard Model expectation.

Contents

Chapter 1

Introduction to B Physics

Recently, we open the door for new world of physics gradually. The Standard Model has been verified from 1960's when it was proposed. The discovery of Neutral current[1], Weak boson(W and Z)[2][3][4] [5] which are mediated paritcle of Weak interaction, and measurement of the Weinberg angle[6][7]. The discovery of six quarks which are predicted in the Standard Model. The top quark that has 175GeV/c^2 mass has been detected in 1995 [8]. The all experiments during these thrity years prove the property of the Standard Model, and all of results are consistent with Standard Model. The most important topics, which is expected in the Standard Model and not verfied experimentally are Higgs particle and CP-Violation. We expect the discovery of Higgs particle in Large Hadron Collider (LHC) which will start from 2007 at CERN [1]. The CP-violation, which is described in next section, was discoved in 1964 in Kaon meson system[9][10][11] and discovered in B meson in 2001 at KEKB-Belle Experiment[12] at KEK in Japan and PEPII-BaBar Experiment[13] at SLAC in USA[2]. In the while, a discovery beyond the Standard Model was reported by Super-Kamiokande group[14] [15] Japan[3]. They found the Neutrino osciilation from up-down asymmetry of atmospheric neutrino flux. The neurino osciilation is ocuured in the case that three neutrino have finite and different mass, while in we assume the neutrino mass is 0 in the Standard Model. This is the first phenomenon which is inconsistency with Standard Model. The Neutrino osciilation was also found in solar neutrino by Super-Kamiokande group[16][17] and SNO group[18], [4] in neutrino from accelarator by K2K experiment[19] and in reactor neutrino by KamLAND group[20] Japan [5]. In near future, T2K and KASKA[6], which look for the solution of neutrino osciilation, will be start in Japan. KEKB-Belle experiment group reported the inconsistency with Standard Model in CP-Violation in 2003 at Lepton-Photon conference[21]. We could got the very important sign which suggest the existence of new physics. By these discovery, we can go to the next step towards new physics. In this report I will report the result of CP-Violation measurement in $B^0 \to K_s \pi^0$ decay mode that is expected to have the inconsistency with Standard Model.

1.1 CKM Matrix and CP Voilation in Standard Model

1.1.1 Standard Model

At present, the Standard Model is the essential theory which explains the elementary particle. The elementary particles can interact through four forces, Electromagnetic interactrion, Weak interaction, Strong interaction and Gravitation. The Standard Model describes the raw of the former three interactions except Gravitation. Electromagnetic-interaction and Weak-interaction are explained by the Grashow-Weinberg-Sarama theory(GWS theory)[22]. The strong-interaction is explained by Quantum ChromoDynamics(QCD). The GWS theory was proposed in 1967 that unified Electromagnetic-interaction and Weak interaction based on

---

[1] http://public.web.cern.ch/Public/Welcome.html

[2] http://www.slac.stanford.edu/BFROOT/

[3] http://www-sk.icrr.u-tokyo.ac.jp/

[4] http://www.sno.phy.queensu.ca/

[5] http://www.awa.tohoku.ac.jp/KamLAND/first_results/index_j.html

[6] http://kaska.hep.sc.niigata-u.ac.jp/

$SU(2) \times U(1)$ gauge theory and Higgs mechanism[23]. The Grand Unified Theory(GUT) which is unified GWS theory and QCD was also proposed, but there is no experimental proof. The GWS theory is described by Lagrangian which is expresses with $SU(2) \times U(1)$ gauge invariance.

$$\begin{aligned} L = {} & L_{lepton-gauge} + L_{quark-gauge} + L_{gauge} + L_{higgs-lepton} + L_{higgs-quark} \\ & + L_{higgs} + L_{gauge-gauge} + L_{higgs-higgs} + L_{gauge-higgs} \end{aligned} \tag{1.1}$$

$$L_{lepton-gauge} = i[\bar{\Psi}_l^L(x) D \Psi_l^L + \bar{\Psi}_l^R(x) D' \Psi_l^R] \tag{1.2}$$

$$L_{quark-gauge} = i[\bar{\Psi}_q^L(x) D \Psi_q^L + \bar{\Psi}_q^R(x) D' \Psi_q^R] \tag{1.3}$$

$$\left\{ \begin{array}{l} D = \gamma_\mu(\partial^\mu + ig\tau_j w_j^\mu \frac{1}{2} - ig' B^\mu \frac{1}{2}) \\ D' = \gamma_\mu(\partial^\mu - ig' B^\mu(x)) \end{array} \right. \tag{1.4}$$

$$\left\{ \begin{array}{l} \Psi_l^L = \left(\begin{array}{c} \nu_e \\ e \end{array} \right)_L, \left(\begin{array}{c} \nu_\mu \\ \mu \end{array} \right)_L, \left(\begin{array}{c} \nu_\tau \\ \tau \end{array} \right)_L \\ \Psi_l^R = e^R, \mu^R, \tau^R \\ \Psi_q^L = \left(\begin{array}{c} u \\ d \end{array} \right)_L, \left(\begin{array}{c} c \\ s \end{array} \right)_L, \left(\begin{array}{c} t \\ b \end{array} \right)_L \\ \Psi_q^R = u^R, d^R, c^R, s^R, t^R, b^R \end{array} \right. \tag{1.5}$$

$$L_{gauge} = \frac{1}{4} B^{\mu\nu} B_{\mu\nu} - \frac{1}{4} G_i^{\mu\nu} G_{i\mu\nu}(x) \tag{1.6}$$

$$\left\{ \begin{array}{l} B^{\mu\nu} = \partial^\nu B^\mu - \partial^\mu B^\nu \\ G_i^{\mu\nu} = F_i^{\mu\nu} + g\epsilon_{ijk} W_j^\mu W_k^\nu \end{array} \right. \tag{1.7}$$

$$L_{higgs-lepton} \quad = \quad -g_l[\bar{\Psi}_l^L \psi_l^R \Phi + \Phi^\dagger \bar{\psi}_l^R \Psi_l^L] - g_\nu[\bar{\Psi}_l^L \psi_\nu^R \tilde{\Phi} + \widetilde{\Phi^\dagger} \bar{\psi}_\nu^R \Psi_l^L] \tag{1.8}$$

$$\left\{ \begin{array}{l} \Phi = \left(\begin{array}{c} \phi_a \\ \phi_b \end{array} \right) \\ \tilde{\Phi}^\dagger = -i[\Phi^\dagger \tau_2]^T = \left(\begin{array}{c} \phi_b^* \\ -\phi_a^* \end{array} \right) \end{array} \right. \tag{1.9}$$

$$L_{higgs-quark} = -g_d[\bar{\Psi}_q^L \psi_d^R \Phi + \Phi^\dagger \bar{\psi}_d^R \Psi_q^L] - g_u[\bar{\Psi}_q^L \psi_u^R \tilde{\Phi} + \widetilde{\Phi^\dagger} \bar{\psi}_u^R \Psi_q^L] \tag{1.10}$$

$$\left\{ \begin{array}{l} g_u = g_u, g_c, g_t \\ g_d = g_d, g_s, g_b \\ \Psi_q^L = \left(\begin{array}{c} \bar{u} \\ \bar{d} \end{array} \right)^L, \left(\begin{array}{c} \bar{c} \\ \bar{s} \end{array} \right)^L, \left(\begin{array}{c} \bar{t} \\ \bar{b} \end{array} \right)^L \\ \Phi_u^R = u^R, c^R, t^R \\ \Phi_d^R = d^R, s^R, b^R \end{array} \right. \tag{1.11}$$

Where $L_{lepton-gauge}(L_{quark-gauge})$ describes the interaction between lepton(quark) and gauge field. These are Electromagnetic interaction and Weak interaction. L_{gauge} is a Lagangian of gauge field, which expresses interaction among of gauge boson. $L_{higgs-lepton}(L_{higgs-quark})$ describes the interaction between lepton(quark) and Higgs particle. Mass of particles are generated through the Higgs mechanism. We can divide the Electromagnetic interaction and Weak interaction from unified Lagrangian, by introducing the mixing angle between the vector field W_μ^3 and the scalar field B^μ.

$$\left(\begin{array}{c} A_\mu \\ Z_\mu \end{array} \right) = \left(\begin{array}{cc} \mathbf{cos\theta_w} & \mathbf{sin\theta_w} \\ \mathbf{-sin\theta_w} & \mathbf{cos\theta_w} \end{array} \right) \left(\begin{array}{c} B_\mu \\ W_\mu^3 \end{array} \right) \tag{1.12}$$

where A_μ is photon field and Z_μ is Z boson, $\cos\theta_{\mathbf{w}}$ is mixing angle which is called Weinberg angle that measured value is $\sin^2\theta_{\mathbf{w}} = 0.23120$[24]. This angle can not be predicted from theory and precise measurement can prove the GWS theory. According to introduce the Weinberg angle, we can divide the Lagrangian to three kinds of interactions.

$$\begin{aligned}
L_{QED} &= i\bar{\psi}_l(\gamma^\mu\partial_\mu)\psi_l && (1.13)\\
L_{CC}^{lepton} &= \frac{g}{2\sqrt{2}}\bar{\psi}_\nu\gamma_\mu(1-\gamma^5)\psi_l W_\mu^+ + \frac{g}{2\sqrt{2}}\bar{\psi}_l\gamma_\mu(1-\gamma^5)\psi_\nu {W_\mu^-}^\dagger && (1.14)\\
L_{CC}^{quark} &= \frac{g}{2\sqrt{2}}\sum_{i=1}^{3}\{\bar{u_i}\gamma^\mu(1-\gamma^5)d_i W_\mu^+ + \bar{d_i}\gamma^\mu(1-\gamma^5)u_i W_\mu^-\} && (1.15)\\
L_{NC}^{lepton} &= \frac{g}{4\mathbf{cos}\theta_w}\bar{\psi}_l\gamma_\mu(1-4\mathbf{sin}^2\theta_w-\gamma^5)\psi_l Z^\mu - \frac{g}{4\mathbf{cos}\theta_w}\bar{\psi}_\nu\gamma_\mu(1-\gamma^5)\psi_\nu Z^\mu && (1.16)\\
L_{NC}^{quark} &= \frac{g}{4\mathbf{cos}\theta_w}\sum_{i=1}^{3}\{\bar{u_i}\gamma_\mu(1-4\mathbf{sin}^2\theta_w-\gamma^5)u_i Z^\mu + \bar{d_i}\gamma_\mu(1-4\mathbf{sin}^2\theta_w-\gamma^5)d_i Z^\mu\} && (1.17)
\end{aligned}$$

The Electromagnetic interaction is written by L_{QED}, this interaction Lagrangian is defined as Dirac equation. The L_{CC}^{lepton} and L_{CC}^{quark} are through weak interaction charged current, which describe $e, \mu, \tau \leftrightarrow \nu_e, \nu_\mu, \nu_\tau$, and up-type quark $\leftrightarrow$ down-type quark. The most famous charged weak current is β-decay, as Fig 1.1. L_{NC}^{lepton} and L_{NC}^{quark} are weak interaction through neutral current, which don't change the flavor, as $e, \mu, \tau \leftrightarrow e, \mu, \tau$, $\nu_e, \nu_\mu, \nu_\tau \leftrightarrow \nu_e, \nu_\mu, \nu_\tau$, up-type quark $\leftrightarrow$ itself and down-type quark $\leftrightarrow$ itself. since the neutral weak current was predicted by only GWS theory, the discovery of neutral weak current is very important for prove the GWS theory. The neutral weak current interaction was discovered in 1973 by elastic scattering of neutrino-muon, $\nu_\mu + e^- \rightarrow \nu_\mu + e^-$, at CERN[1].

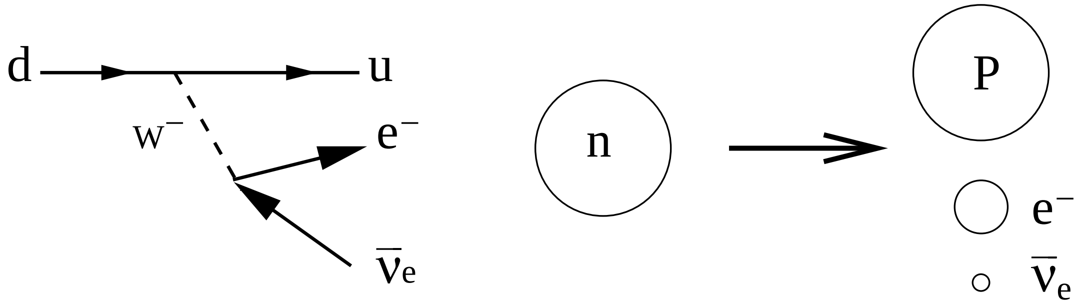

Figure 1.1: β-decay Feynman Diagram

β-decay is d to u transition with Charged Current interaction in quark level. The W^- boson decay to lepton pair.

The Lagrangian included mass are $L_{lepton-higgs}$ and $L_{quark-higgs}$, we can get the mass of lepton and quark by Higgs mechamizm which is called spontaneous symmetry breaking[23].

$$\begin{aligned}
\Phi &= \begin{pmatrix}\phi_a\\ \phi_b\end{pmatrix} \rightarrow \begin{pmatrix}0\\ \nu + h\end{pmatrix} && (1.18)\\
\tilde{\Phi}^\dagger &= -i[\Phi^\dagger\tau_2]^T = \begin{pmatrix}\phi_b^*\\ -\phi_a^*\end{pmatrix} \rightarrow \begin{pmatrix}\nu^* + h^*\\ 0\end{pmatrix} && (1.19)
\end{aligned}$$

Where, ν is the vacuum expectation. Then, the $L_{lepton-higgs}$ and $L_{quark-higgs}$ are,

$$L_{lepton-higgs} = \sum_{l=e,\mu,\tau}\{m_l\bar{\psi}_l\psi_l + \frac{m_l}{\nu}\bar{\psi}_l\psi_l h\} \qquad (1.20)$$

$$\begin{aligned}
L_{quark-higgs} &= \sum_{i=d,s,b} m_{ij}(1+\frac{h}{\nu})(\bar{d}_i^L d_j^R + \bar{d}_i^R d_j^L) + \sum_{i=u,c,t} m_{ij}(1+\frac{h}{\nu})(\bar{u}_i^L u_j^R + \bar{u}_i^R u_j^L) && (1.21)\\
d_{i,j}^{L,R} &= (d^{L,R}, s^{L,R}, b^{L,R}) && (1.22)\\
u_{i,j}^{L,R} &= (u^{L,R}, c^{L,R}, t^{L,R}) && (1.23)
\end{aligned}$$

$L_{quark-higgs}$ is described by mass matrix as,

$$L_{quark-higgs} = \begin{pmatrix} \bar{d^L} & \bar{s^L} & \bar{b^L} \end{pmatrix} \begin{pmatrix} m_{dd} & m_{ds} & m_{db} \\ m_{sd} & m_{ss} & m_{sb} \\ m_{bd} & m_{bs} & m_{bb} \end{pmatrix} \begin{pmatrix} d^R \\ s^R \\ b^R \end{pmatrix} + \begin{pmatrix} \bar{u^L} & \bar{c^L} & \bar{t^L} \end{pmatrix} \begin{pmatrix} m_{uu} & m_{uc} & m_{ut} \\ m_{cu} & m_{cc} & m_{ct} \\ m_{tu} & m_{tc} & m_{tt} \end{pmatrix} \begin{pmatrix} u^R \\ c^R \\ t^R \end{pmatrix} \quad (1.24)$$

where m_l and m_{ij} are defined as $m_l \equiv \nu g_l/\sqrt{2}$, and $m_{ij} \equiv \nu g_{ij}$. While in $L_{lepton-higgs}$, the interaction is self-transition, in $L_{quark-higgs}$, the interaction is not self-transition and mass matrix is not diagonal. Then $(d^L\ s^L\ b^L)$ is not mass eigenstate. To diagonalize the mass matrix, we introduce the following unitary matrix,

$$L_{quark-higgs} = \begin{pmatrix} \bar{d}^L & \bar{s}^L & \bar{b}^L \end{pmatrix} {V_{down}^L}^\dagger V_{down}^L m_d {V_{down}^R}^\dagger V_{down}^R \begin{pmatrix} d^R \\ s^R \\ b^R \end{pmatrix} + \begin{pmatrix} \bar{u}^L & \bar{c}^L & \bar{t}^L \end{pmatrix} {V_{up}^L}^\dagger V_{up}^L m_u {V_{up}^R}^\dagger V_{up}^R \begin{pmatrix} u^R \\ c^R \\ t^R \end{pmatrix} \quad (1.25)$$

where $V_L^\dagger V_L = 1$ because $V_R^\dagger V_R = 1$ for $V_{L,R}$ is unitary matrix,

$$\begin{aligned}
\begin{pmatrix} \bar{d^L}' & \bar{s^L}' & \bar{b^L}' \end{pmatrix} &\equiv \begin{pmatrix} \bar{d^L} & \bar{s^L} & \bar{b^L} \end{pmatrix} V_L^\dagger && (1.26)\\
m_d' &\equiv \begin{pmatrix} m_{dd}' & 0 & 0 \\ 0 & m_{ss}' & 0 \\ 0 & 0 & m_{bb}' \end{pmatrix} \equiv V_L m_d V_R^\dagger && (1.27)\\
\begin{pmatrix} d^{R'} \\ s^{R'} \\ b^{R'} \end{pmatrix} &\equiv V_R \begin{pmatrix} d^R \\ s^R \\ b^R \end{pmatrix} && (1.28)
\end{aligned}$$

According to these definition, the $L_{quark-higgs}$ can be written,

$$L_{quark-higgs} = \sum_{i=d,s,b} \left(1+\frac{h}{\nu}\right) m_i' \bar{q}_i' q_i' + \sum_{i=u,c,t} \left(1+\frac{h}{\nu}\right) m_i' \bar{q}_i' q_i' \quad (1.29)$$

where m_i', $\bar{q}_i'$, q_i' are physical mass(mass eigenvalue) and physical particle field(mass eigenstate). We must apply this unitary matrix to charged and neutral weak current interaction Lagrangian. The quark wave function are not physical filed and we replace these wave function to physical wave function by unitary matrix as follows,

$$\begin{aligned}
\bar{u}_i^L &= \bar{u}_i^L {V_{up}^L}^\dagger V_{up}^L \equiv \bar{u'}_i^L V_{up}^L && (1.30)\\
d_i^L &= {V_{down}^L}^\dagger V_{down}^L d_i^L \equiv {V_{down}^L}^\dagger d_i^{L'} && (1.31)
\end{aligned}$$

$$L_{CC}^{quark} = \frac{g}{2\sqrt{2}} \sum_{i=1}^{3} \{ \bar{u'}_i^L \gamma_\mu V_{up}^L {V_{down}^L}^\dagger d_i'^L W_\mu^+ + \bar{d'}_i^L \gamma_\mu V_{down}^L {V_{up}^L}^\dagger u_i'^L W_\mu^- \} \quad (1.32)$$

We define the $V^L_{up} {V^L_{down}}^\dagger \equiv V_{CKM}$, and $V^L_{down} {V^L_{up}}^\dagger \equiv V^\dagger_{CKM}$, the charged weak current Lagrangian is,

$$L^{quark}_{CC} = \frac{g}{2\sqrt{2}} \sum_{i=1}^{3} \{ \bar{u'}^L_i \gamma_\mu V_{CKM} d'^L_i W^+_\mu + \bar{d'}^L_i \gamma_\mu V^\dagger_{CKM} u'^L_i W^-_\mu \} \tag{1.33}$$

We can define the V_{CKM} as Cabbibo-Kobayashi-Maskawa Matrix[25], and its components are coupling constant of $(u, c, t) \leftrightarrow (d, s, b)$ transition. On the other hand, in the case of neutral currents, since the interaction is self-transition, the V_{CKM} is canceled for unitary condition. Fig 1.2 shows the pattern of charged weak current interaction.

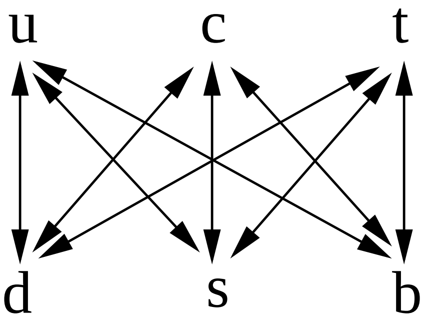

Figure 1.2: Transition through Charged Weak Current

1.1.2 C-transformation, P-transformation and CP-transformation

In general, the C-transformation(Charge-transformation) reverses the sign of charge. For example, applying the C-transformation to electron, the electron is transfered to positron which has positive charge. The P-transformation(Parity-transformation) means space reverse that the change of the sign in space coordinate. It transfers to the $r = (r_x, r_y, r_z)$ to $r' = (-r_x, -r_y, -r_z)$. In quantum field theory, the C and P-transformation are described by operator which keeps the invariance of Dirac equation. In Electromagnetic interaction, we assume the Dirac equation invariant under the C-transformation and P-transformation. To obtain the operator of P-transformation, we consider the P-transformation of Dirac equation,

$$(i\gamma^\mu \partial_\mu - m)\psi(x) = 0. \tag{1.34}$$

We operate the P-transformation, defined operator as 'P', $\partial_\mu \rightarrow \partial^\mu$ and $x \rightarrow -x$. To keep the invariance of Dirac equation, 'P' must satisfy the following conditions.

$$(i\gamma_\mu \partial^\mu - m)\psi(-x) = 0 \tag{1.35}$$

$$P^{-1}\gamma^\mu P = \gamma_\mu \tag{1.36}$$

We define the operator 'P' by Dirac matrix, γ^μ and γ^5. Hence the 'P' can be described as, $P = \gamma^0$. In the same way, we can define the operator of C-transformation by Charge symmetry of Dirac equation. In case of C-transformation, we must consider the Dirac equation includes the Electromagnetic field,

$$\{\gamma^\mu(i\partial_\mu - qA_\mu) - m\}\psi(x) = 0 \tag{1.37}$$

where q is charge of ψ. We operate C-transformation,'C'.

$$\{\gamma^\mu(i\partial_\mu + qA_\mu) - m\}\psi^c(x) = 0 \tag{1.38}$$

For conservate the charge symmetry, the 'C' must satisfies the following condition,

$$\psi^c = C \cdot \bar{\psi}^T \tag{1.39}$$

$$\bar{\psi}^T \equiv (\psi^\dagger \gamma^0)^T \tag{1.40}$$

$$C{\gamma^\mu}^T C^{-1} = -\gamma^\mu. \tag{1.41}$$

Then we can describe the 'C' as $C = i\gamma^0\gamma^2$. We can define the P-transformation and C-transformation by the operation which was describe by Dirac matrix as $P = \gamma^0$, $C = i\gamma^0\gamma^2$. CP-transformation means operating the C-transformation and P-transformation simultaneously. $CP = C \cdot P = (C = i\gamma^0\gamma^2) \cdot (P = \gamma^0) = i\gamma^0\gamma^2\gamma^0$. We summarize the C-transformation, P-transformation and CP-transformation on wave function(Dirac spinor), and on Dirac-field vilinears,

$$\mathbf{P} \quad - \quad \textbf{transformation} \;\; \psi \to \gamma^0\psi \quad \bar{\psi} \to \bar{\psi}\gamma^0 \tag{1.42}$$

$$\mathbf{C} \quad - \quad \textbf{transformation} \;\; \psi \to i\gamma^2\gamma^0\bar{\psi}^T \quad \bar{\psi} \to i\psi^T\gamma^2\gamma^0 \tag{1.43}$$

$$\mathbf{CP} \quad - \quad \textbf{transformation} \;\; \psi \to i\gamma^0\gamma^2\gamma^0\bar{\psi}^T \quad \bar{\psi} \to i\psi^T\gamma^2\gamma^0\gamma^0 \tag{1.44}$$

$$\left\{ \begin{array}{l} S : \bar{\psi}_1\psi_2 \to \bar{\psi}_2\psi_1 \\ P : i\bar{\psi}_1\gamma^5\psi_2 \to -i\bar{\psi}_2\gamma^5\psi_1 \\ V : \bar{\psi}_1\gamma^\mu\psi_2 \to -i\bar{\psi}_2\gamma_\mu\psi_1 \\ A : \bar{\psi}_1\gamma^5\gamma^\mu\psi_2 \to -\bar{\psi}_2\gamma^5\gamma_\mu\psi_1 \\ T : \bar{\psi}_1\sigma^{\mu\nu}\psi_2 \to -\bar{\psi}_2\sigma_{\mu\nu}\psi_1 \end{array} \right. \tag{1.45}$$

where S, P, V, A, T is scalar, psudescalar, vector, axial vector and tensor,respectively.

While the Electromagnetic interaction conserves the C and P and CP symmetry. On the other hand, the weak interaction does not always conserve the C and P and CP symmetry. Lee and Yang expected the P-Violation(Parity Violation) in 1956[26], and in 1957 the Wu found the P-Violation by observing up-down asymmetry of electron from ^{60}Co β-decay, $^{60}\text{Co} \to \text{Ni}^* + e^- + \bar{\nu_e}$[27]. The C-Violation was also proved in this experiment. In 1958, the Goldhaber[28] found the P-Violation by measurement of the neutrino helicity from electron capture by ^{152}Eu. From this experiment, the neutrino helicity is '-1'. This means neutrino is always left handed and P symmetry is 100% violated in weak interaction. Further, in 1964 the CP-Violation was found in $K^0 - \bar{K}^0$ Mixing system[9]. In weak interaction, the paritcle to anti-particle transformation is CP-transformation. Left-handed particle and right-handed anti-paritcle can interact in weak decay. If we operate P-transformation to a particle which has spin=1/2, the direction of motion is reversed, but the direction of spin is not reversed because spin is axial vector, and the helicity is reversed, $helicity = \sigma \cdot p / |\sigma \cdot p|$. This means the left-handed changed to right-handed. Since a particle which has right-handed is not exist in weak interaction, only P-transformation has no meaning in physics, this is same as P-Violation. Similarity, only C-transformation has no meaning in physics. The P and C-transformation must be operated simultaneously, a left-handed particle is transformed to a right-handed anti-particle. We can confirm the C and P Violation with the charge and neutral weak interaction Lagrangian, these Lagrangian include $(\gamma^\mu - \gamma^\mu\gamma^5)$ factor, this is Vector and Axial Vector and we call weak interaction 'V-A interaction', and we operate the C and P-transformation to this $(\gamma^\mu - \gamma^\mu\gamma^5)$ as follows,

$$\left\{ \begin{array}{ll} \textbf{P-transformation} & i\bar{\psi}_1(\gamma^\mu - \gamma^5\gamma^\mu)\psi_2 \Rightarrow i\bar{\psi}_2(\gamma_\mu + \gamma^5\gamma_\mu)\psi_1 \\ \textbf{C-transformation} & i\bar{\psi}_1(\gamma^\mu - \gamma^5\gamma^\mu)\psi_2 \Rightarrow -i\bar{\psi}_2(\gamma_\mu + \gamma^5\gamma_\mu)\psi_1 \end{array} \right. \tag{1.46}$$

While in the case of CP-transformation, we must consider the CKM matrix, because the CP-symmetry is conserved without the CKM matrix. We consider the following Lagrangian,

$$L = L_0 + L_0^\dagger \tag{1.47}$$

where $L_0^\dagger$ is Hermite conjugatoin. If the L_0 describes the particle interactions, the $L_0^\dagger$ describes the anti-paritcle interaction. For example L_0 is $d \to u$ transition, the $L_0^\dagger$ is $\bar{d} \to \bar{u}$ transition as shown in Fig 1.4. We consider the CP-transformation to charged weak current interaction Lagrangian,

$$L_0 = L_{CC} = -\frac{g}{2} V_{ij}\bar{\psi}_j\gamma_\mu(1-\gamma^5)\psi_i W^{\mu+} \tag{1.48}$$

$$\textbf{P-Transformation} \quad \Rightarrow \quad L_0^P = -\frac{g}{2} V_{ij}\bar{\psi}_j\gamma_\mu^\dagger(1+\gamma^5)\psi_i W^{\mu+} \tag{1.49}$$

$$\textbf{Addition to C-Transformation} \quad \Rightarrow \quad L_0^{CP} = -\frac{g}{2} V_{ij}\bar{\psi}_i\gamma_\mu(1-\gamma^5)\psi_j W^{\mu-} \tag{1.50}$$

And we can describe the Hermite conjugation of L_0 as follows,

$$L_0^\dagger = -\frac{g}{2} V_{ij}^*\bar{\psi}_i\gamma_\mu(1-\gamma^5)\psi_j W^{\mu-}. \tag{1.51}$$

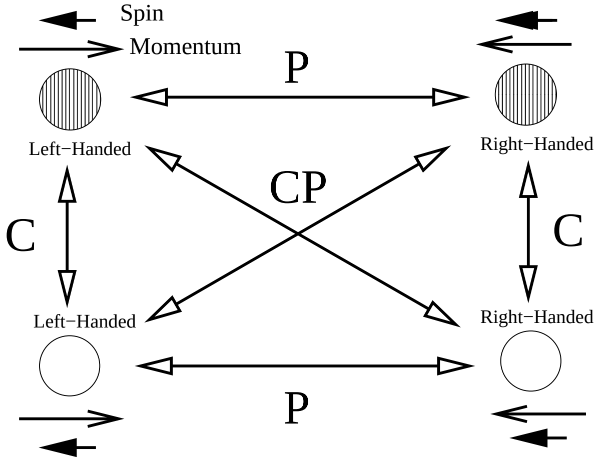

Figure 1.3: C, P and CP Transformation
In Weak interaction the only C and P transformation is forbidden, the CP-transformation is only allowed.

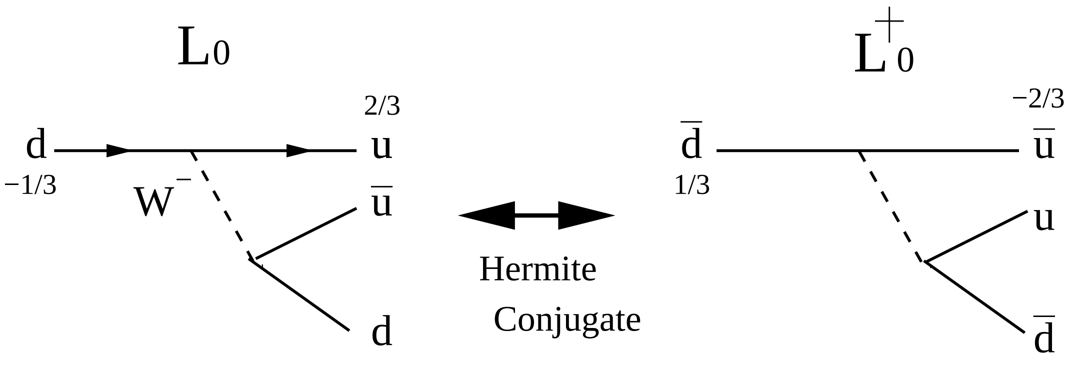

Figure 1.4: The example of Lagrangian and its Hermite conjugate

comparing the L_0^{CP} and $L_0^\dagger$, the difference is only CKM matrix elements, V_{ij} and V_{ij}^*. If the CKM matrix elements has only real part, V_{ij} and V_{ij}^* are identical, $L_0^{CP} = L_0^\dagger$, but if CKM matrix has imaginaly part elements, the V_{ij} and V_{ij}^* has difference. This means $L_0^{CP} \neq L_0^\dagger$, in addition we can find $L_0^{CP} \neq L_0^\dagger \neq L_0$, and we can understand that the kinematics of particle and anti-particle is different. This means 'CP-Voilation'. We can summarize,

$$\begin{cases} L_0^\dagger = L_0^{CP} & \Rightarrow L_0 = L_0^\dagger = L_0^{CP} \rightarrow \textbf{CP-conservation} \\ L_0^\dagger \neq L_0^{CP} & \Rightarrow L_0 \neq L_0^\dagger \neq L_0^{CP} \rightarrow \textbf{CP-violation} \end{cases} \tag{1.52}$$

On the other hand, neutral weak current interaction Lagrangian does not have CKM matrix elements, and conserve CP-symmetry. From all discussion above, in weak interaction, there are possibility that we can measure CP-violation in charged weak current interaction.

1.2 CP Violation in B Physics

1.2.1 Model of Cabbibo-Kobayashi-Maskawa Matrix

Kobayashi and Maskawa proposed the CKM matrix, which is 3 × 3 matrix in 1973[25]. In that time, the number of quark discovered was 3, u-quark, d-quark, and s-quark. Kobayashi and Maskawa predicted that the number of quark more than two is neccessary to explaine the principle of CP-Violation within the Standard Model. The CKM Matrix is defined as 3 × 3 unitary matrix, which has one complex phase. In general, $N \times N$ matrix has $(N-1)(N-2)/2$ complex phase. The definition of the CKM matrix is $V_{CKM} \equiv V_{up}^L V_{down}^{\dagger L}$, and the Matrix elements are described as following,

$$V_{CKM} \equiv \begin{pmatrix} V_{ud} & V_{us} & V_{ub} \\ V_{cd} & V_{cs} & V_{cb} \\ V_{td} & V_{ts} & V_{tb} \end{pmatrix}. \tag{1.53}$$

Each component, V_{ji}, means the coupling constant of transition from i-quark to j-quark. The first parameterization of CKM matrix proposed by Kobayashi and Maskawa is,

$$V_{CKM} \equiv \begin{pmatrix} c_1 & -s_1c_3 & -s_1s_3 \\ s_1c_2 & c_1c_2c_3 - s_2s_3e^{i\delta} & c_1s_2s_3 + s_2c_3e^{i\delta} \\ s_1s_2 & c_1s_2c_3 + c_2s_3e^{i\delta} & c_1s_2s_3 - c_2c_3e^{i\delta} \end{pmatrix}. \tag{1.54}$$

And the Chau and Keung parametrization are proposed in 1984[29],

$$V_{CKM} \equiv \begin{pmatrix} c_3c_2 & -s_3c_2 & -s_2e^{i\delta} \\ -s_3c_1 - c_2s_1s_2e^{i\delta} & c_3c_1 - s_3s_1s_2e^{i\delta} & s_1c_2 \\ s_3c_1 - c_2c_1s_2e^{i\delta} & -c_3s_1 - s_3c_1s_2e^{i\delta} & c_1c_2 \end{pmatrix}. \tag{1.55}$$

where, c_i is $\cos\theta_i$, s_i is $\sin\theta_i$ and δ is complex phase. The most popular parametrization is Wolfstein parameterization[30] as,

$$V_{CKM} \equiv \begin{pmatrix} 1-\lambda^2/2 & \lambda & A\lambda^3(\rho - i\eta) \\ -\lambda & 1-\lambda^2/2 & A\lambda^2 \\ A\lambda^3(1-\rho-i\eta) & -A\lambda^2 & 1 \end{pmatrix} + O(\lambda^4). \tag{1.56}$$

where λ is Cabbibo angle, ρ and η can be modified by power correction in λ , the modified ρ, η are defined as,

$$\bar{\rho} \equiv \rho\left(1 - \frac{1}{2}\lambda^2\right) \tag{1.57}$$

$$\bar{\eta} \equiv \eta\left(1 - \frac{1}{2}\lambda^2\right) \tag{1.58}$$

Since the CKM Matrix is unitary, from unitary relation,

$$\sum_j V_{ij}V_{jk}^* = 0 \tag{1.59}$$

$$\begin{cases} V_{ud}^*V_{us} + V_{cd}^*V_{cs} + V_{td}^*V_{ts} = 0 \ (= O(\lambda) + O(\lambda) + O(\lambda^5) \ ) \\ V_{ud}^*V_{ub} + V_{cd}^*V_{cb} + V_{td}^*V_{tb} = 0 \ (= O(\lambda^3) + O(\lambda^3) + O(\lambda^3) \ ) \\ V_{us}^*V_{ub} + V_{cs}^*V_{cb} + V_{ts}^*V_{tb} = 0 \ (= O(\lambda^4) + O(\lambda^2) + O(\lambda^2) \ ) \\ V_{ud}^*V_{cd} + V_{us}^*V_{cs} + V_{ub}^*V_{cb} = 0 \ (= O(\lambda) + O(\lambda) + O(\lambda^5) \ ) \\ V_{ud}^*V_{td} + V_{us}^*V_{ts} + V_{ub}^*V_{tb} = 0 \ (= O(\lambda^3) + O(\lambda^3) + O(\lambda^3) \ ) \\ V_{cd}^*V_{td} + V_{cs}^*V_{ts} + V_{cb}^*V_{tb} = 0 \ (= O(\lambda^4) + O(\lambda^2) + O(\lambda^2) \ ) \end{cases} \tag{1.60}$$

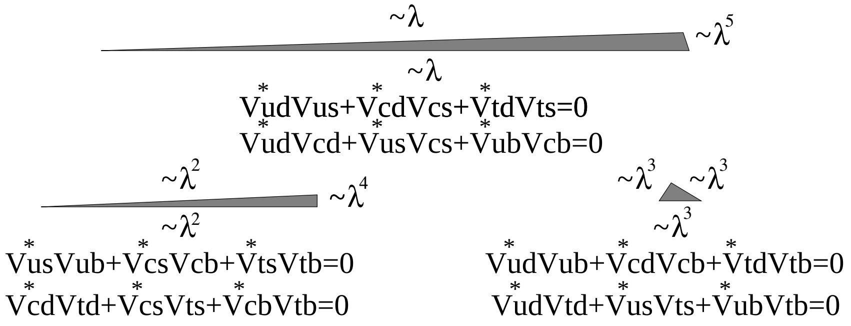

Figure 1.5: Two unbalanced Unitary Triangles and One effective Unitary Triangle for studying CP-Violation

These six equations make closed triangle with Wolfstein parameters on complex plane as Fig 1.5. It can be drawn the three triangles. The first triangle is made from first and fourth equations which relates CP-violation of K-meson system. The second triangle is made by third and sixth equations which relates CP-violation of B_s system, and last triangle is made by second and fifth equations. In the first two triangle, one side is much shorter than other side. Because of this, the effect of CP-violation of K-meson system and B_S system are small. For CP-Violation of B_d-Physics, we use second and fifth equations. We describe these equations with Wolfstein parameters,

$$\begin{aligned} V_{ud}^*V_{ub} + V_{cd}^*V_{cb} + V_{td}^*V_{tb} &= 0 \\ V_{ud}^*V_{td} + V_{us}^*V_{ts} + V_{ub}^*V_{tb} &= 0 \\ &\downarrow \\ V_{ud}V_{ub}^* + V_{cd}V_{cb}^* + V_{td}V_{tb}^* &= 0 \\ &\downarrow \\ A\lambda^3(\bar{\rho} + i\bar{\eta}) - A\lambda^3 + A\lambda^3(1 - \bar{\rho} - i\bar{\eta}) &= 0 \\ &\downarrow \\ A\lambda^3\{(\bar{\rho}, \bar{\eta}) + (-1, 0) + (1 - \bar{\rho}, -\bar{\eta})\} &= 0 \end{aligned} \tag{1.61}$$

The unitary triangle is shown in Fig 1.6, and we define the each angle of triangle,

$$\begin{cases} \phi_1 \equiv \mathbf{Arg}\left[-\frac{V_{cd}V_{cb}^*}{V_{tb}V_{td}^*}\right] \\ \phi_2 \equiv \mathbf{Arg}\left[-\frac{V_{td}V_{tb}^*}{V_{ud}V_{ub}^*}\right] \\ \phi_3 \equiv \mathbf{Arg}\left[-\frac{V_{ud}V_{ub}^*}{V_{cd}V_{cb}^*}\right] \end{cases} \tag{1.62}$$

and we can express these angle by Wolfstein parameters,

$$\begin{cases} \mathbf{sin}\phi_1 = \frac{\bar{\eta}}{\sqrt{(1-\bar{\rho}^2)+\bar{\eta}^2}} \\ \mathbf{sin}\phi_2 = \frac{\bar{\eta}}{\sqrt{\bar{\rho}^2+\bar{\eta}^2}\sqrt{(1-\bar{\rho}^2)+\bar{\eta}^2}} \\ \mathbf{sin}\phi_3 = \frac{\bar{\eta}}{\sqrt{\bar{\rho}^2+\bar{\eta}^2}} \end{cases} \tag{1.63}$$

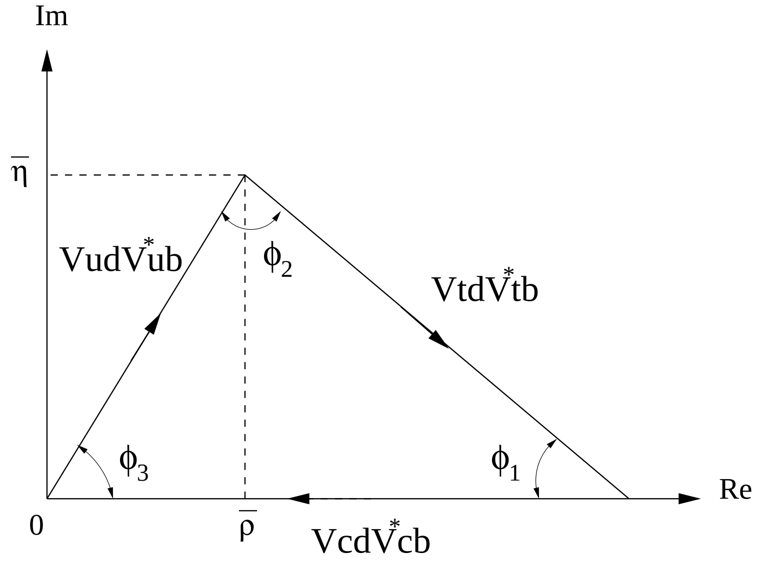

Figure 1.6: The Unitary Triangle used Wolfstein parameter on complex plain

As follows, the sided of the unitary triangle and the magnitude of the CKM matrix elements are measured by nuclear beta decay, $K^{\pm}$, K^0, decay, neutrino production of charm and from semileptonic D decay, and semileptonic B decays to charmed m, and so on[31][32].

$$
\begin{aligned}
\sqrt{\bar{\rho}^2+\bar{\eta}^2} &= 0.36 \ \pm 0.09 && (1.64)\\
\lambda &= 0.2205 \pm 0.0018 && (1.65)\\
A &= 0.80 \pm 0.04 && (1.66)
\end{aligned}
$$

The world average of these elements are[24],

$$
V_{CKM} = \begin{pmatrix} 0.9730 \sim 0.9746 & 0.2174 \sim 0.2241 & 0.0030 \sim 0.0044 \\ 0.213 \sim 0.226 & 0.968 \sim 0.975 & 0.039 \sim 0.044 \\ 0 \sim 0.08 & 0 \sim 0.11 & 0.07 \sim 0.9993 \end{pmatrix} \tag{1.67}
$$

Fig 1.7 shows the constrains to the unitary triangle obtained from various experiments. The mixing parameter $\Delta m_{d,s}$ in the $B_{d,s}$ system, CKM matrix element $|V_{ub}V_{cb}|$, the CP violation parameter ϵ_k in the neutral K system, the CP violation parameter sin$2\phi_1$ in the neutral B meson system are plotted. The four bands crossing at (1,0) represents sin$2\phi_1$ measurement.

1.2.2 Mixing of Neutral B Meson System (B^0-$\bar{B}^0$ Mixing)

In this section, we treat the quantum mechanics of two state of neutral B meson, the system of neutral B mesons which behave like neutral K-Mesons. There are two type of neutral meson involving b-quark. One is B_d^0 meson which consists of b-quark and d-quark. The other one is B_s^0 mesons which consists of b-quark and s-quark. There are two flavor eigenstate. For ample $B_d^0 = \bar{b}d$ and $\bar{B}_d^0 = b\bar{d}$. But B^0 and $\bar{B}^0$ are not CP-eigenstate, because if we operate the CP-transformation to B^0, B^0 transform to $\bar{B}^0$, and $B^0 \neq \bar{B}^0$, $B_d^0 \neq \bar{B}_d^0$. Then we can define the CP-eigenstate of neutral B^0 by linear combination of B^0 and $\bar{B}^0$ as follows,

$$
\begin{cases} |B_{cp+} > \equiv \frac{|B^0>+|\bar{B}^0>}{\sqrt{2}} \\ |B_{cp-} > \equiv \frac{|B^0>-|\bar{B}^0>}{\sqrt{2}} \end{cases} \tag{1.68}
$$

where $|B_{cp+}>$ has eigen value as '+1', and $|B_{cp-}>$ has eigen value as '-1'. If CP are symmetric, the $|B_{cp+}>$ and $|B_{cp-}>$ are mass eigenstate. If, however, CP is not symmetric, the mass eigenstate is difference from

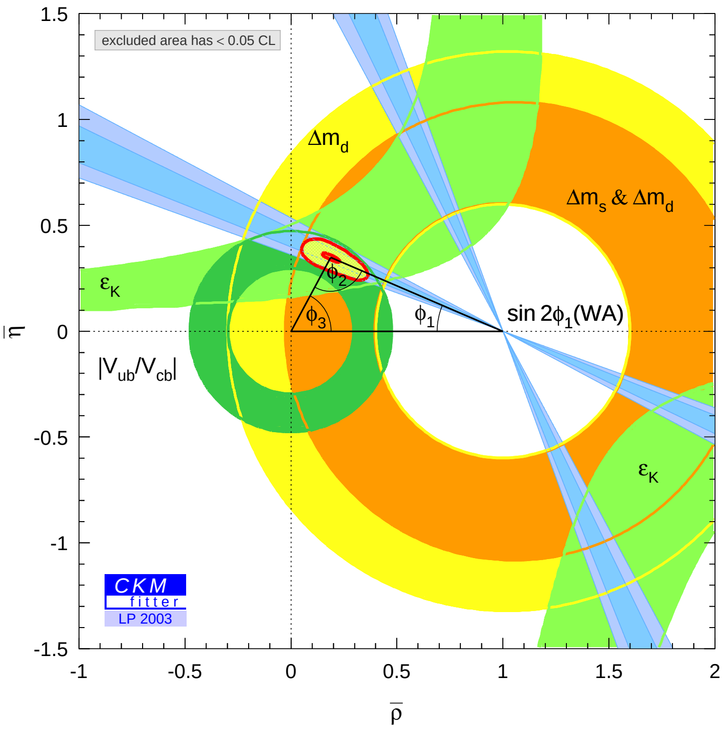

Figure 1.7: Experimental constrains to the unitary triangle

$|B_{cp+}>$ and $|B_{cp-}>$ and the mixing occures between two state. The mass eigenstate are defined as $|B^H>$ and $|B^L>$, the 'H' means 'Heavy' and 'L' means 'Light', and these can be written by linear combination of $|B_{cp+}>$ and $|B_{cp-}>$ and mixing parameter, ϵ, as,

$$\begin{cases} |B^L >\equiv \{|B_{cp+}> +\epsilon|B_{cp-}>\}/\sqrt{1+|\epsilon|^2} \\ |B^H >\equiv \{|B_{cp-}> +\epsilon|B_{cp+}>\}/\sqrt{1+|\epsilon|^2} \end{cases} \tag{1.69}$$

$$\begin{cases} |B^L >\equiv \frac{1}{\sqrt{2(1+|\epsilon|^2)}}\{(1+\epsilon)|B^0> +(1-\epsilon)|\bar{B^0}>\} \equiv p|B^0> +q|\bar{B^0}> \\ |B^H >\equiv \frac{1}{\sqrt{2(1+|\epsilon|^2)}}\{(1+\epsilon)|\bar{B^0}> -(1-\epsilon)|B^0>\} \equiv p|B^0> -q|\bar{B^0}> \end{cases} \tag{1.70}$$

where we define mixing parameters p and q as $p \equiv (1+\epsilon)/\sqrt{2(1+|\epsilon|^2)}$ and $q \equiv (1-\epsilon)/\sqrt{2(1+|\epsilon|^2)}$, p and q satisfy $|p|^2+|q|^2=1$. Then $|B^0>$ and $|\bar{B^0}>$ can be expressed by mass eigenstate and mixing parameter as follows,

$$|B^0> \quad = \quad (|B^H> +|B^L>)/2p \tag{1.71}$$

$$|\bar{B^0}> \quad = \quad -(|B^H> -|B^L>)/2q \tag{1.72}$$

We consider the time evolution of $|B^0>$ and $|\bar{B^0}>$. The time dependent Schrödinger equation and it's solution are,

$$\frac{\partial\psi}{\partial t} = \left(M - i\frac{\Gamma}{2}\right)\psi \rightarrow \psi(t) = \psi(0)e^{-iMt}e^{-\frac{\Gamma}{2}t} \tag{1.73}$$

$$\begin{aligned} M - i\frac{\Gamma}{2} &= \begin{pmatrix} \tilde{M}_{11} & \tilde{M}_{12} \\ \tilde{M}_{21} & \tilde{M}_{22} \end{pmatrix} \quad : \tilde{M}_{ij} = M_{ij} - i\frac{\Gamma_{ij}}{2} \\ &= \begin{pmatrix} M_0 - i\frac{\Gamma_0}{2} & M_{12} - i\frac{\Gamma_{12}}{2} \\ M_{21}^* - i\frac{\Gamma_{21}^*}{2} & M_0 - i\frac{\Gamma_0}{2} \end{pmatrix} \end{aligned} \tag{1.74}$$

where M and Γ are 2×2 effective Hamiltonian matrix. M is mass Hamiltonian and Γ is decay Hamiltonian, the diagonal elements are associated with the flavor conservating transitions, $M^0 \to M^0$ or $\bar{M}^0 \to \bar{M}^0$, while off-diagonal elements are associated with flavor-changing transitions, $M^0 \to \bar{M}^0$. $\phi(0)$ is initial state at $t = 0$. We define the $\lambda_{H,L} = M_{+,-} - i\Gamma_{+,-}/2$. The time evolution of mass eigenstate is $|B^H(t) >= |B^H(0) > e^{-i\lambda_H t}$, $|B^L(t) >= |B^L(0) > e^{-i\lambda_L t}$, and time evolution of $|B^0(t) >$ and $|\bar{B}^0(t) >$ are written by $|B^H(t) >$ and $|B^L(t) >$ as follows,

$$\lambda_{H,L} = \frac{\tilde{M}_{11} + \tilde{M}_{22}}{2} \pm \sqrt{\tilde{M}_{12}\tilde{M}_{21}} \tag{1.75}$$

$$\begin{aligned}
|B^0(t) > &= \frac{1}{2p}\{|B^H(0) > e^{-i\lambda_H t} + |B^L(0) > e^{-i\lambda_L t}\} \tag{1.76}\\
&= \left(\frac{e^{-i\lambda_H t} - e^{-i\lambda_L t}}{2}\right)|B^0(0) > + \left(\frac{q}{p}\right)\left(\frac{e^{-i\lambda_H t} + e^{-i\lambda_L t}}{2}\right)|\bar{B}^0(0) > \tag{1.77}\\
|\bar{B}^0(t) > &= \frac{1}{2q}\{|B^H(0) > e^{-i\lambda_H t} - |B^L(0) > e^{-i\lambda_L t}\} \tag{1.78}\\
&= \left(\frac{p}{q}\right)\left(\frac{e^{-i\lambda_H t} - e^{-i\lambda_L t}}{2}\right)|B^0(0) > + \left(\frac{e^{-i\lambda_H t} + e^{-i\lambda_L t}}{2}\right)|\bar{B}^0(0) > \tag{1.79}
\end{aligned}$$

$$\begin{aligned}
|B^0(t) > &= e^{-iMt}e^{-\frac{\Gamma}{2}t}\{\mathbf{cos}\left(\frac{\Delta mt}{2}\right)|B^0(0) > -i\left(\frac{q}{p}\right)\mathbf{sin}\left(\frac{\Delta mt}{2}\right)|\bar{B}^0(0) >\} \tag{1.80}\\
|\bar{B}^0(t) > &= e^{-iMt}e^{-\frac{\Gamma}{2}t}\{\left(\frac{p}{q}\right)\mathbf{cos}\left(\frac{\Delta mt}{2}\right)|B^0(0) > -\mathbf{sin}\left(\frac{\Delta mt}{2}\right)|\bar{B}^0(0) >\} \tag{1.81}
\end{aligned}$$

where $|B^0(0) >$ and $|\bar{B}^0(0) >$ mean that the initial state is B^0 at t=0 and $\bar{B}^0$ >, respectively. Then we take average of Γ_H and Γ_L, M_H and M_L as $\Gamma \equiv (\Gamma_H + \Gamma_L)/2$, $M \equiv (M_H + M_L)/2$, and take the difference, $\Delta\Gamma \equiv \Gamma_H - \Gamma_L$ and $\Delta m \equiv M_H - M_L$. The Δm and $\Delta\Gamma$ can be written as,

$$\begin{aligned}
\Delta m &= 2\mathbf{Re}\sqrt{\left(M_{12} - i\frac{\Gamma_{12}}{2}\right)\left(M_{12}^* - i\frac{\Gamma_{12}^*}{2}\right)} \tag{1.82}\\
\Delta\Gamma &= -4\mathbf{Im}\sqrt{\left(M_{12} - i\frac{\Gamma_{12}}{2}\right)\left(M_{12}^* - i\frac{\Gamma_{12}^*}{2}\right)} \tag{1.83}
\end{aligned}$$

Matrix elements, M_{12} and Γ_{12} are,

$$\begin{aligned}
M_{12} &= < B^0|\tilde{M}|\bar{B}^0 > \\
&= -\frac{G_F^2}{12\pi^2}m_W^2\eta_{QCD}B_Bf_B^2m_B\lambda_t^2x_tF(x_t) \tag{1.84}\\
\Gamma_{12} &= \frac{G_F^2}{8\pi^2}B_Bf_B^2m_Bm_b^2[\lambda_t^2 + \frac{8}{3}\lambda_t\lambda_c\frac{m_c^2}{m_b^2}] \tag{1.85}
\end{aligned}$$

where, $\eta_{QCD} \sim 0.55$[33], QCD correction factor, $\lambda_t = V_{tb}V_{td}$, $B_B = 1.4 \pm 0.1$[34][35][36], QCD unperturbationi effect factor, and $f_B = 175 \pm 25MeV$[34][35][36].

The probability of $B^0 - \bar{B}^0$ mixing can be calculated from Eq 1.80, Eq 1.81. We can written a four pattern of $B^0 - \bar{B}^0$ mixing probability, $P(B^0 \to B^0)$, the probability that the initial state at t=0 is B^0 and a state at t=t is B^0, and $P(B^0 \to \bar{B}^0)$, $P(\bar{B}^0 \to \bar{B}^0)$, $P(\bar{B}^0 \to B^0)$. The plot of time evolution of $B^0 - \bar{B}^0$

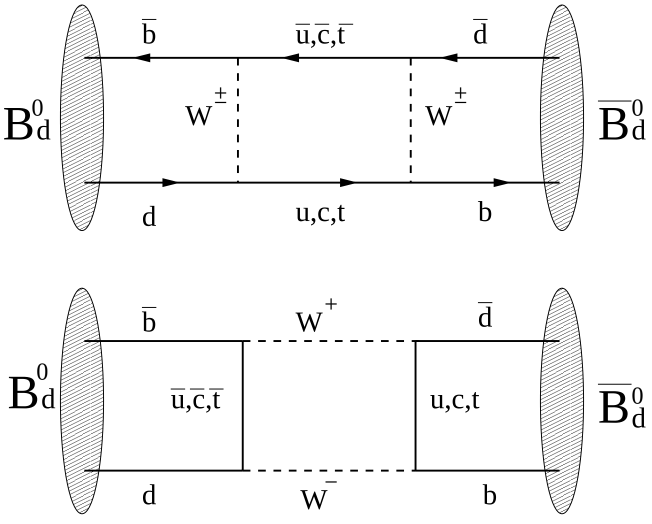

Figure 1.8: The Box-diagram of $B^0 - \bar{B}^0$ Mixing process

The dominant inner quark of $B^0 - \bar{B}^0$ Mixing is top quark, and other two inner quark,u-quark and c-quark do not contribute the $B^0 - \bar{B}^0$ Mixing.

Mixing and decay probability are shown in Fig 1.9.

$$P(B^0 \to B^0) = |<B^0(t)|B^0(0)>|^2 = e^{-\Gamma t}\mathbf{cos}^2\left(\frac{\Delta m t}{2}\right) \quad (1.86)$$

$$P(B^0 \to \bar{B}^0) = |<\bar{B}^0(t)|B^0(0)>|^2 = \left(\frac{q}{p}\right) e^{-\Gamma t}\mathbf{sin}^2\left(\frac{\Delta m t}{2}\right) \quad (1.87)$$

$$P(\bar{B}^0 \to \bar{B}^0) = |<\bar{B}^0(t)|\bar{B}^0(0)>|^2 = \left(\frac{p}{q}\right) e^{-\Gamma t}\mathbf{cos}^2\left(\frac{\Delta m t}{2}\right) \quad (1.88)$$

$$P(\bar{B}^0 \to B^0) = |<\bar{B}^0(t)|B^0(0)>|^2 = e^{-\Gamma t}\mathbf{sin}^2\left(\frac{\Delta m t}{2}\right) \quad (1.89)$$

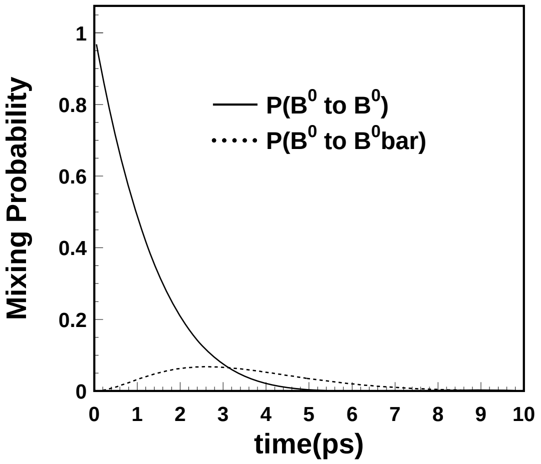

Figure 1.9: Time evolution of $B^0 - \bar{B}^0$-Mixing Probability

The average of mixing probability of $P(B^0 \to B^0)$ and $P(\bar{B}^0 \to \bar{B}^0)$ can be calculated by integrating the time from $t = 0$ to $t = \infty$, and ratio of $P(B^0 \to B^0)$ and $P(\bar{B}^0 \to \bar{B}^0)$ is 0.229[24], where $|q/p| \sim 1$, and $\Delta m/\Gamma = 0.771 \pm 0.012(B_d^0 - \bar{B}_d^0 \text{ system})$[24].

$$\int_0^\infty P(B^0 \to B^0)dt = \frac{1}{2\Gamma}\{\frac{(\Delta m/\Gamma)^2+2}{(\Delta m/\Gamma)^2+1}\} \tag{1.90}$$

$$\int_0^\infty P(\bar{B}^0 \to \bar{B}^0)dt = \frac{1}{2\Gamma}|\frac{q}{p}|^2\{\frac{(\Delta m/\Gamma)^2}{(\Delta m/\Gamma)^2+1}\} \tag{1.91}$$

$$\frac{\int_0^\infty P(\bar{B}^0 \to \bar{B}^0)dt}{\int_0^\infty P(B^0 \to B^0)dt} = |\frac{q}{p}|^2\left(\frac{(\Delta m/\Gamma)^2}{(\Delta m/\Gamma)^2+2}\right) \tag{1.92}$$

$$\frac{\Delta m}{\Gamma} = \frac{\Delta m_d}{\Gamma_d} \equiv x_q \tag{1.93}$$

$$= \tau_{B_q}\frac{G_F^2}{6\pi^2}m_W^2\eta_{QCD}B_B f_B^2 m_B|V_{tb}V_{tq}^*|^2 x_t F(x_t) \tag{1.94}$$

1.3 CP Violation and B-Factory Experiment

The B-factory experiment product large quantities of $B\bar{B}$ pairs, include $B_d^0\bar{B}_d^0$ and $B^+\bar{B}^-$ meson pairs with e^+e^- Collider accelerator. Since $B\bar{B}$ pair can be produced by decay of $\Upsilon(4S)$ resonance, the total energy in center of mass must be 10.58GeV/c^2. The B-factory experiment is much effective for studying CP Violation to compare the property of particle and anti-particle. There are three type of CP Violation, one is direct CP-Violation, second is indirect CP-Violation, and last is interference CP-Violation. In this section we explain the detail of concepts of these CP Violation.

1.3.1 CP-Violation Type-I : Direct CP Violation in the Weak decays

The direct CP-Violation can be occurred in both charged and neutral B decay. We assume the CPT-invariant and define the decay amplitude of B and $\bar{B}$ meson, where B implies neutral meson and charged meson.

$$A(B \to f) = \sum_i^N |D_i|e^{i\phi_i}e^{i\delta_i} \tag{1.95}$$

$$\bar{A}(\bar{B} \to \bar{f}) = \sum_i^N |D_i|e^{-i\phi_i}e^{i\delta_i} \tag{1.96}$$

where f is final state, and D_i is decay amplitude in weak interaction, ϕ_i is weak interaction phase called 'weak phase', δ_i is final scattering phase of strong interaction called 'strong phase', 'N' is number of the different intermediate state, i.e. differenct decay process. In this section, we assume $N = 2$, the number of decay process is two and calculate the decay rate of $B \to f$, $\bar{B} \to \bar{f}$ and define the asymmetry of decay rate as follows,

$$A(B \to f) = |D_1|e^{i\phi_1}e^{i\delta_1} + |D_2|e^{i\phi_2}e^{i\delta_2} \tag{1.97}$$

$$\bar{A}(\bar{B} \to \bar{f}) = |D_1|e^{-i\phi_1}e^{i\delta_1} + |D_2|e^{-i\phi_2}e^{i\delta_2} \tag{1.98}$$

$$|A(B \to f)|^2 = |D_1|^2 + |D_2|^2 + 2|D_1||D_2|\mathbf{cos}(\Delta\phi + \Delta\delta) \tag{1.99}$$

$$|\bar{A}(B \to f)|^2 = |D_1|^2 + |D_2|^2 + 2|D_1||D_2|\mathbf{cos}(\Delta\phi - \Delta\delta) \tag{1.100}$$

$$\begin{aligned} Asymmetry &= \frac{|A(B \to f)|^2 - |\bar{A}(\bar{B} \to \bar{f})|^2}{|A(B \to f)|^2 + |\bar{A}(\bar{B} \to \bar{f})|^2} \\ &= \frac{-2|D_1||D_2|\mathbf{sin}(\Delta\phi)\mathbf{sin}(\Delta\delta)}{|D_1|^2 + |D_2|^2 + 2|D_1||D_2|\mathbf{cos}(\Delta\phi)\mathbf{cos}(\Delta\delta)} \end{aligned} \tag{1.101}$$

Where $\Delta\phi \equiv \phi_1 - \phi_2$, $\Delta\delta \equiv \delta_1 - \delta_2$. If one of the phase difference is zero, the asymmetry is also zero. The different decay rate of $A(B \to f)$ and $\bar{A}(\bar{B} \to barf)$ means CP-Violation in decay. In general, the direct CP-violation needs the interference of two or more difference decay process, and different complex weak phase of CKM matrix and strong phase.

1.3.2 CP-Violation type-II : Indirect CP Violation in Mixing Neutral B^0

The second type is indirect CP Violation. This CP-Violation occurs in mixing, if mass eigenstate is not same as CP-eigenstate. For measurement of this CP-violation, we need observe the $B^0 - \bar{B}^0$ decay to semi-leptoninc decay and measure the time integrated asymmetry. We can determinate the B^0 flavor by a charge of lepton, because b-quark decay to $q + l^- + \bar{\nu}$, and a $\bar{b}$-quark decays to $\bar{q} + l^+ + \nu$. Since we can assume the decay rate of $b \to l$, $\bar{b} \to \bar{l}$ are same, the asymmetry depends on only mixing probability, $P(B^0 \to B^0)$, $P(B^0 \to \bar{B}^0)$, $P(\bar{B}^0 \to \bar{B}^0)$, and $P(\bar{B}^0 \to B^0)$. The decay rate is proportional to mixing probability.

$$Asymmetry = \frac{\Gamma(B^0 \to \bar{B}^0 \to l^-)\Gamma(\bar{B}^0 \to l^-) - \Gamma(B^0 \to l^+)\Gamma(\bar{B}^0 \to B^0 \to l^+)}{\Gamma(B^0 \to \bar{B}^0 \to l^-)\Gamma(\bar{B}^0 \to l^-) + \Gamma(B^0 \to l^+)\Gamma(\bar{B}^0 \to B^0 \to l^+)} \tag{1.102}$$

$$\begin{aligned}
\Gamma(B^0 \to \bar{B}^0 \to l^-)\Gamma(\bar{B}^0 \to l^-) &\propto P(B^0 \to \bar{B}^0) \times P(\bar{B}^0 \to \bar{B}^0) \\
&= \{\frac{1}{2\Gamma}|\frac{q}{p}|^2\frac{x^2}{1+x^2}\} \times \{\frac{1}{2\Gamma}\frac{2+x^2}{1+x^2}\} \qquad (1.103) \\
\Gamma(B^0 \to l^+)\Gamma(\bar{B}^0 \to B^0 \to l^+) &\propto P(B^0 \to B^0) \times P(\bar{B}^0 \to B^0) \\
&= \{\frac{1}{2\Gamma}\frac{2+x^2}{1+x^2}\} \times \{\frac{1}{2\Gamma}|\frac{p}{q}|^2\frac{x^2}{1+x^2}\} \qquad (1.104)
\end{aligned}$$

$$Asymmetry = \frac{|\frac{q}{p}|^2 - |\frac{p}{q}|^2}{|\frac{q}{p}|^2 + |\frac{p}{q}|^2} = \frac{1 - |\frac{q}{p}|^4}{1 + |\frac{q}{p}|^4} \tag{1.105}$$

$$\begin{aligned}
|\frac{q}{p}| &= |\frac{1-\epsilon}{1+\epsilon}| \sim 1 - 4\mathbf{Re}(\epsilon) = \sqrt{\frac{M_{12}^* - i(\Gamma_{12}^*/2)}{M_{12} - i(\Gamma_{12}/2)}} \qquad (1.106) \\
|\frac{p}{q}| &= |\frac{1+\epsilon}{1-\epsilon}| \sim 1 + 4\mathbf{Re}(\epsilon) \qquad (1.107)
\end{aligned}$$

$$\begin{aligned}
Asymmetry &= -4Re(\epsilon) \simeq 1 - Im\left(\frac{\Gamma_{12}}{M_{12}}\right) \qquad (1.108) \\
&\sim O(10^{-3})
\end{aligned}$$

This asymmetry is measured by CLEO and CDF. The value is $Re(\epsilon) = 0.002 \pm 0.007 \pm 0.003$ [24]. This result is consistent with Standard Model. The requirement of measurement of indirect CP-violation is $|q/p| \neq 1$.

1.3.3 CP-Violation type-III : Interference CP Violation of Mixing and Decay

The last type of CP-Violation occures by interference between decays and mixing. We explain this CP-Violation using $B^0 - \bar{B}^0$ pair which is produced from $\Upsilon(4S)$-decay, and one of B^0 decay to CP-eigenstate final state[37]. We measure the decay time difference of two B^0, and we measure the asymmetry of time dependent decay rate. To calculate the time-dependent CP-asymmetry, we consider the time evolution of two-body system of $B^0 - \bar{B}^0$. We define the wave function of two-body system as

$$\Phi(k_1, t_1; k_2, t_2) = |B^0(k_1, t_1) > |\bar{B}^0(k_2, t_2) > \pm|\bar{B}^0(k_1, t_1) > |B^0(k_2, t_2) > \tag{1.109}$$

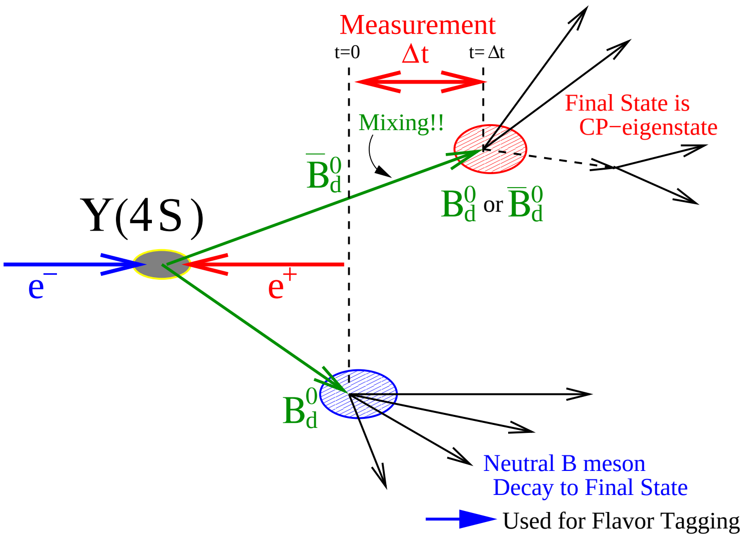

Figure 1.10: Conceptual drawing of the measurement of proper-time difference for $B^0\bar{B}^0$ pairs

Where, t_1 and t_2 are time and k_1 and k_2 are kinematics quantity of each B^0. The B^0 and $\bar{B}^0$ have spin=0, B^0 and $\bar{B}^0$ are produced by $\Upsilon(4S)$ which has J=1. Because of angular momentum conservation, the orbital angular momentum of $B^0\bar{B}^0$ system is '1'. If CP-transformation is operated to Φ, $CP\Phi(k_1,t_1;k_2,t_2) = (-1)^l\Phi(k_1,t_1;k_2,t_2)$, and the oribital angular momentum is $l = 1$, $CP\Phi(k_1,t_1;k_2,t_2) = -\Phi(k_1,t_1;k_2,t_2)$, we can written the wave function of two-body system is as,

$$\Phi(k_1,t_1;k_2,t_2) = |B^0(k_1,t_1)>|\bar{B}^0(k_2,t_2)> - |\bar{B}^0(k_1,t_1)>|B^0(k_2,t_2)> \tag{1.110}$$

The time evolution of $\Phi(k_1,t_1;k_2,t_2)$ can be written with $B^0(t)$ and $\bar{B}^0(t)$ time evolution,

$$\begin{aligned}
&|B^0(k_1,t_1)>|\bar{B}^0(k_2,t_2)> \\
&= e^{-iM(t_1+t_2)}e^{-\frac{\Gamma}{2}(t_1+t_2)}[\mathbf{cos}\,(\Delta m t_1/2)\,\mathbf{cos}\,(\Delta m t_2/2)\,|B^0(k_1)>|\bar{B}^0(k_2)> \\
&\quad - \mathbf{sin}\,(\Delta m t_1/2)\,\mathbf{sin}\,(\Delta m t_2/2)\,|\bar{B}^0(k_1)>|B^0(k_2)> \\
&\quad + i\frac{p}{q}\mathbf{cos}\,(\Delta m t_1/2)\,\mathbf{sin}\,(\Delta m t_2/2)\,|B^0(k_1)>|B^0(k_2)> \\
&\quad + i\frac{q}{p}\mathbf{sin}\,(\Delta m t_1/2)\,\mathbf{cos}\,(\Delta m t_2/2)\,|\bar{B}^0(k_1)>|\bar{B}^0(k_2)>]
\end{aligned} \tag{1.111}$$

$$\begin{aligned}
&\Phi(k_1,t_1;k_2,t_2) \\
&= e^{-iM(t_1+t_2)}e^{-\frac{\Gamma}{2}(t_1+t_2)}[\mathbf{cos}\,(\Delta m t_1/2)\,\mathbf{cos}\,(\Delta m t_2/2)\,\{|B^0(k_1)>|\bar{B}^0(k_2)> - |\bar{B}^0(k_1)>|B^0(k_2)>\} \\
&\quad - \mathbf{sin}\,(\Delta m t_1/2)\,\mathbf{sin}\,(\Delta m t_2/2)\,\{|\bar{B}^0(k_1)>|B^0(k_2)> - |B^0(k_1)>|\bar{B}^0(k_2)>\} \\
&\quad + i\frac{p}{q}\mathbf{sin}\,(\Delta m(t_1-t_2)/2)\,|B^0(k_1)>|B^0(k_2)> \\
&\quad + i\frac{q}{p}\mathbf{sin}\,(\Delta m(t_1-t_2)/2)\,|\bar{B}^0(k_1)>|\bar{B}^0(k_2)>]
\end{aligned} \tag{1.112}$$

$$\begin{aligned}
&= e^{-iM(t_1+t_2)}e^{-\frac{\Gamma}{2}(t_1+t_2)}[\mathbf{cos}\left(\frac{\Delta m(t_2-t_1)}{2}\right)\{|B^0(k_1)>|\bar{B}^0(k_2)> - |\bar{B}^0(k_1)>|B^0(k_2)>\} \\
&\quad + i\mathbf{sin}\left(\frac{\Delta m(t_2-t_1)}{2}\right)\{\frac{p}{q}|B^0(k_1)>|B^0(k_2)> - \frac{q}{p}|\bar{B}^0(k_1)>|\bar{B}^0(k_2)>\}]
\end{aligned} \tag{1.113}$$

In interference CP-Violation, we measure the time difference of two B decay. Since the $\Phi(k_1,t_1;k_2,t_2)$ obey the Bose-Einstein statistic, at a time one is B^0, the opposite site is $\bar{B}^0$. We assume that at $t=t_1$, we determinate the flavor of 'k_1' B as B^0 and the final state is f_{tag}, we can define the decay amplitude of $B^0(k_1)$ to f_{tag} as $< f_{tag}|T|B^0(k_1) >\equiv A_{tag}$, and sine '$k_1$' B is not $\bar{B}^0$, $< f_{tag}|T|\bar{B}^0(k_1) >\equiv A_{tag}=0$, where '$T$' is operator of transition of B^0 to f_{tag}, we can call is as 'Scattering Matrix(S-Matrix)'. Then we can written the amplitude of $\Phi(k_1,t_1;k_2,t_2)$ decay to f_{tag} by,

$$\begin{aligned}< f_{tag}|T|\Phi(k_1,k_2,t_1,t_2) >= e^{-iM(t_1+t_2)}e^{-\frac{\Gamma(t_1+t_2)}{2}}A_{tag}[\mathbf{cos}\left(\frac{\Delta m(t_2-t_1)}{2}\right)|\bar{B}^0(k_2)> \\ + i\mathbf{sin}\left(\frac{\Delta m(t_2-t_1)}{2}\right)(p/q)\,|B^0(k_2)>]\end{aligned} \tag{1.114}$$

Where the above equation is agree with time evolution of $\bar{B}^0(t)$, and we can understand that at $t=t_1$ the another B is $\bar{B}^0$. We assume that at $t=t_2$, the another B decay to CP-eigenstate, f_{cp}, but we need notice that the final state from $\bar{B}^0(k_2)$ is CP-eigenstate, so that we can not determinate the flavor of B at $t=t_2$. We can written the decay amplitude of $\bar{B}^0(k_2)$ decay to f_{cp}, and we need consider their CP-conjugate amplitude.

$$< f_{cp}|T|B^0(k_2) > \;\equiv\; A_{cp} \tag{1.115}$$

$$\begin{aligned}< \bar{f_{cp}}|T|\bar{B}^0(k_2) > &= < f_{cp}|(CP^{-1})\cdot T\cdot(CP)|B^0(k_2) > \\ &= < f_{cp}|\eta_{cp}\cdot T\cdot e^{i2\xi}|B^0(k_2) > \\ &= \eta_{cp}e^{i2\xi}A_{cp} \\ &\equiv \eta_{cp}\bar{A}_{cp}\end{aligned} \tag{1.116}$$

where η_{cp} is CP-eigenvalue, ±1, which depended on final state f_{cp} and $e^{i2\xi}$ is arbitrary phase. We write the decay amplitude of $\Phi(k_1,k_2,t_1,t_2)$ to f_2 as,

$$\begin{aligned}< f_{cp}|T|\Phi(k_1,k_2,t_1,t_2) >= e^{-iM(t_1+t_2)}e^{-\frac{\Gamma(t_1+t_2)}{2}}A_{tag}A_{cp}\left(\frac{p}{q}\right) \\ [\eta_{cp}\left(\frac{q}{p}\right)\left(\frac{\bar{A}_{cp}}{A_{cp}}\right)\mathbf{cos}\left(\frac{\Delta m(t_2-t_1)}{2}\right)+i\mathbf{sin}\left(\frac{\Delta m(t_2-t_1)}{2}\right)]\end{aligned} \tag{1.117}$$

where we define, $\lambda_{cp}\equiv\left(\frac{q}{p}\right)\left(\frac{\bar{A}_{cp}}{A_{cp}}\right)$. We calculate the decay rate,

$$\begin{aligned}P(B^0(k_1,t=t_1)\to f_{tag};\bar{B}^0(k_2,t=t_2)\to f_{cp}) = \Gamma(B^0\to f_{tag};\bar{B}^0\to f_{cp}) \\ \propto e^{-\Gamma(t_1+t_2)}|A_{tag}|^2|A_{cp}|^2\{\lambda^*_{cp}\mathbf{cos}\left(\frac{\Delta m(t_2-t_1)}{2}\right)-i\mathbf{sin}\left(\frac{\Delta m(t_2-t_1)}{2}\right)\} \\ \{\lambda_{cp}\mathbf{cos}\left(\frac{\Delta m(t_2-t_1)}{2}\right)+i\mathbf{sin}\left(\frac{\Delta m(t_2-t_1)}{2}\right)\}\end{aligned}$$

$$\begin{aligned}= e^{-\Gamma(t_1+t_2)}|A_{tag}|^2|A_{cp}|^2\{|\lambda_{cp}|^2\mathbf{cos}^2\left(\frac{\Delta m(t_2-t_1)}{2}\right)+\mathbf{sin}^2\left(\frac{\Delta m(t_2-t_1)}{2}\right) \\ + i(\lambda^*_{cp}-\lambda_{cp})\mathbf{cos}\left(\frac{\Delta m(t_2-t_1)}{2}\right)\mathbf{sin}\left(\frac{\Delta m(t_2-t_1)}{2}\right)\}\end{aligned} \tag{1.118}$$

where we assume $|q/p|\sim 1$, and λ_{cp} is complex, we can express this real part and imaginary part as $\lambda_{cp}=\mathbf{Re}(\lambda_{cp})+i\mathbf{Im}(\lambda_{cp})$, and $i(\lambda^*_{cp}-\lambda_{cp})=2Im(\lambda_{cp})$. Eq 1.118 can be written by,

$$\begin{aligned}= e^{-\Gamma(t_1+t_2)}|A_{tag}|^2|A_{cp}|^2\frac{1}{2} \\ \{\left(1+|\lambda_{cp}|^2\right)+\left(|\lambda_{cp}|^2-1\right)\mathbf{cos}\left(\Delta m(t_2-t_1)\right)+2Im(\lambda_{cp})\mathbf{sin}\left(\Delta m(t_2-t_1)\right)\}\end{aligned} \tag{1.119}$$

We define the time difference of t_1 and t_2 as Δt, and integrate t_1 or t_2 as follows.

In case of $t_2 - t_1 \equiv \Delta t (t_2 > t_1)$, and $t_2 = t_1 + \Delta t$,

$$\begin{aligned}
&\int \Gamma \delta \left(t_2 - t_1 - \Delta t\right) dt_1 dt_2 \\
&\propto \int_0^\infty e^{-\Gamma(2t_1+\Delta t)} \{\left(1 + |\lambda_{cp}|^2\right) + \left(|\lambda_{cp}|^2 - 1\right) \mathbf{cos}\left(\Delta m(t_2 - t_1)\right) + \eta_{cp} 2\mathbf{Im}(\lambda_{cp}) \mathbf{sin}\left(\Delta m(t_2 - t_1)\right)\} dt_1 \\
&= e^{-\Gamma \Delta t)} \{\left(1 + |\lambda_{cp}|^2\right) + \left(|\lambda_{cp}|^2 - 1\right) \mathbf{cos}\left(\Delta m(t_2 - t_1)\right) + \eta_{cp} 2\mathbf{Im}(\lambda_{cp}) \mathbf{sin}\left(\Delta m(t_2 - t_1)\right)\}
\end{aligned} \tag{1.120}$$

$$\begin{aligned}
&\Gamma(B^0 \to f_{tag}; \bar{B^0} \to f_{cp}) \\
&\quad = \frac{1}{4} |A_{tag}|^2 |A_{cp}|^2 e^{-\Gamma|\Delta t|} \{\left(1 + |\lambda_{cp}|^2\right) + \left(|\lambda_{cp}|^2 - 1\right) \mathbf{cos}\left(\Delta m(t_2 - t_1)\right) \\
&\qquad + \eta_{cp} 2\mathbf{Im}(\lambda_{cp}) \mathbf{sin}\left(\Delta m(t_2 - t_1)\right)\}
\end{aligned} \tag{1.121}$$

We can calculate the decay amplitude of the opposite case, $t_2 - t_1 \equiv -\Delta t (t_2 < t_1)$,

$$\begin{aligned}
&\Gamma(\bar{B^0} \to f_{tag}; B^0 \to f_{cp}) \\
&\quad = \frac{1}{4} |A_{tag}|^2 |A_{cp}|^2 e^{-\Gamma|\Delta t|} \{\left(1 + |\lambda_{cp}|^2\right) - \left(|\lambda_{cp}|^2 - 1\right) \mathbf{cos}\left(\Delta m(t_2 - t_1)\right) \\
&\qquad - \eta_{cp} 2\mathbf{Im}(\lambda_{cp}) \mathbf{sin}\left(\Delta m(t_2 - t_1)\right)\}
\end{aligned} \tag{1.122}$$

The normalization factor can be integrated for the $\Gamma(B^0 \to f_{tag}; \bar{B^0} \to f_{cp}) + \Gamma(\bar{B^0} \to f_{tag}; B^0 \to f_{cp})$ from $\Delta t = 0$ to $\Delta t = \infty$. We define the $\Gamma(B^0 \to f_{tag}; \bar{B^0} \to f_{cp}) \equiv \bar{P}\left(\bar{B^0} \to f_{cp}\right) \equiv P(q = +1)$ and, $\Gamma(\bar{B^0} \to f_{tag}; B^0 \to f_{cp}) \equiv P\left(B^0 \to f_{cp}\right) \equiv P(q = -1)$. Then the probability of $\bar{B^0}$ decay to f_{cp} and time dependent decay rate asymmetry as,

$$P(q = \pm 1) = \frac{1}{4\tau_B} e^{-|\Delta t|/\tau_B} \{1 + q\{\left(\frac{|\lambda_{cp}|^2 - 1}{|\lambda_{cp}|^2 + 1}\right) \mathbf{cos}\left(\Delta m \Delta t\right) + \eta_{cp} \frac{2\mathbf{Im}(\lambda_{cp})}{|\lambda_{cp}|^2 + 1} \mathbf{sin}\left(\Delta m \Delta t\right)\} \tag{1.123}$$

$$\begin{aligned}
Asymmetry &= \frac{\bar{P}\left(\bar{B^0} \to f_{cp}\right) - P\left(B^0 \to f_{cp}\right)}{\bar{P}\left(\bar{B^0} \to f_{cp}\right) + P\left(B^0 \to f_{cp}\right)} \\
&= \frac{|\lambda_{cp}|^2 - 1}{|\lambda_{cp}|^2 + 1} \mathbf{cos}\left(\Delta m \Delta t\right) + \eta_{cp} \frac{2\mathbf{Im}(\lambda_{cp})}{|\lambda_{cp}|^2 + 1} \mathbf{sin}\left(\Delta m \Delta t\right)
\end{aligned} \tag{1.124}$$

The first term comes from decay process and second term comes from interference of decay and mixing. We define the first term as A_{cp}, and second term as S_{cp}.

$$A_{cp} \equiv \frac{|\lambda_{cp}|^2 - 1}{|\lambda_{cp}|^2 + 1} \tag{1.125}$$

$$S_{cp} \equiv \eta_{cp} \cdot \frac{2\mathbf{Im}(\lambda_{cp})}{|\lambda_{cp}|^2 + 1} \tag{1.126}$$

A_{cp} and S_{cp} are satisfied,

$$A_{cp}^2 + S_{cp}^2 + \frac{2\mathbf{Re}(\lambda_{cp})}{|\lambda_{cp}|^2 + 1} = 1 \tag{1.127}$$

then, $A_{cp}^2 + S_{cp}^2 \leq 1$. The requirement of interference CP-Violation is, one of B meson decay to CP-eigenstate and have more than two decay process, here $B^0 \to f_{cp}$ and $B^0 \to \bar{B}^0 \to f_{cp}$, and have weak complex phase, here the weak phase is included in $B^0 - \bar{B}^0$ mixing process. We can understand these requirement as $\lambda_{cp} \neq 1$.

1.3.4 Example of CP Violation $\sim B_d^0 \to J/\psi K_s$

$B_d^0 \to J/\psi K_s$ decay is one of the most appropriate mode for measurement of CP-Violation clearly. $B_d^0 \to J/\psi K_s$ is $b \to c\bar{c}s$ decay and its final state is CP-eigenstate. We can take the interference CP-Violation method. We consider the λ_{cp} and mixing parameters q/p is same in all modes. In $B_d^0 \to J/\psi K_s$ decay process, there are two main decay process in Standard Model. One is tree diagram, which is minimum order pertavation, and another one is penguin $b \to sc\bar{c}$ decay, which includes one loop diagram. The decay diagram of tree and penguin process are shown in Fig 1.11, 1.12. The coupling constant of tree diagram are '$V_{cb}V_{cs} \sim A\lambda^2$', while that of penguin diagram are '$V_{tb}V_{ts} \sim A\lambda^2$'. The tree and penguin diagram have no weak complex phase of CKM matrix, while λ_{cp} has one complex weak phase in $B^0 - \bar{B}^0$ mixing process and $|\lambda_{cp}| = 1$. Because of this, direct CP-asymmetry parameter, A_{cp}, must be zero.

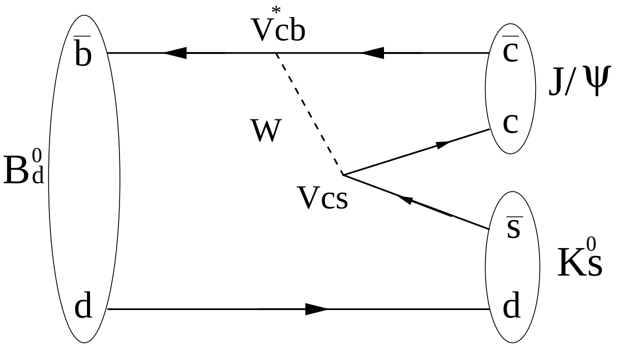

Figure 1.11: Tree diagram of $B^0 \to J/\psi K_S$ decay This diagram is dominant decay process and has no complex phase

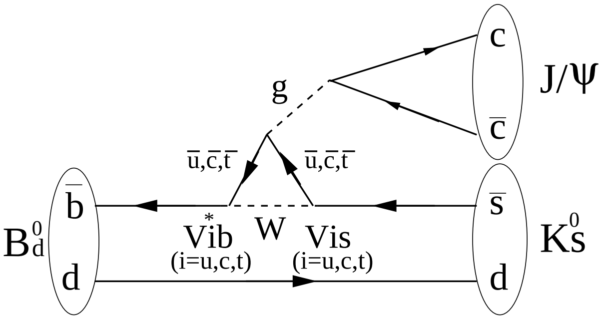

Figure 1.12: Penguin diagram of $B^0 \to J/\psi K_S$ decay This diagram has complex phase, but the contribution to decay process is much small by Zweig rule.

$$Asymmetry \;=\; \eta_{cp}\frac{\mathbf{2Im}(\lambda_{cp})}{|\lambda_{cp}|^2+1}\mathbf{sin}\,(\Delta m \Delta t) \tag{1.128}$$

Since the $J/\psi K_s$ is CP-eigenstate, η_{cp} has ± 1. J/ψ has J=1, and $CP = +1$, while K_s has J=0, and $CP = -1$. From these quantity, we can derive $\eta_{cp} = (+1) \times (-1) \times (-1)^{l=0} = -1$[7]. we consider the expression of λ_{cp} of $J/\psi K_s$, we can also write the decay amplitude with tree and penguin amplitude.

$$\left\{ \begin{array}{l} A(B^0 \to J/\psi K_S) = A_T e^{i\phi_T} e^{i\delta_T} + A_P e^{i\phi_P} e^{i\delta_P} \\ \bar{A}(\bar{B}^0 \to J/\psi K_S) = A_T e^{-i\phi_T} e^{i\delta_T} + A_P e^{-i\phi_P} e^{i\delta_P} \end{array} \right. \tag{1.129}$$

where A_T, A_P are tree and penguin amplitude. The ϕ_T and ϕ_P are weak phase and δ_T, δ_P are strong phase. We can write the amplitude of tree and penguin as,

$$\begin{aligned} A(B^0 \to J/\psi K_S) &= V_{cb}^* V_{cs} A_t + \sum_{i=u,c,t} V_{ib}^* V_{is} A_p^i \\ &= V_{cb}^* V_{cs}(A_t + A_p^c - A_p^t) + V_{ub}^* V_{us}(A_p^c - A_p^t) \end{aligned} \tag{1.130}$$

Where A_t is tree amplitude and A_p^i is penguin ampltitude include weak and strong phase, i is internal quark in penguin loop. We use unitary relation from first equation to second equation. The $V_{cb}^* V_{cs} \sim A\lambda^2$, used Wolfstein parameters, has no weak phase, while $V_{ub}^* V_{us} \sim A\lambda^4$ has weak phase, but its amplitude is much smaller than $V_{cb}^* V_{cs}$, $V_{ub}^* V_{us}/V_{cb}^* V_{cs} \sim 10^{-2}$. Because of this, the second term does not contribute to total decay amplitude. Since tree and penguin has no complex phase as above explanation, we can written $A_{cp} = \bar{A}_{cp}$. The mixing parameter has one complex phase in box diagram and this complex phase make the CP-Violation. There is one more mixing effect, that is $K_0 - \bar{K}_0$ mixing. But there is no complex phase in this process, and the contribution of $K_0 - \bar{K}_0$ mixing CP-Violation is much small. In addition, the penguin

---

[7] From J=1, J/ψK_S system is created in a P-wave state

diagram is suppressed by Zweig rule. The color force between quarks is mediated by gluon which has octet color state, all gluon has color charge. The gluon which is color singlet[8] is only mediated in Meson. Because of this, one gluon can not create any Mesons. For create J/ψ, three gluons are necessary and the decay rate is very small. From all discussion above, the λ_{cp} and The imaginary part of λ_{cp} can be written as follows,

$$\frac{q}{p} = \sqrt{\frac{M_{12}^*}{M_{12}}} = \frac{V_{tb}^* V_{td}}{V_{tb} V_{td}^*} \tag{1.131}$$

$(q/p)_K = V_{cs}^* V_{cd} / V_{cs} V_{cd}^*$

$$\lambda_{cp} = \left(\frac{V_{tb}^* V_{td}}{V_{tb} V_{td}^*}\right) \left(\frac{V_{cs}^* V_{cb}}{V_{cs} V_{cb}^*}\right) \left(\frac{V_{cs}^* V_{cd}}{V_{cs} V_{cd}^*}\right) = \left(\frac{V_{tb}^* V_{td}}{V_{tb} V_{td}^*}\right) \tag{1.132}$$

$$\mathbf{Im} \left(\frac{V_{tb}^* V_{td}}{V_{tb} V_{td}^*}\right) = \mathbf{Im}\{e^{-i2\phi_1}\} = -\mathbf{sin}2\phi_1 \tag{1.133}$$

$$Asymmetry = \mathbf{sin}2\phi_1 \cdot \mathbf{sin}\left(\Delta m \Delta t\right) \tag{1.134}$$

From this asymmetry, we can measure the 'sin$2\phi_1$', which is an angle of unitary triangle. In this mode there is no CKM complex phase in decay diagram. We have no uncertainties likes strong interaction phase and this mode is very clean mode for measurement CP-Violation. A point of view from experiment, $J/\psi K_s$ is clean signal mode. Because the J/ψ has very narrow mass peak, very short lifetime, background is very small, and the decay point of J/ψ is almost same as B^0 decay point. Above all, $J/\psi K_s$ decay mode is very profitable.

1.3.5 Example of CP Violation $\sim B_d^0 \to \pi^+\pi^-$

One more profitable mode for measurement CP-Violation by interference CP-Violation method is $B_d^0 \to \pi^+\pi^-$[38][39]. Basically, this decay mode is used for measurement ϕ_2, which is one of the CKM uncertainty triangle. However this mode is not clean as $J/\psi K_s$. There are theoretical uncertainties. There is possibility that direct CP-term, A_{cp}, has finite value. There are two dominant decay processes likes $J/\psi K_s$, one is tree and another one is penguin, and the amplitude of $B_d^0 \to \pi^+\pi^-$ and $\bar{B}_d^0 \to \pi^+\pi^-$ are written as,

$$\left\{ \begin{array}{l} A\left(B^0 \to \pi^+\pi^-\right) = A_T e^{i\phi_T} e^{i\delta_T} + A_P e^{i\phi_P} e^{i\delta_P} \\ \bar{A}\left(\bar{B}^0 \to \pi^+\pi^-\right) = A_T e^{-i\phi_T} e^{i\delta_T} + A_P e^{-i\phi_P} e^{i\delta_P} \end{array} \right. \tag{1.135}$$

where the definition of A_T, A_P, ϕ_T, ϕ_P, δ_T, δ_P are same as $J/\psi K_s$. The decay diagram of tree and penguin are shown in Fig 1.13, 1.14. From these diagram, the amplitude of tree and penguin are same order and have complex phase. We must consider the tree and penguin process. The penguin diagram has one loop and u-quark, c-quark and t-quark can exist in the loop. The decay amplitude.

$$A\left(B^0 \to \pi^+\pi^-\right) = V_{ub}^* V_{ud} A_T e^{i\delta_T} + \sum_{q=u,c,t} V_{qb}^* V_{qd} A_p^q e^{i\delta_p} \tag{1.136}$$

where we assume that all strong phase are same, because the strong interaction are same in these three type diagrams, $\delta_p^u = \delta_p^c = \delta_p^t \equiv \delta$,

$$\begin{aligned} \sum_{q=u,c,t} V_{qb}^* V_{qd} A_p^q e^{i\delta_p} &= \{V_{ub}^* V_{ud} A_p^u + V_{cb}^* V_{cd} A_p^c + V_{tb}^* V_{td} A_p^t\} e^{i\delta} \\ &= \{V_{ub}^* V_{ud}(A_p^u - A_p^t) + V_{cb}^* V_{cd}(A_p^c - A_p^t)\} e^{i\delta_p} \end{aligned} \tag{1.137}$$

$$A\left(B^0 \to \pi^+\pi^-\right) = V_{ub}^* V_{ud}\{A_T e^{i\phi_T} + (A_p^u - A_p^t) e^{i\delta_p} + V_{cb}^* V_{cd}(A_p^c - A_p^t) e^{i\delta_p} \tag{1.138}$$

---

[8] The color singlet is '$B\bar{B} + R\bar{R} + G\bar{G}$', B, R, G are color blue red and green, repectively.

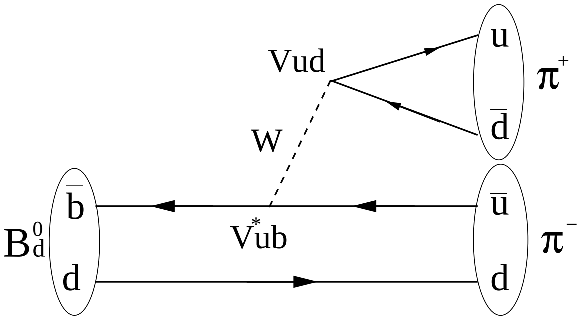

Figure 1.13: Tree diagram of $B^0 \to \pi^+\pi^-$ decay

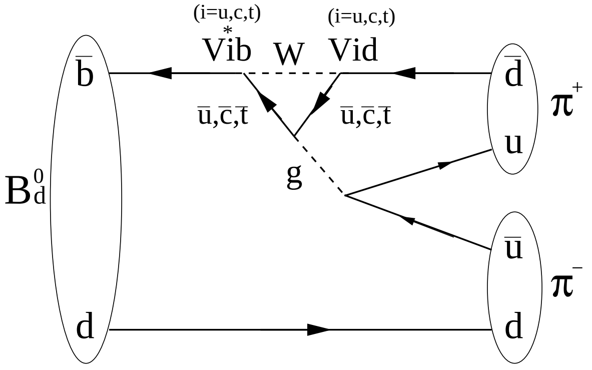

Figure 1.14: Penguin diagram of $B^0 \to \pi^+\pi^-$ decay

Here, we use the unitary relation, $V_{tb}^* V_{td} = -\left(V_{ub}^* V_{ud} + V_{cb}^* V_{cd}\right)$,

$$V_{ub}^* V_{ud} = (\rho, \eta) = \sqrt{\rho^2 + \eta^2} e^{i\phi_3} \tag{1.139}$$

$$V_{cb}^* V_{cd} = 1 \tag{1.140}$$

where ϕ_3 is the last angle of unitary triangle.

$$A_T e^{i\phi_T} + (A_p^u - A_p^t) e^{i\delta_p} = \sqrt{A_T^2 + \left(A_P^u - A_P^t\right)^2 + 2A_T(A_P^u - A_P^t)\mathbf{cos}(\delta_T - \delta_P)}\, e^{i\delta'_T} \tag{1.141}$$

The tree contributuded amplitude and pure penguin amplitude are defined as,

$$|T| \equiv \sqrt{A_T^2 + \left(A_P^u - A_P^t\right)^2 + 2A_T(A_P^u - A_P^t)\mathbf{cos}(\delta_T - \delta_P)} \tag{1.142}$$

$$|P| \equiv A_p^c - A_p^t \tag{1.143}$$

$$A\left(B^0 \to \pi^+\pi^-\right) \equiv A_{\pi^+\pi^-} = |T| e^{i\phi_3} e^{i\delta'_T} + |P| e^{i\delta_P} \tag{1.144}$$

As explained in above section q/p is $e^{-2\phi_1}$, and we define the difference δ'_T and δ_P as $\Delta\delta$, the λ_{cp} can be written by ratio of $|P/T|$, ϕ_3 and $\Delta\delta$ as,

$$\begin{aligned} \lambda_{cp} &= \frac{q}{p} \cdot \frac{\bar{A}_{\pi^+\pi^-}}{A_{\pi^+\pi^-}} \\ &= e^{-i2(\phi_1+\phi_3)} \frac{1 + |P/T| e^{i(\phi_3 + \Delta\delta)}}{1 + |P/T| e^{-i(\phi_3 - \Delta\delta)}} \end{aligned} \tag{1.145}$$

$$|\lambda_{cp}|^2 = \frac{1 + |P/T|^2 + 2|P/T|\mathbf{cos}(\phi_3 + \Delta\delta)}{1 + |P/T|^2 + 2|P/T|\mathbf{cos}(\phi_3 - \Delta\delta)} \tag{1.146}$$

$$\mathbf{Im}(\lambda_{cp}) = \frac{\mathbf{sin}2\phi_2 + |P/T|^2 \mathbf{sin}2(\phi_2 + \phi_3) + 2|P/T|\mathbf{cos}\Delta\delta\mathbf{sin}(2\phi_2 + \phi_3)}{1 + |P/T|^2 - 2|P/T|\mathbf{cos}(\phi_3 - \Delta\delta)} \tag{1.147}$$

We use the equation, $\phi_3 = \pi - (\phi_1 + \phi_2)$, and we replace ϕ_3 to ϕ_1 and ϕ_2. The direct CP-asymmetry term can be written

$$A_{cp} = \frac{-2|P/T|\mathbf{sin}(\phi_2 + \phi_1)\mathbf{sin}\Delta\delta}{1 + |P/T|^2 - 2|P/T|\mathbf{cos}(\phi_2 + \phi_1)\mathbf{cos}\Delta\delta} \tag{1.148}$$

Where we use $\sin 2(\phi_2 + \phi_3) = -\sin 2\phi_1$, $\sin(2\phi_2 + \phi_3) = \sin(\phi_1 - \phi_2)$, and use $|\lambda_{cp}|^2$, the indirect CP-asymmetry parameter can be written by,

$$S_{cp} = \frac{\mathbf{sin}2\phi_2 - |P/T|^2 \mathbf{sin}2\phi_1 + 2|P/T|\mathbf{sin}(\phi_1 - \phi_2)\mathbf{cos}\Delta\delta}{1 + |P/T|^2 - 2|P/T|\mathbf{cos}(\phi_1 + \phi_2)\mathbf{cos}\Delta\delta} \tag{1.149}$$

In this CP-asymmetry, the free parameter are $|P/T|$, ϕ_1, ϕ_2 and $\Delta\delta$. The theoretical estimation of $|P/T|$ is 0.3[39][40][41][42], and $|P|$ is measured from experimental data of $B^+ \to K^0\pi^+$ decay rate assuming the SU(3) flavor symmetry[40], while $|T|$ is measured from $B \to \pi l \nu$ decay rate with factorization[41], and the value is $= 0.28 \pm 0.06$[40]. The ϕ_1 can be measured used $B^0 \to J/\psi K_s$ clearly. The unknown parameters are ϕ_2 and $\Delta\delta$.

1.3.6 History of Belle and BaBar Experiment Results

We present the history of measurement of CP-Violation by $B^0 \to J/\psi K_S$ and other charmonium mode, $\psi(2S)K_S$, $\chi_{c1}K_S$, $\eta_{c1}K_S$, and $J/\psi K_L$ by Belle experiment and $B^0 \to J/\psi K_S$, $\psi(2S)K_S$, and $J/\psi K_L$ by BaBar experiment. The detail of Belle experiment is described in the next chapter. BaBar experiment is also B-factory experiment with asymmetric energy collider(PEP-II) of e^+e^- beam at Stanford Linear Accelerator Center(SLAC) in USA. The BaBar experiment was started from 1999 same as Belle experiment. The measured **sin**$2\phi_1$ by Belle and BaBar experiment are listed in Table 1.1 and The newest world average of **sin**$2\phi_1$ is 0.726 ± 0.037[43].

Table 1.1: Results of Belle and BaBar Experiment of B^0 to $J/\psi K_S$

Experiment	Luminosity (fb^{-1})	**sin**$2\phi_1$	Reference
Belle	10.5	$0.58^{+0.32}_{-0.34}{}^{+0.09}_{-0.10}$	[44]
	29.1	$0.99 \pm 0.14 \pm 0.06$	[45]
	78	$0.714 \pm 0.074 \pm 0.035$	[46]
	140	$0.728 \pm 0.056 \pm 0.023$	[47]
BaBar	9.0	$0.12 \pm 0.37 \pm 0.09$	[48]
	20.7	$0.34 \pm 0.20 \pm 0.05$	[49]
	32(#BB)	$0.59 \pm 0.14 \pm 0.05$	[50]
	56	$0.75 \pm 0.09 \pm 0.04$	[51]
	81	$0.741 \pm 0.067 \pm 0.034$	[52]
	205	$0.722 \pm 0.04 \pm 0.023$	[53]

Belle and BaBar experiment also measure CP-asymmetry by $B^0 \to \pi^+\pi^-$. The measured CP-asymmetry parameters, A_{cp} and S_{cp}, are listed in Table 1.2,

Table 1.2: Results of Belle Experiment of B^0 to $\pi^+\pi^-$

Experiment	Luminosity (fb^{-1})	S_{cp}	A_{cp}	Reference
Belle	41.8	$-1.21^{+0.38}_{-0.27}{}^{+0.16}_{-0.13}$	$+0.94^{+0.25}_{-0.31} \pm 0.09$	[54]
	78	$-1.23 \pm 0.41 {}^{+0.08}_{-0.07}$	$+0.77 \pm 0.27 \pm 0.08$	[55]
	140	$-1.00 \pm 0.21 \pm 0.07$	$+0.58 \pm 0.15 \pm 0.07$	[56]
BaBar	56	$-0.01 \pm 0.37 \pm 0.07$	$+0.02 \pm 0.29 \pm 0.07$	[57]
	81	$+0.20 \pm 0.34 \pm 0.05$	$+0.30 \pm 0.25 \pm 0.04$	[58]
	205	$-0.30 \pm 0.17 \pm 0.03$	$-0.09 \pm 0.15 \pm 0.04$	[59]

1.4 $b \to$ s Flavor Changing Neutral Current Penguin decay

We considered the $B^0 \to J/\psi K_S$ and $B^0 \to \pi^+\pi^-$ decay mode which is $b \to c$, $b \to u$, $b \to d$ transition, $b \to c$, $b \to u$ are tree type and $b \to d$ is penguin. In this section we explain CP-asymmetry in the $b \to s$ transition of penguin decay process, that is called flavor changing neutral current. We expect that there are new physics phase in B_S physics, but since we can use only B^0 or $B^\pm$ at B-factory, it is impossible to measure with B_S. However we expect the measurement **sin**$2\phi_1$ included the new physics effect phase used

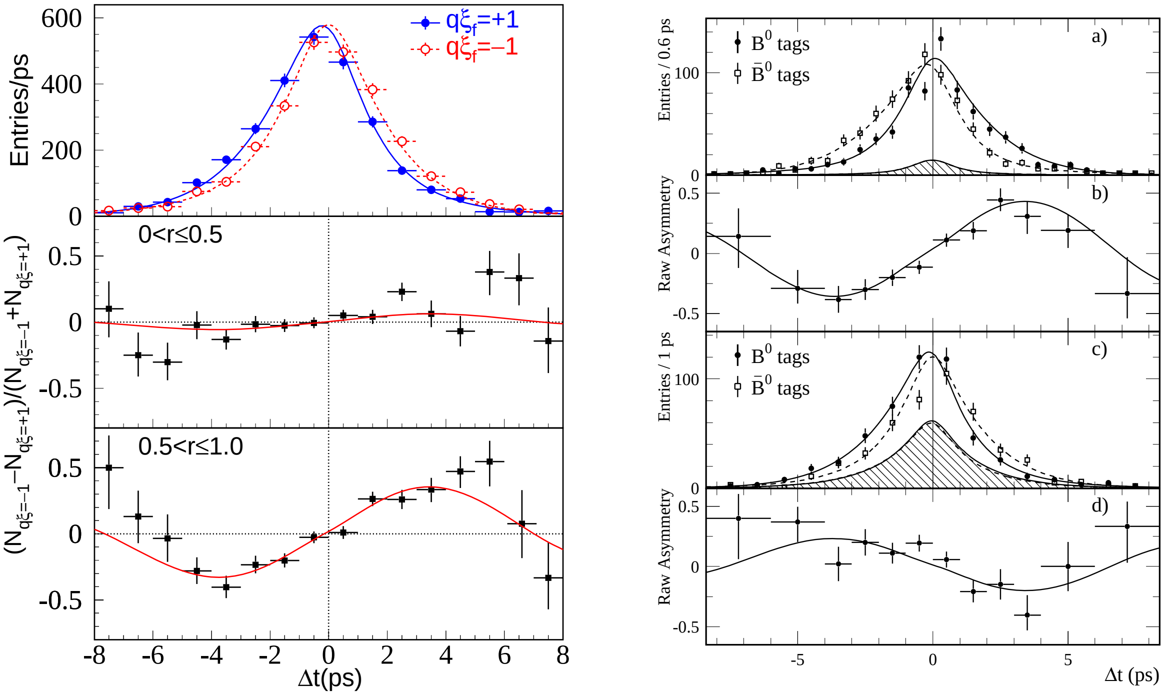

Figure 1.15: Δt distribution and Raw Asymmetry Plots
Left figure shows the results of Belle at $140fb^{-1}$, and right figure shows the results of BaBar at $81fb^{-1}$, a) and b) show $J/\psi K_S + \psi(2S)K_S + \chi_c K_S + \eta_c K_S$ mode. c) and d) show $J/\psi K_L$ mode.

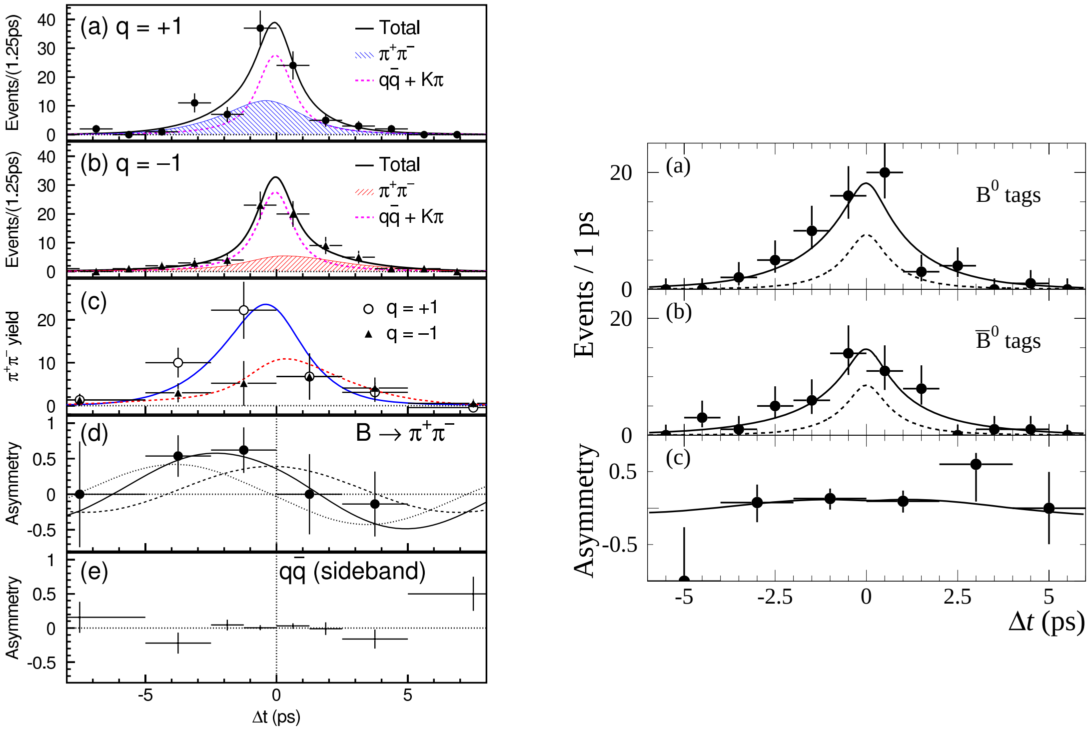

Figure 1.16: Δt distribution and Raw Asymmetry Plots
Left figure shows the results of Belle at $78fb^{-1}$, and right figure shows the results of BaBar at $81fb^{-1}$

$b \to s$ flavor changing neutral current. As $J/\psi K_S$ mode whose the dominant decay process is tree without any complex phase, we can measure the $\mathbf{sin2}\phi_1$ clearly, if the dominate decay process is only penguin decay. Because the dominant penguin has also no complex phase within Standard Model. In addition, if the penguin decay includes the intermediate state of beyond Standard Model, we will observe a variation from $\mathbf{sin2}\phi_1$[60]. For example, $\mathbf{sin2}\phi_1' = \mathbf{sin2}(\phi_1 + \phi')$, here ϕ' is a new physics effect phase. it is possible to search the new physics effect by comparing the $\mathbf{sin2}\phi_1$ which is measured by $J/\psi K_S$ decay mode and the $\mathbf{sin2}\phi_1'$ which is measured by $b \to s$ penguin dominate decay mode. The $b \to s$ flavor changing neutral current dominate mode are, $B^0 \to \phi K_S$, $\eta' K_S$, $K_S \pi^0$, ρK_S, ωK_S and ηK_S. The measurement of CP-Violation by $b \to s$ penguin decay mode is most important method for search the new physics effect.

1.4.1 $b \to$ s Penguin dominant decay ; $B^0 \to \phi\ K_s$ decay

The $B^0 \to \phi K_S$ decay is most important mode in $b \to s$ penguin decay. This decay mode is only $b \to s s \bar{s}$ transition, and the decay diagram has only penguin diagram. The decay amplitude can be expressed as,

$$\begin{aligned} A(B^0 \to \phi K_S) \equiv A_{\phi K_S} &= \sum_{i=u,c,t} V_{ib}^* V_{is} A_p^i \\ &= V_{cb}^* V_{cs}(A_p^c - A_p^t) + V_{ub}^* V_{us}(A_p^c - A_p^t) \qquad (1.150) \end{aligned}$$

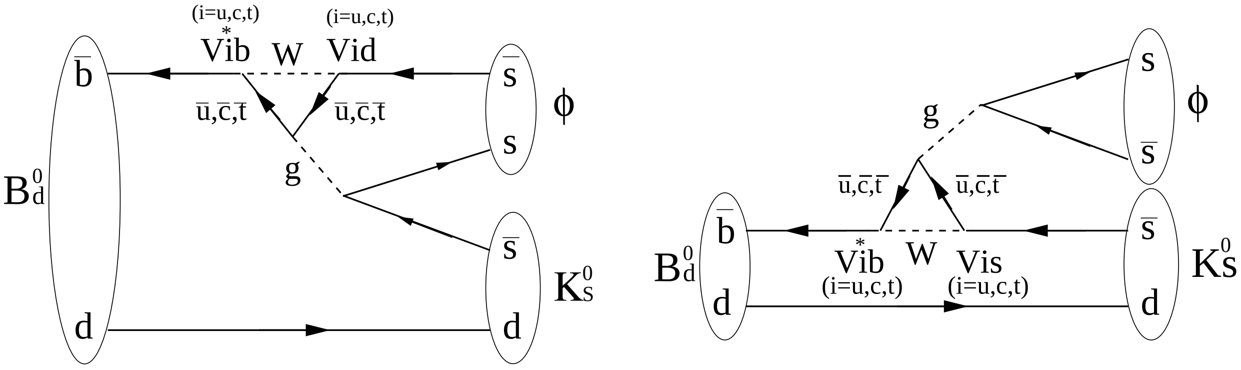

Figure 1.17: Penguin diagram of $B^0 \to \phi K_s$, the right diagram is suppressed by Zweig rule. The allowed diagram is only left.

Where $V_{ub}^* V_{us}$ is much smaller than $V_{cb}^* V_{cs}$. The decay ratio of $A_{\phi K_S}$ and $\bar{A}_{\phi K_S}$ considering $K_0 - \bar{K}_0$ mixing is written by,

$$\frac{\bar{A}_{\phi K_S}}{A_{\phi K_S}} = \frac{V_{cb} V_{cs}^*(A_p^c - A_p^t) + V_{ub} V_{us}^*(A_p^c - A_p^t)}{V_{cb}^* V_{cs}(A_p^c - A_p^t) + V_{ub}^* V_{us}(A_p^c - A_p^t)} \times \frac{V_{cd}^* V_{cs}}{V_{cd} V_{cs}^*} \qquad (1.151)$$

$$\sim \left(\frac{V_{cb} V_{cs}^*}{V_{cb}^* V_{cs}}\right)\left(\frac{V_{cd}^* V_{cs}}{V_{cd} V_{cs}^*}\right) \sim 1 \qquad (1.152)$$

We can neglect the $V_{ub}^* V_{us}$ contribution in the Standard Model and there is no weak phase in decay term. We can consider only weak phase in the $B^0 - \bar{B}^0$ mixing process. Because of this, ϕK_S is the best mode to search new physics effect. In 2003, Belle experiment group reported the result of CP-Violation with ϕK_S at $140 fb^{-1}$, corresponding 150M$B\bar{B}$ sample, which the measurement effective $\mathbf{sin2}\phi_1$ differs from Standard Model expectation by 3.5 standard deviations, $S_{cp} = -0.96 \pm 0.5^{+0.09}_{-0.11}$[21]. This result suggested the new physics effect. Fig 1.18 shows the raw asymmetry plot of ϕK_S. The dashed line is expectation in Standard Model and the solid line is fitted result. On the other hand, BaBar experiment also reported the result of measurement CP-asymmetry used $B^0 \to \phi K_S$ and ϕK_L with 114M$B\bar{B}$ sample. The results are $S_{cp} = 0.47 \pm 0.34^{+0.08}_{-0.06}$ and $A_{cp} = 0.01 \pm 0.33 \pm 0.10$[61], which is consistent with the expectation of Standard Model within error.

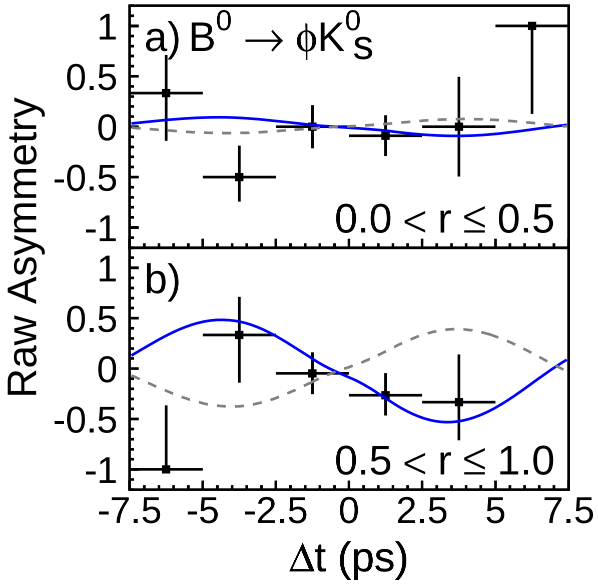

Figure 1.18: The result of Belle in $B^0 \to \phi K_S$ decay with $140 fb^{-1}$ data. Points is data, solid line shows the fitted results, and the dashed line shows the Standard Model expectation.

1.4.2 $b \to$ s Penguin dominant decay ; $B^0 \to K_s \pi^0$ decay

The $B^0 \to K_S \pi^0$ decay is also important decay mode for search new physics effect through flavor changing neutral current process. However there is difference from ϕK_S. This decay mode has two decay diagram. One is $b \to u$ tree decay and another is $b \to s$ penguin decay diagram show in Fig 1.19. The decay amplitude can be written by,

$$\begin{aligned} A(B^0 \to K_s \pi^0) &= V_{ub}^* V_{us} A_t + \sum_{i=u,c,t} V_{ib}^* V_{is} A_p^i \\ &= V_{cb}^* V_{cs}(A_p^c - A_p^t) + V_{ub}^* V_{us}(A_t + A_p^c - A_p^t) \\ &\sim V_{cb}^* V_{cs}(A_p^c - A_p^t) \end{aligned} \tag{1.153}$$

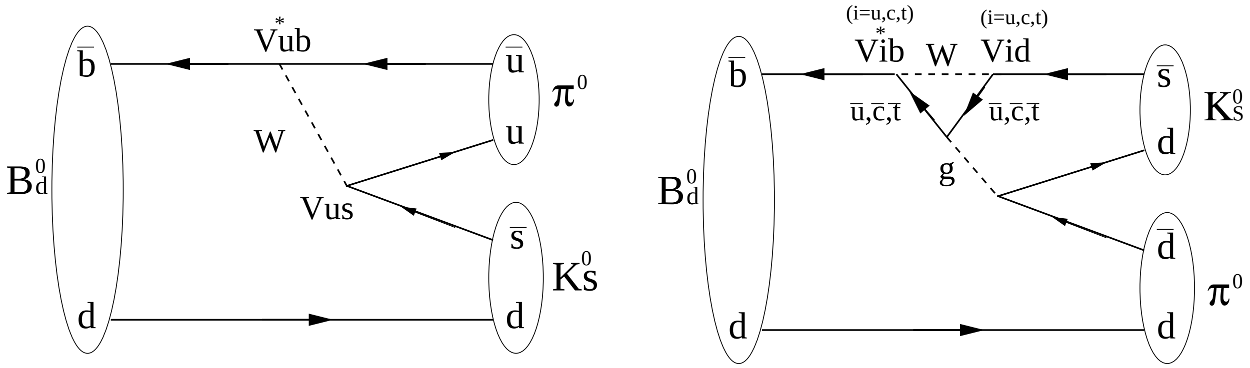

Figure 1.19: Left is Tree diagram of $B^0 \to K_s \pi^0$ and right is Penguin diagram of $B^0 \to K_s \pi^0$

In tree decay, there is one weak complex phase, 'V_{ub}' and we can measure the CKM matrix phase, ϕ_3. The coupling constant are $V_{ub} V_{us} \sim \lambda^4$ in tree decay and $V_{tb} V_{ts} \sim \lambda^2 \gg \lambda^4$ in penguin decay. Since the contribution of tree decay is small, the dominant decay is penguin decay. In addition to that, the penguin

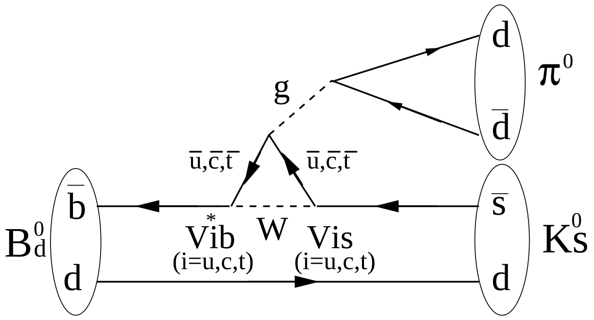

Figure 1.20: This diagram is also Penguin diagram of $B^0 \to K_s\pi^0$ but this decay is suppressed by Zweig rule as $J/\psi K_S$ and ϕK_S

decay has no complex phase, so that we can measure the $\mathbf{sin2}\phi_1$ as ϕK_S case and search the new physics with $b \to s$ penguin. The $K_S\pi^0$ is also CP-eigenstate and, the CP-eigenvalue is $\eta_{cp} = (K_S)^{cp} \cdot (\pi^0)^{cp} \cdot (-1)^l = (-1) \cdot (1) \cdot (1) = -1$. According to Eq 1.153, we can approximate the $|V_{cb}^* V_{cs}| \gg |V_{ub}^* V_{us}|$, and ignore $V_{ub}^* V_{us}$ term. However, for studying new physics we must consider the $V_{ub}^* V_{us}$ term and estimate the uncertainties of S_{cp} in Standard Model, because the $V_{cb}^* V_{cs}$ and $V_{ub}^* V_{us}$ term has strong phase and $V_{ub}^* V_{us}$ has CKM phase. We can express the decay amplitude of $K_S\pi^0$ as,

$$A(B^0 \to K_s\pi^0) = A\lambda^2 e^{i\delta_c} + A\lambda^4\sqrt{\rho^2+\eta^2}e^{i\phi_3}e^{i\delta_u} \tag{1.154}$$

where, δ_c and δ_u are strong phase This amplitude has Direct CP term and Indirect CP term. The S_{cp} can be expressed as $S_{cp} = \mathbf{2Im}\lambda_{cp}/(|\lambda_{cp}^2| + 1)$, and can be written by,

$$S_{cp} \sim \mathbf{sin2}\phi_1 + 2\lambda_{cp}^2\sqrt{\rho^2+\eta^2}\,\mathbf{sin}(2\phi_1 - \phi_3 - \Delta\delta) + \O(\lambda_{cp}^4) \tag{1.155}$$

where the $\Delta\delta$ is defined as $\delta c - \delta u$. The ϕ_3 is constrained by several experiments which are indirect measurement. Allowed ϕ_3 region is 61^{+8}_{-11} degree[62], while the $\Delta\delta$ is allowed '0' to '2π'. The uncertainties of $\mathbf{sin2}\phi_1$ in $K_S\pi^0$ can be estimated by uncertainties of ϕ_3 and $\Delta\delta$ in Standard Model ≤ 0.1. If the new physics phase, ϕ', makes larger deviation much more than 0.1 in $\mathbf{sin2}\phi_1$, we can suggest the source of the deviation is new physics. Then we calculated the expected deviation of S_{cp} from Standard Model expectation, $S_{cp} = \mathbf{sin2}\phi_1$, we assume that we ignore the tree diagram and we parameterize the Standard Model and New Physics amplitude,

$$A^{SM} \equiv |A^{SM}|e^{i\delta_{SM}} \tag{1.156}$$

$$A^{NP} \equiv |A^{NP}|e^{i\theta_{NP}}e^{i\delta_{NP}} \tag{1.157}$$

$$S_{cp} = \frac{\mathbf{sin2}\phi_1 + r \cdot \mathbf{cos}\Delta\delta\,\mathbf{sin}(\theta_{NP} + 2\phi_1) + r^2\mathbf{sin}(2\theta_{NP} + 2\phi_1)}{1 + 2 \cdot r \cdot \mathbf{cos}\Delta\delta\,\mathbf{cos}\theta_{NP} + r^2} \tag{1.158}$$

where we defined $r \equiv |A^{NP}|/|A^{SM}|$, and $\Delta\delta \equiv \delta_{NP} - \delta_{SM}$. Fig 1.21 shows S_{cp} as a function of θ_{NP} for various value of r by fixing $\Delta\delta = 0$. From Fig 1.21, we require the large r, and $\theta_{NP} \sim -\pi/2$ for large deviation from Standard Model expectation.

1.4.3 Example of theoretical New physics scenario

Many model beyond Standard Model has been proposed. One of the most hopefull scenario is super-symmetry model(SUSY model) and many extended model are proposed based on the model. In this section, we introduce some new physics models and these effect.

There are several model of new physics which can lead to new physics in the $b \to s$ flavor changing neutral current[60][64]. For example, the four generation model, non-minimal super-symmetric model such

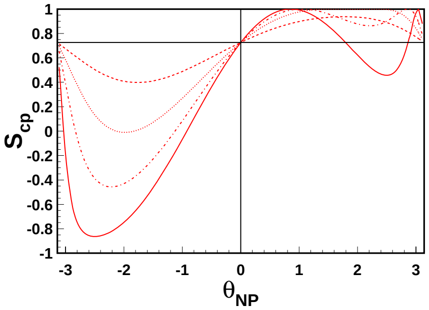

Figure 1.21: S_{cp} including New Physics contributions, S_{cp} as a function of difference values of r: $r = 0.2$(dashed-line), $r = 0.4$(dotted-line), $r = 0.6$(dashed-dotted), and $r = 0.8$(solid-line). Here we assume that the strong phase difference between SM and NP is '0'

as effective super-symmetry and model with enhanced chromomagnetic dipole operators, and the model with Z-mediated flavor changing neutral current will affect $b \to s$ hadronic penguins only marginally. After the result of CP-Violation with $B^0 \to \phi K_S$ were reported[21], many model which explain the anomaly of ϕK_S results were suggested.

First example is 'MSSM Chargino contribution'. MSSM means minimal super-symmetric of extension of Standard Model[65] from these model, there is possibility that chargino contributes to CP-Violation in $B^0 \to \phi K_s$ decay at large tanλ, here tanλ is ratio of two vacuum expectation of Higgs fields of SUSY. According to this model, the enhanced C_{8g} which is Wilson Coefficient of chromomagnetic penguin operator allows large deviation in the $S_{\phi K_S}$ from Standard Model expectation. We can consider the penguin diagram which has two loop as Fig 1.22[66] left diagram shows Electro-Dipole-Moment contribution diagram, and right diagram shows Chromo-Electro-Dipole-Moment contribution diagram. The correlation of calculated deviation of $S_{\phi K_S}$ and C_{8g} is shown in Fig 1.23.

Second one is 'Large s-b mixing, right-handed dynamics', or 'Supersymmetric Grand Unified theory(GUT) with the right-handed neutrinos as new physics[67] [68]. In such a model, the right handed down-type squarks can be coupled with the right-handed neutrinos and colored Higgs, of course the low energy scale in such a Tree Level can be ignored. The right-handed squark, $\tilde{s}_R$ or $\tilde{b}_R$, can be mixed by the off-diagonal component of mass matrix, $m^2_{\tilde{b}_R\tilde{s}_R}$. The magnitude of this mixing parameter depends on the magnitude of SUSY breaking. With this model we can express the $b \to s$ diagram as Fig 1.24, in penguin diagram the b quark radiative the gluino and changed to right-handed b-squark, and the right-handed b-squark transformed to right-handed s-squark by mixing parameter, $m^2_{\tilde{b}_R\tilde{s}_R}$. the right-handed s-squark radiative one gluon, at last the right-handed s-squark coupled with gluino and changed to s-quark. Since there are many unknown parameters, > 100 in SUSY model, the magnitude of new phase, ϕ', depends on these parameters, In simple assumption, all scalar fermion mass is same in plank scale, and gluino mass is $\sim 500\ GeV/c^2$. The ϕ' has $\sim O(0.1)$, shown in Fig 1.25. If the new physics phase has $\sim O(0.1)$, $\mathbf{sin2}\phi'_1$ has 0.4∼0.9 region, this region is larger than uncertainties of Standard Model.

In addition to that, 'Large left-handed squark mixing Model'[69][70], which the CP-violation difference from Standard Model expectation is occurred by generation mixing of left-handed squarks rather than that of right-handed ones. If $\tilde{b}_L$ and $\tilde{s}_L$ can be mixed we must consider the left-handed squark effect, or left-handed and right-handed squark can be mixed, we can expect the large ϕ' more than only right-handed model expectation. And if this model is good model, the direct CP asymmetry of the inclusive $b \to s\gamma$ can be as large as few percent with a positive sign. From all discussion above, we can understand that $B^0 \to \phi K_S$ mode has sensitivity for search the new physics. The same effect can affect to $B^0 \to K_S\pi^0$ CP-violation. Since there are many model and uncertaintly parameters, it is very important to constrain these theoretical model using $B^0 \to K_S\pi^0$.

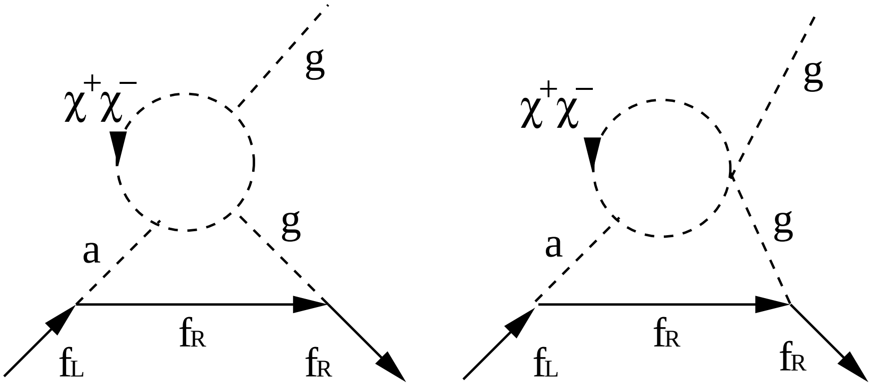

Figure 1.22: Two-loop contribution to EDM and CEDM in supersymmetric theories (mirror graphs are not displayed.)

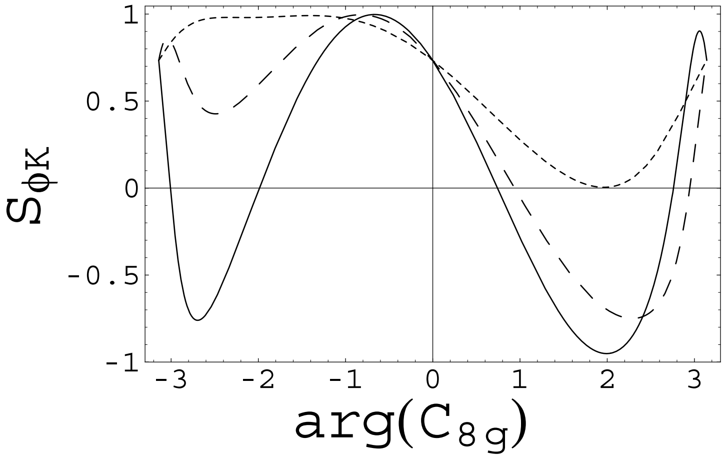

Figure 1.23: $S_{\phi K_S}$ as function of arg(C_{8g}) for $|C_{8g}| = 0.33$(short dashed line), 0.65(long dashed line) and 1.0(solid line).

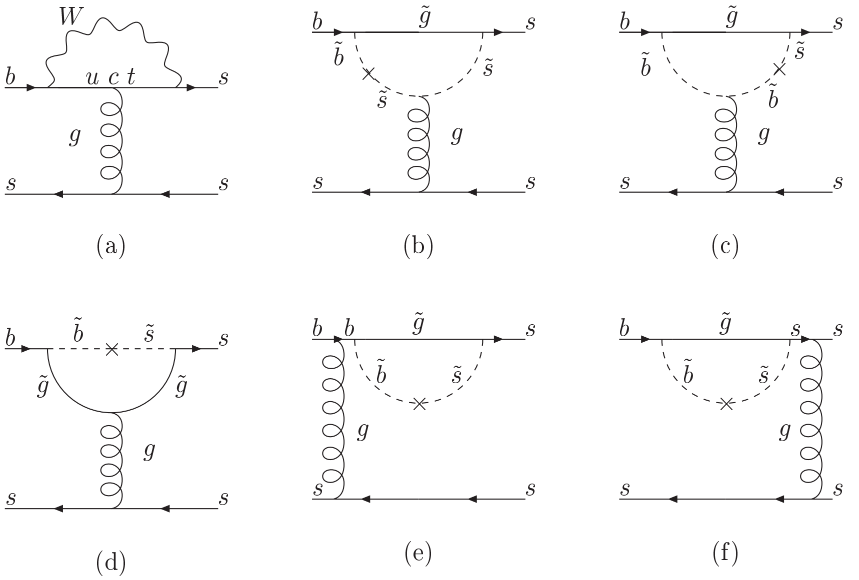

Figure 1.24: The Standard Model contribution (a), and the gluino-down squark contributions (b)-(f) to $B^0 \to \phi K_S$ decay, if we consider $K_S\pi^0$ we replace the $s\bar{s}$ to $d\bar{d}$ in each diagram.

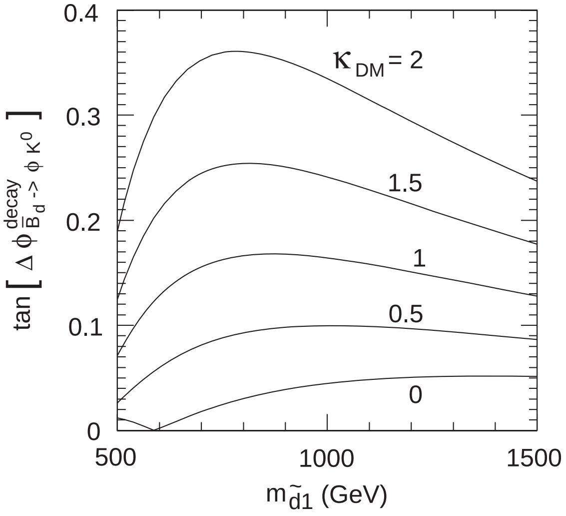

Figure 1.25: new phase as a function of the lightest down-type squark mass with $m_{\tilde{G}} = 500 GeV$

Chapter 2

Experimental Apparatus

2.1 KEKB Accelerator

The KEKB accelerator is an asymmetric energy collider of 8.0GeV electron and 3.5GeV positron. The total energy at center of mass is 10.58GeV same as mass of $\Upsilon(4S)$. More than 96% of $\Upsilon(4S)$ decay into $B^0\bar{B}^0$ or $B^+\bar{B}^-$ with same probability. Since the $\Upsilon(4S)$ run with $\beta\gamma = 0.425$ in the laboratory system because the lifetime of B meson are 1.5ps - 1.7ps, the decay producted $B\bar{B}$ mesons run about 200μm before. Therefore it is possible to measure the CP-violation by interference CP-Violation method.

Fig 2.1 shows the illustration of KEKB accelerator. Electrons and positrons are injected from linear accelerator(Linac) into two main rings respectively at Fuji area, one is High energy ring for electron beam while another one is Low energy ring for positron beam. The storage rings are about 3km long in circumference. After focused by quad pole magnet which are located around interaction point, electron and positron beam collide at one interaction point at Tsukuba area. The crossing angle of two beam at the interaction position is ±11mrad in order to avoid parasitic collisions near the interaction point. RF cavities are placed to excite bunches by electromagnetic wake. When a bunch goes through it.

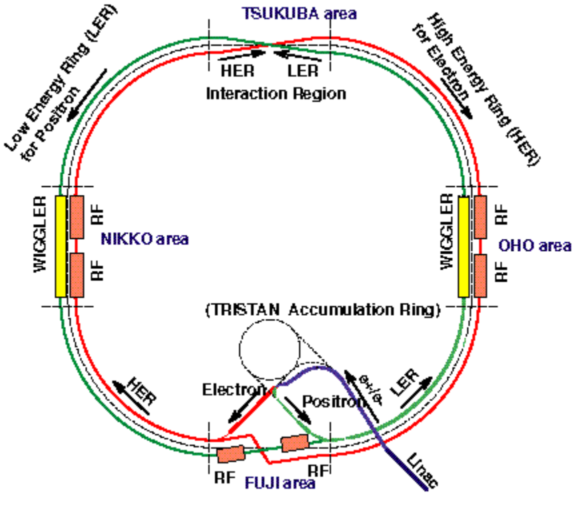

Figure 2.1: Configuration of the KEKB accelerator system

The luminosity can be expressed as,

$$L = 2.2 \times 10^{34} \cdot \xi \cdot (1 + r) \cdot \left(\frac{EI}{\beta_y^*}\right) \tag{2.1}$$

where, ξ is beam-beam tune shift parameter, r is aspect ratio of the beam shape, E is beam energy in GeV, I is circulating current in A and β_y^* is vertical beta function at interaction point in cms. This luminosity can also be written by,

$$L = f \cdot N_{bunch} \cdot \frac{n_{HER} n_{LER}}{4\pi \sigma_x' \sigma_y'} = \frac{I_{HER} I_{LER}}{4\pi \cdot f \cdot e^2 \cdot N_{bunch} \sigma_x' \sigma_y'} \tag{2.2}$$

where f is frequency of electron and positron beam crossing, $f \sim 3.0 \times 10^8 \text{(m/s)}/3.0 \times 10^3 \text{(m)} = 10^5 \text{(Hz)}$. N_{bunch} is number of bunch of electron and positron beam in storage ring, n_{HER} and n_{LER} are number of particles in a bunch. I_{HER} and I_{LER} are current of HER and LER, σ_x' and σ_y' are size of beam in x and y direction in detector coordinate system, the typical value is $\sigma_x' \sim 100\mu$ m, and $\sigma_y' \sim 5\mu$ m. These and other main machine parameters are listed in the Table 2.1.

Table 2.1: Main machine parameters of KEKB

Date	June 3, 2004		Unit
	LER	HER	
Beam Current	1580	1200	mA
Number of Bunches	1289		
Bunch Current	1.23	0.931	mA
Bunch spacing	2.34		m
Beam trains	1		m
Total RF voltage	8.0	14.0	MV
Betatron tune(x)	45.505	44.513	
Betatron tune(y)	43.535	41.582	
Beta function(β_x^*)	59	56	cm
Beta function(β_y^*)	0.52	0.65	cm
Estimated vertical beam size at IP(σ_y^*)	2.1	2.1	μm
Beam-beam parameter ξ_x	0.113	0.072	
Beam-beam parameter ξ_y	0.074	0.057	
Beam lifetime	152	178	min
Peak Luminosity	13.92		$10^{33}/cm^2/s$
Integrated Luminosity	944		/pb/day

The commissioning of the KEKB accelerator started in December 1998. The first beam collision was observed in Febuary 1999. The time variance of peak luminosity are shown in the Fig 2.2. The design luminosity($1.0\times 10^{34}\text{cm}^{-2}\text{s}^{-1}$) was achived in May 9 in 2003. The record peak luminosity is $1.392\times 10^{34}\text{cm}^{-2}\text{s}^{-1}$ which was recorded in June 3 in 2004. KEKB accelerator has achieved highest luminosity as e^+e^- collider in the world and can generate $B\bar{B}$ pairs with 10Hz.

2.1.1 Continuos Injection Method(CIM)

Until December 2003, we need to inject electron and positron beam at least every one and half hours because beam current and luminosity decreased. Injection takes about fitteen minuites and we can not take the data by Belle detector during injection.

The new method, Continuos Injection method(CIM), was started from January 2004. It was very important for CIM to improve the injector LINAC, and that was completed the end of 2003. The CIM means that electron and positron beam are injected with about 10Hz wihtout stop of taking data in order to avoid the decrease of the beam current and keep high luminosity. Before CIM started, we must repeat the beam injection twenty times per day, and we need three hour time-loss, while after started CIM method the time-loss is suppressed to 40 minuites. The integrated lumnosity of a day increase from $600\text{pb}^{-1}\text{day}^{-1}$ to $900\text{pb}^{-1}\text{day}^{-1}$, the record value is $944.2\text{pb}^{-1}\text{day}^{-1}$ (May 23 in 2004). The beam current, number of bunch, peak luminosity before and after used CIM are listed in Table 2.2[71].

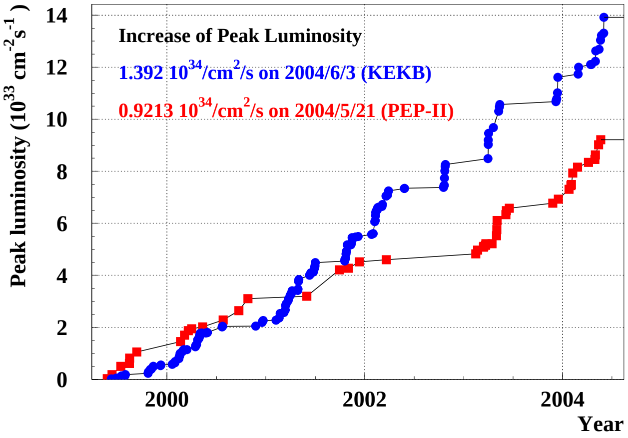

Figure 2.2: Time variation of peak Luminosity during data taking, horizontal axis is time scale, the vertical axis is peak luminosity($\mathrm{cm}^{-1}\mathrm{s}^{-1}$), the circle shows the KEKB peak luminosity, while the square shows the PEP-II peak luminosity

Table 2.2: Main Parameters before and after used CIM

Date	After : June.3.2004		Before : May.13.2003		Unit
	LER	HER	LER	HER	
Beam Current	1580	1200	1380	1050	mA
Number of Bunches	1289		1265		
Bunch Current	1.23	0.931	1.09	0.83	mA
Peak Luminosity	13.92		10.57		$10^{33}/\mathrm{cm}^2/\mathrm{s}$
Integrated Luminosity	944		579		/pb/1day
Integrated Luminosity	6.01		3.88		/fb/7day
Integrated Luminosity	24.00		12.81		/fb/30day

2.2 The Belle Detector

The Belle detector is installed surroundings the interction point which electron and positron beam collide in Tsukuba experimental hall[72]. Because of the asymmetric beam energy, the detector is configurated to be asymmetric. It means the detector acceptance is larger in the direction of electrons, which is defined as "forward" direction. The detector is configurated with 1.5T super-conductiong solenoid and iron structure surrounding the beam. The decay vertex of B meson are measured by silicon vertex detetctor(SVD)[73] which is located just outside of beam pipe made by Beryllium. The track information of charged particles, $e^{\pm}$, $\mu^{\pm}$, $\pi^{\pm}$, $K^{\pm}$, $p/\bar{p}$, are reconstructed by central wire drift chamber(CDC)[74]. The partcle identification is provided by dE/dx measurements in CDC, the aerogel Cherenkov counter(ACC)[75], time of flight counter (TOF)[76]. The electron identification and photon energy measurement are performed by electromagnetic shower in array of electromagnetic calorimeter(ECL)[77] which is made by thallium doped CsI crystal located inside the solenoid coil. Muon anf K_L meson are detected by resistive plate counter(KLM)[78] interspersed in the iron return yoke of the magnet. The coverage of belle detector is from 17° to 150° in polar angle for beam axis. The part of uncovered small angle region is instrumented with BGO crystal arrays(EFC)[79] placed on the surface of cryostats in the forward and backward direction. Fig 2.4. shows the cut-off view of the Belle Detector. The performance of each detector is summaried in Table 2.3. The coordinate system of the Belle detector is defined as,

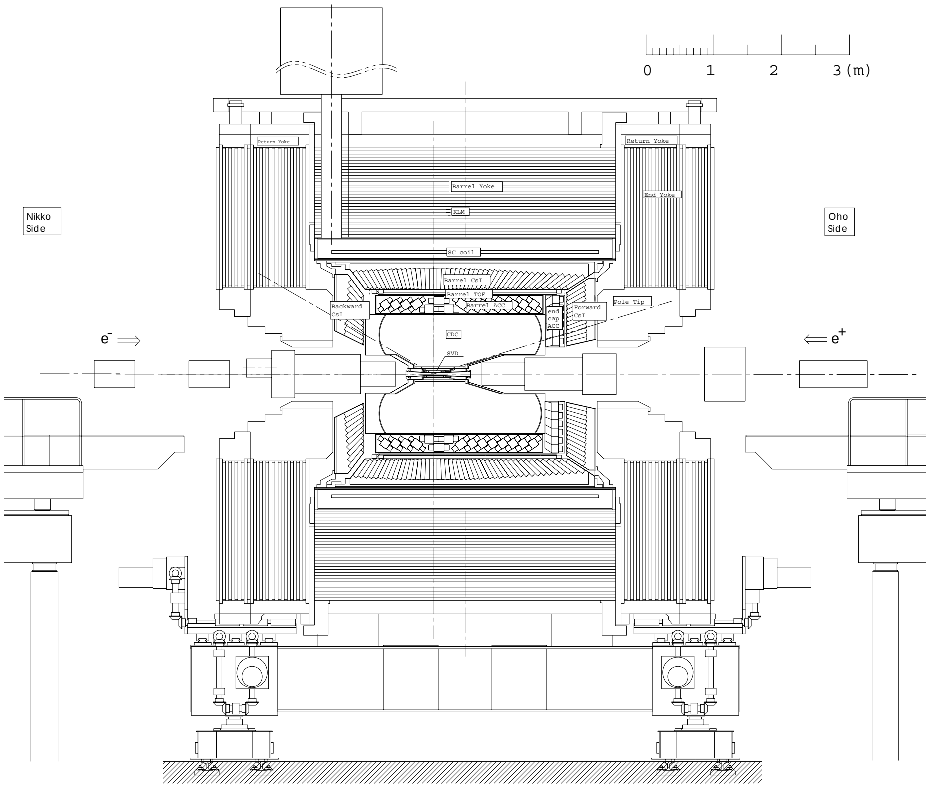

Figure 2.3: Sideview of the Belle Detector

x : horizontal outward to the KEKB ring

y : vertical upward

z : opposite of the position beam direction

r : $\sqrt{x^2 + y^2}$

θ : polar angle measured from +z direction

ϕ : azimuthal angle around z axis

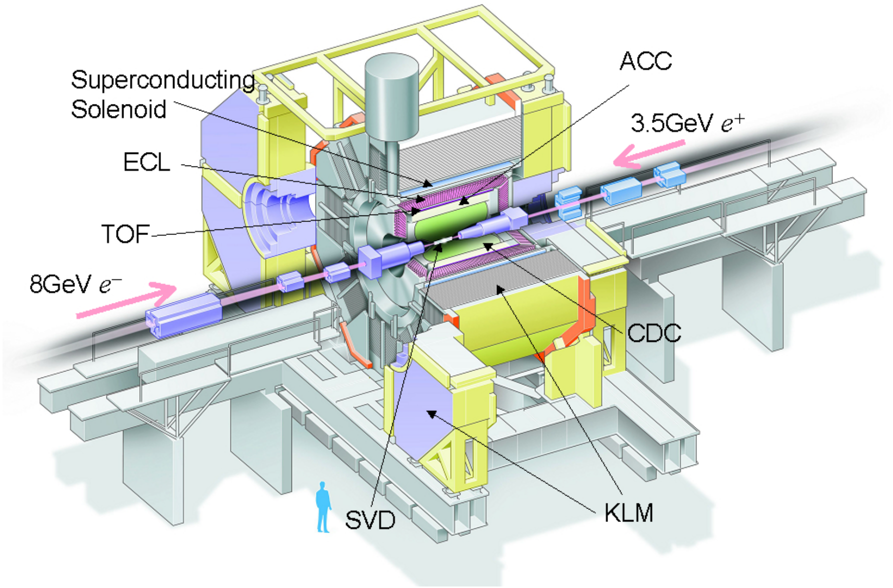

Figure 2.4: Overview of the Belle Detector

2.2.1 Beam pipe and Silicon Vertex Detector I (SVD-I)

The beam pipe consists of two difference radii cylinder, inner one is r=20.0mm, and outer one is r=23.0mm. The thickness of each cylinder is 0.5mm, the 0.3% radiation length. The space within two cylinder is filled with cooled He gas. The beam pipe is made of beryllium to reduce the multiple Coulomb scattering at the beam pipe wall. In addition, for protect from synchrotron radiation producted by electron and positron beam, the surface of outer cylinder are plated by gold with 20μm thickness, 0.6% radiation length. Fig 2.5 shows the cross section of beam pipe at the interaction region.

The silicon vertex detector is located at just outside of the beam pipe. It is crucially important for studying CP-Vioaltion to measure the B meson flight length along the z-direction. SVD is used for measurement the precise B decay vertices position, and the position resolution of z-direction is required to be $\sim 200\mu m$. In addition, this SVD also have important role for track reconstruction. The layout of SVD(SVD-I) is shown in Fig 2.6. The SVD-I comprises three cylindrical detection layers. The layer consists of 8, 10, 14 ladders, respectively. The radii of each layers are 3.0cm, 4.55cm, and 6.05cm, where the ladder is composed of 2, 3 or 4 double-side silicon strip detector(DSSDs). The polar angle coverage is from 23° to 140°, which is 86% of full solid angle. In order to achieve a vertex resolution better than 200μm, good alignment is required. Each ladder in turn is made from two half-ladders. In the innermost layer, each half ladder has one DSSD. In the second layer, one half ladder has two DSSDs and another half ladder has one DSSD. In the outermost layer all half ladders have two DSSDs. There are 16, 30, and 56 DSSDs in first and second and third layer, respectively, and the total number of DSSD is 102. The DSSD is essentially a large area p-n diode and the size is $57.5\times 33.5\text{mm}^2$ with thickness of 300μm. The N-side of the DSSD has n^+-strips oriented perpendicular to the beam direction to measure the z coordinate and the P-side with longitudinal p^+-strips for the ϕ coordinate measurement. The bias voltage of 75V is supplied to the N-side, while the P-side is grounded. In typical case, a charged particle running through the depletion region of the n-bulk

Table 2.3: Summary of the subcomponent of Belle detector

Component	Type	Configuration
	Readout channel	Performance/Note
Beam Pipe for SVD-I	Beryllium double-wall	Inner radius = 20 mm Thickness = 0.5(Be)/2.5(He)/0.5(Be)mm
		Helium gas chilled
Beam Pipe for SVD-II	Beryllium double-wall	Inner radius = 15 mm Thickness = 0.5(Be)/2.5(PF200)/0.5(Be)mm
SVD-I	Double sided silicon strip	300μm thickness, 3 layers: r=30.0$\sim$60.5mm, Strip pitch: 25(p)/50(n) μm
	$r-\phi$:40.96 k z:40.96 k	Δz resolution $\sim$ 144 μm from J/ψ Vertex from MC
SVD-II	Double sided silicon strip	300μm thickness, 4 layers: r=20.0$\sim$88.0mm, Strip pitch: 1$\sim$3layer:75(p)/50(n) μm Strip pitch: 4layer:73(p)/65(n) μm
	$r-\phi$:55296 z:55296	Δz resolution $\sim$ 127 μm from J/ψ Vertex from MC Radiation Hardness : $>$ 20Mrad
CDC	Small-cell Drift Chember	Anode: 50 layers, Cathode: 3 layers r = 83 $\sim$ 863 mm, z = -77 $\sim$ 160 cm
	Anode:8.4k Cathod:1.8k	$\sigma_{r-\phi} = 130\mu$m, $\sigma_z = 200 \sim 1400$ μm, $\sigma_{p_t}/p_t = (0.29 \oplus 0.20 \cdot p_t[GeV/c])$, $\sigma_{dE/dx} = 7\%$
ACC	Silica aerogel Cherenkov counter	$\sim$120$\times$120$\times$120mm^3 block: 960 barrel and 228 forward end-cap, Fine Mash PMT readout
	1788	$\pi^{\pm}/K^{\pm}$ separation: $1.2 < p < 3.5 GeV/c$
TOF	Scintillation counter	128ϕ segments, r=1201mm, 3m long
	128$\times$2	$\sigma_t = 100$ps, $\pi^{\pm}/K^{\pm}$ separation: $p < 1.2 GeV/c$
TSC	Scintillation counter	64ϕ segments, r=1175mm, 3m long, attached TOF
ECL	CsI(Tl)	Towered structure, $\sim 55 \sim 55 \sim 300 mm^3$ block, r=125$\sim$162cm(barrel), z=-102,196cm(end-cap)
	Barrel:6624 Forward:1152 Backward:960	$\sigma_E/E = (1.34 \oplus 0.066 \cdot E^{-1} \oplus 0.81 \cdot E^{-1/4})\%$, $\sigma_{position} = 0.27 + 3.4 \cdot E^{-1/2} + 1.8 \cdot E^{-1/4}$ mm(E in GeV)
Magnet	Super-conducting solenoid	Inner radius=1,700mm
		B=1.5T
KLM	Glass resistive plate counter	14 layers: 50 mm Fe + 40 mm gap, 2RPCs(θ strips and ϕ strips) in each gap
	ϕ:16k θ:16k	$\Delta theta = \Delta\phi = 30$ mrad for K_L, σ_t = a few ps
EFC	$Bi_4Ge_3O_{12}$	32 Segments in ϕ, 5 segments in θ, Photodiode readout $2 \times 1.5 \times 12 cm^3$
	ϕ : 5 θ : 32	Energy Resolution(R.M.S) = 7.3%(8.0GeV), Energy Resolution(R.M.S) = 5.8%(3.5GeV)

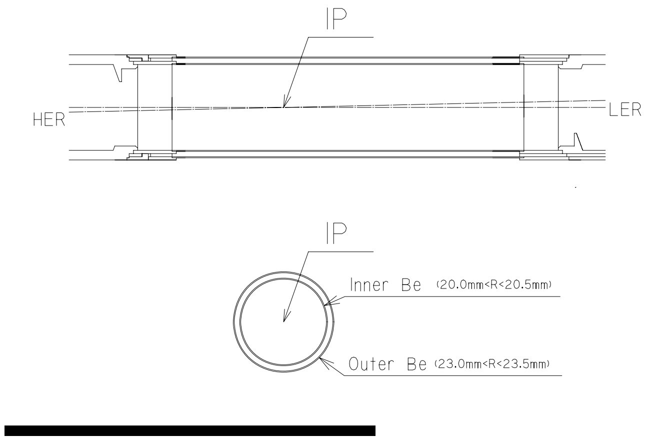

Figure 2.5: Cross section of the beryllium beam pipe for SVD-I at the interaction point

silicon, generates approximately 20,000 electron-hole pairs. Electron drift to n^+-strip while holes drift to p-strip by electric field. The DSSD strips pitch for P-side is 25μm and N-side is 42μm and the readout pitch for P-side is 50μm and N-side is 84μm. A DSSD has 1280 strips and 640 readout strips in the both N and P-side. Then the total number of readout channel is 81920(=640×2 × 32 × 2). The front-end readout is performed by 128 channel VA1 chips that include pre-amplifiers, shapers and hold circuit[80][81]. The scanned analog signals are transfered to the electronics hut by repeater modules, and are digitized by flash ADC modules, where event buffering and zero suppression are performed together with the A/D conversion.

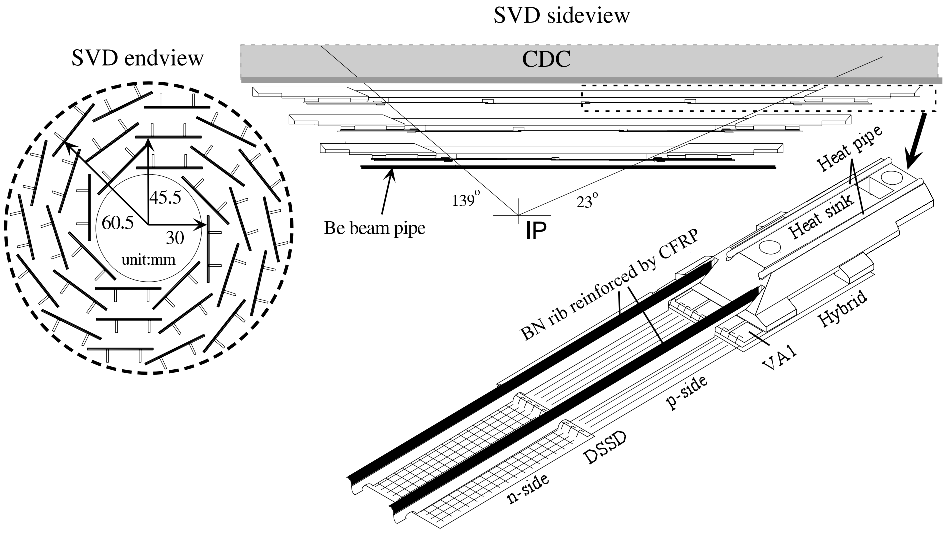

Figure 2.6: The configuration of the Silicon Vertex Detector I

Performance of the SVD-I is introduced about S/N ratio and matching efficiency and impact parameter resolution. The typical measured S/N ratio is 47 for P-side and 19 for N-side. The matching efficiency is probability that a CDC tracks within the SVD acceptance has associated SVD hits in at least two layers in $r-\phi$ side, and at least one layer in z-side. The time variation of matching efficiency is shown in Fig 2.8. The average matching efficiency is measured to be better than 98.7%. The impact parameter(IP) resolution provides us capability of SVD as a vertex detector. The IP resolution, $\sigma_{\mathbf{IP}}$, involves two factors, one is

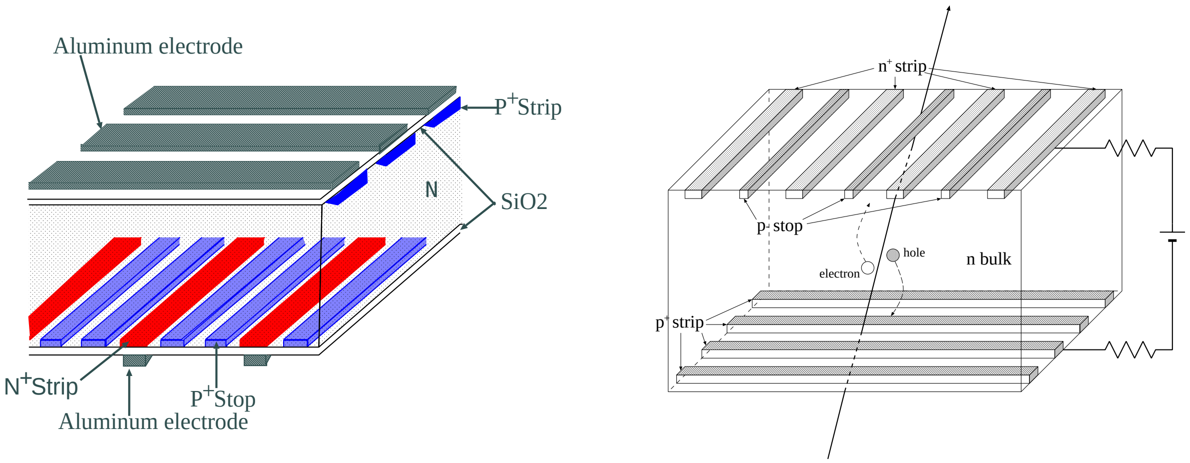

Figure 2.7: The schematic view of double silicon strip detector

intrinsic resolution of the vertex detector itself, and another is related to multiple Coulomb scattering which depends on momentum. It can be expressed as,

$$\sigma_{\mathbf{IP}} = a \oplus b/\tilde{p} \tag{2.3}$$

$$\tilde{p} = \begin{cases} p\beta\mathbf{sin}^{\frac{3}{2}}\theta & \mathbf{for} \;\; d\rho \\ p\beta\mathbf{sin}^{\frac{5}{2}}\theta & \mathbf{for} \;\; dz \end{cases} \tag{2.4}$$

where p is the track momentum, β is the velocity of the particle and θ is the dip angle. The IP resolution measured by cosmic-ray data from standard deviation of difference of two track poistion which is reconstructed by CDC and SVD taken in 2003 is $(19.2\pm0.8)\oplus(54\pm0.8)/\tilde{p}(\mu\text{m})$ in $d\rho$ and the $(42.2\pm1)\oplus(44.3\pm1)/\tilde{p}(\mu\text{m})$ in dz shown in Fig 2.12[82]. the plots of IP resolution.

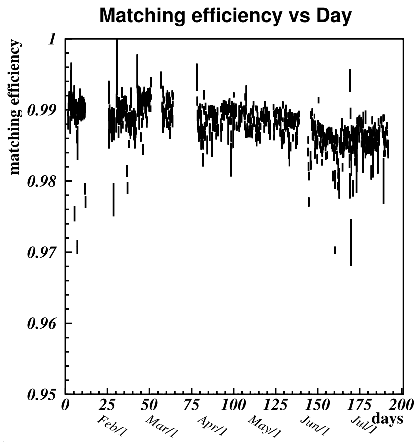

Figure 2.8: SVD-CDC track matching efficiency

2.2.2 Silicon Vertex Detector II (SVD-II)

New SVD(SVD-II) has been installed in the summer of 2003. There are many improvement from SVD-I. The geometrical configuration of SVD-II is shown in Fig 2.9 and 2.10. The SVD-II consists of four cylindrical layers whose the radii are 20.0mm, 43.5mm, 70.0mm, and 88.0mm. The angular acceptance coverages from 17° to 150°, which is same as CDC acceptance. The four layers have 6,12,18,and 18 ladders to cover all the ϕ region. and in each ladder are consisted with 2,3,5, and 6 DSSDs which are fabricated by Hamamatsu Photonics. There are two kinds of DSSDs. One is used in 1st, 2nd and 3rd layers, the size is $28.4\times79.6\text{mm}^2$, the strip pitch is 75 μm on P-side and 50μm on N-side. The another one is used in 4th layer, the size is $34.9\times76.4\text{mm}^2$ the strip pitch is 73μm on P-side and 65μm on N-side. The N-side of DSSDs is used for measurement of the $r-\phi$ coordinate and the other side, P-side, is used for measurement of the z coordinate. The number of strip is 1024 in the both N-side and P-side. The number of readout strips is 512 in the both N-side and P-side. The total number of DSSDs is 246. Therefore the total number of readout channel is 110592(=216×512). As in SVD-I, each ladder is read out by four hybrids. Each hybrid employs four VA1TA chips, each VA1TA chips amplifies the signals from 128 strips, whose pulse heights are held and sent out serially. To minimize the readout deadtime, the four chips on each hybrid are readin parallel. In contrast to SVD-I, where the chips were raed sequentially. This represents a significant reduction in the overall deadtime of the Belle DAQ system. The VA1TA also in corporates a fast shaper and discriminator that provide digital signal fir use in the trigger. The signals are demultiplexed in the FADC boards, housed in the electronics hut[83].

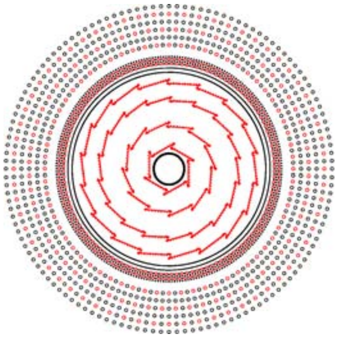

Figure 2.9: Cross section of the SVD-II

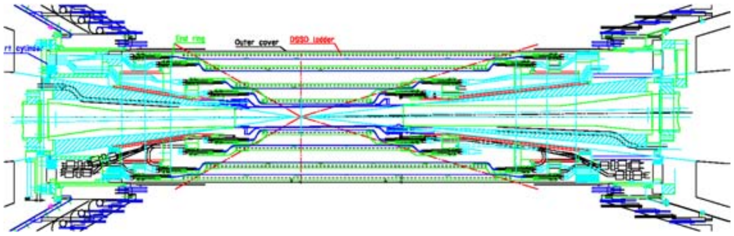

Figure 2.10: Sideview of the SVD-II

We can evaluate the performance of the SVD-II compairing with that of SVD-I. The S/N ratio were measured in each layers by cosmic-ray data, the S/N ratio of P-side(N-side) in 1st layer is 57(60), in 2nd layer is 36(37), in 3rd layer is 27(27),and in 4th layer is 27(33), respectively[84]. The matching efficiency is measured and monitored during taking data. Fig 2.11 shows the time variation of matching efficiency during Jan.2004 to Feb.2004. The typical value is 97%. The IP resolution measured by cosmic-ray data are $(17.4 \pm 0.3) \oplus (34.4 \pm 0.7)/\tilde{p}(\mu\mathbf{m})$ in $d\rho$ and the $(26.3 \pm 0.4) \oplus (32.9 \pm 0.8)/\tilde{p}(\mu\mathbf{m})$ in dz[82]. Fig 2.12 shows the IP resolution as function of $\tilde{p}$ in $d\rho$ and dz compared with those of the SVD-I. Note that the first layer of SVD-II is closer to the beam pipe than that of the SVD-I. This is shown as the improved intrinsic resolution with SVD-I and SVD-II separately. Due to a replacement of the vertex detector, we must evaluate the vertex resolution for CP-violation study. The physics performance with SVD-I and SVD-II are described in Chapter 3.2

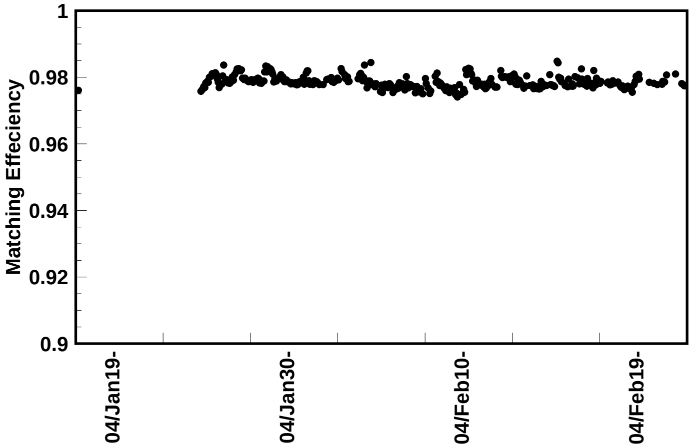

Figure 2.11: Time variation of Matching Efficiency of SVD-II(2004/01/19-2004/02/10)

Table 2.4: Comparison of IP resolution with SVD-I and SVD-II

	SVD-I	SVD-II
$d\rho$	$(19.2 \pm 0.8) \oplus (54 \pm 0.8)/\tilde{p}(\mu m)$	$(17.4 \pm 0.3) \oplus (34.4 \pm 0.7)/\tilde{p}(\mu m)$
dz	$(42.2 \pm 1) \oplus (44.3 \pm 1)/\tilde{p}(\mu m)$	$(26.3 \pm 0.4) \oplus (32.9 \pm 0.8)/\tilde{p}(\mu m)$

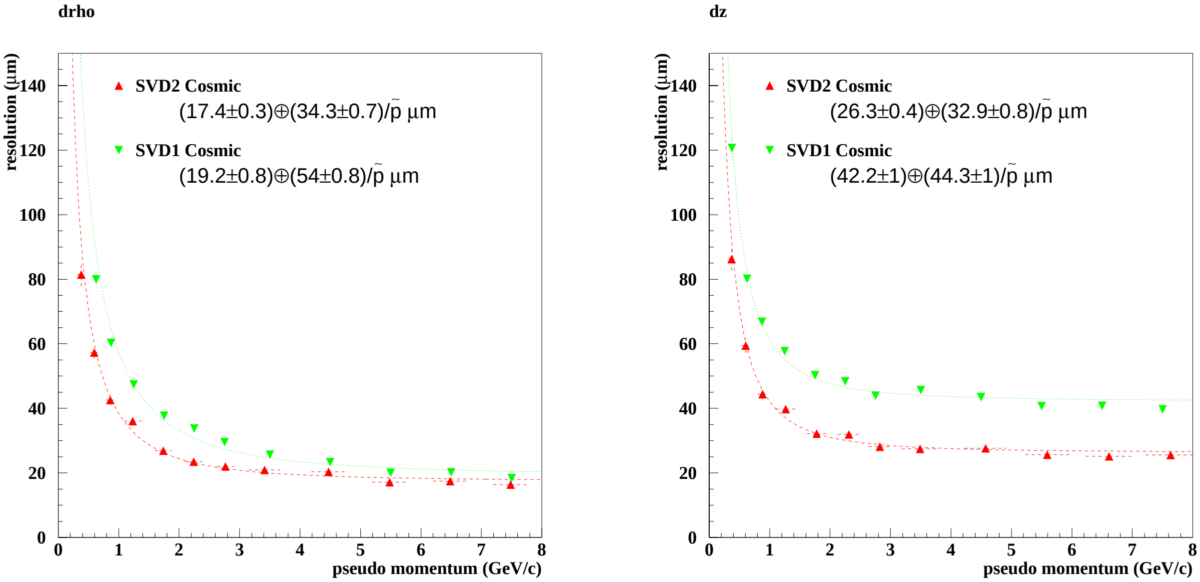

Figure 2.12: Comparing Impact Parameter resolution of SVD-I and SVD-II in the $r - \phi$ plane(left) and the z plane(right)

2.2.3 Central Drift Chamber(CDC)

The primary role of Central Drift Chamber(CDC) is to reconst the track and to measure momentum of charged particles. The goal of physics required the momentum resolution $\sigma_{pt}/p_t \sim 0.5\%\sqrt{1+p_t^2}$. The CDC also provides the particle identification of charged particle from energy loss by ionization, since the energy loss, dE/dx, depends on the velocity of particle, $\beta = v/c$. The coverage of polar angle is from 17° to 150°. The inner and outer radii of the CDC are 8cm and 88cm, respectively. The detector coverage in the z direction is from -702.2mm to 1502.2mm. The CDC is small cell drift chamber and consist of 50 cylindrical sense-wire layers, which consist of 32 axial-wire layers(6 super layers) and 18 stereo wire layers(5 super layers). The axial wires are configured to be parallel to z-axis, while the stereo wires are slanted approximately ±50 mrad to provide the z coordinate information. The one cell is made by one sense wire which supplied by 2.2k voltage, and eight electric field wire. The sense wires are gilded tungsten of 30μm in diameter and the field wires are unplated aluminum of 126μm in diameter to reduce the material of the chamber. The CDC has 8400 drift cell which corresponding to number of readout wire, 5280 axial wires and 3120 stereo wires. The size of cell is 16×17mm^2. A mixture of He(50%) and C_2H_6 are filled in the chamber. The use of the helium minimizes the multiple Coulomb scattering contributing to the momentum resolution. The radiation length and the drift velocity of the He-C_2H_6 mixture are about 640m and 4cm/μs, respectively. A charged particle traveling in the CDC produces ionized gas($\sim$ 100/cm). A charge avalanche is caused by the ionized gas and it drift to the sense wire with a finite drift time, then signal is measured.

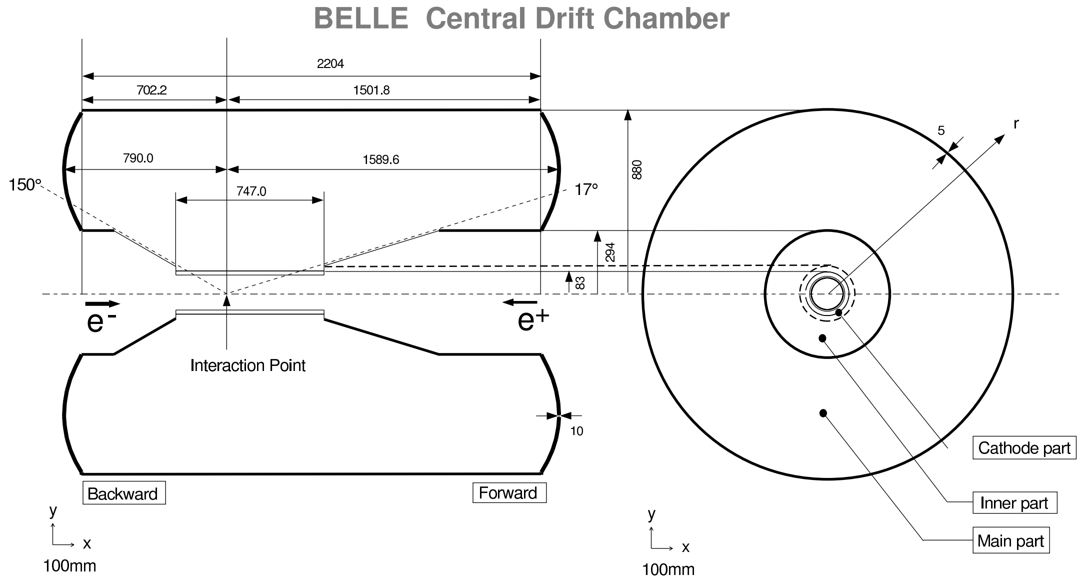

Figure 2.13: Overview of the Central Drift Chamber

The spatial resolution depends on the drift distance. The average of position resolution is approximately $\sigma_{r-\phi} = 130\mu m$, which was measured by beam test. The transverse momentum resolution is measured to be σ_{p_t}/p_t is $(0.20p_t \oplus 0.29)\%$, where p_t is transverse momentum. Fig 2.15 shows the σ_{p_t} as function of p_t, which is measured by cosmic-ray data. The CDC is involved in the particle identification for the track with $p < 0.8$GeV/c and $p > 2.0$GeV/c measuring energy loss, dE/dx. The mean rate of energy loss of charged particles are obey by Bethe-Bloch equation,

$$-\frac{dE}{dx} = 4\pi N_A r_e^2 m_e^2 c^2 \left(\frac{Z}{A}\right)\left(\frac{z}{\beta}\right)^2 [ln\left(\frac{2m_e c^2\beta^2\gamma^2}{I}\right) - \beta^2 - \frac{\delta}{2}] \tag{2.5}$$

Where N_A is Avogadro's number, r_e is classical electron radius, A is mass number of the atom of the medium, $\gamma = 1/\sqrt{1-\beta^2}$, and $I \sim 16Z^{0.9}$(eV) means excitation energy of medium, x is path length of

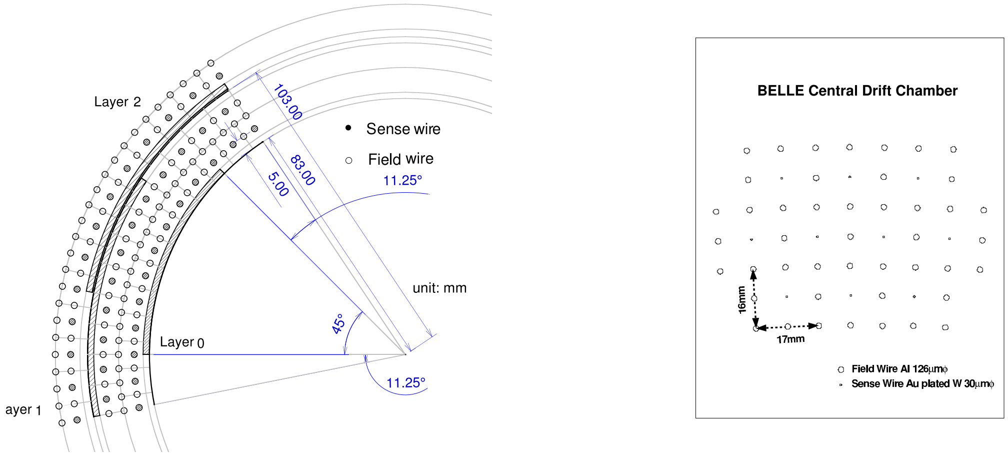

Figure 2.14: The c ell structure of CDC

particle. A scatter plot of measured $< dE/dx >$ and the particle momentum is shown in Fig 2.16, together with the expected mean energy loss for different particles. The resolution of dE/dx is 6.9% for minimum ionizating pion from K_S decays as shown in Fig 2.17

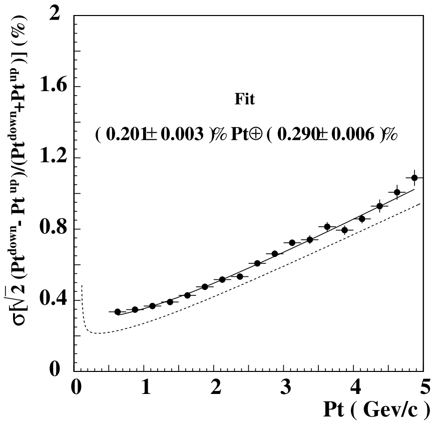

Figure 2.15: The transverse momentum resolution of CDC as function of itself(GeV/c)
The solid line shows the fitted result and the broken line represents and ideal expectation for $\beta = 1$ particle

Fit of reconstructed track is done by Kalman filtering method[85][86] taking into account the effect of multiple Coulomb scattering, energy loss, and non-uniformity of magnetic field.

2.2.4 Aerogel Cherenkov Counter(ACC)

The ACC provides $\pi^{\pm}/K^{\pm}$ separation for the measurement from 1.2 to 3.5GeV/c by the detection of Cherenkov light from particle penetrating through silica aerogel radiator. The requirement of the Cherenkov emission is

$$n > 1/\beta = \sqrt{1 + (m/p)^2} \tag{2.6}$$

where m and p are particle mass and momentum, and the n is refractive index of radiator, silica aerogel. The critical energy for emission can be written by,

$$E = \frac{n}{\sqrt{n^2 - 1}} mc^2 \tag{2.7}$$

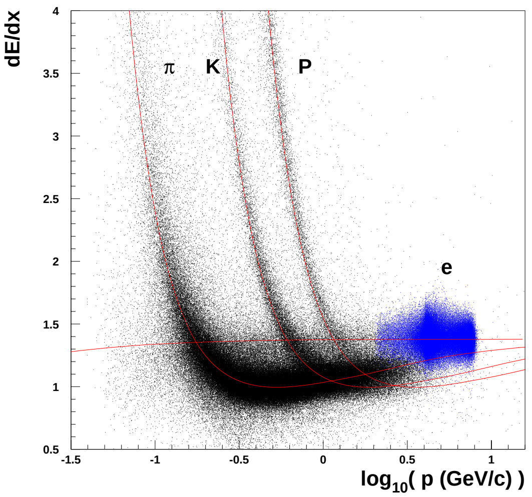

Figure 2.16: The expected mean dE/dx of e,π,K,P as function of momentum in collision data

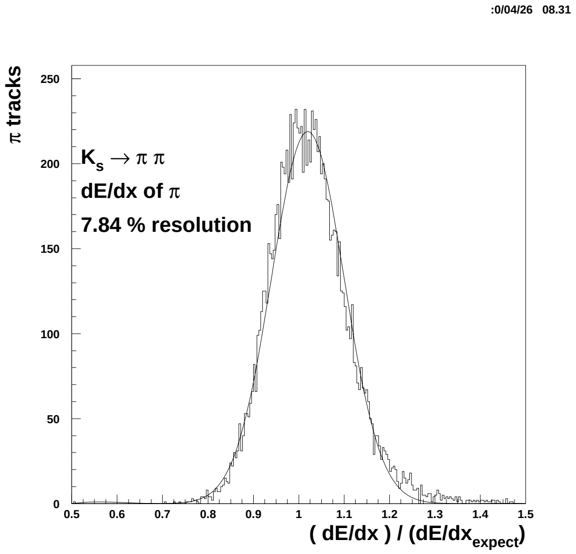

Figure 2.17: Distribution of measured dE/dx divided by expected dE/dx for pion from K_S decay

and the critical energy for electron, muon, pion, kaon, and proton are summarized in the Table 2.5, where we used the refractive index as 1.2.

Table 2.5: Critical Energy for emission Cherenkov light

	mass(GeV/c^2)	E(GeV)
$e^{\pm}$	0.000511	0.000924
$\mu^{\pm}$	0.105	0.190
$\pi^{\pm}$	0.138	0.250
$K^{\pm}$	0.496	0.897
$P/\bar{P}$	0.938	1.700

The basic concept for particle identification by ACC is that the light meson such as pion fire the ACC while heavier mesons such as kaon do not. The $\pi^{\pm}/K^{\pm}$ separation and consequent kaon detection and one of essential issue for CP-Violation study because a sum of kaon charges in an event gives good information for the flavor of B Meson. To get the high $\pi^{\pm}/K^{\pm}$ separation performance in the multi-GeV/c momentum range, the threshold type Cherenkov counter are required to have refractive index between those of liquid and solid[75]. The silica aerogel provides a good refractive index for this requirement. The silica aerogel is a porous colloidal form of $(SiO_2)_2$ with more than 95% prity. It has low density because of structure, and consequently it has low refractive index, The density and refractive index is determined according to its chemical production procedure. The ACC has barrel part and end-cap part, the barrel part consist of 960 module container divided by 60 in ϕ direction, while the forward end-cap and backward end-cap have 228 module counter consist of 5 concentric layer. One counter module is made by Alluminium container box which one side-12cm, 0.2mm-thick and silica aerogel in the box, and the Fine-mesh PMT which is connected to one or two plane of the box. The inner surface of the box is lined with Goretex sheet as reflector. Cherenkov light is generated by penetrating particle in the silica aerogel as radiator, and the light is fed to Fine-mesh PMT and make signal. The Fine-mesh PMT can be operated in 1.5T magnetic field[88]. The barrel part module is consist of five layers which have difference refractive index. The momentum of particles which are producted from B-meson decay depend on polar angle. Each refractive index are determined in order to have good separation depend on polar angle of momentum. The each

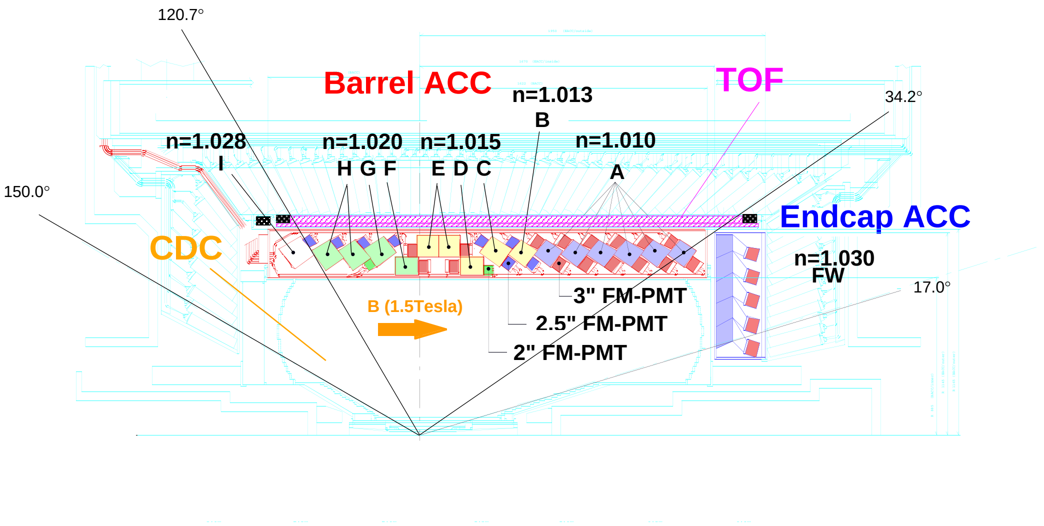

Figure 2.18: Arrangement of the ACC at the central part of the Belle detector

a) Barrel ACC Module

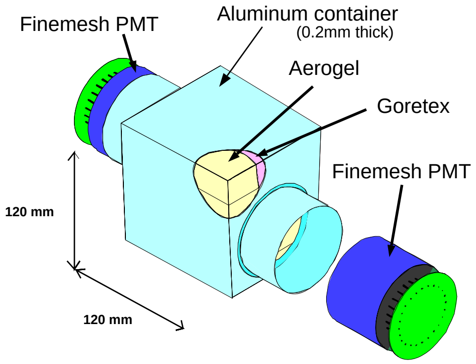

b) Endcap ACC Module

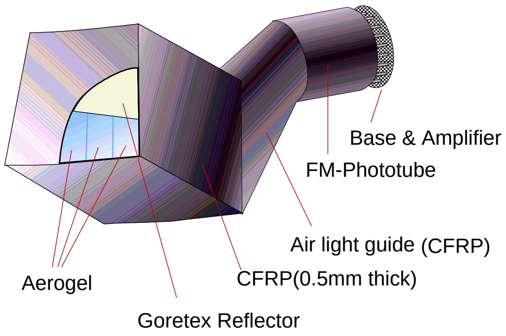

Figure 2.19: Schematic drawing of the typical ACC counter module for barrel(a) and end-cap(b)

refractive index and number of module from forward direction are 1.028 and 60 module, 1.020 and 240 module, 1.050 and 240 module, 1.013 and 60 module, 1.010 and 360 module, respectively. The refractive index in forward and backward end-cap is same as n=1.030. A number of readout channel is 1560 in barrel part and 228 in the end-cap part. The typical pulse height of ACC is shown in Fig 2.20. Kaon can not generate pulse, while the electron can generate pulse. The pulse height of electron is measured by Bhabha scattering data.

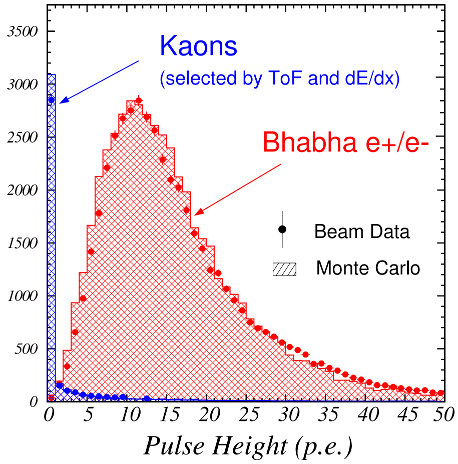

Figure 2.20: The distribution of pulse height of kaon and electron/positron
Point is pulse height observed at barrel part ACC. Electron and Kaon are identified by CDC dE/dx and TOF information. The hatched histogram is Monte Calro expectation.

2.2.5 Time Of Fight(TOF)

The Time Of Flight(TOF) counter, which is made of plastic scintillation counter, is used to distinguish kaon from pion in the momentum range below 1.2GeV/c. The minimum transverse momentum to reach TOF counter is 0.28GeV/c. In addition to particle identification, the TSC provides fast timing signal for the trigger system to gate signal for ADCs and stop signal for TDCs(Thin Trigger Scintillation Counter). The counters measure the elapsed time between a collision at the interaction point and the time when the particle hits the TOF layer. For the measured flight time with an appropriate correction, T, a particle mass, m, is represent by,

$$m = p\sqrt{\frac{T}{L_{path}^2} - 1} \tag{2.8}$$

where L_{path} is flight path-length, and p is momentum of particle, The particle momentum and path-length are given from the CDC track fit assuming a muon mass. The time of flight at p=1.2GeV/c is 4.3ns for $K^{\pm}$, and 4.0ns for $\pi^{\pm}$, respectively. The time resolution of 100 ps gives $\pi^{\pm}/K^{\pm}$ separation capability in 3 σ. Fig 2.21,2.22 shows an illustration of one TOF/TSC counter and its both ends. One 5mm thick TSC layer and one 4cm thick TOF counter layer, which is scintillator, are arrayed cylindrically with 1.5cm gap at the position of L=1.2m in radius from interaction point. The total number of TSC counters and TOF counter is 64 and 128, respectively. The scintillator are wrapped with 45μm thick polyvinly film for light tightness and surface protection. Two Fine-mesh PMT, are glued to each TOF counter at both ends, and one FM-PMT is glued to each TSC at backward. The the total number of readout channel is 256(=128×2) for the TOF and 64 for the TSC. Fig 2.23 shows the time resolution of forward and backward PMT of TOF, and for the weighted average of time resolution as function of hit position.

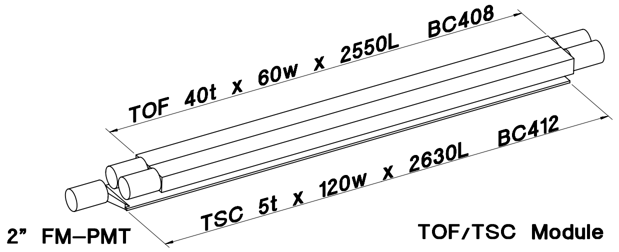

Figure 2.21: Overview of TOF/TSC module

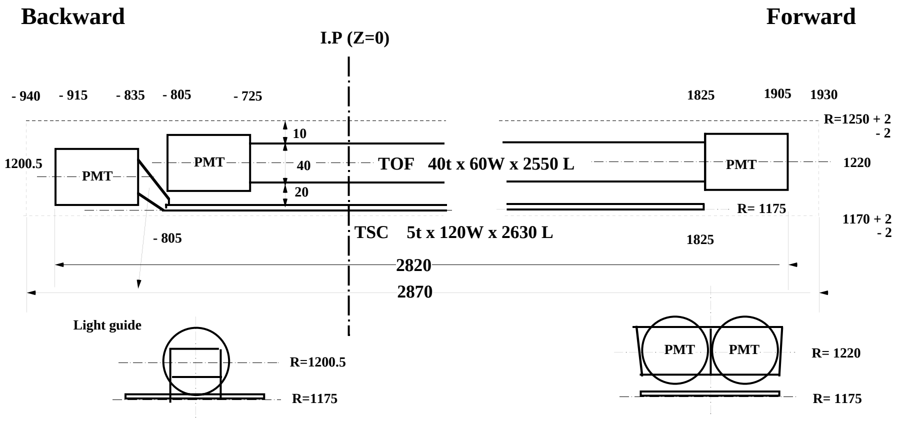

Figure 2.22: Demensions of TOF/TSC module

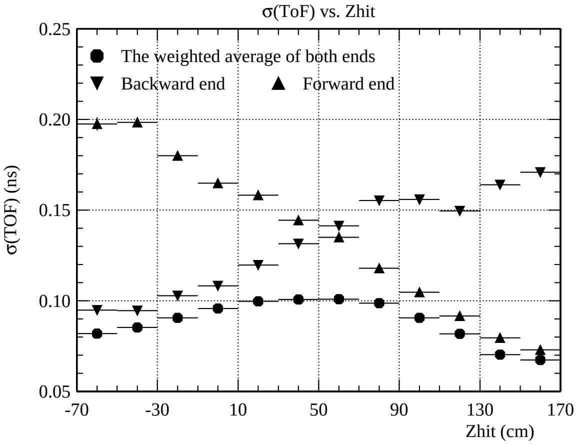

Figure 2.23: The time resolution of TOF for $e^+e^- \rightarrow \mu^+\mu^-$ events as function of the track position in beam direction

Fig 2.25 shows the capability of $\pi^{\pm}/K^{\pm}$ separation, which is defined as,

$$\sigma = \frac{T_{obs}(K) - T_{obs}(\pi)}{\sqrt{\sigma_K^2 + \sigma_\pi^2}} \tag{2.9}$$

It shows 2σ separation up to particle momentum of 1.25GeV/c with this accuracy, we have clearly separated distributions of Kaon mass from pion mass as shown in Fig 2.24.

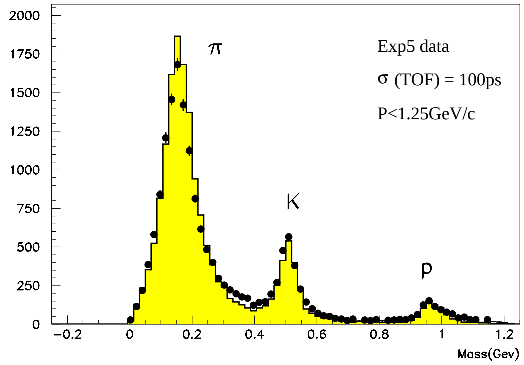

Figure 2.24: Mass distribution from TOF measurement for particles momenta below 1.2GeV/c
The point shows the data obtained from hadronic events, while the histogram shows the expectation from Monte Calro by assuming time resolution is 100ps.

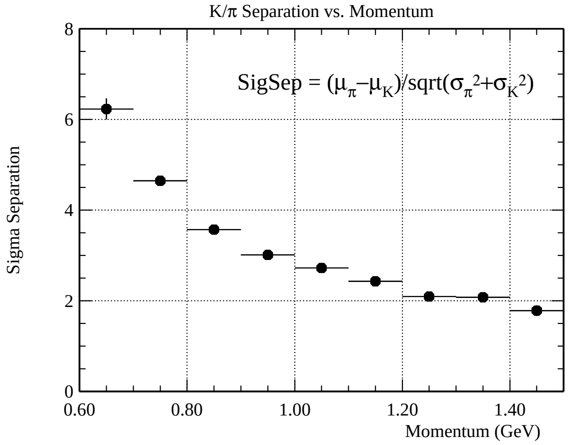

Figure 2.25: The separation of Kaon and pion as function of momentum

2.2.6 Electromagnetic Clorimeter(ECL)

For typical B-meson decays approximately 1/3 of final state particle are π^0. The π^0 mass resolution is dominated by the photon energy resolution. The main purpose of ECL is to detect the electron and photon with high efficiency and high energy and position resolution. In specially the electron identification is main role for ECL. It relies primarily on comparison of the CDC and the energy deposit at the ECL clusters. Electron deposit most of its energy in the ECL by electromagnetic shower, while muon and hadron deposit small fraction of their energies. Good energy resolution results in better hadron rejection. Since most photon from π^0 are the end product of cascade B decays, the photon have low energies. It is also important to detect up to about 4GeV photon for $B \to K_S\pi^0$ decay studies. Therefore, the ECL is designed to provide good sensitivity of photon from low to high energy.

The overall configuration of the ECL is shown in Fig 2.26. The ECL consist of 8736 thallium doped CsI crystal counters. CsI(Tl) crystals have various nice features such as a large photon yield, weak hygroscopicity, mechanical stability, and moderate price. Each CsI(Tl) crystal is 30cm long, which corresponds to 16.2 radiation length. Each crystal has a tower-like shape and is arranged almost to the interaction point. The barrel crystal are located at from r=1.25m to 1.62m region, while forward and backward ECLs are located from z=+1.96m to -1.02m. The polar angle coverage of ECL counter is from 17° to 150°. The barrel part of ECL has 6624 crystal counters which 46-fold segment in the ϕ direction and 144-fold segmentation in the θ-direction. The forward end-caps part of ECL has 1152 crystal counters which is segmented into 13-folds in the θ direction, while the segmentation in the ϕ direction varies from 48 to 144. The backward end-caps has 960 crystal counters which is segmented in 10-fold in the ϕ direction. The typical dimensions of a crystal are 55mm×55mm at front surface and 65mm×65mm at rear surface, and the each crystal is readout by two 2cm×1cm photo diode. A total readout channels of ECL is 17422. The weight of ECL is 43ton in total.

The position resolution is measured to be depend on the photon energy,

$$\sigma_{pos} = \left(0.27 + \frac{3.4}{\sqrt{E(GeV)}} + \frac{1.8}{\sqrt{E^{1/4}(GeV)}}\right) \quad \textbf{(mm)} \tag{2.10}$$

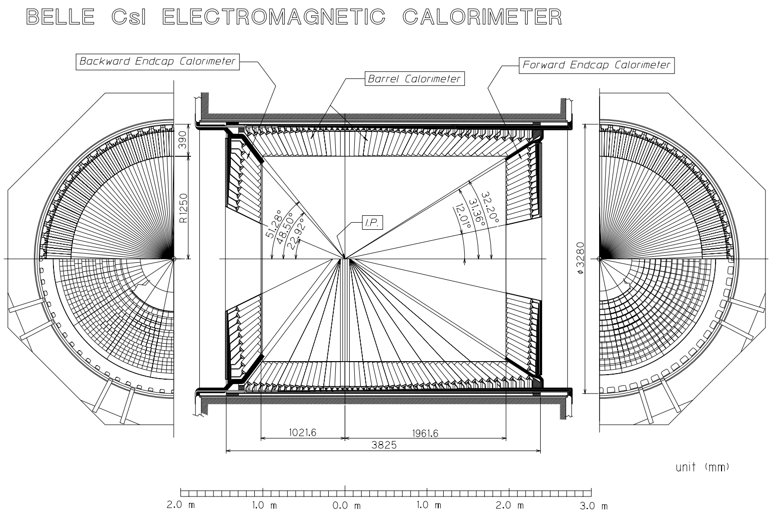

Figure 2.26: Overall structure of the ECL

The position resolution is shown in Fig 2.27. The energy resolution is measured as a function of incident photon energy for 3×3 matrices and for 5×5 matrices of the ECL counters. The nominal resolution is measured to be

$$\frac{\sigma_E}{E} = \left(1.34 \oplus \frac{0.066}{E} \oplus \frac{0.81}{E^{1/4}}\right) \quad (\%) \tag{2.11}$$

with the study of 3×3 ECL matrices. The measurement are shown in Fig 2.28. These performance enable us, for example, to reconstruct $\pi^0 \to \gamma\gamma$ candidate with invariant mass resolution of 4.8 MeV/c^2.

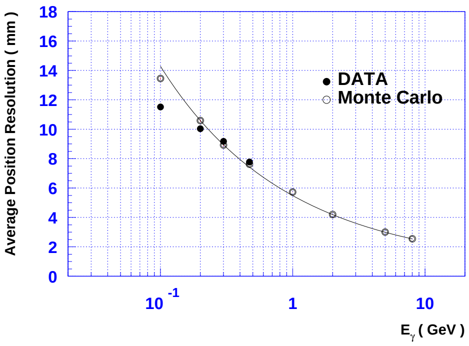

Figure 2.27: The average position resolution as a function of the measured cluster energy

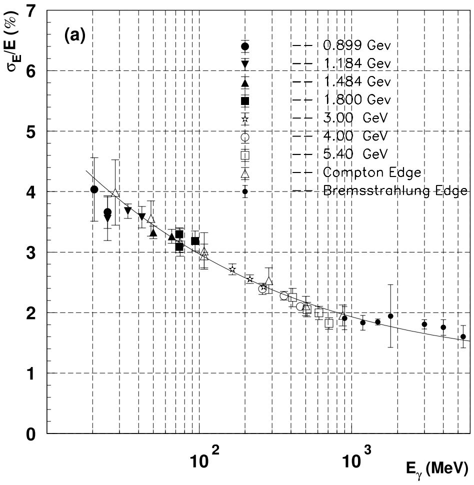

Figure 2.28: The energy resolution as a function of incident photon energy

2.2.7 Super Conductive Solenoid

The 1.5T magnetic field is applied parallel to the beam pipe to measure the charged particles momentum by CDC. The magnetic filed is provided by super conducting coil consisting of a single layer of niobium-titanium/copper embedded in high purity aluminum stabilizer. The coil are chilled by liquid helium, and the radius is 1.7m and longitude is 4.4m, and thickness is 5cm cylindrical coil. The return path of the magnetic flux is provided by the iron structure. The iron structure also works as an absorber material for KLM and a support for all the detector components.

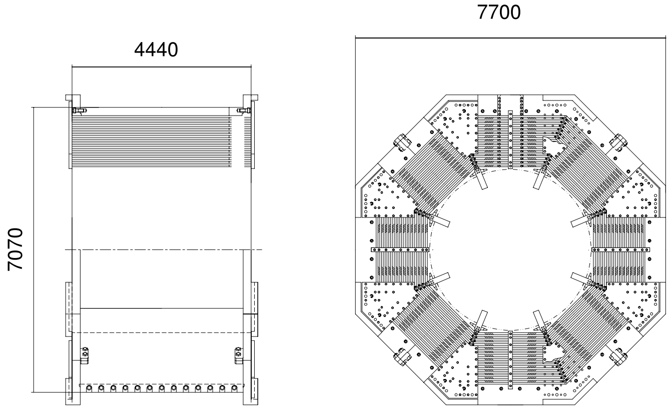

Figure 2.29: The sideview and cross section of the solenoid

2.2.8 K_L and Muon Detector (KLM)

Muon are used in the CP-violation measurements to identify the flavor of B meson. The KLM is located outside of magnetic field. The KLM is designed to detect K_L meson and muon has momentum more than 600MeV/c. In K_L case, the measurement of energy is not important, but the angular resolution is required for CP measurement in $B \to J/\psi K_L$. The muon, which has momentum less than 500MeV/c, can not arrive KLM by energy loss. KLM consist of alternating layers of charged particle detector and 4cm thick iron plate. There are 15 detector layers and 14 iron layers in octagonal barrel region, and 14 detector layers and 14 iron layer in forward and backward end-cap. The polar angle coverage of KLM is from 20° to 125°. The detection of charged particle is provided by glass-electrode resistive plate counters(RPCs). RPC has two electrodes with high resistively of 10^{10} Ω·cm separated by gas-filled gap that consist of 30% argon, 8% butane, and 62% freon. In the streamer mode, an ionizing particle traveling the gap initiates a streamer in the gas that results in a local discharge of the plates. This discharge is limited by the high resistivity of the plates and the quenching characterics of the gas. The discharge induces a signal on external pickup strip, which can be used to record the location and the time of the ionization. The strips are roughly 5cm wide, and configurated in the θ and ϕ directions. Total number of the readout channel is 37984.

2.2.9 Extreme Forward Calorimeter (EFC)

In order to improve the sensitivity to a specific physics process, for example $B \to \tau\nu$, the Extreme Forward Calorimeter(EFC) is needed in the extend the ECL coverage from 17° to 150°. The EFC covers the angular range from 6.4° to 11.5° in forward direction and from 163.3° to 171.2° in backward direction. Since the EFC is placed in the very high radiation-level area by photons or electrons due to synchrotron radiation and spent electrons, radiation hardness is required upto a few Mrad. We adopt a crystal calorimeter made of $Bi_4Ge_3O_{12}$ as the EFC, which satisfies the radiation hardness and provides good energy resolution for electrons and photons, (-0.3-1.0%)$/\sqrt{E(\mathbf{GeV})}$, with reasonable costs. Both forward and backward EFC consist of $Bi_4Ge_3O_{12}$ crystals segmented into 5 regions in the θ direction and 32 regions in the ϕ direction

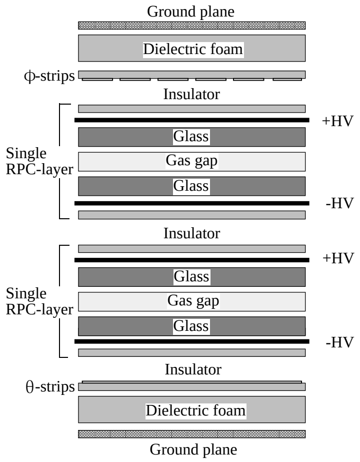

Figure 2.30: The KLM RPC super-layer module

in order to provide better position resolution. Typical cross-section of a crystal is about 2×2 cm^2 with 12 radiation length in forward and 10.5 radiation length in backward.

2.2.10 Trigger System for Belle Experiment

The main role of Trigger system is to decide whether hit signal from detector is recorded or discarded and reduce the beam-related background rate, while keep the high efficiency for physics events. The expected physics event rate is about 100Hz with $1.0\times10^{34}\mathrm{cm}^{-2}\mathrm{s}^{-1}$ luminosity The cross section and event rate various physics process are listed in Table 2.6. The cross section of $\Upsilon(4S) \to B\bar{B}$ decay is much smaller than other process, on the other hand, high beam-related background are also expected. There are many background source which are based on electrical noise, spent electron, photon from Bremsstrahlung, Coulomb scattering electron, radiative Bhabha scattering electron and synchrotron radiation.

Table 2.6:

Process	Cross Section(nb)	Rate(Hz)	Note
$e^+e^- \to \Upsilon(4S)$	1.2	12	
$e^+e^- \to q\bar{q}(q = u, d, s, c)$	2.8	28	
$e^+e^- \to \mu^+\mu^-$	0.8	8	
$e^+e^- \to \tau^+\tau^-$	0.8	8	
Bhabha:$e^+e^- \to e^+e^-(\theta_{lab} > 17^\circ)$	44	4.4	pre-scaled by factor 1/100
$e^+e^- \to \gamma\gamma(\theta_{lab} > 17^\circ)$	2.4	0.24	pre-scaled by factor 1/100
2γ process $\gamma\gamma \to$ *anything* $(\theta_{lab} > 17^\circ, p_t > 100\mathrm{GeV/c})$	∼15	35	
total	∼67	∼96	

The trigger system of Belle experiment has four levels, L0 and L1 triggers are Hardware-level trigger[89][90]. L3 and L4 are Software-level trigger[91][92]. The L0-level is used to hold SVD hit signal. The L0-level trigger signal is generated by coincidence of TOF and TSC hit. The The Level-1 trigger is the Global Trigger for DAQ of whole Belle detector generated by the signal from each sub-detector. Fig 2.31 shows the schematic view of L1-trigger, which is generated by using information of CDC, TOF, ECL, KLM and EFC. CDC provides the trigger signal with number of track of $r-\phi$ and $r-z$ and topology. TOF provides the trigger signal from the information of hit multiplicity and their topology. ECL generates the trigger signal by total energy deposit and number of clusters. These trigger signal from sub-detectors are sent to Global Decision Logic(GDL). The GDL make the final decision within 2.2μs from beam cross timing. Once the GDL trigger is generated, the trigger signal is send to each DAQ sub-system. The Level-3 trigger is done on Online computer farm. The Raw data is sent to off-line computer farm and reduction is performed with the track information and ECL cluster information as Level-4 trigger. The 78% triggered events are rejected by Level-4 trigger, but the almost 100% B-decay events are retained. This reduction is based on number of reconstructed track and total momentum on $r-\phi$ plane. The reduction power is 38%, the remaining events are stored in tape device as Raw Data. The last level-4 trigger is process of reduction the background events on Off-line computer. The detail of the background reduction of L4 trigger is described in next chapter of Hadron event selection.

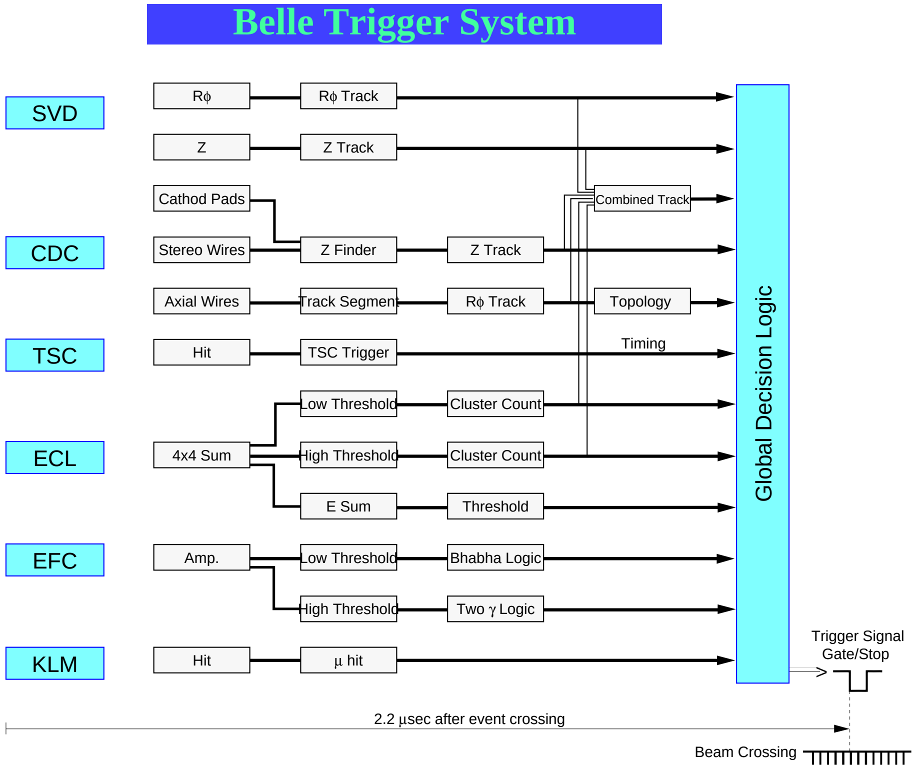

Figure 2.31: Schematic view of the Level-1 trigger system of Belle

2.2.11 Data Acquisition(DAQ)

The goal of DATA Acquisition(DAQ) system is to catch up the 500Hz trigger rate and to keep the dead time less than 10% under the high luminosity operation of KEKB. The DAQ system of Belle experiment are segmented by 12 DAQ sub-systems which are comprised in VME crate, and are running in parallel. 12 DAQ sub-systems consist of 4 SVD DAQ sub-systems, 2 CDC DAQ sub-systems, 1 ACC, TOF, ECL, KLM, EFC DAQ sub-systems and one more. The distributed global scheme of the system is shown in Fig 2.32[93][94].

Once the GDL trigger signal is generated, it is sent to DAQ sub-system by Sequence controller(SEQ). The TDMs, which is installed in each sub-system, recieves the trigger signal from SEQ and start readout signal on each DAQ sub-system. After that, the analog hit signal except SVD and KLM signal is digitized by 'Q-to-T' technique. The 'Q-to-T' module converts the charge amount to time interval, and time interval digitize

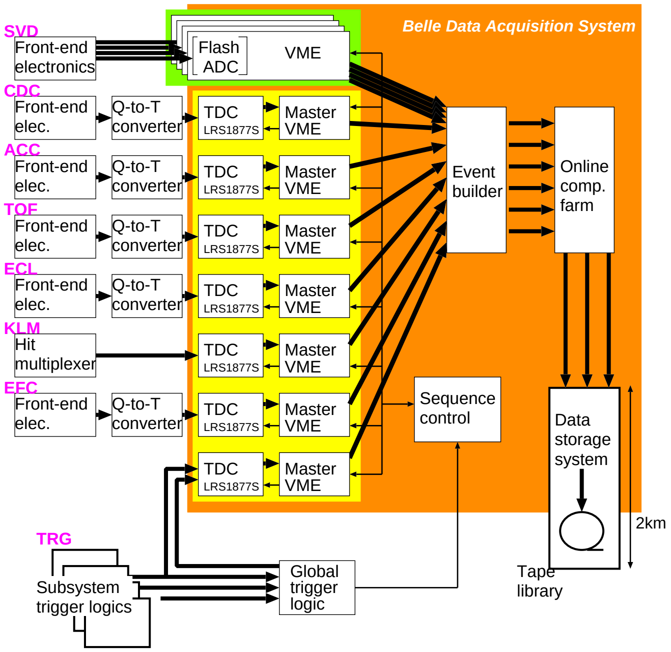

Figure 2.32: Schematic view of Belle DAQ system

by time-digitized module(TDC) which is controlled by VME and FASTBUS system[95]. The digitized data is read by DAQ sub-system and transfered to Eevent-Builder[96]. The Event-Builder provie 'event-by-event' data from 'detector-by-detector' data. The output data from Eevent-Builder is sent to online computer and reconstructed and for Level-3 trigger. After that the data is transfered to data storage system, mass storage system, which is located at the computer center, 2km apart from Belle detector. The typical data size of a hadronic event is measured to be about 30 kB, which corresponds to the maximum data transfer rate of 15MB/sec.

2.2.12 Off-line Computing

The off-line computer is used for analysis of data collected by the Belle detector, and for studying the Monte Carlo Simulation. The required processing power of the offline computers amounts to 15,000 SPECint95s. Because this computational power can not be achieved by a single CPU, we developed the parallel processing scheme by multi-CPUs. We use the Symmetric Multi Processor(SMP) architecture as a platform. The total storage capability of the off-line computer farm is $\sim$ 10TB.

We developed our own data processing frameworks called BASF/FPDA(Belle AnalysiS Framework/ Framework for Parallel Data Analysis)[97][98], which are especially suitable for both the production of the data summary tape(DST) and physics analysis. The recorded events are sequentially scanned by one process. Each bulk of around 10 events is distributed to another process. The number of process is equal to the number of embedded CPUs on the SMP machine. The distributed bulks of the events are processed on CPUs in parallel, and then returned to another process to be stored onto a tape, a hard disk, or the other storage media. The branching output path for the HBOOK format[99] is also equipped. With the framework running on the offline computer farm, the production speed of the DST is $\sim 1\ fb^{-1}$ per day.

The processing framework also provides a scheme of the Monte Calro events generation. The bulks of speeds of a random numbers instead of events themselves are distributed to the generator processes running on CPUs. In MC Generation, on-line PC farm, which consist of a few hundreds PCs, reinforce our computaing capability. This kind of PC farm are built not only at experimental site, KEK, but also at many collaboration instite. A decay simulator is program that generates particles tracing the decay chains according to the given manuscripts. The initial state of the particle generation is typically chosen to be

$\Upsilon(4S)$ or $q\bar{q}$. The event generator used in Belle analysis are QQ98 and EveGen. GEANT3 is used as a full detector simulation in the Belle. It was originally developed at CERN. The GEANT simulator takes the generated events by QQ98 or EveGen and produced the hit records at each sub-detector associated to the generated particles. The outputs from the full simulator are stored in the same format at the real data so that one can use the same analysis program for both real and simulated data samples.

Chapter 3

$B^0 \to K_s\ \pi^0$ Reconstruction

Fig 3.1 shows time variation of peak luminosity, Daily Integrated lumnosity, peak current and integrated luminosity from Oct.1999. The Integrated luminosity from Jan.2000 to Jun.2004 is $288 fb^{-1}$.

3.1 Data Set for Analysis

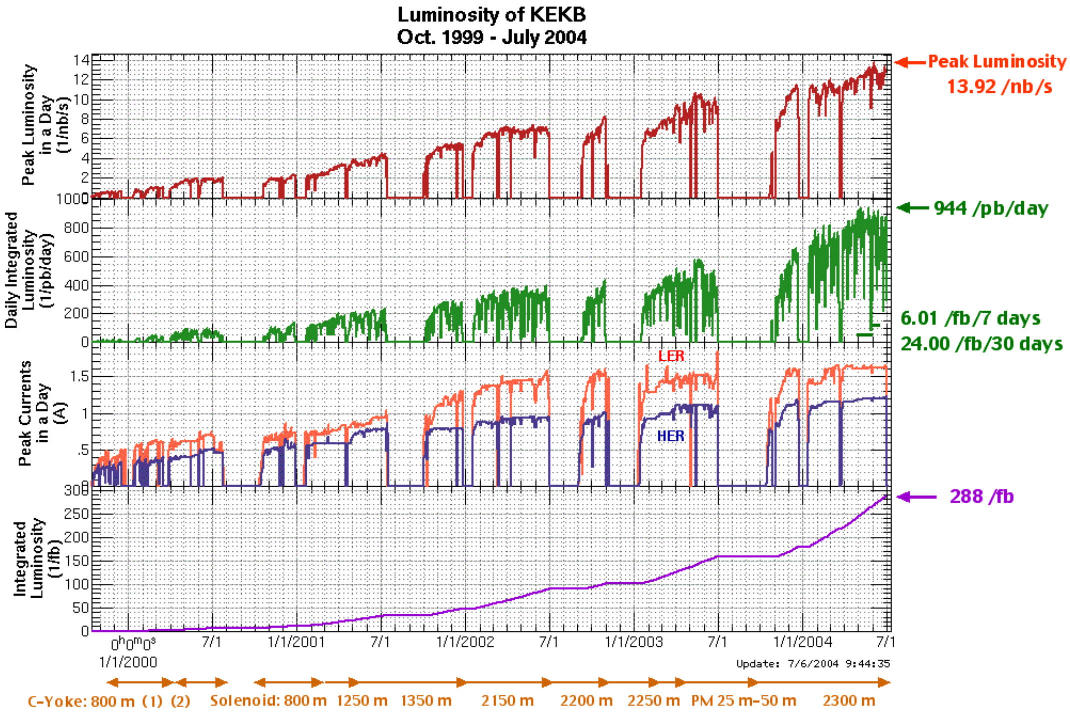

Figure 3.1: History of Luminosity of KEKB
The top figure shows the peak luminosity(1/nb/s), the second figure shows the daily integrated luminosity(1/pb/day), and third figure shows the peak current in a day(A), and bottom figure shows the integrated luminosity(1/fb)

Data sample that we used for analysis was accumulated with Belle detector. In this analysis, we reconstrust B^0 from K_s and π^0. We used $253 fb^{-1}$ data sample that contains 275×10^6 $B\bar{B}$ pairs. According to PDG, the branching ratio of $B^0 \to K^0\ \pi^0$ is 11.92×10^{-6}, branching ratio of $K_s \to \pi^+\ \pi^-$ is 0.68, and branching ratio of $\pi^0 \to \gamma\gamma$ is 0.98, then we can expect about 820 $K_s\ \pi^0$ events are included in data sample.

We noticed that we must separate SVD-I data sample and SVD-II data sample, because those data have different quality, especially on vertex resolution. We must optimize the event selection criteria and vertex resolution parameters[1] for each data set . The data sets with SVD-I and SVD-II are summarized in Table 3.1.

Table 3.1: Data Sets of SVD-I and SVD-II Data

	Period of Data taking	Integrated Luminosity(fb^{-1})	Number of $B\bar{B}$ pair
SVD-I	Jan.2000∼Jun.2003	140	152×10^6
SVD-II	Sep.2003∼Jun.2004	113	123×10^6
Total		253	275×10^6

3.2 Hadronic Event Selection

We select $B\bar{B}$ events from data sample and eliminate the e^+e^- events (Bhabha event), radiative Bhabha events, $\mu^+\mu^-$ events, two-photon process events, and beam background events. To reject these events, we require the following some primary selection criteria.

1 : Track selection

Events with only two tracks or less can be considered to be come from the QED process. Even if the event come from some hadronic processes, we can not utilize them because of few track. Therefore, at least three tracks are required, where a good track is defined by $|\delta r| < 2.0$cm and $|\delta z| < 4.0$cm measured from an nominal interaction point(IP) and the transverse momentum of good track must be greater than 100 MeV/c.

2 : Cluster of ECL selection

At least two clusters must be detected by ECL within the volume of $-0.7 < \cos\theta < 0.9$, and the energy deposit of each cluster is lager than 100 MeV, because most of clusters which are producted by QED process have a very shallow angle.

3 : Energy cut

Total visible energy which is sum of tracks momenta and photon energy, these tracks must satisfy the criteria 1 and photon clusters must satisfy 2 and we required that photon does not associated to the charged particle in ECL, in an event should be greater than 20% of the $\Upsilon(4S)$ energy. The fraction of total energy deposit in the ECL in an event must be between 10% and 80%. However the QED events have larger energy deposit in the ECL, around 100%.

Those criteria are used for rejection of QED events. Beam background is also very serious. To suppress it, we use two criteria as,

4 : Momentum of z components Cut

The sum of z components of track momentum and photons is required to be balanced around zero to eliminate the beam backgrounds. The sum of the absolute momentum must be smaller than a half of $\Upsilon(4S)$ energy(∼5.29GeV).

5 : Vertex Cut

Since the Beam background events are not originated from IP region, we use primary vertex to reject these background events. The primary vertex, which is recontructed by all charged tracks, must be between 1.5 cm and 3.5cm from the IP in $r-\phi$ and z planes, respectively.

With above selection, almost QED and beam background events are rejected, while 99% of $B\bar{B}$ events are remained. The contamination of non-hadronic components are smaller than 5%. The remaining background

---

[1] The resolution parameters are used in measurement of CP-asymmetries parameter

is continuum background, $e^+e^- \to q\bar{q}$. Since the cross section of $e^+e^- \to q\bar{q}$ process is about tree times lager than that of the $e^+e^- \to \Upsilon(4S)$, these continuum events are dominant background for $B\bar{B}$ events. To suppress these continuum background, we use one selection criteria, $R_2 < 0.5$. R_2 is give by,

$$R_2 \equiv \frac{\sum_i^N \sum_j^N [|\vec{p_i}||\vec{p_j}| \cdot (3\mathbf{cos}^2\phi_{ij} - 1)]}{2\sum_i^N \sum_j^N |\vec{p_i}||\vec{p_j}|} \tag{3.1}$$

where $\vec{p_i}$ is momentum vector of i-th particle which is charged track or neutral track, ϕ_{ij} is an angle between $\vec{p_i}$ and $\vec{p_j}$ in the cms, and N is a total number of charged and neutral particles in an event. In continuum events, $\cos\phi_{ij}$ tend to get ~ 1. On the other hand, spherical events like B decays becomes $R_2 \sim 0$. The efficiency loss due to R_2 selection is smaller than 0.5%. The data sample selection with criteria above is classified as Hadronic sample. Even if applied above selection, number of continuum background is larger than $B\bar{B}$ events. We need futher suppression of continuum background. It will be discribed later.

3.3 K_S Reconstruction

We use the decay mode of only $K_S \to \pi^+\pi^-$. To reconstruct K_S, we used oppositely charged tracks pair and apply some selection criteria depends on momentum of K_S, track information and flight length as Table 3.2,

Table 3.2: K_S Selection Criteria

K_S Momentum	$\lvert dr\rvert$ (cm)	$\lvert dz\rvert$ (cm)	Flight Length (cm)	$d\phi$ (rad)
$P_{K_S} < 0.5$GeV/c	> 0.05	< 0.8	no cut	< 0.3
$0.5 < P_{K_S} < 1.5$GeV/c	> 0.03	< 1.8	> 0.08	< 0.1
$P_{K_S} > 1.5$GeV/c	> 0.02	< 2.4	> 0.08	< 0.1

Where P_{K_S} is reconstructed K_S momentum, $\vec{P}_{K_S} = \vec{P}_{\pi^+} + \vec{P}_{\pi^-}$, $|dr|$ is defined as distance from pivot point[2] to track. we can define $|dr|$ by π^+ track and π^- track, but we select smaller one. $d\phi$ is defined as azimuthal angle between position vector of decay vertex of candidate K_S and K_S momentum vector, $|dz|$ is defined as distance on r-z plane of two daughter tracks at K_S vertex point and Flight Length is the distance from K_S decay vertex position to IP. We regire invariant mass of reconstructed K_S to satisfy $|M_{\pi^+\pi^-} - M_{K_S}| < 15\text{MeV/c}^2$, where M_{K_S} is PDG value.

3.4 π^0 Selection

The π^0 is recontructed from two photon(γ). We select π^0 with the following criteria,

1 : $E_\gamma > 0.05GeV$

2 : $0.118 < M_{\gamma\gamma} < 0.150GeV/c^2$

3 : Cluster of γ in the ECL is not associated with any charged tracks

Where E_γ is energy of π^0 daughter γ. Criteria (1) is applied for both daughter γ. $M_{\gamma\gamma}$ is invariant mass of two γ. Last criteria is for rejection the radiative γ. If radiative γ is produced by charged particle, there is cluster of charged particle near the cluster of γ.

---

[2] 'pivot' is one of the helix parameters, the definition of the helix is described in Appendix A

3.5 B^0 Selection

B^0 is reconstructed from K_S and π^0 by Beam constrained mass, M_{bc}, and Energy difference, ΔE. The definition of M_{bc} and ΔE are,

$$
\begin{aligned}
M_{bc} &= \sqrt{{E_{beam}^{cms}}^2 - |\overrightarrow{P}_B^{cms}|^2} && (3.2)\\
\Delta E &= E_B^{cms} - E_{beam}^{cms} && (3.3)\\
\overrightarrow{P}_B &= \overrightarrow{P}_{K_S} + \overrightarrow{P}_{\pi^0} && (3.4)\\
E_B &= E_{K_S} + E_{\pi^0} && (3.5)
\end{aligned}
$$

$$V_{boost} = (E_{e^+}, \sqrt{E_{e^+}^2 - m_{e^+}^2}\cdot \mathbf{sin}\theta_{cross}, 0, -\sqrt{E_{e^+}^2 - m_{e^+}^2}\cdot \mathbf{cos}\theta_{cross}) + (E_{e^-}, 0, 0, \sqrt{E_{e^-}^2 - m_{e^-}^2}) \quad (3.6)$$

E_{beam}^{cms} is half of total e^+e^- energy in cms[100], $E_{beam}^{cms} = \sqrt{s}/2 \sim$5.29GeV[3], P_B^{cms} is momentum of B^0 candidate in cms, E_B^{cms} is B^0 energy in cms. V_{boost} is the Lorentz boost vector which is calculated 4-momentum of e^+ and e^-, θ_{cross} is rotation angle of e^+, θ_{cross}=22mrad. If the B^0 candidate is true B^0 particle M_{bc} has same value as mass of B^0 because in cms, and ΔE has 0 because E_{beam}^{cms} is same as B^0 energy. In this $B^0 \to K_S\pi^0$ reconstruction, the signal region is defined as $5.27 < M_{bc} < 5.29$(GeV/c^2) and $-0.15 < \Delta E < 0.10$(GeV), Fig 3.2 shows the M_{bc} and ΔE distribution of $B^0 \to K_S\pi^0$ obtained by MC simulation. At last, if more than two B^0 candidates are found, we select one best candidate. We used χ^2 which is given by M_{bc} and ΔE, we select one candidate that has minimal χ^2.

$$\chi^2 \equiv \left(\frac{M_{bc}^{mean} - M_{bc}}{\sigma_{M_{bc}}}\right)^2 + \left(\frac{\Delta E^{mean} - \Delta E}{\sigma_{\Delta E}}\right)^2 \quad (3.7)$$

M_{bc}^{mean} and ΔE^{mean} is the mean value of M_{bc} and ΔE, which are defined by $B^0 \to K_S\pi^0$ MC simulation.

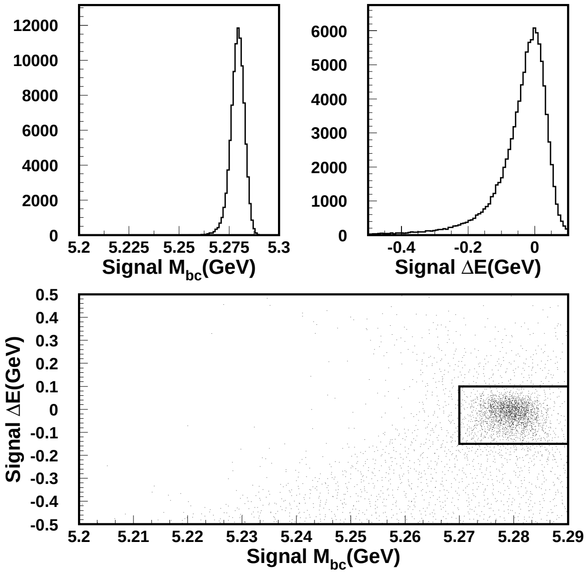

Figure 3.2: The distribution of Beam constrained mass, Energy difference and these scatter plots of $B^0 \to K_S\pi^0$ signal Monte Calro

---

[3] The detail of E_{beam}^{cms} is described in Appendix X

3.6 Flavor Tagging

To measure CP asymmetry, the flavor of the other B-meson has to be determinated. In this analysis, we use the same flavor tagging method as what is used in the sin2ϕ_1 measurement using $B^0 \to$ charmonuim + $K^{(*)0}$ decays[44]-[47]. Detail of flavor tagging method are described in Ref [101].

Lepton, charged pions and kaon that are not associated with a reconstructed CP eigenstate decay are used to identify the flavor of the accompanying B meson.

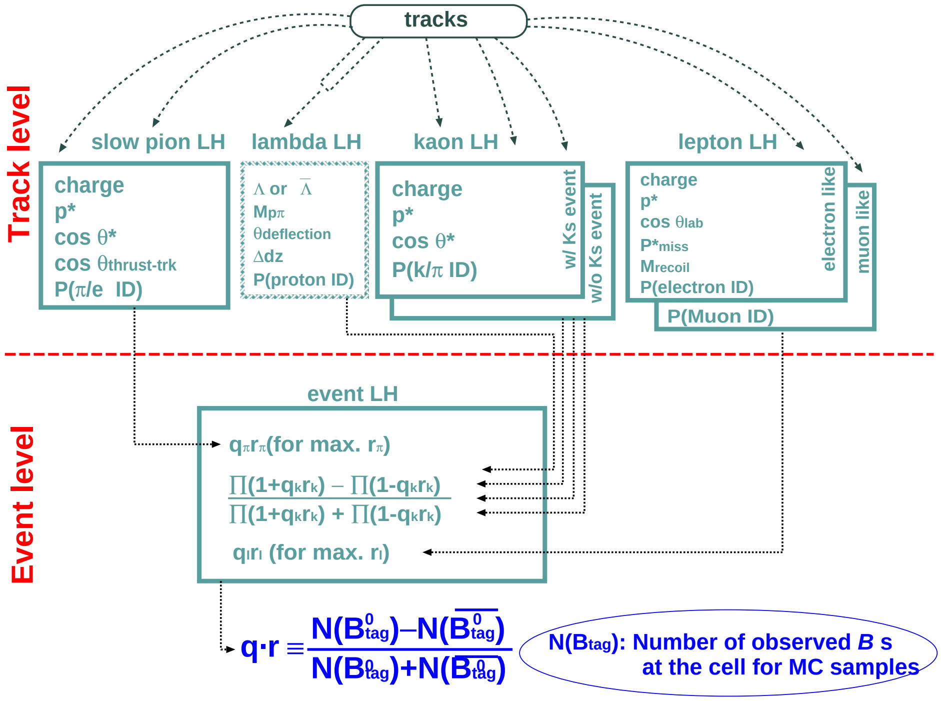

Figure 3.3: Algorithm of Multi-Dimensional Likelihgood Method for Flavor Tagging

We developed a flavor tagging method which consists of two stages. Fig.3.3 shows the schematic view of flavor tagging method. Initially, the b flavor determination is performed at the track level. Several categories of well measured tracks that distinguish the b-flavor by the track's charge are selected: high momentum leptons from $b \to cl^-\bar{\nu}$, lower momentum leptons from $c \to sl^+\nu$, charged kaon and Λ baryons from $b \to c \to s$, high momentum pions that originate from decays of the type $B^0 \to D^{(*)-}(\pi^+, \rho^+, a_1^+, etc)$, and slow pions from $D^{*-} \to \bar{D}^0\pi^-$. We use the MC to determinate a category-dependent variable that indicates whether a track originates from a B^0 or $\bar{B}^0$. The values of this variables range from -1 for a reliably identified $\bar{B}^0$ to +1 for reliably identified B^0 and depend on the tagging particle's charge, cms momentum. polar angle and particle-identification probability, as well as other kinematics and event shape quantities. The results from the separate track categories are then combined to take into account corrections in the case of multiple track-level tags. This stage determines two level event-level parameters, q and r. The first, q, has the discrete values q=+1 when the tag-side B meson is more likely to be a B^0 and -1 when it is mode likely to be a $\bar{B}^0$. The parameter r is an event-by-event flavor tagging dilution factor which ranges from r=0 for no flavor discrimination to r=1 for unambiguous flavor assignment.

Although the calculated r for each can be put into the CP fit, in this analysis we use r just to categorize candidate events, not use for CP-fit as wrong tag fraction. We specify the following six regions : $0 < r \leq 0.25$, $0.25 < r \leq 0.5$, $0.5 < r \leq 0.625$, $0.625 < r \leq 0.75$, $0.75 < r \leq 0.875$ and $0.875 < r \leq 1.0$. We obtain incorrect flavor assignment probability for each region from the data which is fed into the CP fit. In this way the analysis is rather free from some possible systematic difference between MC and real data due to some imperfection of detector response modeling, decay branching fractions, fragmentation and so forth in our MC. The probability that we can assign non-zero value for r is greater than 99.5% in MC; i.e. almost all the reconstructed candidate events can be used.

3.7 Vertex Reconstruction

For measurement time-dependent CP-asymmetry, we need to measure proper-time difference, Δt, which can be calculated as

$$\Delta t \cong \frac{z_{cp} - z_{tag}}{c\,(\beta\gamma)_{\Upsilon(4S)}} \tag{3.8}$$

where, z_{cp} and z_{tag} are z-component of decay vertex of B meson on cp-side and tagging-side in z direction, respectively. $\beta\gamma$ is Lorentz boost factor, $c\beta\gamma$=0.425, c is light velocity. We reconstruct decay vertex of two B meson for time-dependent CP-fit. The vertex of tagging-side B meson is reconstructed with normal method in Belle, on the other hand the vertex of cp-side can not be reconstructed same as normal method. In $B^0 \to J/\psi\ K_s$ decay, the decay vertex is reconstructed by J/ψ which have very short lifetime, while $B^0 \to K_s\,\pi^0$ mode has not short lifetime particle, lifetime of K_s is τc=2.68cm, and has no charged daughter particles of B meson.

We used special vertex reconstruction method for $K_S\pi^0$. The decay vertices of B_{cp} and B_{tag} are obtained from the kinematic fit based on the least χ^2 method with Lagrange multiplier technique. Track positions and momentum are tuned according to measurement errors so that all tracks pass a center point. The point is regarded as the propagated from the errors of the tracks. The estimated error of the reconstructed vertex is propagated from the error of the track parameter determination, i.e. momentum and position. Therefore. event even there is large displacement of tracks from the estimated vertex position, the estimated error of the vertex can still be small when the track parameters are determined well. The displacement reffects onto χ^2 of the vertex reconstruction. The χ^2 is defined as

$$\chi^2 \equiv \sum_i \left(\delta\vec{h}\right)_i^T V_i \left(\delta\vec{h}\right)_i \tag{3.9}$$

$\vec{h}$ is track parameters, V_i is Inverted error matrix. In vertex fit, the IP constraint is used. The χ^2 of IP constraint is defined as

$${\chi_{IP}}^2 \equiv \left(\frac{\delta l_x}{{\sigma_x}^{IP}}\right)^2 + \left(\frac{\delta l_y}{{\sigma_y}^{IP}}\right)^2 + \left(\frac{\delta l_z}{{\sigma_z}^{IP}}\right)^2 \tag{3.10}$$

where δl is the distance from IP to fitted vertex position, $\sigma_{x,y,z}$ is the size of IP-distribution. The typical value are $\sigma_x \sim 100\mu$m, $\sigma_y \sim 5\mu$m, $\sigma_z \sim 3$mm. The merit of IP constraint is improvement on the vertex resolution and we can reconstruct vertex with only one track. We define the special goodness instead of normal χ^2 of vertex fit. Since the normal χ^2 depend on IP, it is not enough as goodness. The special goodness is ξ. which is defined as,

$$\xi \equiv \frac{1}{2n}\sum_i^n [(z^i_{after} - z^i_{before})\,/\epsilon^i_{before}]^2 \tag{3.11}$$

where z^i_{before} and z^i_{after} are z-component of $i-th$ track position before vertex fit and after vertex fit, respectively. ${\epsilon_{before}}^i$ is error of $i-th$ track before vertex fit. This goodness is independent on IP and used in Resolution Function at CP-fit[4].

3.7.1 CP-side Vertex Reconstruction

Since K_s has long lifetime for B^0 vertex reconstruction, we can not get the B^0 vertex correctly, and the new method was developed. The concepts of nominal vertex method by J/ϕ and new vertex method by K_S is shown in Fig 3.4. In basically, cp-side vertex is reconstructed by only K_s, called K_s-B Vertexing. K_s-B

---

[4] The detail of resolution function is described in Chapter 4

Vertexing do fitting the B vertex with K_s vertex and K_s virtual momentum calculated by daufhter pions with IP-constrainted. In pricticaly the B vertex and K_s vertex are fitted simultaneously with K_s virtual momentum and two canstrainted, one is IP-constrainted and another is that K_s daughter $\pi^+\pi^-$ must pass though same vertex position. Further more, we modify the calculation of error matrix of K_s daughter pion track parameters. With this special vertex reconstruction method, we can get good B^0 vertex and error of the vertex. In addition to that, we define the new goodness instead on ξ, The ξ is defined by only z-side vertex information, but since K_s flight length in $r-\phi$ plane is a few cm, the goodness is modified by given the transverse momentum, and new goodness is defined as ζ. we use this new goodness in Resolution Function at CP-fit.

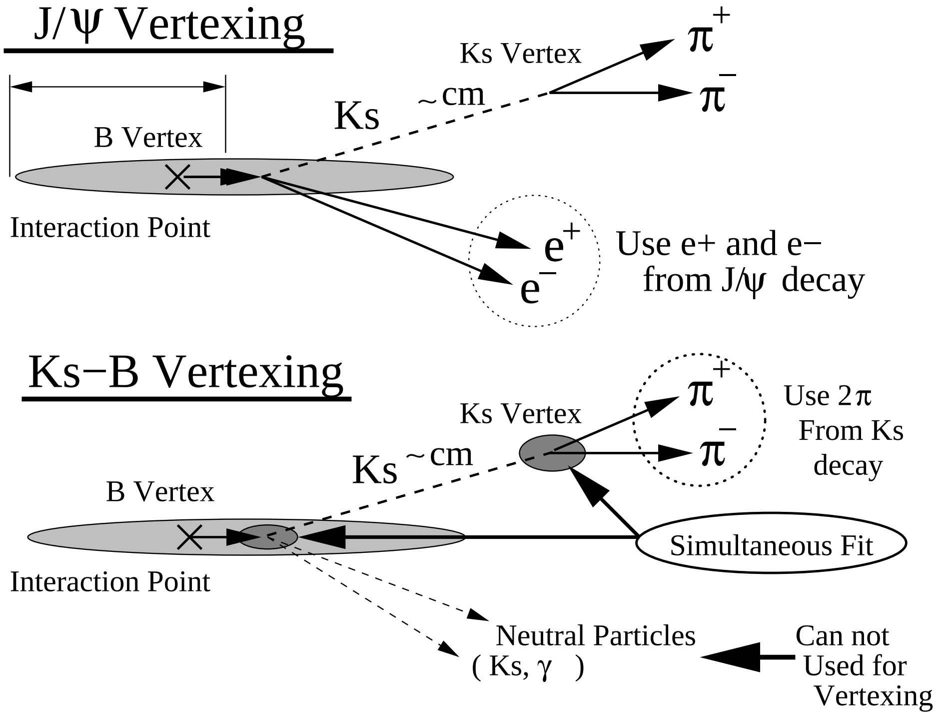

Figure 3.4: Concept of J/ψ Vertexing and $K_S - B$ Vertexing

3.7.2 The Performance of K_s-B Vertexing

In this section, we describe the performance of K_s-B Vertexing. To compare the method with nominal vertex method, we use the $B^0 \to J/\psi\ K_s$ decay mode, because this decay has J/ψ which can reconstruct the B^0 decay vertex, and can be compared the resolution of vertex with J/ψ, J/ψ-Vertexing, and with K_s, K_s-Vertexing event-by-event.

We checked the vertex reconstruction efficiency and vertex resolution from signal MC, and Lifetime of B^0 and sin2ϕ_1 from Real Data. Vertex efficiency is $\sim$ 95% in J/ψ-Vertexing, while in the case of K_s-Vertexing, the vertex efficiency is ~40%. Because the K_s flight length is long, the number of daughter pion which has SVD hits is small. We evaluated the vertex efficiency of $K_S\pi^0$ with SVD-I is 23.4% and SVD-II is 32.0% from MC. The efficiency of SVD-II is larger than SVD-I. Because the SVD-II has larger radius than SVD-I. And number of layer is also larger than SVD-I. The vertex efficiency of $K_s\pi^0$ is smaller than $J/\psi K_s$, Because the momentum of K_s in $K_s\pi^0$ is higher than that of $J/\psi K_s$, the K_s flight length of $K_s\pi^0$ is longer than $J/\psi K_s$. Vertex resolution is elstimated by MC. Fig 3.5 shows the Δz residual plots of J/ψ-Vertexing and K_S-Vertexing for $J/\psi K_s$ MC in case of SVD-I and SVD-II. The Δz distribution are fitted by 2-D Gaussian, and the weight mean are 144μm, 127μm in J/ψ-Vertexing in SVD-I and SVD-II, respectively, and 185μm, 195μm in K_S-Vertexing in SVD-I and SVD-II, respectively. The resolution of K_s-Vertexing is worse than J/ψ-Vertexing. In J/ψ-Vertexing, the resolution of SVD-II is better than that of SVD-I, because the radius of beam pipe is smaller and the distance from first layer to IP is closer at SVD-II case. On the ohter hand, the vertex resolution of SVD-II is worse than that of SVD-I in K_S-Vertexing case. The main reason is that the distance from vertex of K_S to nearest sencer in SVD-II case is loger than SVD-I case. If K_S decays within first layser, the vertex resolution of SVD-II is better than SVD-I case.

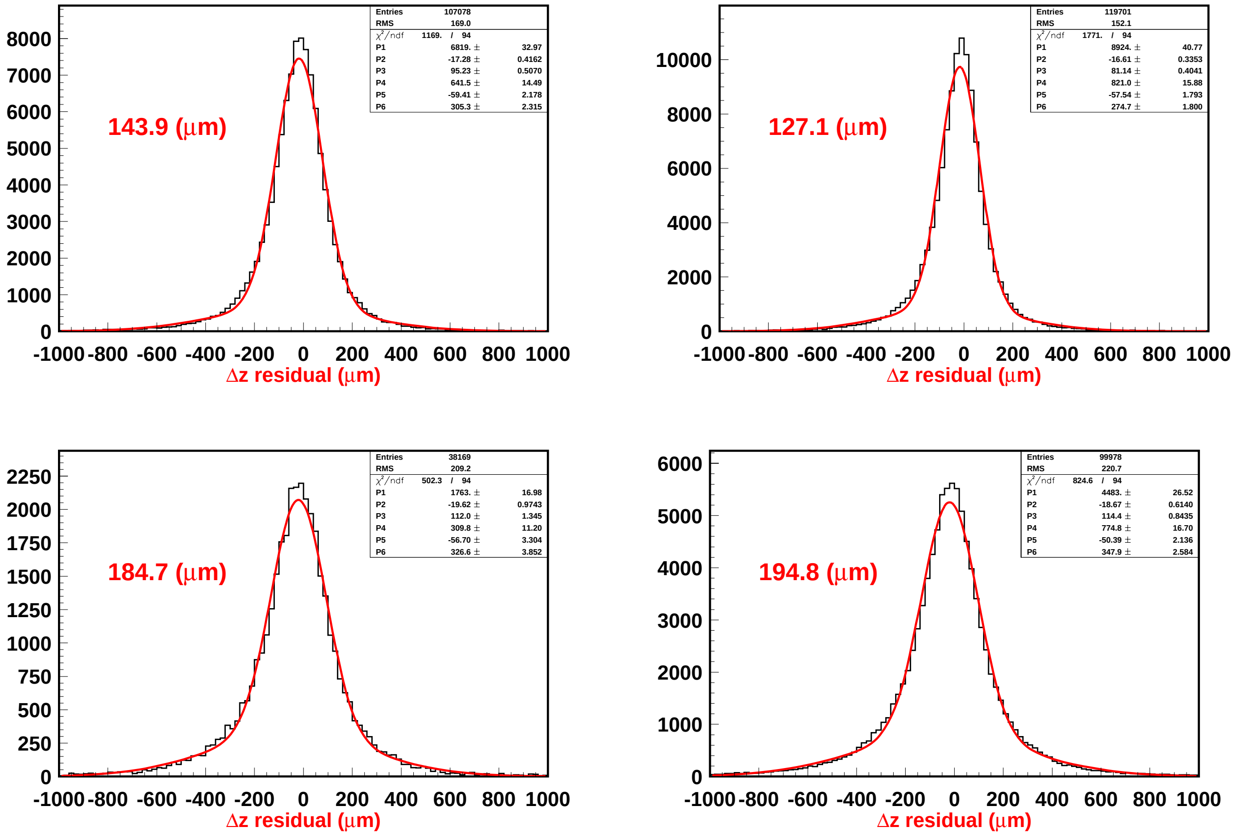

Figure 3.5: Δz resolution by J/ψ-Vertexing(Upper) and K_S-Vertexing(Lower) used SVD-I(left) and SVD-II(right) obtained by $J/\psi K_s$ MC

The lifetime of B^0 is measured with real data of $J/\psi K_s$. The measurement result and number of used events are summarized in Table 3.3. In J/ψ vertexing sample, there are three different mode, $B^0 \to J/\psi K_S(K_S \to \pi^+\pi^-)$, $J/\psi K_S(K_S \to \pi^0\pi^0)$, and $B^0 \to J/\psi K_L$. These value are agreed within error and consistent with PDG value. The result of CP-asymmetry measurement is also summarized in Table 3.3. Fig 3.6 shows the raw asymmetry plots for good tag events. The measurement sin$2\phi_1$ is agreed within error. From these results, we found that the K_s-Vertexing is good method to measure CP-asymmetry. The detail of CP-fit measurement is described in Chapter 4.

Table 3.3: Fitting result of B^0 Lifetime and CP-fit with $J/\psi K_S$ by J/ψ-Vertexing and K_S-Vertexing used Real Data, The number of event in J/ψ-Vertexing mean, 3805($B^0 \to J/\psi K_S(K_S \to \pi^+\pi^-)$), 509($B^0 \to J/\psi K_S(K_S \to \pi^0\pi^0)$), and 4313($B^0 \to J/\psi K_L$).

Vertexing method	J/ψ-Vertexing	K_s-Vertexing
Number of Events	3805+509+4313	1729
measured Lifetime	1.534±0.034(ps)	1.51±0.05(ps)
sin$2\phi_1(=S_{J/\psi K_s})$	+0.666±0.046	+0.68±0.10
$A_{J/\psi K_s}$	+0.023±0.031	+0.02±0.04

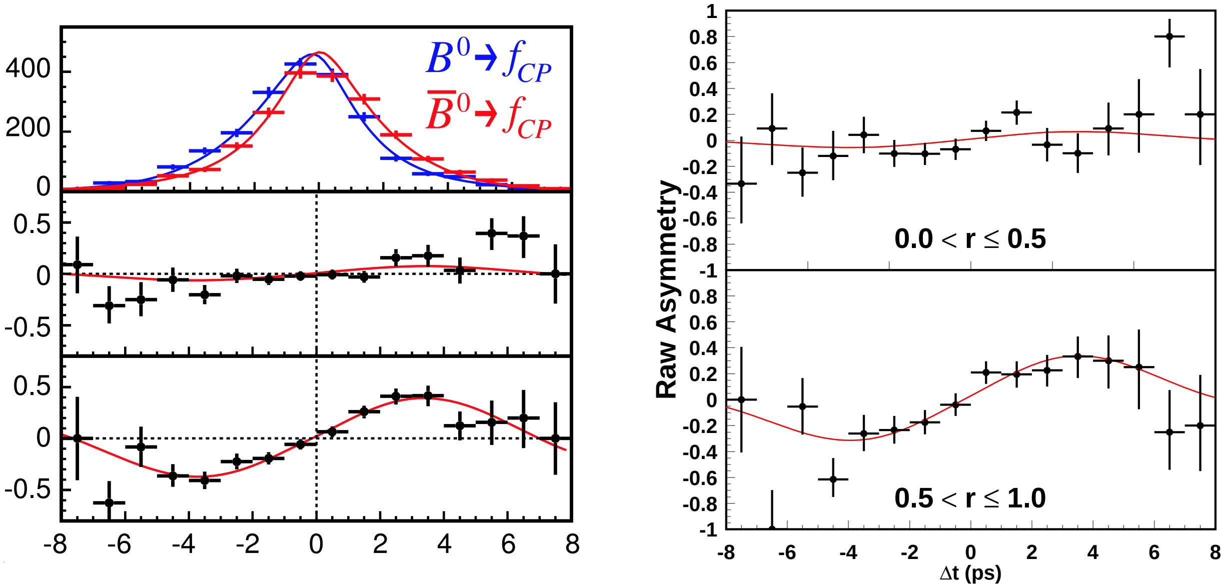

Figure 3.6: Raw asymmetry plots and fitted line used good tag events obtained by J/ψ Vertexing, used $B^0 \to J/\psi K_S$ events(left), and K_S vertexing(right)

3.7.3 Tag-side Vertex Reconstruction

The reconstruction of B_{tag} decay vertex is rather complicated than B_{cp} decay vertex. The main reason is that B_{tag} side track may contain the decay product of meson with finite lifetime such as charm mesons or K_s. The B_{tag} vertex is reconstructed with all tracks in event except particles used for B_{cp}. In $K_s\pi^0$ the daughter $\pi^+\pi^-$ are not used for B_{tag} vertex reconstruction. Although we discard some badly reconstructed tracks or non-primary tracks to improve the B_{tag} vertex resolution. The track elimination is,

1 : One track must have enough SVD hits

One track are required to have at least one hit in the $r-\phi$ plane and two hits in the $r-z$ plane on SVD as well as the vertex reconstruction of B_{tag}, But in case of SVD-II case, we requirement criteria for single-track events that it must have 2 SVD hits in 2nd, 3rd, and 4th layer .

2 : $|\sigma_z| < 500\mu$m and $|dr| < 500\mu$m

$|\sigma_z|$ is calculated error track position in z direction. $|dr|$ is the distance from track position to B_{cp} decay vertex in $r-\phi$ plane. With these cuts, tag side vertex resolution improve from $160\mu m$ to 150μm.

3 : K_s-Veto

The track which can make K_S candidate, $|M_{\pi^+\pi^-} - M_{K_s}| < 15\text{MeV/c}^2$, is removed.

The vertex reconstruction is iterated until the reduced χ^2 of the vertex becomes smaller than 20. All tracks are assumed to have pion mass approximately, which yields only negligible discrepancy between the usage of pion mass and usage of tagged species masses. The efficiency loss due to the track selection is measured to be smaller than 4%. The overall reconstruction efficiency of B_{tag} is $\sim$ 93%.

We reconstruct cp-side and tagging-side vertex, but we do not reject the events which can not be reconstructed vertex. Therefore, we defined the two sample, one is W/ Vertex sample which can be reconstructed cp and tag vertex, another is W/o Vertex sample, which can not be reconstructed cp or tag side vertex.

3.8 Background Suppression

As noticed in Chapter 3.2, the non-hadronic background and beam background events are rejected. The remain dominant background for $K_s\pi^0$ is jet-like continuum events, $e^+e^- \to q\bar{q}$. The q is u, d, s, and c quark[5]. These backgrounds can be suppressed with using the event topology. Because the momentum of B meson is around 0.34GeV/c, the topology of final state particle from $B\bar{B}$ events are almost spherical. On the other hand, in the case of continuum events, the final state particle has high momoentum and the jet-like topology along a single axis. Fig 3.7 shows the topology of continuum events and $B\bar{B}$ events.

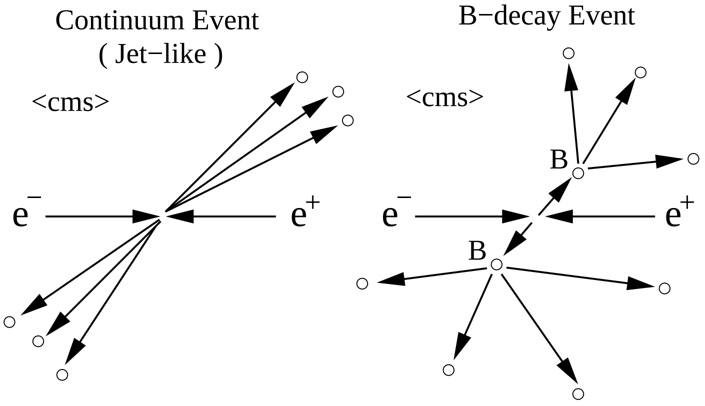

Figure 3.7: Event Topology of Continuum Event and $B\bar{B}$ decay event in cms

3.8.1 Super Fox-Wolfram Method

Super Fox-Wolfram consists of modified Fox-Wolfram moments that are defined as[102],

$$h_l{}^{so} = \sum_{i,j} p_i p_j P_l(\mathbf{cos}\theta_{ij}) \tag{3.12}$$

$$h_l{}^{oo} = \sum_{j,k} p_j p_k P_l(\mathbf{cos}\theta_{jk}) \tag{3.13}$$

$$\tag{3.14}$$

where the sum i iterates over particles of B signal candidate including charged particles($\pi^\pm$, $K^\pm$), neutral particle, γ. The indices j and k iterates over the remained particles in event. These particle implies also charged and neutral particles. The p is momentum of the particle, and $P_l(\cos\theta)$ is the l-th Legendre polynomial with respect to two particles in the sum. The Super Fox-Wolfram(SFW) is defined as

$$SFW = \sum_{i=2,4} \alpha_i \left(H^{so}{}_i\right) + \sum_{i=1-4} \beta_i \left(H^{oo}{}_i\right), \tag{3.15}$$

$$H^{so}{}_i \equiv \frac{h_i{}^{so}}{h_0{}^{so}}, \tag{3.16}$$

$$H^{oo}{}_i \equiv \frac{h_i{}^{oo}}{h_0{}^{oo}}. \tag{3.17}$$

This equation is called Fisher discriminant, and α_i and β_i are called Fisher coefficients. The $h_i{}^{so}$ terms contains information on the correlation between the B candidate direction and remainad part of event. The odd $h_i{}^{oo}$ terms partially reconstruct the kinematics of the other B in the event, while the even terms quantify the sphericity of the remainad part of events.

---

[5] The ratio of $(u\bar{u} + d\bar{d} + s\bar{s}) : c\bar{c} \sim 1.6 : 1.0$

3.8.2 New Super Fox-Wolfram Method

The Super-Fox-Wolfram method does not suppress the continuum background complitly. We found there is correration with Super-Fox-Wolfram with missing energy, and a new Super-Fox-Wolfram correrated with missing energy are need in order to increase the significance in the measurement of CP violation, the Super Fox-Wolfram Method was improved to improve signal purity in final sample. The new SFW defined as[103],

$$NSFW = \sum_{i=0,1} R_i{}^{so} + \sum_{i=0,1} R_i{}^{oo} + \gamma \sum_{n=1}^{N_t} |\,(P_t)_n\,| \tag{3.18}$$

where $R_i{}^{so}$ is defined as,

$$R_i{}^{so} = \frac{(\alpha_c)\cdot(H_{charged})^{so}{}_l + (\alpha_n)\cdot(H_{neutral})^{so}{}_l + (\alpha_m)\cdot(H_{missing})^{so}{}_l}{E_{beam} - \Delta E} \tag{3.19}$$

For $l = 1$ and 3,

$$(H_{charged})^{so}{}_l = \sum_i \sum_{jX} \beta_i{}^{so} Q_i Q_{jX} |p_{jX}| P_l\left(\mathbf{cos}\theta_{ijX}\right) \tag{3.20}$$

$$(H_{neutral})^{so}{}_l = (H_{missing})^{so}{}_l = 0 \tag{3.21}$$

For $l = 0$, 2 and 4,

$$(H_X)^{so}{}_l = \sum_i \sum_{jX} \beta_i{}^{so} |p_{jX}| P_l\left(\mathbf{cos}\theta_{ijX}\right) \tag{3.22}$$

where i iterates over the particles of the B signal candidate, and the index jX iterates over those in the tag side in the category X (X = charged, neutral, and missing). $P_l\left(\mathbf{cos}\theta_{ijX}\right)$ is the l-th Legendre Polynomial with the respect to two particles(i,jX). In new SFW method, the missing momentum is added, the missing momentum definition is as follows,

$$MM^2 = \left(E_{\Upsilon(4S)} - \sum_{n=1}^{N_t} E_n\right)^2 - |\sum_{n=1}^{N_t} P_n|^2 \tag{3.23}$$

There are 2($= 1 \times 2$) parameters of $(\alpha_X)_l$, $\beta_l{}^{so}$ for $l = 1$ and since the terms with $(\alpha_n)_l$ and $(\alpha_m)_l$ =0. There are 9($= 3 \times 3$) parameters of $(\alpha_X)_l$, $\beta_l{}^{so}$ for $l = 0, 2$ and 4. Thus there are 11(=2+9) parameters in $R_i{}^{so}$.

$R_l{}^{oo}$ is defined as,
For $l = 1$ and 3,

$$R_l{}^{oo} = \frac{\sum_j \sum_k \beta_l{}^{oo} Q_j Q_k |p_{jX}| P_l\left(cos\theta_{jk}\right)}{\left(E_{beam} - \Delta E\right)^2} \tag{3.24}$$

For l = 0,2 and 4,

$$R_l{}^{oo} = \frac{\sum_j \sum_k \beta_l{}^{oo} |p_{jX}| P_l\left(cos\theta_{jk}\right)}{\left(E_{beam} - \Delta E\right)^2} \tag{3.25}$$

where j and k iterates over the particles in tag side. Q_j is the charge of the particle j. Thus $R_l{}^{oo}$ for $l = 1$ and 3 is the sum for the charged particles in the tag side. Three are 5 parameters of $\beta_l{}^{oo}$ in $R_l{}^{oo}$.

$\sum_{n=1}^{N_t} |\,(P_t)_n\,|$ is the scalar sum of the traverse momenta P_t. SFWof all the particles in the signal side and the tag side. N_t is the number of all the particles. The 3rd term in Eq 3.18 has 1 free parameter(γ). In total, there are 17(=11+5+1) parameters in NSFW.

There is correlation between NSFW and MM^2. We divide MM^2 region into 7 regions (MM^2 < -0.5(GeV/c^2) , -0.5(GeV/c^2) < MM^2 < +0.3(GeV/c^2), +0.3(GeV/c^2) < MM^2 < +1.0(GeV/c^2), +1.0(GeV/c^2) < MM^2 < +2.0(GeV/c^2), +2.0(GeV/c^2) < MM^2 < +3.5(GeV/c^2), +3.5(GeV/c^2) < MM^2 < +6.0(GeV/c^2), and MM^2 < +6.0(GeV/c^2)).

3.8.3 B flight direction

The B flight direction is used for continuum background rejection, where the definition of B flight direction is the angle between B candidate momentum and z-axis(beam direction) in cms, cosθ_B. In e^+e^- annihilation, e^+ and e^- must have opposite helicity because of helicity conservation in electro-magnetic interaction. Since e^+ and e^- are fermion, spin=1/2, the pattern of helicity of collision are $e^+_R\,e^-_L$ or $e^+_L\,e^-_R$ as Fig 3.8, where $e_{R,L}$ means right or left handed, and the total angulre momentum is '1' and the direction is along z-axis(Beam direction). In case of $e^+e^- \to \Upsilon(4S)$, since the spin of $\Upsilon(4S)$ is '1' and that of B, $\bar{B}$ are '0', the orbital angulre momentum of two body system of $B\bar{B}$ is '1'. Because of this, the momentum direction of $B\bar{B}$ obey with $|Y_{1,m}|^2 \propto |d^1_{1,0}|^2$ =sin$^2\theta_B$=1-cos$^2\theta_B$, where $Y_{l=1,m}$ is spherical hermonic, and $d^1_{1,0}$ is rotation matrix. On the other hand, the momentum direction of $q\bar{q}$ obey with 1+cos$^2\theta_B$ as $e^+e^- \to \mu^+\mu^-$, in case of $e^+e^- \to q\bar{q}$. Because the spin of q and $\bar{q}$ are 1/2. Since the B candidates however are reconstructed with tracks randanly selected from continuum events, the momentum of reconstructed B from continuum background does not obey the 1+cos$^2\theta_B$ distribution. Because of these reason, the distributions of cosθ_B are different in signal and continuum background.

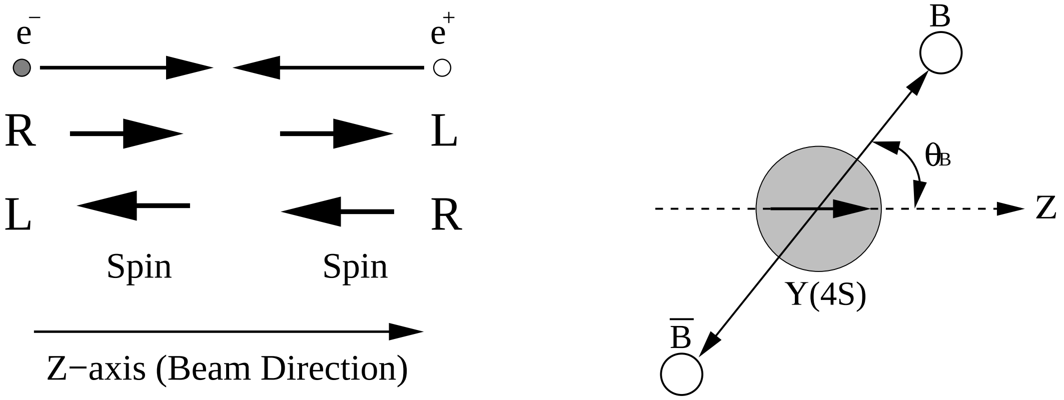

Figure 3.8: The pettern of helicity in e^+e^- collision(left). B flight direction from $\Upsilon(4S)$ decay(right)

3.8.4 Likelihood Ratio Cut

For suppression of the continuum background, a likelihood ratio is defined from the likelihood value as signal and background calcluated with NSFW and cosθ_B distributions. The distribtion of likelihood is obtained for signal B events by MC and for background from sideband region of experimental data. Fig 3.9 shows the signal region and sideband region in Beam constrained mass and Beam difference. Signal region is 5.27 $< M_{bc} <$ 5.29(GeV/c^2) and -0.15 $< \Delta E <$ 0.1(GeV), sideband region is 5.20 $< M_{bc} <$ 5.26(GeV/c^2) and -0.2 $< \Delta E <$ 0.5(GeV), or, 5.26 $< M_{bc} <$ 5.29(GeV/c^2) and 0.2 $< \Delta E <$ 0.5(GeV). The example of NSFW distribution of Signal MC and sideband date are shown in Fig 3.10 which used SVD-II W/ vertex sample. The B flight direction, cosθ_B, of signal MC and sideband date are shown in Fig 3.11. Likelihood function is defined by fitting distribution of NSFW and B flight direction.

Fitting function of NSFW is asymmetric two Gaussian,

$$\begin{cases} f(\mu) = \frac{f_l}{f_l+f_r}\cdot\frac{1}{\sqrt{2\pi}\sigma_{ln}}\cdot\mathbf{exp}\{\frac{-(\mu-<\mu>)^2}{2\sigma_{ln}^2} + A\cdot\mathbf{exp}\{\frac{-(\mu-<\mu>)^2}{2\sigma_{lw}^2}\} & (\mu << \mu >) \\ f(\mu) = \frac{f_r}{f_l+f_r}\cdot\frac{1}{\sqrt{2\pi}\sigma_{rn}}\cdot\mathbf{exp}\{\frac{-(\mu-<\mu>)^2}{2\sigma_{rn}^2}\} + A\cdot\mathbf{exp}\{\frac{-(\mu-<\mu>)^2}{2\sigma_{rw}^2}\} & (\mu >< \mu >) \end{cases} \tag{3.26}$$

where free parameters are $f_{l,r}$, μ, $\sigma_{ln,lw,rn,rw}$ and A, μ is NSFW. We define this asymmetric two Gaussian function as likelihood of NSFW. This likelihood ratio is defined in seven MM^2 region, respectively. Thus, likelihood function is $L \equiv L(NSFW, MM^2) = f(\mu, MM^2)$.

Fitting function of B flight direction is polynomial function. The signal B events is defined by 2nd order function and continuum background is defined by 1st-order function.

$$f(x) = 1 + c_1\cdot x + c_2\cdot x^2 \tag{3.27}$$

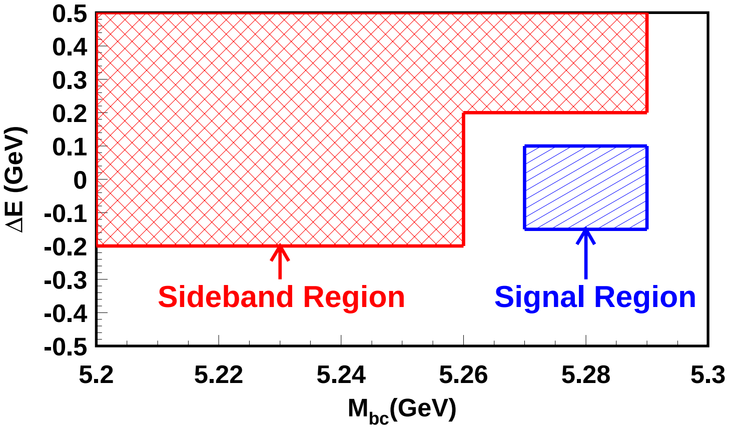

Figure 3.9: Signal and Sideband Region of $K_S\pi^0$

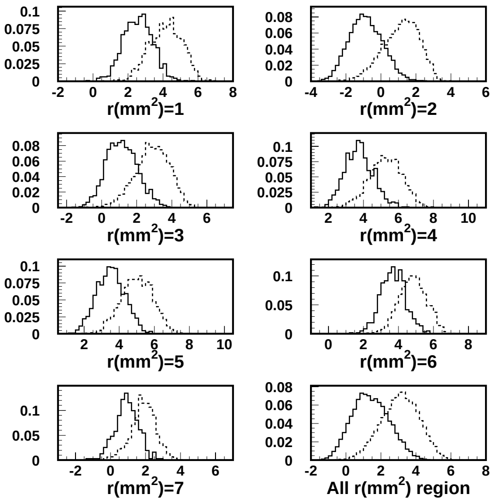

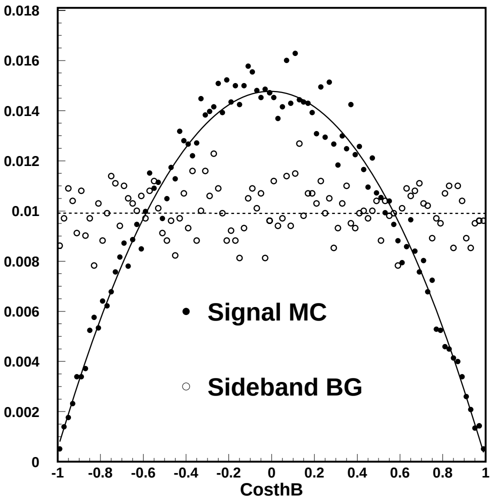

Figure 3.10: Distribution of new Super Fox-Wolfram of Signal MC and Sideband data in each missing mass region. The solid histogram is sideband data, and dashed histogram is Signal MC

Figure 3.11: Distribution of B flight direction of Signal MC and Sideband data. Black circle and solid line is Signal MC and while circle and broken line is sideband data

where free parameter are c_1 and c_2. In continuum background we fix as $c_2 = 0$. We defined the likelihood of B flight direction as $L(\mathbf{cos}\theta_B) = f(x)$.

We defined the likelihood of Signal B events and continuum background by prducting the likelihood of NSF and B flight direction.

$$\begin{aligned} L_{B\bar{B}} &= L(NSFW, MM^2)_{B\bar{B}} \times L(\mathbf{cos}\theta_B)_{B\bar{B}} && (3.28) \\ L_{q\bar{q}} &= L(NSFW, MM^2)_{q\bar{q}} \times L(\mathbf{cos}\theta_B)_{q\bar{q}} && (3.29) \end{aligned}$$

And the likelihood ration is given as,

$$\textbf{Likelihood Ratio}(LR) \equiv \frac{L_{B\bar{B}}}{L_{B\bar{B}} + L_{q\bar{q}}} \tag{3.30}$$

Fig 3.12,3.13 shows the Likelihood Ratio of signal B events and sideband data of W/ vertex sample and W/o vertex sample, and S-I and SVD-II.

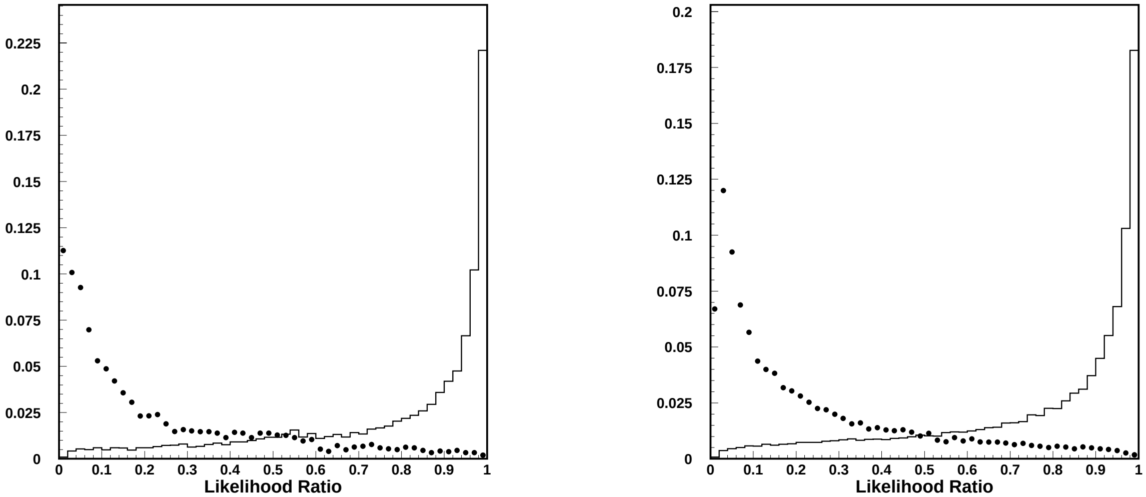

Figure 3.12: Likelihood Ratio Distribution of Signal MC(Solid Histogram) and Sideband Data(Dotted Histogram) with W/ Vertex(left) and HLR W/o Vertex(right) SVD-I sample

We select $LR > 0.78$ for W/ vertex sample of SVD-I, $LR > 0.74$ for W/o vertex sample of SVD-I, $LR > 0.78$ for W/ vertex sample of SVD-II, $LR > 0.76$ for W/o vertex sample of SVD-II, respectively. These sample are defined as 'High Likelihood ratio (HLR) events'. The threshold of LR are chosen to maximize Figure of Merits(F.o.M), which is defined as $FoM = N_{signal}/\sqrt{(N_{signal} + N_{background})}$, where N_{signal} is the expected number of signal in signal box assuming the branching fraction of $B^0 \to K^0\pi^0 = 1.0 \times 10^{-5}$. $N_{background}$ is expected number of background in signal box which is calculated using sideband data, and $N_{background}$ is calculated as follows,

$$N_{background} = N_{sidenband} \times \frac{V_{signal}}{V_{sidenband}} \tag{3.31}$$

where $N_{sidenband}$ is number of events in sideband region and $V_{signal,sideband}$ is the calculated background volume of signal and sideband region using background shape[6]. The FoM depends on LR of W/ and W/o vertex sample(SVD-I and SVD-II) are shown in Fig 3.14, 3.15 and threshold of each sample are summarized in Table 3.4.

As described above, we used event which has higher LR than threhold as HLR sample. But we use not only HLR sample, but also below these LR events. We optimize LR cut for each r regions, r is an event-by-event flavor-tagging dilution factor described in section 3.6. The threshold of each regions are

---

[6] the detail of background shape is described in next section

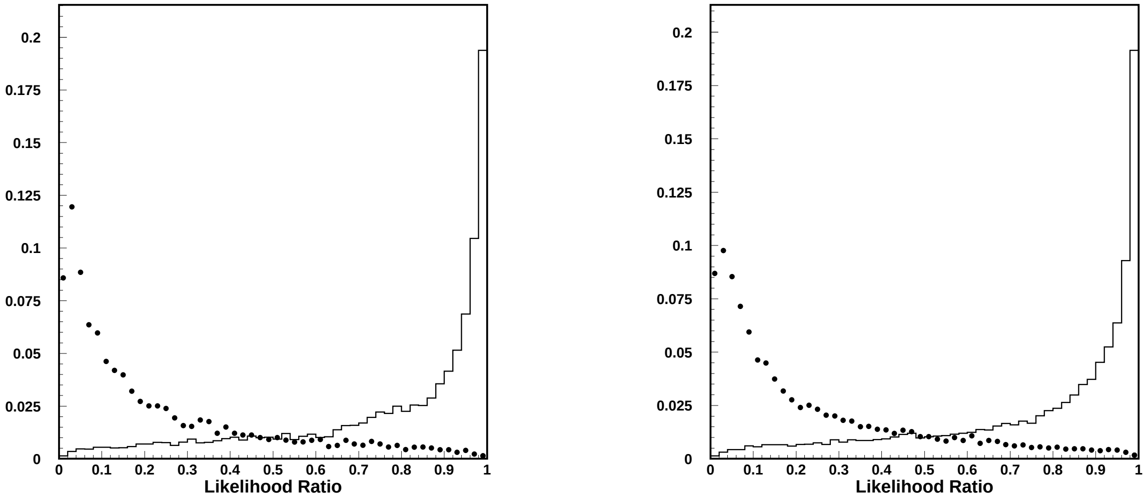

Figure 3.13: Likelihood Ratio Distribution of Signal MC(Solid Histogram) and Sideband Data(Dotted Histogram) with W/ Vertex(left) and HLR W/o Vertex(right) SVD-II sample

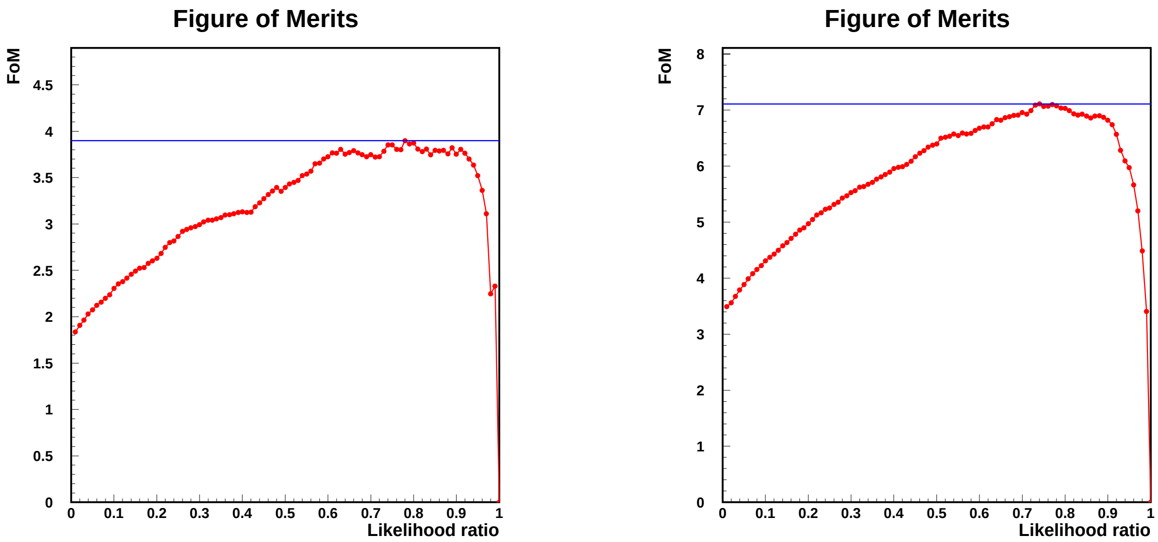

Figure 3.14: Figure of Merits as function of Likelihood ratio with W/ Vertex(left) and HLR W/o Vertex(right) SVD-I sample

Table 3.4: Threshold of Likelihood Ratio Cut

	W/ Vertex	W/o Vertex
SVD-I	0.78	0.74
SVD-II	0.78	0.76

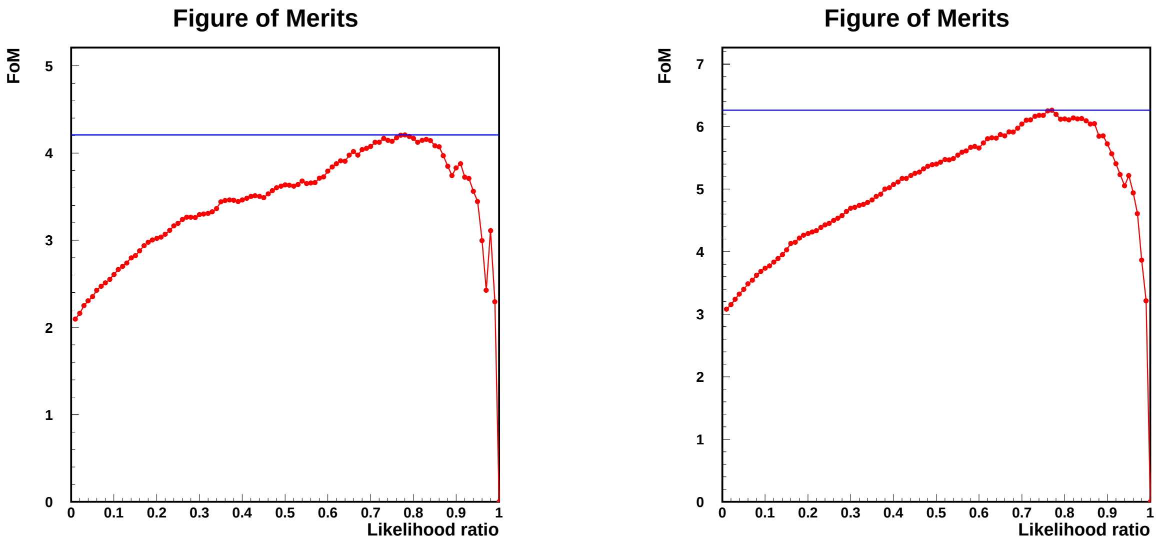

Figure 3.15: Figure of Merits as function of Likelihood ratio with W/ Vertex(left) and HLR W/o Vertex(right) SVD-II sample

determinate by F.o.M. The figure of LR plots and F.o.M depends on LR in r-region are shown in Appendix B. We determined the same threshold, $LR > 0.4$ in all r region. We define these sample as 'Low Likelihood ratio (LLR) events'. The $K_s\pi^0$ reconstruction efficiency after LR cut of each sample, which are estimated by $K_s\pi^0$ signal MC, are summarized in Table 3.5. With high LR and low LR cut, we can reject about 95% and 84% background, respectively.

Table 3.5: Reconstruction Efficiency after Likelihood Ratio Cut

Data Sample	SVD-I(%)	SVD-II(%)
High Likelihood Ratio(HLR) W/ vertex	4.5	6.3
High Likelihood Ratio(HLR) W/o vertex	15.5	14.0
Low Likelihood Ratio(LLR) W/ vertex	1.7	2.5
Low Likelihood Ratio(LLR) W/o vertex	4.8	5.0
total	26.5	27.8

3.8.5 $B\bar{B}$ Background(Rare B Background)

We consider the $B\bar{B}$ Background . $B\bar{B}$ background means the conbinatrial background from B-decay events, and can not be ignored in low ΔE region, because some B decay mode is similar kinematics to $K_S\pi^0$ decay. We estimate the expectation number of $B\bar{B}$ background from MC, and compare the number extracted by fitting the Real data. From the MC study, we found the dominant $B\bar{B}$ background come from $K^*\pi^0$, $K^\pm\pi^0$, $X_{sd}\gamma$ and $X_{ud}\gamma$. These decay mode has very small branching ratio, less than 10^{-5}, and we called these background as 'Rare B background'. The total number of $B\bar{B}$ background expected in W/ vertex and W/o vertex events are summarized in Table 3.6. The M_{bc} and ΔE plots of these events from MC are shown in Fig 3.16.

3.9 Signal Yield Extraction

Signal yield of $K_s\pi^0$ is extracted by M_{bc}-ΔE 2D-Unbinned Maximum likelihood Method, We used four data sample, SVD-I and SVD-II data are combined.

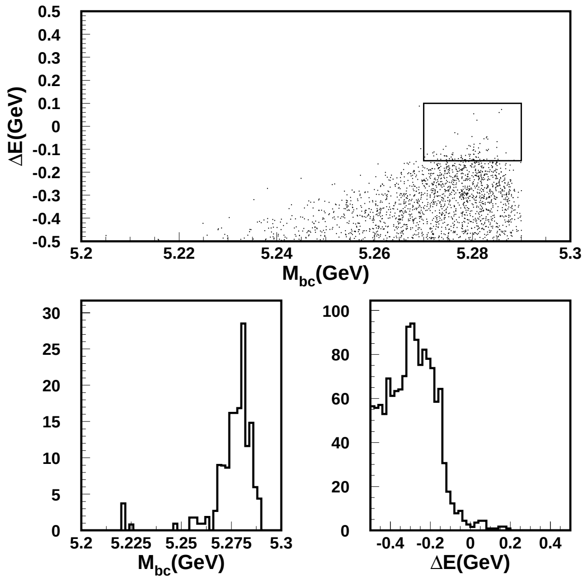

Figure 3.16: Distribution of Beam Constrained mass(lower left) and Energy difference(lower right) and their scatter plots of $B\bar{B}$ background Monte Carlo

Table 3.6: Expected Number of $B\bar{B}$ Background obtained by MC

	HLR		LLR	
	W/ Vertex	W/o Vertex	W/ Vertex	W/o Vertex
SVD-I	1.3	3.6	0.9	1.4
SVD-II	1.2	2.9	0.8	1.1

3.9.1 Unbinned Maximum likelihood Method

The unbinned maximum likelihood method is effective to determine a parameter when a number of events is small. In addition, we can take into account event-by-event effect to the probability density function(PDF). The likelihood is described with the normalized PDF as,

$$L = \prod_{i=1}^{N} P_i\left(x_i; m\right) \tag{3.32}$$

where P_i is PDF and m is the free parameter which is determine by fitting, x_i is i-th measurement of x, and N is a number of events. This likelihood is transformed to,

$$L' = -2ln[L]. \tag{3.33}$$

this is log likelihood, and we determine the m by minimizing L'.

3.9.2 Signal Yield extraction

For extraction of the signal yield, we used the PDF with Beam constrained mass, M_{bc} and Energy difference,ΔE, as follows,

$$P_i\left(M_{bc}, \Delta E\right) = f_{sig}\cdot P_{sig}\left(M_{bc}, \Delta E\right) + f_{rare}\cdot P_{rare}\left(M_{bc}, \Delta E\right) + f_{bkg}\cdot P_{bkg}\left(M_{bc}, \Delta E\right) \tag{3.34}$$

$$f_{bkg} \equiv 1 - \left(f_{sig} + f_{rare}\right) \tag{3.35}$$

where f_{rare} is rare B background fraction, f_{sig} is signal fraction, P_{rare} is normalized Rare B background PDF using M_{bc} and ΔE, P_{sig} is normalized signal PDF using M_{bc} and ΔE, P_{bkg} is normalized background PDF using M_{bc} and ΔE. P_{rare} and P_{sig} are determined by Monte Carlo. The free parameters are f_{rare}, f_{sig} and P_{bkg} shape.

P_{sig} is determined by the M_{bc} and ΔE 1-D binned fitting using $K_s\pi^0$ signal MC. Fig 3.2 shows the M_{bc} and ΔE distribution of signal MC. We determine the function of M_{bc} is single Gaussian function, and ΔE is determinate by Crystal Ball function. single Gaussian and crystal ball function are given as,

$$Gaussian(M_{bc}) = \frac{1}{\sqrt{2\pi}\sigma_{M_{bc}}}\left(\frac{-(M_{bc}-\mu_{M_{bc}})^2}{2\sigma^2_{M_{bc}}}\right) \tag{3.36}$$

$$Crystal\ Ball(\Delta E) = \begin{cases} \mathbf{exp}\left(-\frac{1}{2a^2}\right)\{1-\frac{a}{n}\left(\frac{\Delta E-\mu_{\Delta E}}{\sigma_{\Delta E}}-a\right)\}^{-n} & \textbf{for}\ \ \Delta E-\mu_{\Delta E} < -a\sigma_{\Delta E} \\ \mathbf{exp}\left(-\frac{\Delta E-\mu_{\Delta E}}{2\sigma^2_{\Delta E}}\right) \ \ \textbf{for}\ \ \Delta E-\mu_{\Delta E} > -a\sigma_{\Delta E} & \end{cases} \tag{3.37}$$

The Crystal Ball function[7] is asymmetric Gaussian, and this is effective for fitting the shape including π^0, because energy spectrum including π^0 is asymmetric due to energy loss of daugther γ. In $K_s\pi^0$, Crystal Ball is the best function for ΔE.

Background probability, P_{bkg}, is determined by the M_{bc} and ΔE 2-D unbinned fitting. M_{bc} shape is determinate by ARGUS[8] function, ΔE shape is determined by Chebyshev Function. The definition of ARGUS function is as follows,

$$ARGUS = N\cdot x\cdot\sqrt{1-x^2}\cdot\mathbf{exp}\left(\alpha(1-x^2)\right) \tag{3.38}$$

---

[7] The Crystal Ball is detector made of NaI in Mainz Microtron(MAMI), it was build at SLAC and used for J/ψ measurement. The Crystal Ball function was defined for J/ψ measurement; http://wwwa2.kph.uni-mainz.de/cb/

[8] ARGUS is experiment which study strong, weak and electromagnetic interaction by B-meson decay from $\Upsilon(4S)$. The experiment is peformned with ARGUS detector and DORIS II which is electron-position storage ring at DESY. ARGUS function was defined as Background shape by ARGUS experiment. http://hep.phy.tu-dresden.de/iktp/engl/argus.html

where $x \equiv M_{bc}/E^{cms}_{beam}$, E^{cms}_{beam} is beam energy in cms ($= 5.29\mathrm{GeV/c^2}$). The Chebyshev polynomial n-order Function is

$$Chebyshev = \sum_{i=0}^{n} c_i \cdot C_i(x) \begin{cases} C_0(x) = 1 \\ C_1(x) = x \\ C_2(x) = 2 \cdot x - 1 \\ C_3(x) = 4 \cdot x^3 - 3 \cdot x \\ \ldots. \\ C_n(x) = 2 \cdot x \cdot C_{n-1}(x) - C_{n-2}(x) \end{cases} \tag{3.39}$$

$$x \equiv \frac{2\Delta E - X_{min} - X_{max}}{X_{max} - X_{min}} \tag{3.40}$$

where X_{min} and X_{max} are minimum and maximum limitation of ΔE region. Fig 3.17 shows the example of ARGUS and Chebyshev 2-order function shape for M_{bc} and ΔE background.

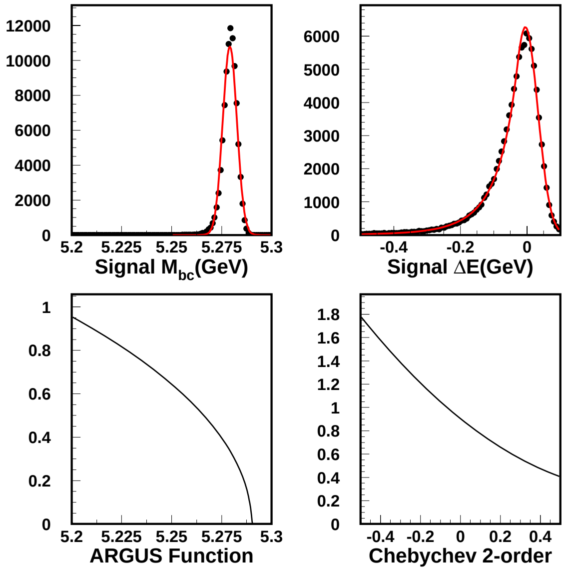

Figure 3.17: Fitted Function for signal MC(Left:Beam Constrained Mass, Right:Energy Difference) and demonstration of ARGUS and Polynomial Chebyshev 2-order function

The rare B background shape are determined from MC by 2D-Smoothed Histogram which is fitted by PAW(Physics Analysis Workstation[9]), and the plots of M_{bc} and ΔE and $M_{bc} - \Delta E$ are shown in Fig 3.18.

We must correct the M_{bc} peak position and width because these values are affect by the beam energy and a its spread. Thus, we use the $B^\pm \to D^0(\to K^+\pi^-\pi^0)\pi^\pm$ decay as the control sample to get correction parameter, it's called fudge factor, by comparing the MC and Data sample. The ΔE peak position and width must also be corrected by fudge factor. We can use $B^\pm \to D^0\pi^\pm$ decay to calibrate these parameters. On the other hand, the ΔE is dominated by the momentum resolution, since the control sample, $B^\pm \to D^0\pi^\pm$ decay, and includes the low momentum particle, while the $K_S\pi^0$ is two body-decay and the momentum of K_S and π^0 are high. Because of this, we require the $p^*_{D^0} > 2.3GeV/c$ to both MC and Data. The plots of M_{bc} and ΔE distribution of MC which was made by EvtGen[104] and Data of $140fb^{-1}$ are shown in Fig 3.19,3.20. In M_{bc}, The signal is fitted by Crystal Ball function, the background is fitted by ARGUS function. In ΔE, the signal is is fitted by Crystal Ball function, the background is fitted by Chebyshev polynomial 2-order. The results of fudge factors are summarized in Table 3.7.

---

[9] http://wwwasd.web.cern.ch/wwwasd/paw/

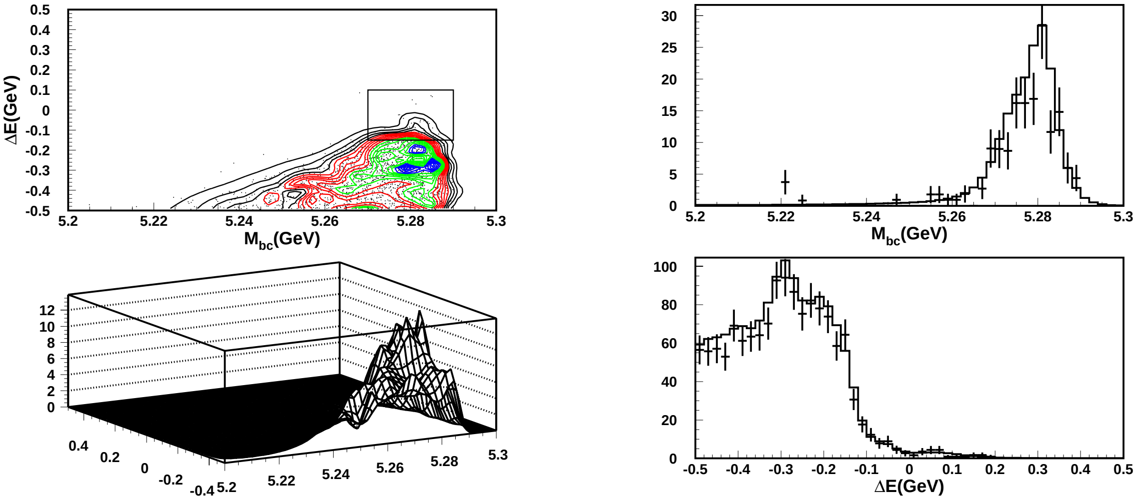

Figure 3.18: Fitted smoothed Histogram of Rare B decay MC
The upper left shows the contour Plot of Beam constrained mass and energy difference

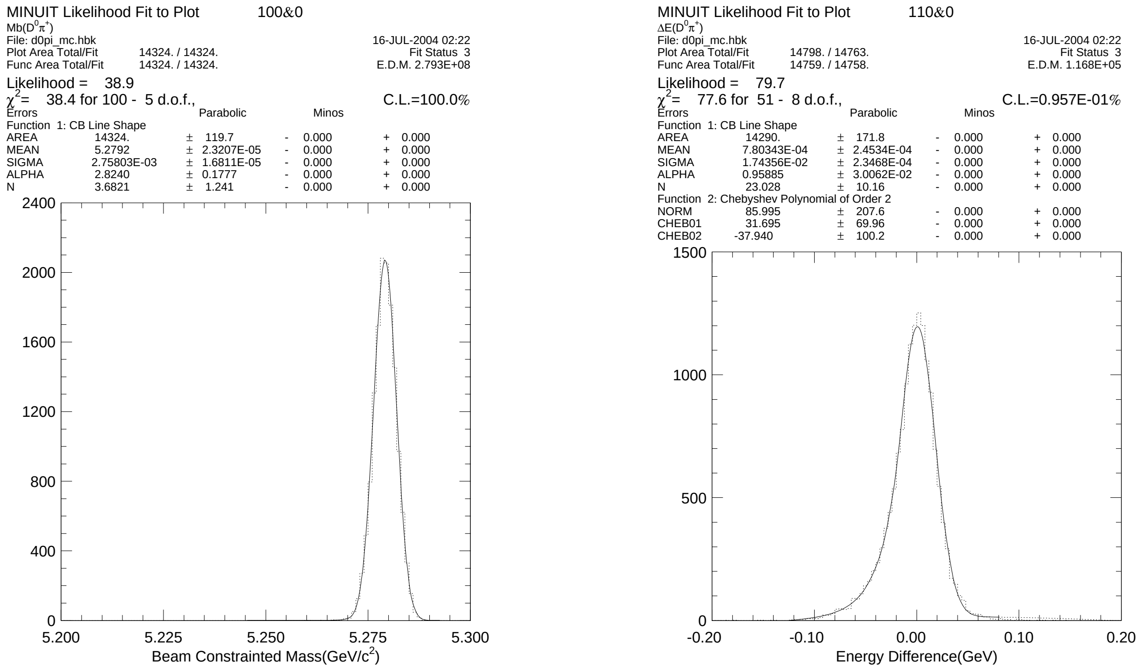

```
MINUIT Likelihood Fit to Plot          100&0
Mb(D0π+)
File: d0pi_mc.hbk                                        16-JUL-2004 02:22
Plot Area Total/Fit        14324. / 14324.                    Fit Status  3
Func Area Total/Fit        14324. / 14324.                E.D.M. 2.793E+08
Likelihood =    38.9
χ2=   38.4 for 100 -  5 d.o.f.,                             C.L.=100.0%
Errors                          Parabolic           Minos
Function  1: CB Line Shape
AREA             14324.       ±   119.7         -   0.000      +   0.000
MEAN             5.2792       ±  2.3207E-05     -   0.000      +   0.000
SIGMA           2.75803E-03   ±  1.6811E-05     -   0.000      +   0.000
ALPHA            2.8240       ±  0.1777         -   0.000      +   0.000
N                3.6821       ±   1.241         -   0.000      +   0.000
```

```
MINUIT Likelihood Fit to Plot          110&0
ΔE(D0π+)
File: d0pi_mc.hbk                                        16-JUL-2004 02:22
Plot Area Total/Fit        14798. / 14763.                    Fit Status  3
Func Area Total/Fit        14759. / 14758.                E.D.M. 1.168E+05
Likelihood =    79.7
χ2=   77.6 for  51 -  8 d.o.f.,                        C.L.=0.957E-01%
Errors                          Parabolic           Minos
Function  1: CB Line Shape
AREA             14290.       ±   171.8         -   0.000      +   0.000
MEAN            7.80343E-04   ±  2.4534E-04     -   0.000      +   0.000
SIGMA           1.74356E-02   ±  2.3468E-04     -   0.000      +   0.000
ALPHA           0.95885       ±  3.0062E-02     -   0.000      +   0.000
N                23.028       ±   10.16         -   0.000      +   0.000
Function  2: Chebyshev Polynomial of Order 2
NORM             85.995       ±   207.6         -   0.000      +   0.000
CHEB01           31.695       ±   69.96         -   0.000      +   0.000
CHEB02          -37.940       ±   100.2         -   0.000      +   0.000
```

Figure 3.19: Distribution of Beam constrained mass and energy difference of $B^+ \to D^0\pi^+$ Monte Cairo
Fitted function of Beam constrained mass is single Gaussian and energy difference is Crystal Ball function.

Table 3.7: Results of fudge factor for M_{bc} and ΔE

	$D^0\pi^\pm$ MC	$D^0\pi^\pm$ DATA	fudge factor
M_{bc} mean	5279.2(MeV/c^2)	5279.1(MeV/c^2)	$< M_{bc} >^{DATA}_{mean}$ - $< M_{bc} >^{DATA}_{mean}$ = -0.1MeV
M_{bc} sigma	2.75MeV	2.73MeV	$\sigma^{DATA}_{M_{bc}}$ / $\sigma^{MC}_{M_{bc}}$ = 0.9898
ΔE mean	0.7803MeV	-2.0819MeV	$< \Delta E >^{DATA}_{mean}$ - $< \Delta E >^{DATA}_{mean}$ = -2.8622MeV
ΔE sigma	17.44MeV	20.15MeV	$\sigma^{DATA}_{\Delta E}$ / $\sigma^{MC}_{\Delta E}$ = 1.1556

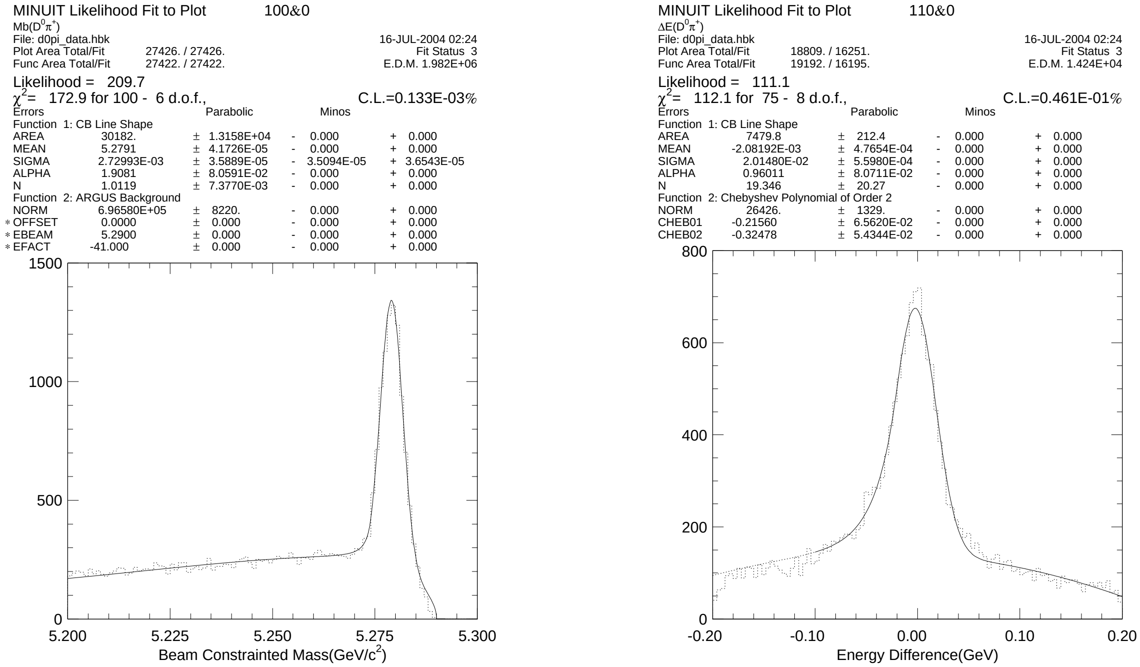

```
MINUIT Likelihood Fit to Plot          100&0
Mb(D0π+)
File: d0pi_data.hbk                                          16-JUL-2004 02:24
Plot Area Total/Fit       27426. / 27426.                         Fit Status  3
Func Area Total/Fit       27422. / 27422.                      E.D.M. 1.982E+06
Likelihood =   209.7
χ2=   172.9 for 100 -  6 d.o.f.,                           C.L.=0.133E-03%
Errors                          Parabolic          Minos
Function  1: CB Line Shape
 AREA          30182.       ±  1.3158E+04   -   0.000       +   0.000
 MEAN          5.2791       ±  4.1726E-05   -   0.000       +   0.000
 SIGMA         2.72993E-03  ±  3.5889E-05   -  3.5094E-05   +  3.6543E-05
 ALPHA         1.9081       ±  8.0591E-02   -   0.000       +   0.000
 N             1.0119       ±  7.3770E-03   -   0.000       +   0.000
Function  2: ARGUS Background
 NORM          6.96580E+05  ±   8220.       -   0.000       +   0.000
*OFFSET        0.0000       ±   0.000       -   0.000       +   0.000
*EBEAM         5.2900       ±   0.000       -   0.000       +   0.000
*EFACT       -41.000        ±   0.000       -   0.000       +   0.000
```

```
MINUIT Likelihood Fit to Plot          110&0
ΔE(D0π+)
File: d0pi_data.hbk                                          16-JUL-2004 02:24
Plot Area Total/Fit       18809. / 16251.                         Fit Status  3
Func Area Total/Fit       19192. / 16195.                      E.D.M. 1.424E+04
Likelihood =   111.1
χ2=   112.1 for  75 -  8 d.o.f.,                           C.L.=0.461E-01%
Errors                          Parabolic          Minos
Function  1: CB Line Shape
AREA           7479.8       ±   212.4       -   0.000       +   0.000
MEAN          -2.08192E-03  ±  4.7654E-04   -   0.000       +   0.000
SIGMA          2.01480E-02  ±  5.5980E-04   -   0.000       +   0.000
ALPHA          0.96011      ±  8.0711E-02   -   0.000       +   0.000
N              19.346       ±   20.27       -   0.000       +   0.000
Function  2: Chebyshev Polynomial of Order 2
NORM           26426.       ±   1329.       -   0.000       +   0.000
CHEB01        -0.21560      ±  6.5620E-02   -   0.000       +   0.000
CHEB02        -0.32478      ±  5.4344E-02   -   0.000       +   0.000
```

Figure 3.20: Distribution of Beam constrained mass and energy difference of $B^+ \to D^0\pi^+$ $140fb{-}1$ Data Fitted function of Beam constrained mass is single Gaussian for signal and ARGUS function for background, while energy difference is Crystal Ball function for signal and Polynomial Chebyshev 2-order function.

Table 3.8: Fit Parameters of Signal and Background Shape

Parameter	SVD-I		SVD-II	
	HLR(W/ Vertex)	HLR(W/o Vertex)	LLR(W/ Vertex)	LLR(W/o Vertex)
μ_{M_bc}	5.27902 ± 0.00005			
σ_{M_bc}	0.00351 ± 0.00005			
$\mu_{\Delta E}$	-0.0078 ± 0.0006			
$\sigma_{\Delta E}$	0.0431 ± 0.0006			
n	0.6398 ± 0.0095			
a	7.1678 ± 0.3150			
α	-26.6 ± 4.4	-14.6 ± 2.5	-21.5 ± 2.2	-20.4 ± 1.4
c_0	-0.690 ± 0.050	-0.577 ± 0.302	-0.705 ± 0.250	-0.612 ± 0.017
c_1	0.095 ± 0.047	0.086 ± 0.029	0.170 ± 0.024	0.119 ± 0.159

Finally, the PDF for extraction of signal yield is

$$\begin{aligned}
P_{sig} &= Gaussisan\,(M_{bc}) \times Crysral\ Ball\,(\Delta E) & (3.41)\\
P_{bkg} &= ARGUS\,(M_{bc}) \times Chebyshev\,(\Delta E) & (3.42)\\
P_{rare} &= 2D - Smoothed\ Histogram(M_{bc}, \Delta E) & (3.43)
\end{aligned}$$

We used common signal shape in W/ and W/o vertex sample, and HLR sample and LLR sample. The background shape, however, are different for W/ and W/o vertex sample, HLR and LLR sample. The definition of signal region is explained in last chapter. The fitted signal shape parameters corrected by fudge factor and fitted background shape parameters are listed in Table 3.8. The signal yield of each sample are summarized in Table 3.9. Fig 3.21 and 3.22 shows the M_{bc} and ΔE fitting results.

Table 3.9: Extracted Signal Yield and Rare B Background Yield

Sample	Signal Yield	Rare B	Continuum
W/ vertex (HLR)	59.0±9.0	0.5±0.4	39.2±0.8
W/o vertex (HLR)	108.7±13.4	9.7±2.1	97.0±1.1
W/ vertex (LLR)	11.5±9.4	1.9±2.1	127.5±1.2
W/o vertex (LLR)	67.3±17.0	3.8±3.1	306.9±1.8

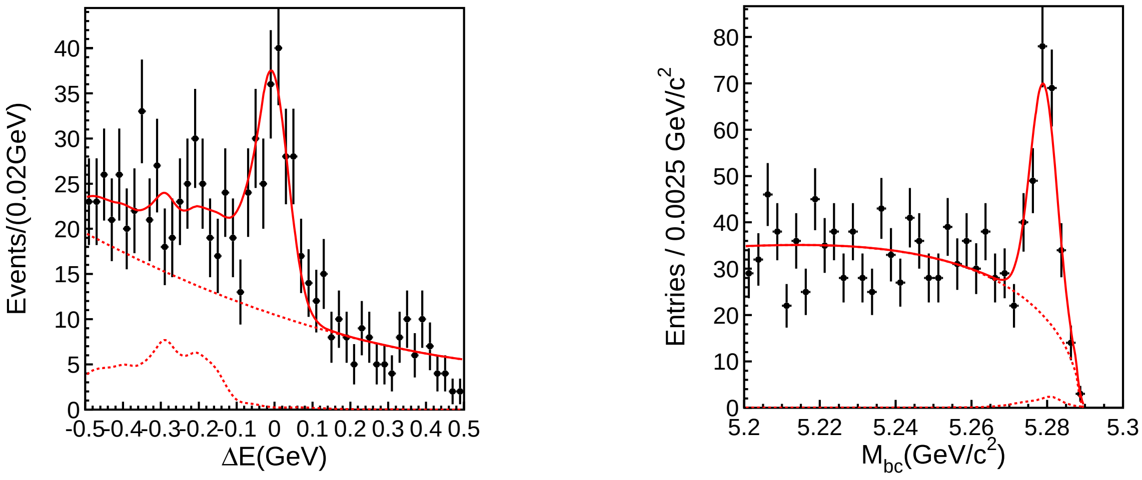

Figure 3.21: ΔE and M_{bc} plots of HLR W/+W/o combined Vertex events
Left is ΔE distribution and right is M_{bc} distribution. The solid line shows Signal and Background component. The dashed line shows Background(upper one is continuum background and lower one is $B\bar{B}$ background.)

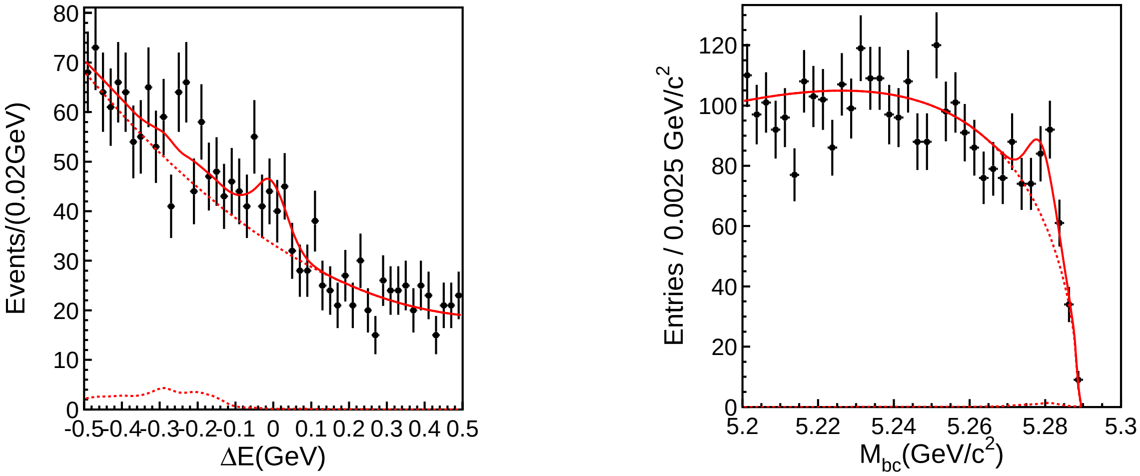

Figure 3.22: ΔE and M_{bc} plots of LLR W/+W/o combined Vertex events
Left is ΔE distribution and right is M_{bc} distribution. The solid line shows Signal and Background component. The dashed line shows Background(upper one is continuum background and lower one is $B\bar{B}$ background.)

Chapter 4

Determination of CP Asymmetries

We measure the CP-asymmetry parameters, $A_{K_s\pi^0}$, the direct CP-parameter, and $S_{K_s\pi^0}$, the indirect CP-parameter by the unbinned maximum likelihood method which is explained in the last chapter. Probability density function(PDF) for CP-asymmetry measurement is defined as function of proper time-difference. PDF is smeared by wrong tagging fraction factor of flavor tag, and by detector resolution. In $K_s\pi^0$ analysis, we measure not only time dependent CP-asymmetry, but also time integrated CP-asymmetry, because the number of reconstructed W/ vertex events is small. Since the $A_{K_s\pi^0}$ is direct CP-parameter, it can be measured from W/o vertex event which has flavor information. Thus, we use W/o vertex sample to increase statistics for $A_{K_s\pi^0}$ measurement. The PDF for CP-asymmetry measurement includes signal PDF and Background PDF. Signal PDF is for $K_s\pi^0$. Background PDF is for continuum background and Rare B Background($B\bar{B}$ Background).

4.1 PDF for measurement CP-Asymmetries

The exact description of full PDF is presented in this section. The probability density function(PDF) for the CP-asymmetry measurement is made by Signal PDF, Rare B Background PDF and Continuum Background PDF. Each PDF consist of two parts, time dependent and time integrated one. The time-dependent PDF can be expressed as,

$$\begin{aligned} &P_i\left(\Delta t_i; A_{K_s\pi^0}, S_{K_s\pi^0}\right) \\ &\qquad = f_{K_s\pi^0}\cdot P_{K_s\pi^0}(\Delta t; q; A_{K_s\pi^0}, S_{K_s\pi^0}) + f_{BB}\cdot P_{BB}(\Delta t; q; A_{rare}, S_{rare}) + f_{q\bar{q}}\cdot P_{q\bar{q}}(\Delta t) \end{aligned} \tag{4.1}$$

while the time-integrated PDF can be expressed as,

$$P_i\left(q_i; A_{K_s\pi^0}\right) \quad = \quad f_{K_s\pi^0}\cdot P_{K_s\pi^0}(q_i) + f_{BB}\cdot P_{BB}(q_i) + f_{q\bar{q}}\cdot P_{q\bar{q}} \tag{4.2}$$

where $f_{K_s\pi^0}$ is the signal PDF, which depends on M_{bc} and ΔE and these parameters are given event-by-event. f_{BB} is the rare B background PDF, which depends on M_{bc} and ΔE and these parameters are also event-by-event. $f_{q\bar{q}}$ is continuum background PDF. $P_{K_s\pi^0}$, P_{BB}, and $P_{q\bar{q}}$ are signal, rare B background, and continuum background PDF, repectively. Using these PDF, the Likelihood can be written by,

$$\begin{aligned} L_i\left(\Delta t_i; A_{K_s\pi^0}, S_{K_s\pi^0}\right) &= P_i\left(\Delta t_i; A_{K_s\pi^0}, S_{K_s\pi^0}\right) && (4.3)\\ L_j\left(q_j; A_{K_s\pi^0}\right) &= P_j\left(q_j; A_{K_s\pi^0}\right) && (4.4)\\ Likelihood &= \prod_i^N L_i\left(\Delta t_i; A_{K_s\pi^0}, S_{K_s\pi^0}\right)\cdot\prod_j^{N'} L_j\left(q_j; A_{K_s\pi^0}\right) && (4.5) \end{aligned}$$

We describe the detail of signal PDF, rare B background PDF, and continuum background PDF in the following section.

4.1.1 Signal Probability Density Function

Signal PDF is described for $K_s\pi^0$ signal events which has CP-parameters, $A_{K_s\pi^0}$ and $S_{K_s\pi^0}$. The theoretical time-dependent PDF is given as,

$$P_{K_s\pi^0}(\Delta t; q; A_{K_s\pi^0}, S_{K_s\pi^0}) = \frac{e^{-|\Delta t|/\tau_{B^0}}}{4\tau_{B^0}}[1 + q\cdot(A_{K_s\pi^0}\mathbf{cos}\,(\Delta m_d\Delta t) + S_{K_s\pi^0}\mathbf{sin}\,(\Delta m_d\Delta t))] \tag{4.6}$$

where Δt is measured time difference defined as Eq 3.8, the q is the flavor of tag-side B^0, $q = 1(-1)$ means $B^0(\bar{B^0})$, the Δm_d is mass difference of between B^0 eigenstate mass which was defined as Eq (1.82).

The theoretical time-integrated PDF is given as,

$$P_{K_s\pi^0}(q; A_{K_s\pi^0}) = \frac{1}{2}\{1 + q\cdot(1-2\chi_d)\cdot A_{K_s\pi^0}\} \tag{4.7}$$

the factor 1/2 is a normalization factor, χ_d is time-integrated mixing probability parameter, it is given as follows,

$$\begin{aligned}
\chi_d &\equiv \frac{\int_0^\infty |\langle\bar{B^0}|B^0(t)\rangle|^2dt}{\int_0^\infty |\langle\bar{B^0}|B^0(t)\rangle|^2dt + \int_0^\infty |\langle B^0|\bar{B^0}(t)\rangle|^2dt} \\
&= \frac{x^2+y^2}{x^2+y^2+|\frac{p}{q}|^2(2+x^2-y^2)} \\
&= \frac{x^2}{2(1+x^2)}
\end{aligned} \tag{4.8}$$

where $x = \Delta m/\Gamma$, $y = \Delta\Gamma/\Gamma$, in approximately $y \sim 0$ and $|\frac{p}{q}| \sim 1$. We calculate x^2 from PDG value of Δm and Γ, and use it in measurement of CP-asymmetry parameter.

The theoretical signal PDF must be smeared by wrong tag fraction. The PDF for CP-asymmetry measurement is made by linear combination of $P_{K_s\pi^0}(\Delta t; q=1; A_{K_s\pi^0}; S_{K_s\pi^0})$ and $P_{K_s\pi^0}(\Delta t; q=-1; A_{K_s\pi^0}; S_{K_s\pi^0})$. The Signal PDF for B^0 is defined by

$$(P_{K_s\pi^0})^{B^0}_{exp} = (1-w)\cdot P_{K_s\pi^0}(\Delta t; q=1; A_{K_s\pi^0}; S_{K_s\pi^0}) + w\cdot P_{K_s\pi^0}(\Delta t; q=-1; A_{K_s\pi^0}; S_{K_s\pi^0}) \tag{4.9}$$

$$(P_{K_s\pi^0})^{\bar{B^0}}_{exp} = w\cdot P_{K_s\pi^0}(\Delta t; q=1; A_{K_s\pi^0}; S_{K_s\pi^0}) + (1-w)\cdot P_{K_s\pi^0}(\Delta t; q=-1; A_{K_s\pi^0}; S_{K_s\pi^0}) \tag{4.10}$$

where w is wrong tag fraction, which has $0 \sim 0.5$ value. From these equations, the $P_{K_s\pi^0}$ are given as,

$$\begin{aligned}
&P_{K_s\pi^0}(\Delta t; q; w; A_{K_s\pi^0}, S_{K_s\pi^0}) \\
&\qquad = \frac{e^{-|\Delta t|/\tau_{B^0}}}{4\tau_{B^0}}[1 - q\cdot(1-2w)\,(A_{K_s\pi^0}\mathbf{cos}\,(\Delta m_d\Delta t) + S_{K_s\pi^0}\mathbf{sin}\,(\Delta m_d\Delta t))]
\end{aligned} \tag{4.11}$$

Since the detector response is different between particle and anti-particle, the wrong tag fraction for B^0 and $\bar{B^0}$ is different. We distinguish the wrong tag fraction of B^0 and $\bar{B^0}$ as following,

$$(P_{K_s\pi^0})^{B^0}_{exp} = (1-w_{B^0})\cdot P_{K_s\pi^0}(\Delta t; q=1; A_{K_s\pi^0}; S_{K_s\pi^0}) + w_{\bar{B^0}}\cdot P_{K_s\pi^0}(\Delta t; q=-1; A_{K_s\pi^0}; S_{K_s\pi^0}) \tag{4.12}$$

$$(P_{K_s\pi^0})^{\bar{B^0}}_{exp} = w_{B^0}\cdot P_{K_s\pi^0}(\Delta t; q=1; A_{K_s\pi^0}; S_{K_s\pi^0}) + (1-w_{\bar{B^0}})\cdot P_{K_s\pi^0}(\Delta t; q=-1; A_{K_s\pi^0}; S_{K_s\pi^0}) \tag{4.13}$$

And, w_{B^0} and $w_{\bar{B^0}}$ are defined by,

$$\Delta w \equiv w_{B^0} - w_{\bar{B^0}} \tag{4.14}$$

$$w_{tag} \equiv \frac{w_{B^0} + w_{\bar{B^0}}}{2} \tag{4.15}$$

Δw is defined as difference of wrong tag fraction, and w_{tag} is the average wrong tag fraction for B^0 and $\bar{B}^0$. Then adding this wrong tag fraction and difference wrong tag fraction, the time-dependent $P_{K_s\pi^0}$ of B^0 and $\bar{B}^0$ is given by,

$$\begin{aligned} &P_{K_s\pi^0}\left(\Delta t; q; w; A_{K_s\pi^0}, S_{K_s\pi^0}\right) \\ &\quad = \frac{e^{-|\Delta t|/\tau_{B^0}}}{4\tau_{B^0}}[1 - q\cdot\Delta w + q\cdot(1-2\cdot w_{tag})\left\{A_{K_s\pi^0}\mathbf{cos}\left(\Delta m_d \Delta t\right) + S_{K_s\pi^0}\mathbf{sin}\left(\Delta m_d \Delta t\right)\right\}], \end{aligned} \tag{4.16}$$

and, the normalized time-integrated PDF, which is corrected by wrong tag fraction, is,

$$P_{K_s\pi^0}\left(q; w; A_{K_s\pi^0}\right) = \frac{1}{2}\{1 - q\cdot\Delta w + q\cdot(1-2\cdot w_{tag})\cdot(1-2\chi_d)\cdot A_{K_s\pi^0}\} \tag{4.17}$$

Where w_{tag} and Δw is determined in each r-bin. We notice that this w_{tag} and Δw is not 'event-by-event', but constant value. These wrong tag fraction are determined by time dependent $B^0\bar{B}^0$ Mixing analysis using flavor-specific B decay mode, $B^0 \to D^{(*)}\pi$, $D^{(*)}\rho$, $D^{*}l\nu$. The wrong tag fraction, w_{tag}, and Δw of each r-bin are summarized in Table 4.1, we determinate SVD-I and SVD-II, respectively. The error of each value are combined error of statistical error and systematic error.

Table 4.1: Wrong Tag fraction and Difference Wrong Tag fraction

SVD-I						
r-bin	w_{tag}	Error(+)	Error(-)	Δw	Error(+)	Error(-)
0.0 - 0.250	0.464	0.005	-0.005	-0.011	0.006	-0.006
0.250 - 0.500	0.331	0.007	-0.008	0.004	0.010	-0.009
0.500 - 0.625	0.231	0.009	-0.009	-0.011	0.010	-0.010
0.625 - 0.750	0.161	0.008	-0.007	-0.007	0.009	-0.009
0.750 - 0.875	0.109	0.007	-0.007	0.016	0.009	-0.009
0.875 - 1.000	0.020	0.004	-0.005	0.003	0.006	-0.005
SVD-II						
r-bin	w_{tag}	Error(+)	Error(-)	Δw	Error(+)	Error(-)
0.0 - 0.250	0.464	0.005	-0.007	0.008	0.006	-0.007
0.250 - 0.500	0.320	0.008	-0.007	-0.022	0.009	-0.010
0.500 - 0.625	0.224	0.011	-0.008	0.029	0.011	-0.011
0.625 - 0.750	0.158	0.010	-0.009	0.003	0.010	-0.011
0.750 - 0.875	0.109	0.008	-0.009	-0.028	0.011	-0.010
0.875 - 1.000	0.015	0.005	-0.005	0.007	0.006	-0.007

4.1.2 Rare B Background Probability Density Function

The shape of Rare B background PDF is basically same as signal PDF. But the lifetime and CP-parameter are different. In rare B background, the neutral B and charged B are included and we determine a effective lifetime from Rare B Monte Carlo. The effective lifetime is determinate as $\tau'_B = 1.515 \pm 0.068$(ps), which is showm in Fig 4.1. The time-integrated PDF is exactly same as signal PDF. We must consider the CP-asymmetry effect of B background because in rare B event, the CP-eigenstate, which may have cp asymmetry, are included. We estimate the asymmetry effect of Rare B and the deviation are included in systematic error which is described in Chapter 4.8.

$$\begin{aligned} &P_{rare}\left(\Delta t; q; w; A_{rare}, S_{rare}\right) \\ &\quad = \frac{e^{-|\Delta t|/\tau'_B}}{4\tau'_B}[1 - q\cdot\Delta w + q\cdot(1-2\cdot w_{tag})\left\{A_{rare}\mathbf{cos}\left(\Delta m_d \Delta t\right) + S_{rare}\mathbf{sin}\left(\Delta m_d \Delta t\right)\right\}], \end{aligned} \tag{4.18}$$

We assume $A_{rare} = S_{rare} = 0$ and fixed when fitting the CP-asymmetry of $K_S\pi^0$.

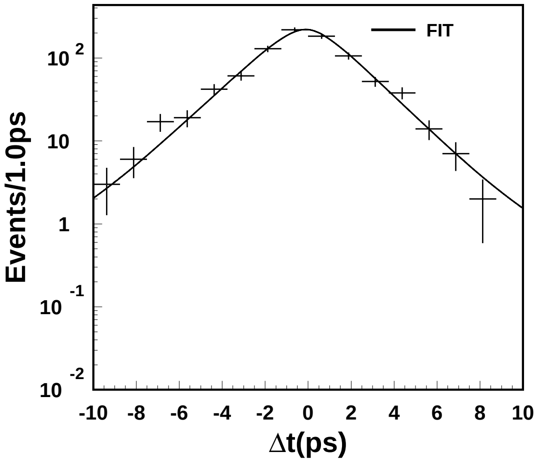

Figure 4.1: Δt distribution of Rare B Background by MC. The solid line is fitted function. Point is MC data

4.1.3 Continuum Background Probability Density Function

Dominant background for $K_s\pi^0$ come from continuum event. We use the background PDF defined as time-dependent PDF.

$$P_{q\bar{q}}(\Delta t) = \frac{1}{2}\{(1-f_\delta)\cdot\frac{e^{-(|\Delta t|-\mu_\tau^{bkg})/\tau_{bkg}}}{2\tau_{bkg}} + f_\delta\cdot\delta(\Delta t-\mu_\delta^{bkg})\} \tag{4.19}$$

Time-dependent PDF is given by an exponential function and δ function, a exponential function express effect of the finite lifetime particles where τ_{bkg} is a effective lifetime, and δ function means zero lifetime event. The τ_{bkg}, f_τ, μ_τ^{bkg} and μ_δ^{bkg} are determined by sideband data of $K_s\pi^0$ sample. The normalized time-integrated PDF is given as follows,

$$P_{q\bar{q}} = \frac{1}{2} \tag{4.20}$$

Table 4.2: The Parameters of Continuum Background PDF

Parameters	multi-track	single-track
f_δ	$0.966^{+0.015}_{-0.024}$	$0.859^{+0.038}_{-0.048}$
μ_τ^{bkg}	$-0.008^{+0.026}_{-0.026}$	——
τ_{bkg}	$4.591^{+1.888}_{-1.058}$	——
μ_{delta}^{bkg}	$-0.008^{+0.026}_{-0.026}$	——

4.2 Final PDF for measurement of CP-asymmetry parameters

The Eq 4.1 must be smeared by resolution function, since the detector has finite resolution and uncertain in Δt. Resolution function[105] consist of three components, detector resolution, smearing due to non-primary tracks, and kinematic approximation. Resolution function is much complicated function and has many parameters. These parameters are determinate by Real data and MC. The PDF included resolution function is defined as,

$$\begin{aligned}P_i\left(\Delta t_i; q_i; w_i; A_{K_s\pi^0}, S_{K_s\pi^0}\right) = (1-f_{ol}) \int_{-\infty}^{\infty} [\{f_{K_s\pi^0} \cdot P_{K_s\pi^0}\left(\Delta t'; q_i; w_i; A_{K_s\pi^0}, S_{K_s\pi^0}\right) \\ + f_{BB} \cdot P_{BB}\left(\Delta t'; q_i; w_i; A_{rare}, S_{rare}\right)\} \cdot R_{sig}\left(\Delta t_i - \Delta t'\right) \\ + f_{q\bar{q}} \cdot P_{q\bar{q}}(\Delta t') \cdot R_{q\bar{q}}\left(\Delta t_i - \Delta t'\right)] d\Delta t' + f_{ol} \cdot P_{ol}\left(\Delta t_i\right) \quad (4.21)\end{aligned}$$

R_{sig} is resolution function of signal and rare decay background component, $R_{q\bar{q}}$ is the resolution function of continuum background. The parameters of resolution function of continuum background are determined by sideband data of $K_s\pi^0$. The $P_{ol}\left(\Delta t_i\right)$ is Outlier function which has log tail in Δt distribution. The long tail is considered be caused by the mis-reconstruction of the track independent on whether the event is signal or background. The outlier can not be described by resolution function, then we use more one background function as outlier. The f_{ol} is the fraction of outlier component. This PDF is time-dependent PDF, while the time-integrated PDF is defined by,

$$P_i\left(q_i; w_i; A_{K_s\pi^0}\right) = f_{K_s\pi^0} \cdot P_{K_s\pi^0}\left(q_i, w_i; A_{K_s\pi^0}\right) + f_{BB} \cdot P_{BB}\left(q_i, w_i; A_{K_s\pi^0}\right) + f_{q\bar{q}} \cdot P_{q\bar{q}} \quad (4.22)$$

The final likelihood for CP-asymmetry measurement are expressed as,

$$\begin{aligned}L_i\left(\Delta t_i; q_i; w_i; A_{K_s\pi^0}, S_{K_s\pi^0}\right) &= P_i\left(\Delta t_i; q_i; w_i; A_{K_s\pi^0}, S_{K_s\pi^0}\right) && (4.23)\\ L_j\left(q_j; w_j; A_{K_s\pi^0}\right) &= P_j\left(q_j; w_j; A_{K_s\pi^0}\right) && (4.24)\\ Likelihood &= \prod_i^N L_i\left(\Delta t_i; q_i; w_i; A_{K_s\pi^0}, S_{K_s\pi^0}\right) \cdot \prod_j^{N'} L_j\left(q_j; w_j; A_{K_s\pi^0}\right) && (4.25)\end{aligned}$$

The resolution function for signal can be written by,

$$\begin{aligned}R_{sig}(\Delta t) = \iiint_{-\infty}^{\infty} d(\Delta t')d(\Delta t'')d(\Delta t''') \\ R_{ful}(\Delta t - \Delta t')R_{asc}(\Delta t' - \Delta t'') \\ R_{np}(\Delta t'' - \Delta t''')R_k(\Delta t''') \quad (4.26)\end{aligned}$$

where the resolution function for the signal is constructed as convolution of four different contribution, the detector resolution of cp-side(full reconstructed side = full-side), R_{ful}, the detector resolution of tag-side(associated side = asci-side), R_{asci}, non-primary track effect, R_{np}, and kinematic approximation, R_k. The detail of Resolution Function is described in Appendix C.

4.3 Signal Probability function

The $f_{K_s\pi^0}$, f_{BB} and $f_{q\bar{q}}$ are calculated from Beam constrained mass, M_{bc}, and Energy difference, ΔE. The signal probability is defined by the follows,

$$\begin{aligned}f_{K_s\pi^0} &= \frac{F_{K_s\pi^0}\left(\Delta t, M_{bc}, \Delta E\right) \cdot f_{sig}}{F_{K_s\pi^0}\left(\Delta t, M_{bc}, \Delta E\right) \cdot f_{sig} + F_{rare}\left(\Delta t, M_{bc}\right), \Delta E \cdot f_{rare} + F_{q\bar{q}}\left(\Delta t, M_{bc}, \Delta E\right) \cdot f_{bkg}} && (4.27)\\ f_{BB} &= \frac{F_{rare}\left(\Delta t, M_{bc}, \Delta E\right) \cdot f_{rare}}{F_{K_s\pi^0}\left(\Delta t, M_{bc}, \Delta E\right) \cdot f_{sig} + F_{rare}\left(\Delta t, M_{bc}, \Delta E\right) \cdot f_{rare} + F_{q\bar{q}}\left(\Delta t, M_{bc}, \Delta E\right) \cdot f_{bkd}} && (4.28)\\ f_{q\bar{q}} &= 1 - \left(f_{K_s\pi^0} + f_{rare}\right) && (4.29)\end{aligned}$$

$$F_{K_s\pi^0}\left(\Delta t, M_{bc}, \Delta E\right) = Gaussisan\left(M_{bc}\right) \times CrysralBall\left(\Delta E\right) \quad (4.30)$$

$$F_{rare}\left(\Delta t, M_{bc}, \Delta E\right) = Smoothed\ Histogram(M_{bc}, \Delta E) \quad (4.31)$$

$$F_{q\bar{q}}\left(\Delta t, M_{bc}, \Delta E\right) = ARGUS\left(M_{bc}\right) \times Chebyshev\left(\Delta E\right) \tag{4.32}$$

Where f_{sig} and f_{rare} are signal and rare B background fraction used signal yield extraction, and the definition of *Crysral Ball* function, *ARGUS* function, *Chebyshev* function are explained last Chapter. For measurement the CP-asymmetry parameters, we calculate these fraction in W/ vertex of HLR, W/o vertex of HLR, W/ vertex of LLR, W/o vertex of LLR and in 6 r-bin regions, total number of signal fraction is 24. The signal region is, 5.27(GeV/c^2) $< M_{bc} <$ 5.29(GeV/c^2) and -0.15(GeV) $< \Delta E <$ -0.10(GeV). The signal fraction in 6 r-bins is calculated by Signal MC and sideband Data. From the fit to $M_{bc} - \Delta E$ 2D distribution, for $K_S\pi^0$ candidate with Likelihood ratio cut, High LR and Low LR cut, we obtain the fraction or fitted events of $K_S\pi^0$ signal, rare B background events, and continuum background evetns in $M_{bc} - \Delta E$ signal region. We estimate the number of $K_S\pi^0$ events for each r-bin by $K_S\pi^0$ signal MC, and obtain the r-bin fraction. We also estimate the number of rare B background events for r-bin by MC, while to obtain the estimated number of continuum background for each r-bin, the fit to the sideband data for each r-bin with LR cut events, The expected fraction of $K_S\pi^0$, Rare B Background and continuum background are listed in Table 4.3. The table listed the expected number of each events and M_{bc} and ΔE plots in each r-region are shown in Appendix D.

Table 4.3: Expected fraction of each r-bin

Expected fraction of $K_S\pi^0$ Event				
r-bin	High Likelihood Ratio		Low Likelihood Ratio	
region	W/ Vertex	W/o Vertex	W/ Vertex	W/o Vertex
1	0.499±0.077	0.402±0.050	0.061±0.028	0.143±0.025
2	0.667±0.124	0.527±0.085	0.090±0.061	0.193±0.051
3	0.569±0.149	0.493±0.104	0.093±0.076	0.182±0.061
4	0.572±0.145	0.522±0.104	0.083±0.070	0.166±0.056
5	0.655±0.158	0.635±0.118	0.099±0.094	0.240±0.085
6	0.901±0.091	0.844±0.080	0.322±0.228	0.501±0.131

Expected fraction of Rare B Background Event				
r-bin	High Likelihood Ratio		Low Likelihood Ratio	
region	W/ Vertex	W/o Vertex	W/ Vertex	W/o Vertex
1	0.004±0.010	0.037±0.019	0.008±0.010	0.007±0.006
2	0.007±0.021	0.042±0.034	0.016±0.027	0.009±0.012
3	0.006±0.024	0.047±0.044	0.017±0.035	0.011±0.016
4	0.005±0.021	0.041±0.041	0.015±0.031	0.009±0.014
5	0.005±0.024	0.068±0.062	0.017±0.041	0.018±0.026
6	0.007±0.026	0.073±0.058	0.069±0.124	0.040±0.052

4.4 Result of CP-asymmetry Parameter measurement

We extracted the best value for $A_{K_s\pi^0}$ and $S_{K_s\pi^0}$ by using unbinned maximum likelihood fit as explained in last Chapter. The number of $B^0 \to K_s\pi^0$ candidates is 825, the W/ vertex event in HLR is 93, W/ vertex event in LLR is 148, W/o vertex event in HLR is 216, W/o vertex event in LLR is 368. The number of candidates in each sample are summarized in Table 4.4. The measurement results of $A_{K_s\pi^0}$ and $S_{K_s\pi^0}$ are

$$\begin{cases} A_{K_s\pi^0} = -0.11 \pm 0.20(\mathbf{stat}) \\ S_{K_s\pi^0} = +0.32 \pm 0.61(\mathbf{stat}) \end{cases} \tag{4.33}$$

Fig 4.2 shows the Δt distribution of $q = \pm 1$ events and raw asymmetry plots. We checked the likelihood to confirm if the fitted value has maximum likelihood or not. The results of the checking is shown in Fig 4.3. In checking the $S(A)_{K_S\pi^0}$, we varied $S(A)_{K_S\pi^0}$ and only $A(S)_{K_S\pi^0}$ is fitted. In Fig 4.3, vertical axis

Table 4.4: Event list used for CP-fit in Signal Box

	SVD-I		SVD-II	
	High Likelihood	Low Likelihood	High Likelihood	Low Likelihood
W/ Vertex events	39	75	54	73
W/o Vertex events	139	208	77	160

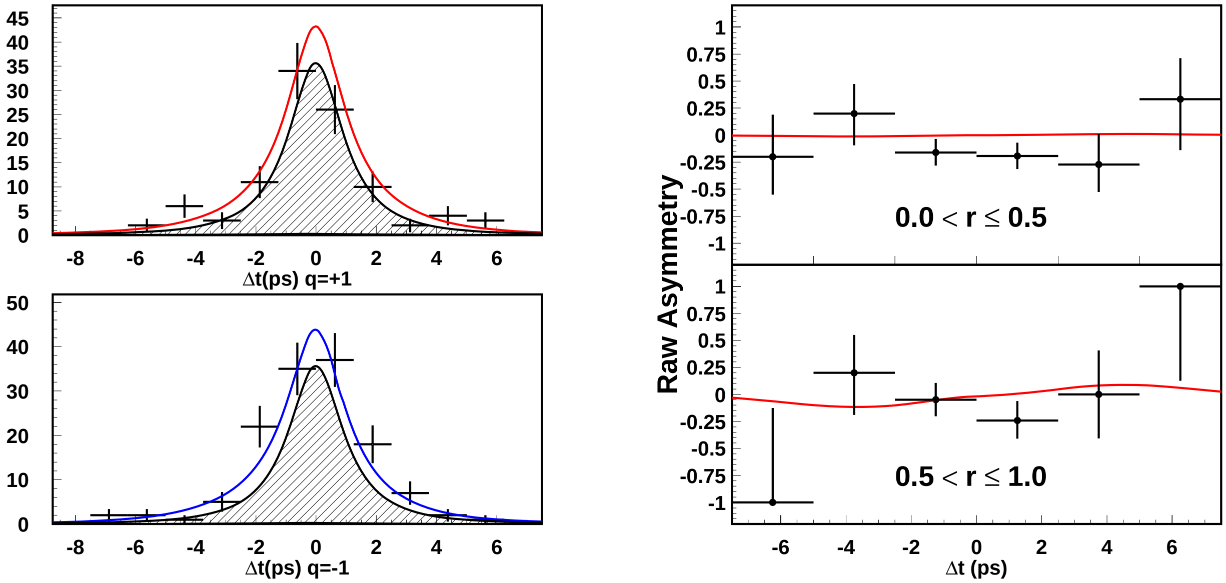

Figure 4.2: Δt distribution of HLR+LLR combined data and Fitted function

In left figure, Upper figure shows the Δt plot of q=1 tagged events, and lower figure shows the Δt plot of q=-1 tagged events, solid line is fitted function and the hatched histogram is background + outlier fitted function. In fight figure, Raw Asymmetry plots of poor(upper) and good(lower) tagged events of HLR+LLR combined data shows the $-2ln(L/L_{max})$, where L is likelihood and the L_{max} is likelihood in $S(A)_{K_S\pi^0} = +0.32(-0.11)$. The similar check is shown in Fig 4.4. The contour shows $-2lnL_{max} + n^2$, $n = 1, 2, 3, 4, ...$ line. We can understand the statistical error is defined when the likelihood is $-2lnL_{max} + 1$. The point is maximum likelihood value, and the circle is physical boundary, $S^2_{K_S\pi^0} + A^2_{K_S\pi^0} = 1$. The outside of outer boundary has negative PDF value and we could not calculated.

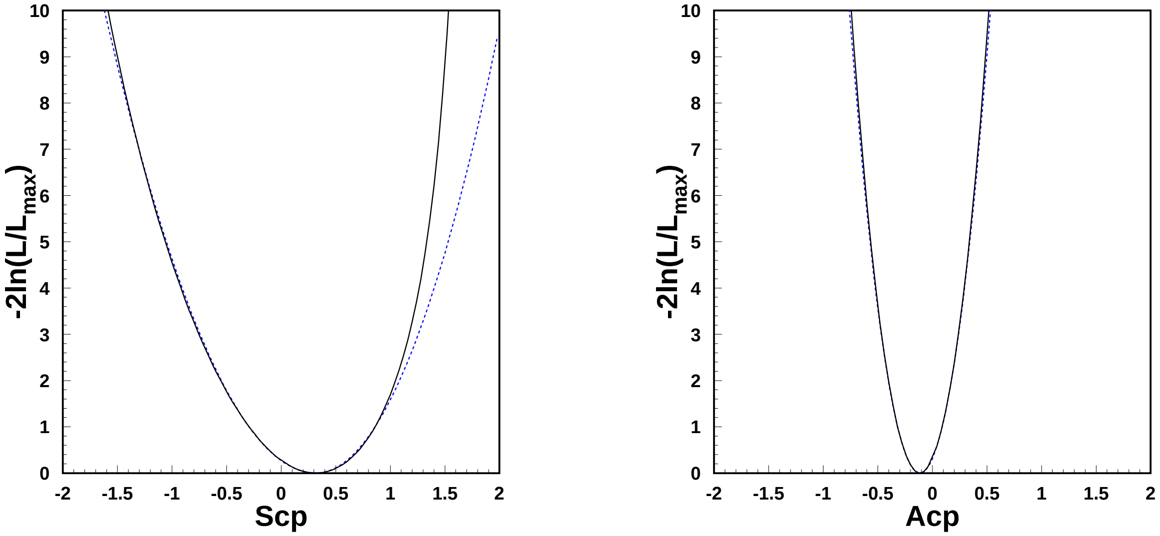

Figure 4.3: The value of -2ln(L/L_{max}) vs $S_{K_S\pi 0}$(Left) and -2ln(L/L_{max}) vs $A_{K_S\pi 0}$(right) The solid line shows -2ln(L/L_{max}), while the dotted line shows $(X_{K_S\pi^0} - X^{mean}_{K_S\pi^0})^2/\sigma^2_{X_{K_S\pi^0}}$, $X = S$ or A, the $X^{mean}_{K_S\pi^0}$ means the fitted value, ($S^{mean}_{K_S\pi^0}$, $A^{mean}_{K_S\pi^0}$)=(0.32, -0.12). And the $\sigma_{X_{K_S\pi^0}}$ means the error of $S_{K_S\pi^0}$ or $A_{K_S\pi^0}$, ($\sigma_{S_{K_S\pi^0}}$, $\sigma_{A_{K_S\pi^0}}$)=(0.61,0.20).

We also measured the $A_{K_s\pi^0}$, $S_{K_s\pi^0}$ used only SVD-I data and SVD-II data, respectively. In addition that we measured only one parameter, only $S_{K_s\pi^0}$ is free parameter and $A_{K_s\pi^0}$ is fixed to '0'. These results are summarized in Table 4.5, where errors are the statistical error. The results of SVD-I and SVD-II are consistent.

Table 4.5: SVD-I and SVD-II cp-fit results or one parameter fit

	$A_{K_s\pi^0}$	$S_{K_s\pi^0}$	$S_{K_s\pi^0}$ (1 parameter fit)
SVD-I	-0.12±0.27	+0.16±1.00	+0.23±0.97
SVD-II	-0.12±0.31	+0.43±0.81	+0.45±0.81
SVD-I+II	-0.12±0.20	+0.32±0.61	+0.35±0.61

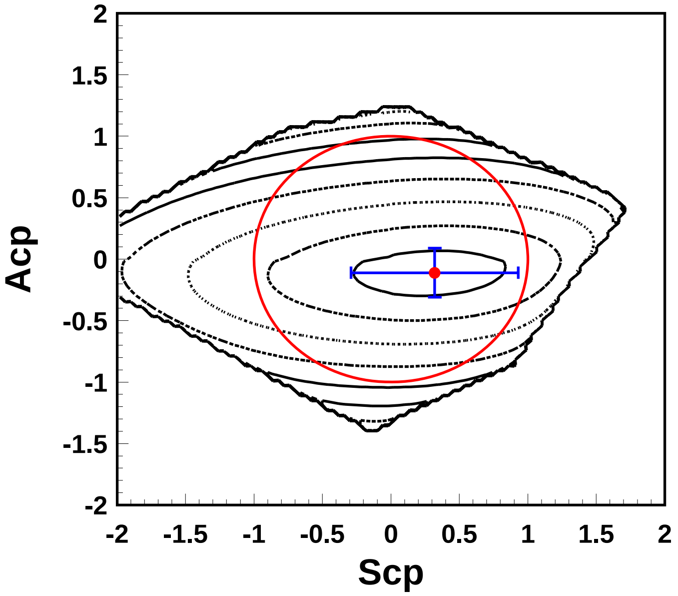

Figure 4.4: The contour of -2ln(L/L_{max}) in $S_{K_S\pi0}$=S_{cp}(horizontal) and $A_{K_S\pi0}$=A_{cp}(vertical) plane The point is a fitting result and the error bar is statistical error, and contour are $1, 2^2, 3^2, ...$ from the most probably point, the circle is physical boundary

Chapter 5

Validity Check and Systematic Uncertainties

In this Chapter, we describe the validuty check with Real data and Monte Carlo, and calculate the systematic error. Finally, we summarize the final result of $A_{K_s\pi^0}$ and $S_{K_s\pi^0}$ including systematic error.

5.1 Validation Check

In this section, we perform Monte Carlo pseudo-experiment with various value in order to studies validity of our result. Each Monte Carlo pseudo-experiment contains same events as real data which is generated based on the PDF which we obtained from real data. We check the linearity of input value, $A_{K_s\pi^0}$ or $S_{K_s\pi^0}$, and output value, the expected error of $A_{K_s\pi^0}$ and $S_{K_s\pi^0}$. We check the B^0 lifetime using the $K_s\pi^0$ real data. And we checked the null asymmetry using in $B^0 \to K_s\pi^+$.

5.1.1 Monte Carlo pseudo-experiment

We check if our CP-fitting procedure is reasonable or not with Monte Carlo pseudo-experiment. Input value is same as measurement results ($A_{K_s\pi^0}$ = -0.11 $S_{K_s\pi^0}$ = +0.32). We generated 30,000 sets of Monte Carlo pseudo-experiments, 1 set has same events as real data. Fig 5.1 shows the distribution of fitting results of $A_{K_s\pi^0}$ and $S_{K_s\pi^0}$, we fit this distribution by single Gaussian. The mean of fitting results are $A_{K_s\pi^0}$ = -0.099. and $S_{K_s\pi^0}$ = +0.30. Fig 5.2 shows the distribution of error of fitting parameters. The mean of these distribution must be error of $A_{K_s\pi^0}$ and $S_{K_s\pi^0}$. We do not find any important deviation from experimental results. The mean value and expected error are summarized in Table 5.1. Fig 5.3 shows the pull distribution of $A_{K_s\pi^0}$ and $S_{K_s\pi^0}$, which is defined as $(X_{fit} - X_{input})/(Error\ of\ fit)$, where X_{fit} is fit result and X_{input} is input value, '$Error\ of\ fit$' is error of fitting result. We fit this distribution using single Gaussian. The mean of pull distribution is almost '0', and the σ of this Gaussian is almost '1'. The last check is linearity check by Monte Carlo pseudo-experiment. We generated 30,000 sets with various value of $A_{K_s\pi^0}$(0.0, 0.2, 0.4, 0.6, 0.8, 1.0), and $S_{K_s\pi^0}$(0.0, 0.2, 0.4, 0.6, 0.8, 1.0). Fig 5.4 shows the linearity plots between input value and output(fitting results) of $A_{K_s\pi^0}$ and $S_{K_s\pi^0}$, we can see the good linearity between input and output in $A_{K_s\pi^0}$ and $S_{K_s\pi^0}$. We also checked the $S_{K_s\pi^0}$ input-output linearity by full detector simulation used GEANT3, and the results are shown in Fig 5.5. From these result, we can see there is no bias in CP-fit procedure.

5.1.2 Lifetime Check using $K_s\pi^0$ Real Data

We checked the B^0 lifetime with $B^0 \to K_s\pi^0$. In CP-fit, the lifetime value is fixed in PDG value, but the lifetime value must be checked for verification of vertex resolution. The lifetime measurement is done with 241 events which is W/ Vertex events. In this fit, the free parameter is only lifetime of B^0, and we used

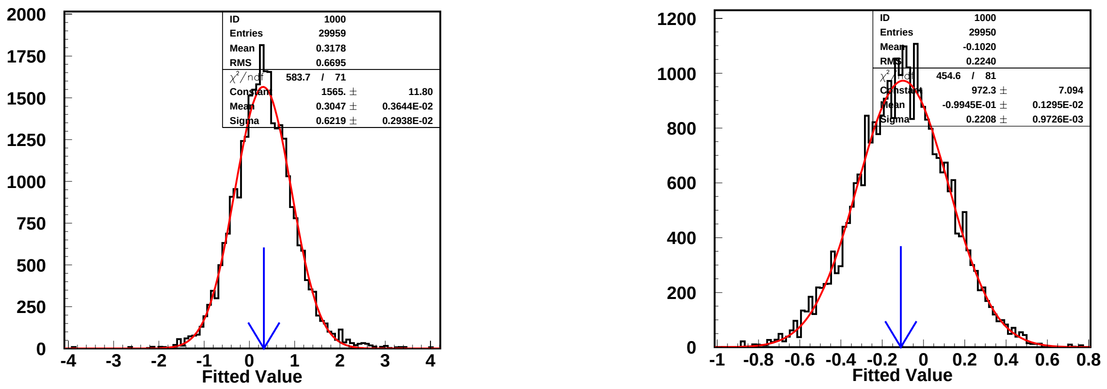

Figure 5.1: Distribution of output value of $S_{K_S\pi^0}$(left) and $A_{K_S\pi^0}$(right) of MC pseudo-experiment

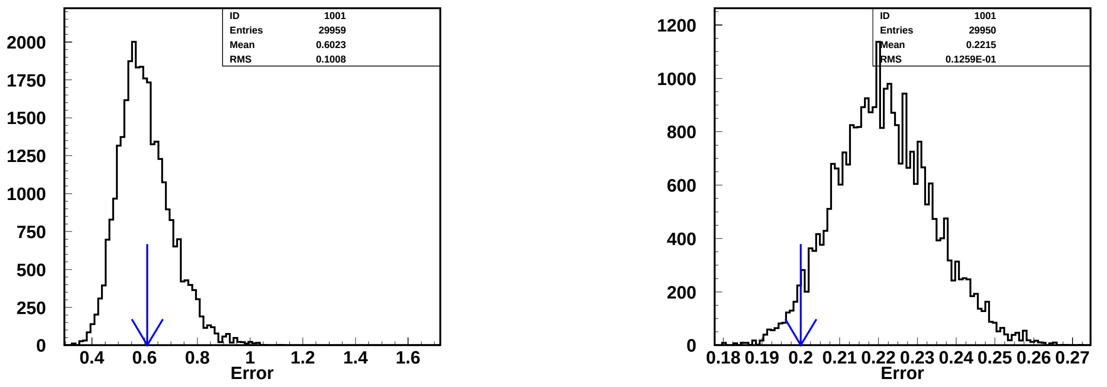

Figure 5.2: Error Distribution of $S_{K_S\pi^0}$(left) and $A_{K_S\pi^0}$(right) of MC pseudo-experiment

Table 5.1: Results of CP-fit by Monte Carlo pseudo-experiment

Monte Carlo pseudo-experiment				
CP-asymmetry Parameter	Input Value	Output Value	MINOS Error	pull
$A_{K_s\pi^0}$	-0.11	-0.0995±0.20	0.2215	0.9878±0.004
$S_{K_s\pi^0}$	+0.32	+0.3047±0.62	0.6023	0.9952±0.004

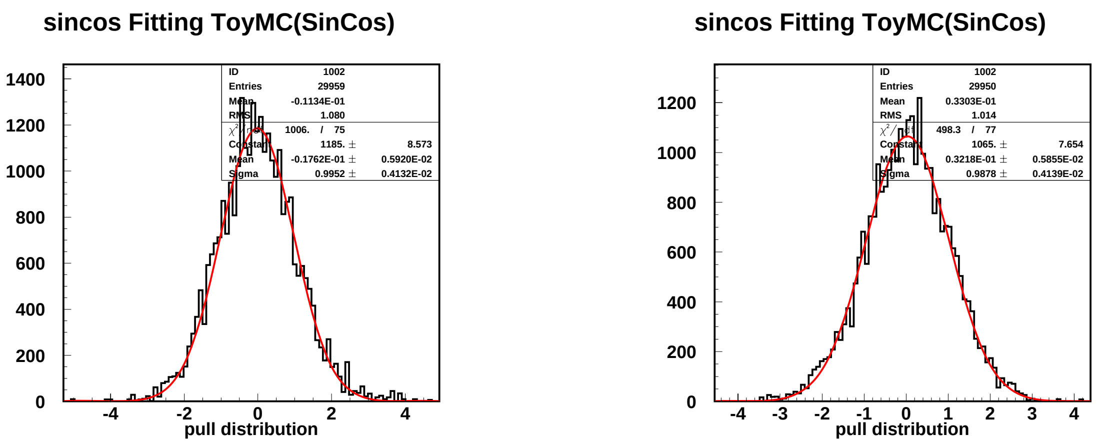

Figure 5.3: Pull Distribution of $S_{K_S\pi^0}$(left) and $A_{K_S\pi^0}$(right) of MC pseudo-experiment

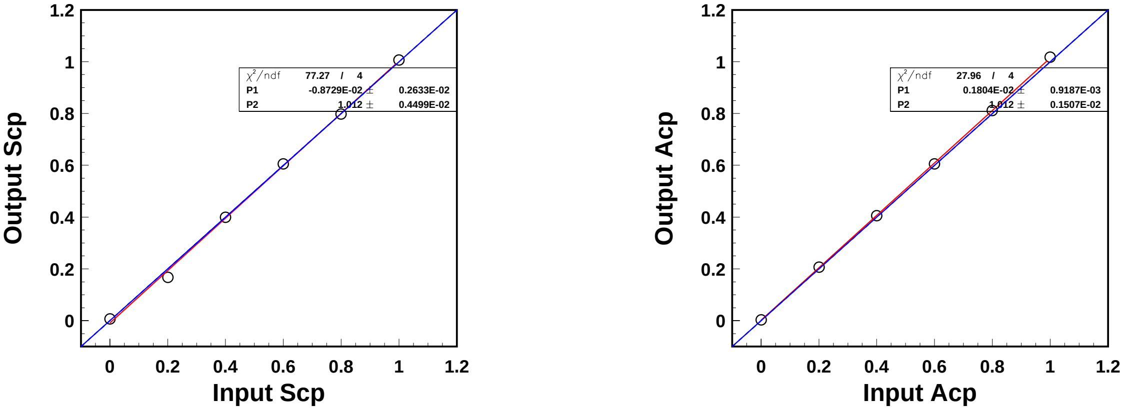

Figure 5.4: Plots of input $S_{K_S\pi0}$ vs mean of output $S_{K_S\pi0}$ (left), and input $A_{K_S\pi0}$ vs mean of output $A_{K_S\pi0}$ (right) of MC pseudo-experiment, the line is input=output line

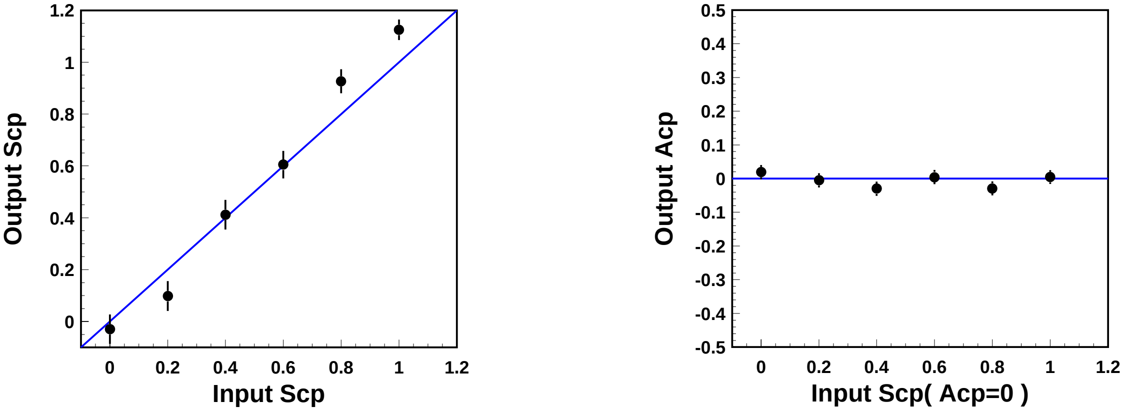

Figure 5.5: Plots of input $S_{K_S\pi0}$ vs mean of output $S_{K_S\pi0}$ (left), and input $A_{K_S\pi0} = 0$ vs mean of output $A_{K_S\pi0}$ (right) of Geant Belle full MC simulation, the line is input=output line

same resolution function as CP-fit. The result of lifetime measurement is,

$$\tau_{B^0} = 1.76 \pm 0.32(\mathbf{ps}) \tag{5.1}$$

The result is consistent with PDG value, $\tau_{B^0} = 1.536 \pm 0.014$(ps)[24], within error. Fig 5.6 shows the fit results of proper time-difference distribution.

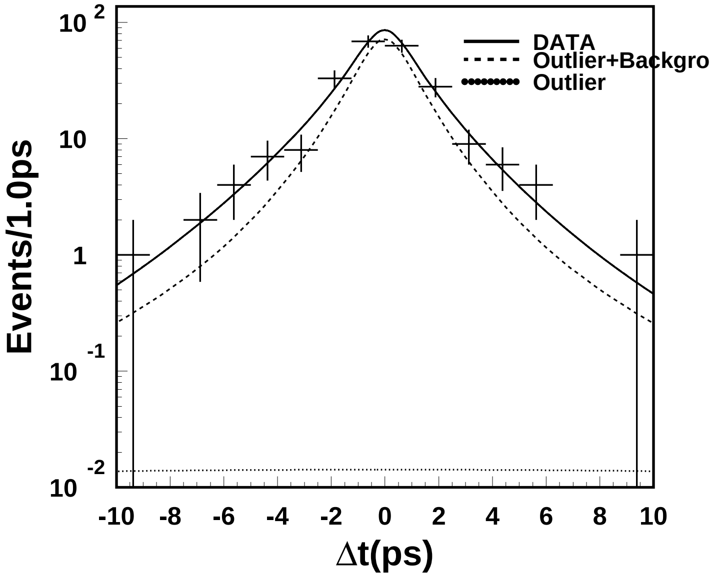

Figure 5.6: Δt distribution of $K_S\pi^0$ data and Fitted function
The solid line is fitted function and the dashed line is background + outlier fitted function and the dotted histogram is outlier function

5.1.3 Test of CP fit on Control Sample ($B^+ \to K_s\pi^\pm$)

We check the CP-fit with $B^+ \to K_s\pi^\pm$, because $B^+ \to K_s\pi^\pm$ is similar to $K_s\pi^0$ in kinematics, and need $K_s - B$ Vertexing, and zero or null CP-asymmetry is expected. We reconstructed $K_s\pi^\pm$, and obtained the 716 $B^\pm$ candidates. We applied the same CP-fitting procedure which is used for $K_s\pi^0$ analysis and we obtained $A_{K_s\pi^\pm}$ and $S_{K_s\pi^\pm}$ as follows,

$$\begin{cases} A_{K_s\pi^\pm} = +0.15 \pm 0.13(stat) \\ S_{K_s\pi^\pm} = +0.19 \pm 0.27(stat) \end{cases} \tag{5.2}$$

This result is consistent with null asymmetry, the raw asymmetry plots of $K_s\pi^\pm$ using the good tagging events are shown in Fig 5.8 We checked also the lifetime of $B^\pm$, and we obtain $\tau_{B^\pm}$ =1.86±0.19(ps) which is consistent with PDF value, PDG vaule of $B^\pm$ is $\tau_{B^\pm}$ =1.671±0.018(ps)[24]. From these results, we can conclude there is no problem in checking the control sample.

5.2 Systematic Uncertainties

We consider the following sources contributing to systematic errors for $A_{K_s\pi^0}$ and $S_{K_s\pi^0}$. We used K_s real data and $B^0 \to J/\phi K_s$ as control sample, and Monte Carlo pseudo-experiments to estimate the systematic errors. The results are summarized in Table 5.5

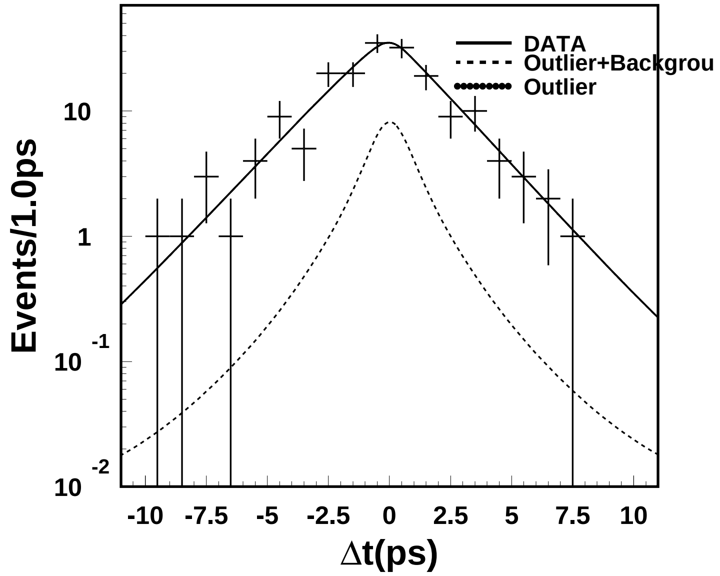

Figure 5.7: Δt distribution of $K_S\pi^{\pm}$ data and Fitted function
The solid line is fitted function and the broken histogram is background + outlier fitted function, the dotted histogram is outlier function

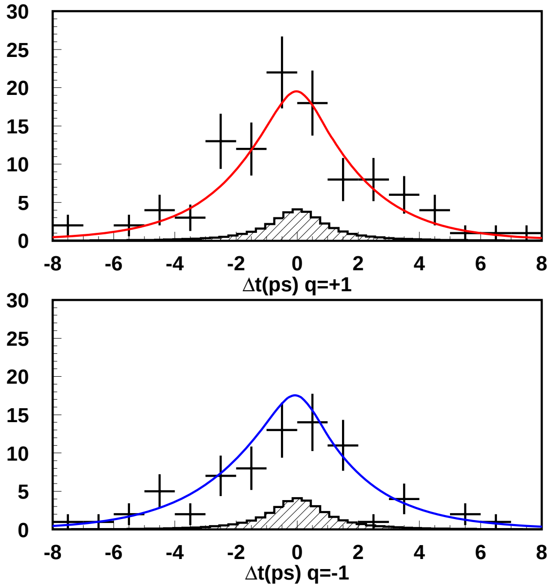

Figure 5.8: Δt distribution of data and Fitted function
Upper figure shows the Δt plot of q=1 tagged events, and lower figure shows the Δt plot of q=-1 tagged events, solid line is fitted function and the hatched histogram is background + outlier fitted function

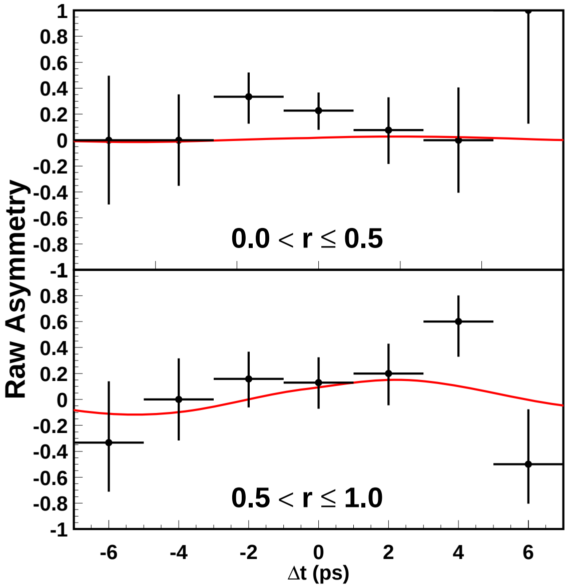

Figure 5.9: Raw Asymmetry plots of poor(upper) and good(lower) tagged events

5.2.1 Incorrect flavor assignment probability

We considered the systematic error due to uncertainties in 6 incorrect flavor assignment probabilities (w_{tag} in 6 r-bin) and difference incorrect flavor assignment probabilities (Δw in 6 r-bin). We estimated the systematic uncertainties by varying the average value of incorrect flavor assignment probabilities by their error. We used $K_s\pi^0$ of real data to estimate this systematic error.

5.2.2 Physics Parameters (τ_B, Δm_d, m_B, τ'_B)

The following physics parameters are fixed to the world average values or determined by MC. The B meson lifetime , τ_B, the $B^0-\bar{B}^0$ mixing parameter, Δm_d, B^0 mass, m_{B^0}, and the effective rare B lifetime, τ'_B,

$$\tau_{B_0} = (1.536 \pm 0.014) \times 10^{-12}\mathbf{s}[24] \tag{5.3}$$

$$\Delta m_d = (0.502 \pm 0.007) \times 10^{-12}\mathbf{s}^{-1}[24] \tag{5.4}$$

$$m_{B^0} = 5.2794 \pm 0.0005\mathbf{GeV/c^2}[24] \tag{5.5}$$

$$\tau'_B = (1.515 \pm 0.068) \times 10^{-12}\mathbf{s}. \tag{5.6}$$

We estimate the systematic error by repeating the fit by varying these parameters by their errors. We used $K_s\pi^0$ to estimate this systematic error.

5.2.3 Resolution function

We estimate the contribution due to the uncertainly in the resolution function by varying the parameters by 1σ in DATA, and 2σ in MC. To estimate this systematic error we used $J/\phi K_s$ real data.

5.2.4 Fit Bias

The systematic error from signal Monte Carlo events includes statistical error of Monte Carlo events and the error from SVD alignment, and the difference from input values and the mean fitted value $A_{K_s\pi^0}$ and $S_{K_s\pi^0}$. We used Signal MC generated by GEANT3, and we take the statistical error as systematic error.

5.2.5 Vertexing

1 : CP and Tag-side vertex reconstruction

We require $\xi < 100$ for CP and tag side as the default. We estimate the systematic error by repeating the fit for $\xi < 50$ and $\xi < 200$ for CP-side by $K_s\pi^0$ real data and Tag-side by $J/\psi K_s$ real data.

2 : Charge asymmetry of charged tracks

According to the result from analysis of cosmic-ray data and 2γ data, we do not observe significant charge asymmetry in z position within error. We estimated the systematic error by repeating the fit varying by $\pm 3\mu$m for positive-charged tracks and negative-charged tracks individually. We used $J/\psi K_s$ real data to estimate this error.

3 : Track selection for tagging side vertexing

We estimated the systematic error by repeating the fit with varying
-$|dr|$ by 0.05 ± 0.01cm,
-error of dz by 0.05 ± 0.01cm.
We used $J/\psi K_s$ real data to estimate this error.

4 : Flight length of B mesons

The IP constrained fit might change the uncertainty of the B-meson decay point due to the flight length of the B meson in the $r-\phi$ plane. This uncertainty is estimated to be about 20 μm assuming a Gaussian function although it is actually an exponential function. We estimated the systematic error by repeating the fit by varying it $+20\mu$m and -10μm. We used $J/\psi K_s$ real data to estimate this error.

5 : Δt cut

We require the $|\Delta t| < 70$(ps) in CP-fit. We estimate the systematic error by repeating the fit for $|\Delta t| < 40$(ps) and $|\Delta t| < 100$(ps) for $K_s\pi^0$ real data, and we take large one as systematic error.

6 : W/o Scale Error

Scale error is the correction function of charged track parameters(helix parameter), The incorrect error of track parameter gives the incorrect Δt measurement error through vertex reconstruction, and every events is weighed by Δt measurement error. To avoid incorrect weigh assignment to events, track parameters are corrected by scale error function. To estimate systematic error of scale error, we measure the CP-asymmetry parameters without correction by scale error function. We used $J/\psi K_s$ real data to estimate this error.

7 : SVD Mis-Alignment Effect

Systematic error due to imperfect SVD alignment are determined from MC samples that have artificial mis-alignment effects.

5.2.6 Tag side interference

In time-dependent CP-asymmetry measurement, the flavor of B is tagged using the opposite side of B to CP-eigenstate. The flavor is tagged by charge of Kaon, pion from $b \to c\bar{u}d$ decay, and lepton from semi-lepton decay. The tag side interference is effect which gives deviations from standard time evolution assumed in CP-asymmetry measurement by interference between Cabbibo-Kobayashi-Maskawa(CKM) favored $b \to c\bar{u}d$ and doubly-CKM-suppressed $\bar{b} \to \bar{u}c\bar{d}$ amplitudes of final states used for B-flavor tagging[106]. To estimate the uncertainty by this effect, we generate Monte Carlo pseudo data sets with tag side interference for the input values without background.

5.2.7 Background shape

The parameters of $P_{qq}(\Delta t)$ are varied by their errors and fits are repeated.

5.2.8 Background fraction

We estimated the systematic error due to background fraction by varying M_{bc} and ΔE signal shape and background shape parameters by 2σ for signal and 1σ for background shape. In addition, the error due to signal fraction is estimated by varying signal fraction and rare-B background fraction of each r-bin by 1σ.

5.2.9 Signal shape Model

We checked dependence on the signal shape model dependence. In this analysis, we used the signal shape with Single Gaussian(M_{bc})×Crystal Ball function(ΔE), we called default shape, while we can determine the signal shape by Smoothed Histogram as rare B background shape. We checked the difference of CP-fit results from default shape to Smoothed Histogram shape, and take a systematic error as difference from CP-fit result with default shape to that with smoothed histogram. Fig 5.10 shows the Smoothed Histogram shape which is obtained by Signal MC. The signal yield which obtained by smoothed histogram is summarized in Table 5.2

Table 5.2: Signal Yield obtained by smoothed Histogram

Sample	Signal Yield	Rare B
W/ vertex (HLR)	60.6± 9.1	0.5±1.3
W/o vertex (HLR)	110.2±13.4	9.8±2.1
W/ vertex (LLR)	12.1± 8.9	1.9±2.1
W/o vertex (LLR)	65.7±15.3	3.8±3.1

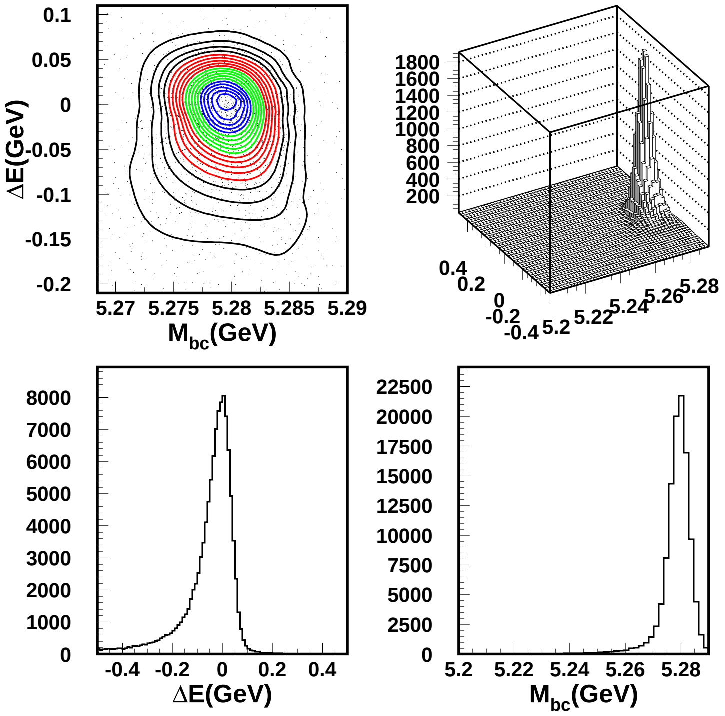

Figure 5.10: Plots of Smoothed Histogram of $K_S\pi 0$ Signal MC

5.2.10 CP-asymmetry in Rare B Background CP-asymmetry

In CP-fit, we fixed the asymmetry parameters of rare B background are zero, but we must consider the asymmetry effect of these background. We make pseudo-experiment Monte Carlo where rare B asymmetry is varied from +1 to −1 in A_{rare} and S_{rare}. The results are summarized in Table 5.3. We defined the systematic error as maximum deviation.

Table 5.3: Results of Rare B asymmetry Effect by MC pseudo-experiment

S_{rare}	A_{rare}	$\Delta S_{K_S\pi 0}$	$\Delta A_{K_S\pi 0}$
+1	0	+0.026	+0.002
-1	0	-0.059	-0.005
0	+1	+0.058	+0.053
0	-1	-0.022	-0.040

5.3 The final results

For each source, we take the larger magnitude of the systematic error among the positive and negative systematic errors. Total systematic errors for $A_{K_s\pi^0}$ and $S_{K_s\pi^0}$ are obtained by adding these contributions from all the systematic errors in quadrature as shown in Table 5.5. Thus we obtained the final result as follows,

$$A_{K_s\pi^0} = -0.11 \pm 0.20(\mathbf{stat}) \pm 0.09(\mathbf{syst}) \quad (5.7)$$

$$S_{K_s\pi^0} = +0.32 \pm 0.61(\mathbf{stat}) \pm 0.13(\mathbf{syst}) \quad (5.8)$$

Table 5.4: Summary of systematic error of Vertex information

	$A_{K_s\pi^0}$	$S_{K_s\pi^0}$
Source Vertex Category	syst. errors	syst. errors
CP and Tag-side vertex reconstruction	<0.01	<0.01
Charge asymmetry of charged track	+0.02 -0.01	<0.01
Track selection for tagging side	<0.01	<0.01
Flight leght of B	<0.01	<0.01
Δt cut	<0.01	<0.01
W/o Scale error	+0 -0.01	+0 -0.02
SVD Mis-Alignment	+0.03 -0.03	+0.01 -0.01
Total	+0.04/-0.03	+0.01/-0.02

Table 5.5: Summary of total systemtic error

	$A_{K_s\pi^0}$		$S_{K_s\pi^0}$	
Source	syst. errors	sys. errors for conf.interval	syst. errors	syst. errors for conf.interval
wrong tag fraction	+0.01 -0.01	±0.01	+0.01 -0.01	±0.01
Physics parameters	<0.01 <0.01	<0.01	+0.02 -0.02	±0.02
Resolution function	<0.01 <0.01	<0.01	+0.05 -0.05	±0.05
Background shape	<0.01 <0.01	<0.01	+0.05 -0.05	±0.05
Rare B Background Asymmetry	+0.05 -0.04	±0.05	+0.03 -0.06	±0.06
Background fraction	+0.04 -0.03	±0.04	+0.08 -0.07	±0.08
Signal Shape Model	+0 -0.01	±0.01	+0.03 -0	±0.03
Fit bias	+0.01 -0.01	±0.01	+0.02 -0.02	±0.02
Vertexing	+0.04 -0.03	±0.04	+0.01 -0.02	±0.02
Tag side interference	+0.05 -0.05	±0.05	<0.01 <0.01	<0.01
Total		±0.09		±0.13

Chapter 6

Discussions

In Chapter 4, we described the measurement of $S_{K_S\pi^0}$ and $A_{K_S\pi^0}$ in $B^0 \to K_S\pi^0$ with $253fb^{-1}$ data sample, and we obtained,

$$\left\{ \begin{array}{l} S_{K_S\pi^0} = +0.32 \ \pm 0.61(\mathbf{stat}) \ \pm 0.13(\mathbf{syst}) \\ A_{K_S\pi^0} = -0.11 \ \pm 0.20(\mathbf{stat}) \ \pm 0.09(\mathbf{syst}) \end{array} \right. \tag{6.1}$$

In this Chapter, we make discussion on this results, statistical error and systematic error. At first, we compare the result of Belle with that of BaBar which was reported in ICHEP04 summer conference. The result of CP-asymmetry in $B^0 \to K_S\pi^0$ presented by BaBar used $205fb^{-1}$ data[107] is,

$$\left\{ \begin{array}{l} S_{K_S\pi^0}(\mathbf{BaBar}) = +0.35^{+0.30}_{-0.33}(\mathbf{stat}) \ \pm 0.04(\mathbf{syst}) \\ A_{K_S\pi^0}(\mathbf{BaBar}) = +0.06 \ \pm 0.18(\mathbf{stat}) \ \pm 0.06(\mathbf{syst}). \end{array} \right. \tag{6.2}$$

the results is consistent with our results within error. The average of Belle and BaBar experiment is $S_{K_S\pi^0} = 0.34^{+0.34}_{-0.35}(\mathrm{stat})$, $A_{K_S\pi^0} = -0.03 \pm 0.13(\mathrm{stat})$, the deviation from Standard Model expectation is 1.1σ in $S_{K_S\pi^0}$. The dominant systematic error of our results, $S_{K_S\pi^0}$ and $A_{K_S\pi^0}$ are signal fraction and rare B background asymmetry effect and resolution function, Δt background shape. The main reason of these large systematic error are low statistical and low S/N ratio and worse vertex resolution. To reduce systematic error of signal fraction, rare B background asymmetry effect and Δt background shape, we need more statistics and use only high S/N ratio sample. For example we can use only high likelihood region. To reduce the systematic error from vertex resolution, we need futher study and understand more about the $K_S - B$ vertexing method and resolution, the correlation with resolution and K_S vertex position and hit pattern of daughter tracks of K_S in SVD and so on.

As described in Chapter 1, the measured $S_{K_S\pi^0}$ is the effective $\sin2\phi_1$, which is defined as $\sin2\phi_1' \equiv \sin2(\phi_1 + \phi')$. The ϕ_1 is one of the angle of Unitary Triangle is shown in Fig 1.6, and the world average of $\sin2\phi_1$ is 0.726±0.037[43]. The ϕ' is the phase of new physics effect and the Standard Model expectation is '0'. The experimental result is consistent with Standard Model expectation within 1σ, however since the statistical error of $S_{K_S\pi^0}$ is so large, that we need more data to obtain any conclusion. The direct CP parameter, $A_{K_S\pi^0}$, also consists with '0' with in 1σ. We estimated the expected statistical error of $S_{K_S\pi^0}$ and $A_{K_S\pi^0}$ as function of integrated luminosity obtained in future. We generated Monte Carlo pseudo experiment with $S_{K_S\pi^0} = +0.32$ and $A_{K_S\pi^0} = -0.11$. The results is shown in Fig 6.1. The points are for $253fb^{-1}$, $300fb^{-1}$, $400fb^{-1}$, $500fb^{-1}$ and $1000fb^{-1}$. The line is simple expectation as function of luminosity, which is $\propto \sqrt{Luminosity}$. In addition to that we estimated statistical significant for new physics with large statistics. We assume the difference of $\sin2\phi_1$ from Standard Model from '0' to '1.0'. The significant is shown in Fig 6.2. In the future, we will accumulate the $400fb^{-1}$ by end of 2005 summer and $500fb^{-1}$ by end of 2006 summer. In addition, the next step of Belle experiment is high luminosity *B*-factory experiment, proposed as Super-KEKB[108]. With Super-KEKB, the peak luminosity target is $\sim 5 \times 10^{35}(\mathrm{cm}^{-2}\mathrm{s}^{-1})$ and we can accumulate the $10ab^{-1}$ until 2014. The verification of $K_S\pi^0$ CP-Violation will be concluded with Super-KEKB experiment. From all discussion above, Super-KEKB experiment is very necessary to conclude about CP-Violation of $K_S\pi^0$.

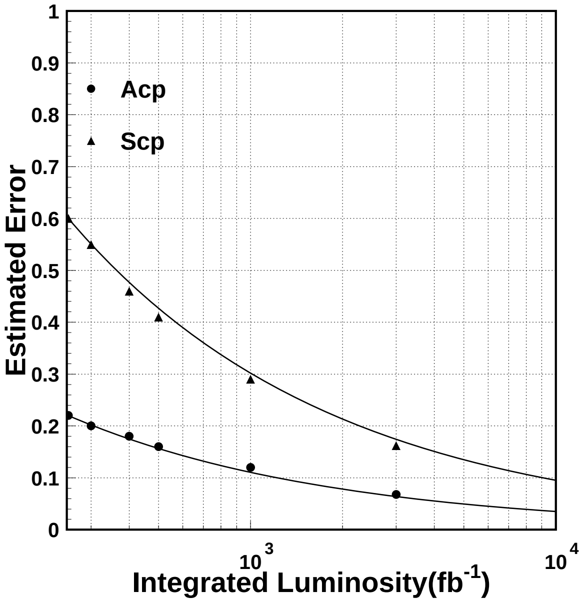

Figure 6.1: The expected statistical error of $S_{K_S\pi^0}$ and $A_{K_S\pi^0}$ as function of integrated luminosity The points are MINOS error obtained by Monte Carlo pseudo experiment, while the line shows the estimated statistical error obtained by $a/\sqrt{Luminosity}$, a is calculated from $a = 0.60 \times\sqrt{253}$ in $S_{K_S\pi^0}$ case and $a = 0.20 \times\sqrt{253}$ in $A_{K_S\pi^0}$ case.

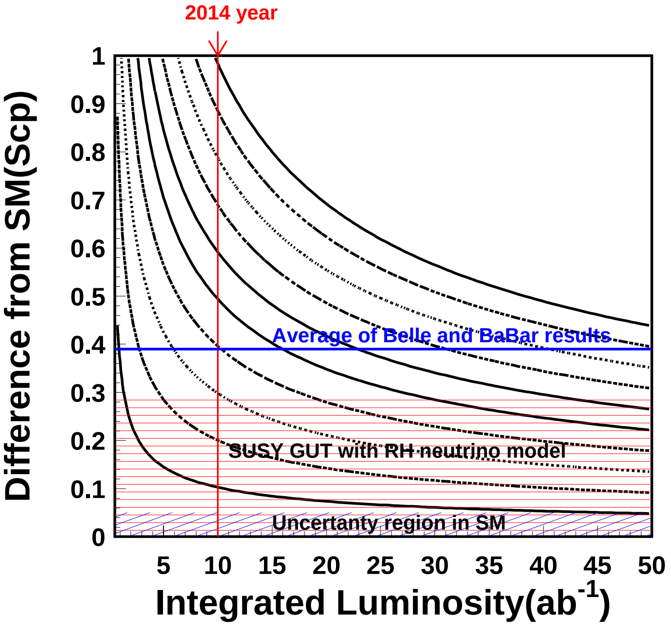

Figure 6.2: Statistical significant for New phase in sin2ϕ_1 as function of statistics. The most left-lower line is significance=1, and the most right-upper line is significance=10. We shows the each significance line as 1,2,3,4,,,10.

Chapter 7

Conclusion

Since $B^0 \to K_S\pi^0$ is $b \to s$ penguin dominant decay mode, this mode is sensitive for new physics search in loop diagram. The tree-level contribution is much smaller than penguin contribution. It is approximately $O(0.1)$. There are some model of new physics, and the one of the most popular model is SUSY-GUT model. According to this model, we can expect the large deviation of $\sin 2\phi_1$ from Standard Model expectation. We accumulated the $253 fb^{-1}$ data sample, corresponding to 275×10^6 $B\bar{B}$ pairs at the KEKB factory. We reconstructed 247 candidates with the flavor information. We measured the CP-violation parameters, $S_{K_S\pi^0}$ and $A_{K_S\pi^0}$ by unbinned maximum likelihood fit. The fitted results are,

$$\begin{cases} S_{K_S\pi^0} = +0.32 \ \pm 0.61(\mathbf{stat}) \ \pm 0.13(\mathbf{syst}) \\ A_{K_S\pi^0} = -0.11 \ \pm 0.20(\mathbf{stat}) \ \pm 0.09(\mathbf{syst}) \end{cases} \tag{7.1}$$

Fig 7.1 shows the Belle, BaBar and their average value. These results are first measurement of CP-asymmetries measurement in Belle experiment. In this analysis, we used some new analysis methods. One is vertex reconstruction with only K_S particle and interaction point constrained. Since K_S has long lifetime, $\tau c \sim 2.68$cm, the vertex resolution is different from that of vertexing by J/ψ. Because of that a part of resolution function is modified. The second is measurement of direct CP-violation parameter, $A_{K_S\pi^0}$, in basically we used proper time-difference CP-violation, but we can measure the $A_{K_S\pi^0}$ only from flavor information, and we measured $A_{K_S\pi^0}$ from time-difference and time-integrated information. With second method, we could reduce the statistical error of $A_{K_S\pi^0}$. The results are consistent with Standard Model expectation within 1σ, but the statistical error are still large. We need more statistics and must wait for Super-B factory experiment to conclude that CP-violation of $K_S\pi^0$ resides within or beyond the Standard Model expectation.

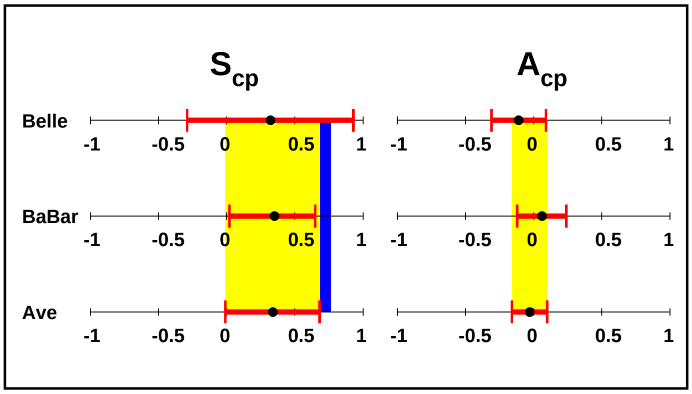

Figure 7.1: $K_S\pi^0$ results of Belle, BaBar and their average value. The light belt shows the average value $\pm$ 1σ. The deepen belt in S_{cp} is world average of $\sin 2\phi_1$ using $B^0 \to J/\psi K_S$

Appendix A

Track Parametrization

In this Chaper, we describe the track parametrization. Track parameter consists of helix parameter which there are five parameters, and pivotal point(pivot). The helix parameter is defined as $h = (d_\rho, \phi_0, \kappa, d_z, \mathbf{tan}\lambda)$. The pivot is defined as (x_0, y_0, z_0). The charged particle in a uniform magnetic field is represented by a helical trajectory. The position along the helix is given by

$$\begin{cases} x = x_0 + d_\rho \mathbf{cos}\phi_0 + \frac{\alpha}{\kappa}\{\mathbf{cos}\phi_0 - \mathbf{cos}(\phi_0 + \phi)\} \\ y = y_0 + d_\rho \mathbf{sin}\phi_0 + \frac{\alpha}{\kappa}\{\mathbf{sin}\phi_0 - \mathbf{sin}(\phi_0 + \phi)\} \\ z = z_0 + d_z - \frac{\alpha}{\kappa}\mathbf{tan}\lambda \cdot \phi \end{cases} \tag{A.1}$$

where α is magnetic-filed-constant, $\alpha = 1/cB = 222.375973(\mathrm{cm}(\mathrm{GeV/c})^{-1})$ at the strenght of magnetic field, *phi* is the tuning angle.
The helix center in x-y plane is

$$x_c = x_0 + \left(d_\rho + \frac{\alpha}{\kappa}\right)\mathbf{cos}\phi_0 \tag{A.2}$$

$$y_c = y_0 + \left(d_\rho + \frac{\alpha}{\kappa}\right)\mathbf{sin}\phi_0, \tag{A.3}$$

and the radius of the circle, ρ, is

$$\rho = \frac{\alpha}{|\kappa|}. \tag{A.4}$$

The transverse momentum, p_t, is

$$p_t = \frac{1}{|\kappa|}, \tag{A.5}$$

And the relation between transverse momentum and $\tan\lambda$ is

$$\mathbf{tan}\lambda = \frac{p_z}{p_t}, \tag{A.6}$$

where p_t is z-component of momentum. We defined the relation between sign of track parameters, (d_ρ, κ, ϕ) and charge of particle as,

$$\textbf{Positive Charged Track} \;\rightarrow\; \kappa > 0 \textbf{ and } d_\rho > 0 \textbf{ and } \phi < 0 \tag{A.7}$$

$$\textbf{Negative Charged Track} \;\rightarrow\; \kappa < 0 \textbf{ and } d_\rho < 0 \textbf{ and } \phi > 0 \tag{A.8}$$

The schematic representation of the helix parametrization for positive and negative charged track in x-y and $\rho\phi$-z plane are shown in Fig A.1, A.2

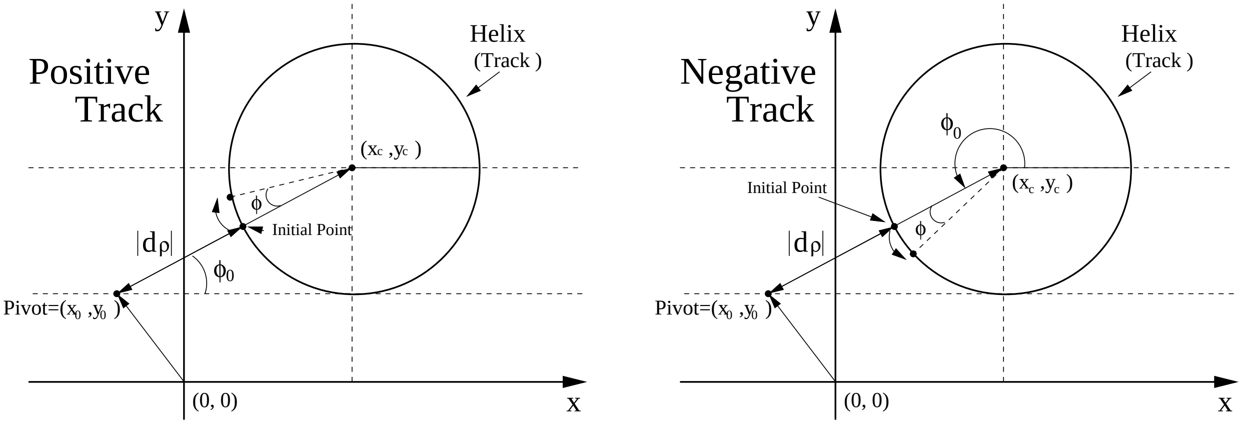

Figure A.1: Schematic representation of the helix parametrization for positive and negative charged track in x-y

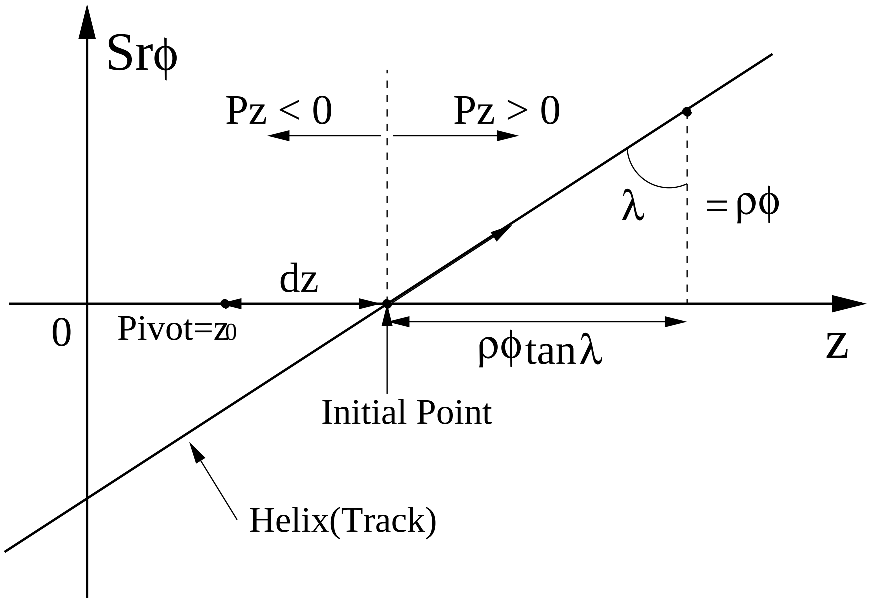

Figure A.2: Schematic representation of the helix parametrization in $\rho\phi$-z plane

Appendix B

Likelihood Ratio Plots and F.o.M in each r-region

In this chapter we show the Likelihood Ratio (LR) plot and F.o.M depend on LR in r-region. To determine the threshold of Low Likelihood sample, we divide 6 r-region, r is the wrong tagging dilution factor of event-by-event. The FigB.1, B.2, B.3, B.4 shows the F.o.M depends on *LR* in each r region. In LR plots, the white histogram shows the LR from signal MC, while the hatched histogram shows the LR from sideband data. We determined the same threshold, $LR > 0.4$ in all r region.

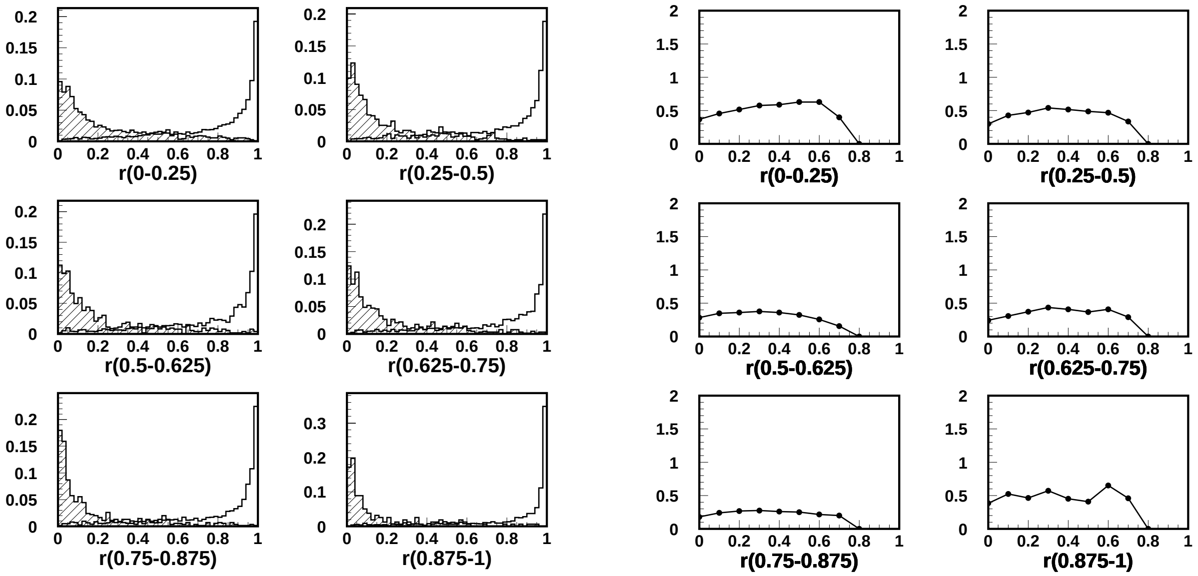

Figure B.1: Likelihood Ratio distribution in each r-bin region with W/ vertex sample of SVD-I, White histogram is Signal MC and Hatched histogram is sideband data. Figure of merits in each r-bin region with LR<0.78 W/ vertex sample of SVD-I

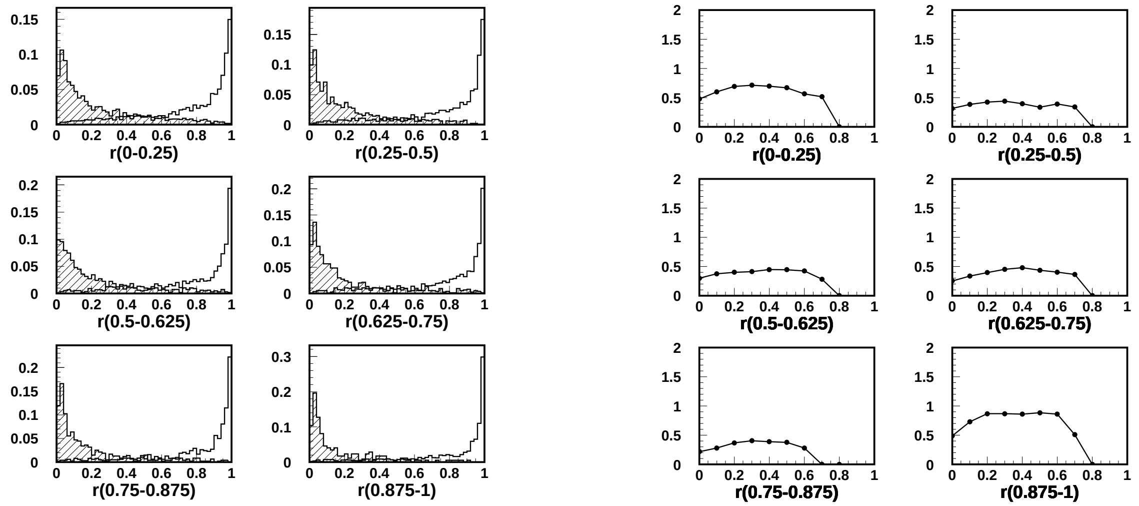

Figure B.2: Likelihood Ratio distribution in each r-bin region with W/o vertex sample of SVD-I, White histogram is Signal MC and Hatched histogram is sideband data. Figure of merits in each r-bin region with LR<0.74 W/o vertex sample of SVD-I

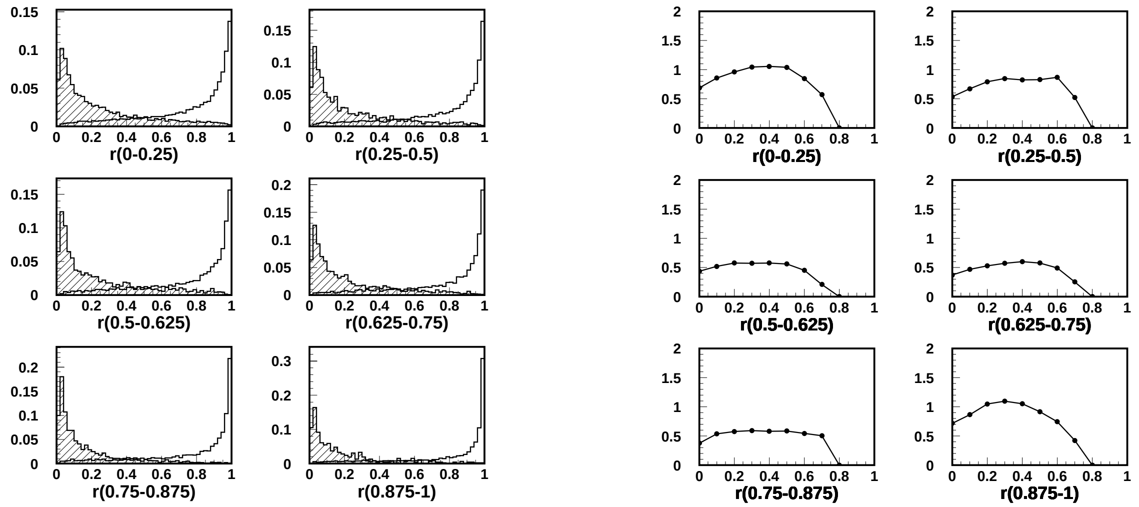

Figure B.3: Likelihood Ratio distribution in each r-bin region with W/ vertex sample of SVD-II, White histogram is Signal MC and Hatched histogram is sideband data. Figure of merits in each r-bin region with LR<0.78 W/ vertex sample of SVD-II

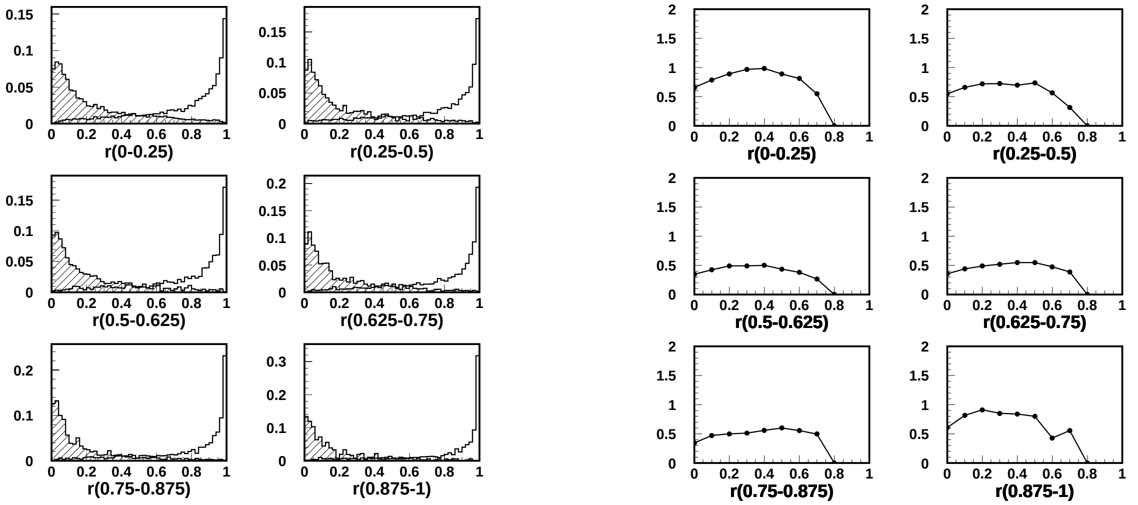

Figure B.4: Likelihood Ratio distribution in each r-bin region with W/o vertex sample of SVD-II, White histogram is Signal MC and Hatched histogram is sideband data. Figure of merits in each r-bin region with LR<0.76 W/o vertex sample of SVD-II

Appendix C

The Detail of Resolution Function

In this Chapter we explain the detail of Resolution Function.

C.1 Detector Resolution

The detector resolution for cp-side and tag-side depend on number of track using vertex reconstruction, and we need distinguish from single track and multi tracks case. The function of detector resolution is based on Gaussian function, the resolution function of multi-track event for cp-side and tag-side are defined as,

$$R_{full}(\Delta t - \Delta' t) = G(\Delta t - \Delta' t; (s^0_{full} + s^1_{full}\xi_{full})\sigma^z_{full}) \tag{C.1}$$

$$R_{asci}(\Delta t - \Delta' t) = G(\Delta t - \Delta' t; (s^0_{asci} + s^1_{asci}\xi_{asci})\sigma^z_{asci}) \tag{C.2}$$

$$G(x;\sigma) = \frac{1}{\sqrt{2\pi}\sigma} exp\left(-\frac{x^2}{2\sigma^2}\right) \tag{C.3}$$

where $s^0_{full,asci}$ and $s^1_{full,asci}$ are scale factor, $\sigma^z_{full,asci}$ are error of decay vertex positions, and ξ is special goodness for vertex reconstruction as Eq 3.11. In SVD-II case, the R_{full} is defined double Gaussian as follows,

$$\begin{aligned} R_{full}(\Delta t - \Delta' t) = (1 - f^{mult}_{tail})G(\Delta t - \Delta' t; (s^0_{full} + s^1_{full}\xi_{full})\sigma^z_{full}) \\ + f^{mult}_{tail} G(\Delta t - \Delta' t; s^{mult}_{tail}\sigma^z_{full}) \end{aligned} \tag{C.4}$$

While the resolution function for single track events is,

$$R_{full}(\Delta t - \Delta' t) = (1 - f_{tail})G(\Delta t - \Delta' t; s_{main}\sigma^z_{full}) + f_{tail}G(\Delta t - \Delta' t; s_{tail}\sigma^z_{full}) \tag{C.5}$$

$$R_{asci}(\Delta t - \Delta' t) = (1 - f_{tail})G(\Delta t - \Delta' t; s_{main}\sigma^z_{asci}) + f_{tail}G(\Delta t - \Delta' t; s_{tail}\sigma^z_{asci}) \tag{C.6}$$

where, $s_{main,tail}$ are global scale factor and these are same value for cp and tag-side. The fitted parameters of detector resolution function are listed in Tabl C.1.

C.2 Non-Primary Track Effect

The third component of resolution function is non-primary track effect, R_{np}, which represent the smearing of decay vertex position of tag-side B due to track that do not originate from the associated B vertex such as charm meson and K_S meson. The R_{np} is defined by two component, the main part is Dirac-function and another part is exponential function as follows,

$$R_{np} = f_\delta \delta^{Dirac}(\Delta t'' - \Delta t''') + (1 - f_\delta)[f_p E_p(\Delta t'' - \Delta t'''; \tau^p_{np}) + (1 - f_p)E_n(\Delta t'' - \Delta t'''; \tau^n_{np}) \tag{C.7}$$

Table C.1: The Parameters of Detector Resolution Function

Parameters	SVD-I	SVD-II
s^0_{full}	$0.970^{+0.142}_{-0.069}$	$0.702^{+0.294}_{-0.262}$
s^1_{full}	$0.086^{+0.117}_{-0.011}$	$0.132^{+0.027}_{-0.052}$
s^0_{asci}	$0.800^{+0.183}_{-0.037}$	$0.698^{+0.493}_{-0.063}$
s^1_{asci}	$0.035^{+0.002}_{-0.006}$	$0.050^{+0.011}_{-0.025}$
f_{tail}	0.0	$0.035^{+0.026}_{-0.005}$
s_{main}	$0.924^{+0.218}_{-0.032}$	$1.106^{+0.365}_{-0.042}$
s_{tail}	—	$10.01^{+2.171}_{-2.841}$
f^{mult}_{tail}	—	$0.095^{+0.191}_{-0.048}$
s^{mult}_{tail}	—	$4.867^{+0.583}_{-1.136}$

$$E_p(x;\tau) = \frac{1}{\tau} exp\left(-\frac{x}{\tau}\right) \quad x > 0 \ ; \ \textbf{otherwise } 0 \tag{C.8}$$

$$E_n(x;\tau) = \frac{1}{\tau} exp\left(+\frac{x}{\tau}\right) \quad x < 0 \ ; \ \textbf{otherwise } 0 \tag{C.9}$$

The $\tau^{p,n}_{np}$ are bilinear with σ_{asc} and ξ_{asci}, and we define this parameter in multi-track and single-track event respectively. The definition of $\tau^{p,n}_{np}$ for multi-track are,

$$\tau^p_{np} = s^3_{asci}[\tau^0_p + \tau^1_p(1 + s^2_{asci}\xi_{asci})\sigma_{asci}/c(\beta\gamma)_\Upsilon] \tag{C.10}$$

$$\tau^n_{np} = s^3_{asci}[\tau^0_n + \tau^1_n(1 + s^2_{asci}\xi_{asci})\sigma_{asci}/c(\beta\gamma)_\Upsilon] \tag{C.11}$$

while the definition of $\tau^{p,n}_{np}$ for single-track are,

$$\left(\tau^p_{np}\right)_{main} = s^3_{asci}[\tau^0_p + \tau^1_p\sigma_{asci}/c(\beta\gamma)_\Upsilon] \tag{C.12}$$

$$\left(\tau^p_{np}\right)_{tail} = s^3_{asci}[\tau^0_p + \tau^1_p\sigma_{asci}/c(\beta\gamma)_\Upsilon] \tag{C.13}$$

$$\left(\tau^n_{np}\right)_{main} = s^3_{asci}[\tau^0_n + \tau^1_n\sigma_{asci}/c(\beta\gamma)_\Upsilon] \tag{C.14}$$

$$\left(\tau^n_{np}\right)_{tail} = s^3_{asci}[\tau^0_n + \tau^1_n\sigma_{asci}/c(\beta\gamma)_\Upsilon] \tag{C.15}$$

The fitted parameters of non-primary track effect resolution function are listed in Tabl C.2.

Table C.2: The Parameters of Non-Primary Track Effect Resolution Function

Parameters	SVD-I		SVD-II	
	multi-track	single-track	multi-track	single-track
f_δ	$0.557^{+0.040}_{-0.041}$	$0.692^{+0.035}_{-0.037}$	$0.458^{+0.060}_{-0.068}$	$0.790^{+0.027}_{-0.028}$
f_p	$0.940^{+0.002}_{-0.002}$	$0.791^{+0.009}_{-0.009}$	$0.774^{+0.021}_{-0.021}$	$0.774^{+0.021}_{-0.021}$
τ^0_p	$0.050^{+0.006}_{-0.006}$	$0.458^{+0.047}_{-0.046}$	$0.132^{+0.005}_{-0.005}$	$1.319^{+0.040}_{-0.039}$
τ^1_p	$0.704^{+0.014}_{-0.014}$	$1.326^{+0.064}_{-0.063}$	$0.680^{+0.013}_{-0.013}$	0.0
τ^0_n	$0.044^{+0.035}_{-0.035}$	$0.293^{+0.087}_{-0.085}$	$0.151^{+0.008}_{-0.008}$	$0.638^{+0.062}_{-0.056}$
τ^1_n	$1.287^{+0.071}_{-0.068}$	$1.450^{+0.142}_{-0.134}$	$0.673^{+0.019}_{-0.019}$	0.0
s^2_{asci}	$0.060^{+0.374}_{-0.503}$		$0.098^{+0.002}_{-0.002}$	
s^3_{asci}	$0.930^{+0.166}_{-0.079}$		$1.064^{+0.092}_{-0.134}$	

C.3 Kinematic Approximation

The fourth component of resolution function, kinematic approximation, is the difference between the measured proper time interval,Δt and true proper time interval, Δt_{true}. That is calculated from the kinematics of the $\Upsilon(4S)$ two-body decay. The difference between Δt and Δt_{true}, defined as x, can be written by,

$$x \equiv \Delta t - \Delta t_{true} = [\frac{(\beta\gamma)_{full}}{(\beta\gamma)_{\Upsilon}} - 1]t_{full} - [\frac{(\beta\gamma)_{asci}}{(\beta\gamma)_{\Upsilon}} - 1]t_{asci} \tag{C.16}$$

where $(\beta\gamma)_{full}$ and $(\beta\gamma)_{asci}$ are Lorentz boost factor of the c-side and tag-side B mesons, respectively, and their ratios to $(\beta\gamma)_{\Upsilon}$ are given as,

$$\frac{(\beta\gamma)_{full}}{(\beta\gamma)_{\Upsilon}} = \frac{E_B^{cms}}{m_B} + \frac{p_B^{cms}\mathbf{cos}\theta_B^{cms}}{\beta_{\Upsilon}m_B} \sim 1 + 0.165\mathbf{cos}\theta_B^{cms} \tag{C.17}$$

$$\frac{(\beta\gamma)_{asci}}{(\beta\gamma)_{\Upsilon}} = \frac{E_B^{cms}}{m_B} - \frac{p_B^{cms}\mathbf{cos}\theta_B^{cms}}{\beta_{\Upsilon}m_B} \sim 1 - 0.165\mathbf{cos}\theta_B^{cms} \tag{C.18}$$

where $\beta_{\Upsilon} = 0.391$ is velocity of $\Upsilon(4S)$ in units of c, $E_B^{cms} \sim 5.292$GeV, $p_B^{cms} \sim$0.340GeV/c and θ_B^{cms} are the energy, momentum and polar angle of the cp-side reconstructed B in the cms. The R_k is expressed as,

$$R_k = \begin{cases} E_p\left(x - [a_k\Delta t_{true} + c_k|\Delta t_{true}]; |c_k|\tau_B\right) & ; \ c_k > 0 \\ \delta^{Dirac}(x - (a_k - 1))\Delta t_{true}; \ c_k = 0 & \\ E_n\left(x - [a_k\Delta t_{true} + c_k|\Delta t_{true}]; |c_k|\tau_B\right) & ; \ c_k < 0 \end{cases} \tag{C.19}$$

Where the definition of $a_k \sim E_B^{cms}/m_B$ and $c_k \sim p_B^{cms}cos\theta_B^{cms}/\beta_{\Upsilon}m_B$. The expected theoretical Δt distribution $P(\Delta t)$ can be expressed as a convolution of the true PDF with R_k as,

$$P(\Delta t_{true}; \tau_B) = \frac{1}{2\tau_B}exp\left(-\frac{|\Delta t_{true}|}{\tau_B}\right) \tag{C.20}$$

$$\begin{aligned} P(\Delta t) &= \int_{-\infty}^{\infty} d(\Delta t')P(\Delta t'; \tau_B)R_k(\Delta t - \Delta' t) \\ &= \frac{m_B}{2E_B^{cms}\tau_B}exp\left(-\frac{|\Delta t|}{a_k} \pm c_k)\tau_B\right)\left\{\begin{array}{ll} + & \textbf{for} \ \ \Delta t > 0 \\ - & \textbf{for} \ \ \Delta t < 0 \end{array}\right. \end{aligned} \tag{C.21}$$

C.4 Background

The source of the backgrounds are the continuum production of $u\bar{u}$, $d\bar{d}$, $s\bar{s}$, and $c\bar{c}$ pair and combinatorial background from B^+B^- and $B^0\bar{B}^0$ events. The PDF of background has two component. One is Dirac function for combinatorial background and the other is exponential function for combinatorial background. The resolution function of background is based on Gaussian function, The definition of resolution function of background is,

$$\begin{aligned} R_{q\bar{q}}(\Delta t - \Delta' t) = (1 - f_{tail}^{bkg})G(\Delta t - \Delta' t; s_{main}^{bkg}\sqrt{\sigma_{full}^2 + \sigma_{asci}^2}) \\ + f_{tail}^{bkg}G(\Delta t - \Delta' t; s_{tail}^{bkg}\sqrt{\sigma_{full}^2 + \sigma_{asci}^2}) \end{aligned} \tag{C.22}$$

Table C.3: The Parameters of Resolution Parameters for Continuum Background

Parameters	multi-track	single-track
f_{bkg}^{tail}	$0.741^{+0.061}_{-0.080}$	0.0
s_{main}^{bkg}	$2.776^{+0.401}_{-0.353}$	$1.233^{+0.070}_{-0.069}$
s_{tail}^{bkg}	$0.426^{+0.042}_{-0.039}$	—

C.5 Outlier

There still exist a very log tail that cannot be described by the resolution functions introduced above. The outlier term is introduced to describe this long tail and is represented by single Gaussian with zero mean event-independent width,

$$P_{ol}(\Delta t) = G(\Delta t, \sigma_{ol}) \tag{C.23}$$

We determine the σ_{ol} for multi-track and single-track events, respectively. The fitted parameters of outlier function are listed in table.C.4.

Table C.4: The Parameters of Outlier Function

Parameters	SVD-I	SVD-II
f_{ol}	$38.8948^{+1.7584}_{-12.5085}$	$44.5257^{+6.6416}_{-19.8601}$
σ_{ol} (multi-track)	$0.0002^{0.0030}_{-0.0060}$	$0.00031^{+0.0004}_{-0.0001}$
σ_{ol} (single-track)	$0.0312^{+0.0001}_{-0.0001}$	$0.01208^{+0.0038}_{-0.0017}$

C.6 Special Resolution for $K_S - B$ Vertexing method

We must modify the resolution function for $K_S - B$ Vertexing method, because the $K_S - B$ Vertexing method has only one K_S meson and IP-constrained. The resolution is different from $B^0 \to J/\psi K_S$ mode. Since the $K_S - B$ Vertexing method can use two charged track, the daughter $\pi^+\pi^-$, we modified the detector resolution for multi-track events.

$$R^{K_S}_{full}(\Delta t - \Delta' t) = G(\Delta t - \Delta t'; S_{dia}(s^0_{full} + s^1_{full}\zeta_{full})\sigma^z_{full}) \tag{C.24}$$

Where we added the new factor S_{dia} for adjust the $K_S - B$ Vertexing resolution, and we use ζ as the special goodness of vertex instead of ξ. We applied this resolution function to event in which the most inner hits of each daughter pion tracks in SVD are on difference layer. The S_{dia} depends on K_S decay vertex position in $r - \phi$ plane, and we defined the S_{dia} as function of K_S decay vertex position as follows,

$$S_{dia} = \begin{cases} S^0_{dia} \quad \textbf{for } r_{K_S} < r_0 \ \textbf{(cm)} \\ S^0_{dia} \cdot (1 + S^1_{dia}(r_{K_S} - r_0)) \quad \textbf{for } r_{K_S} \geq r_0 \ \textbf{(cm)} \end{cases} \tag{C.25}$$

Where r_{K_S} is K_S decay vertex position in $r - \phi$ plane, and r_0 is constant value which differ between SVD-I and SVD-II data. The fitted special resolution parameter for $K_S - B$ vertex are listed in Table C.5.

Table C.5: The Parameters of Resolution Parameters for $K_S - B$ Vertexing

Parameters	SVD-I	SVD-II
s^0_{full}	$1.425^{+0.185}_{-0.185}$	$0.561^{+0.105}_{-0.101}$
s^1_{full}	$0.061^{+0.144}_{-0.053}$	$0.357^{+0.096}_{-0.210}$
S^0_{dia}	$1.141^{0.374}_{-0.503}$	$1.710^{+1.225}_{-0.314}$
S^1_{dia}	$0.21^{+0.3}_{-0.19}$	$0.653^{+0.136}_{-0.126}$
r_0	2.0	4.0

Appendix D

Estimated Signal Fraction in each r-region

To measure the CP-asymmtry parameters exactly, we estimated the signal fraction in each r-region, because the signal fraction depend on wrong tag fraction. In low r region, signal fraction is small, while the that is high in high r region. The signal fraction in each r-region are estimated by Signal MC, sideband data. The estimated number of signal Rare B Background and Continuuim background is listed in tableD.1, and the M_{bc} and ΔE plots are shown in this Chapter.

Table D.1: Expected number of event in each r-bin

Expected $K_S\pi^0$ Event				
r-bin region	High Likelihood Ratio		Low Likelihood Ratio	
	W/ Vertex	W/o Vertex	W/ Vertex	W/o Vertex
1	20.88	39.21	4.58	27.63
2	9.61	18.20	1.96	11.71
3	6.28	11.49	1.35	7.39
4	6.69	12.00	1.28	7.23
5	5.93	10.63	1.01	6.05
6	9.59	17.15	1.35	7.25
Expected Rare B Background Event				
1	0.16	3.60	0.62	1.42
2	0.09	1.44	0.36	0.57
3	0.07	1.11	0.26	0.44
4	0.06	0.95	0.24	0.37
5	0.05	1.14	0.18	0.45
6	0.08	1.49	0.29	0.59
Expected Continuum Background Event				
1	20.81	54.70	69.64	164.48
2	4.67	14.89	19.50	48.50
3	4.67	10.73	12.91	32.76
4	4.94	10.05	13.90	35.88
5	3.08	4.96	9.01	18.65
6	0.97	1.67	2.55	6.65

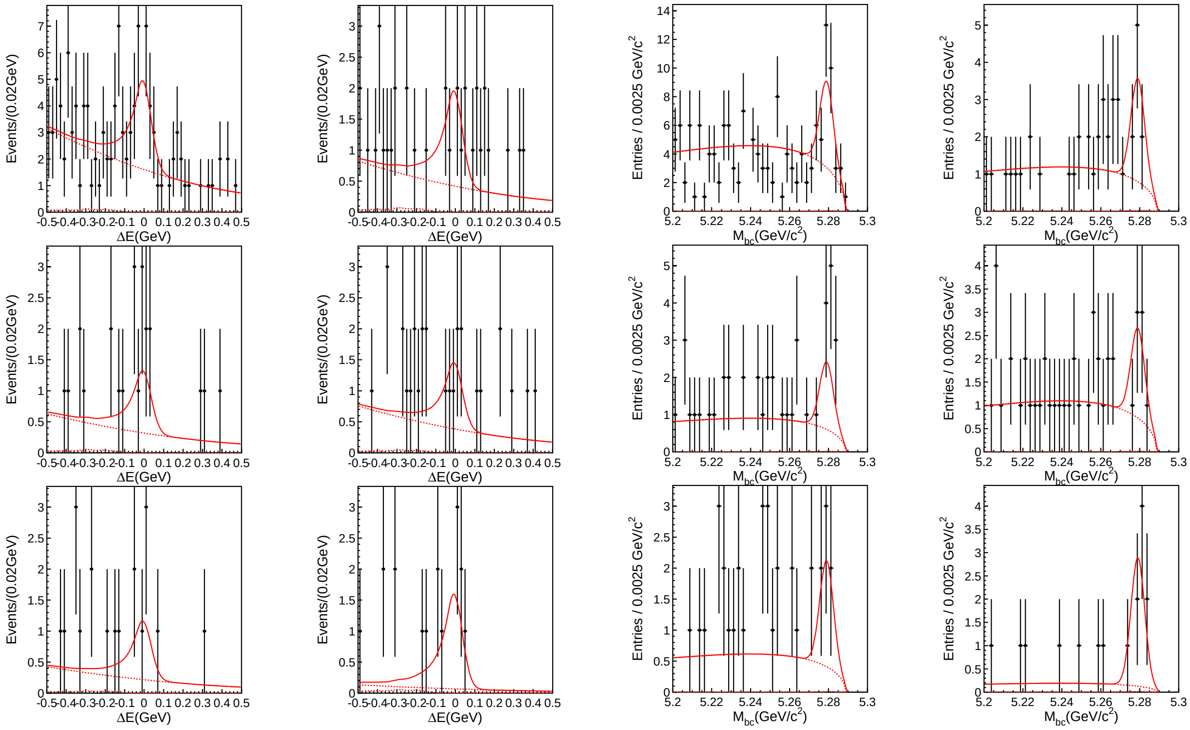

Figure D.1: ΔE and M_{bc} plots of HLR W/ Vertex in each r-bin

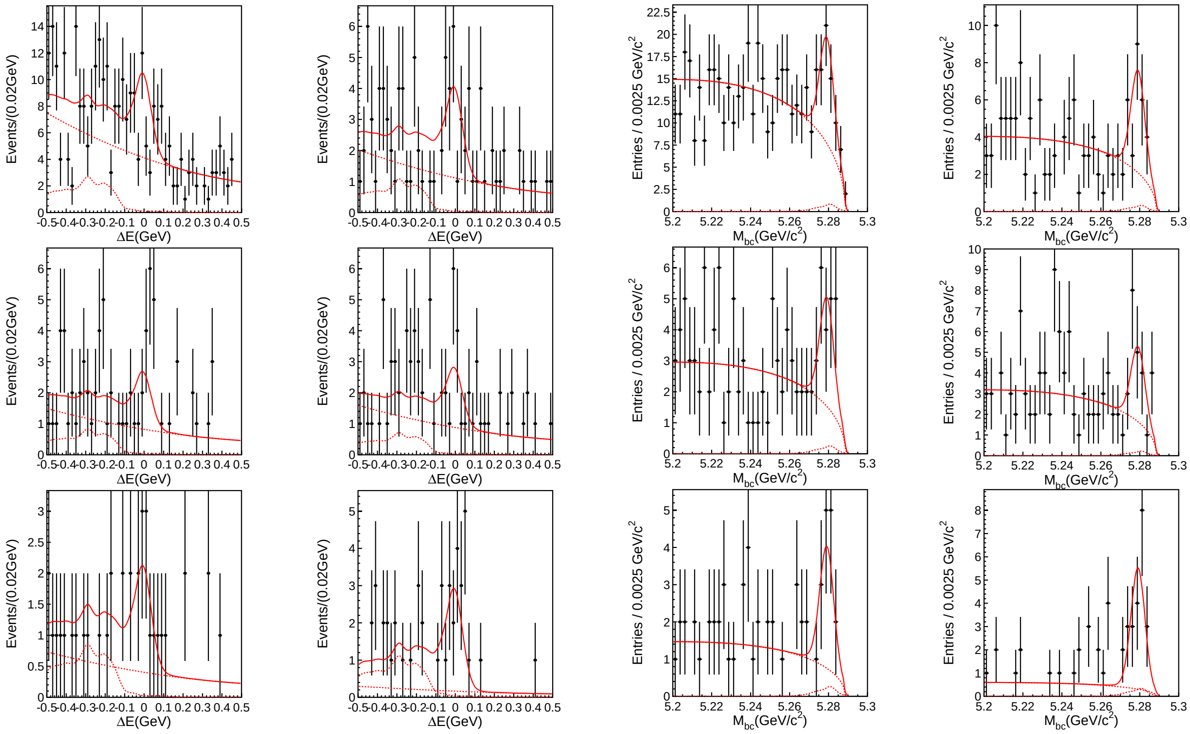

Figure D.2: ΔE and M_{bc} plots of HLR W/o Vertex in each r-bin

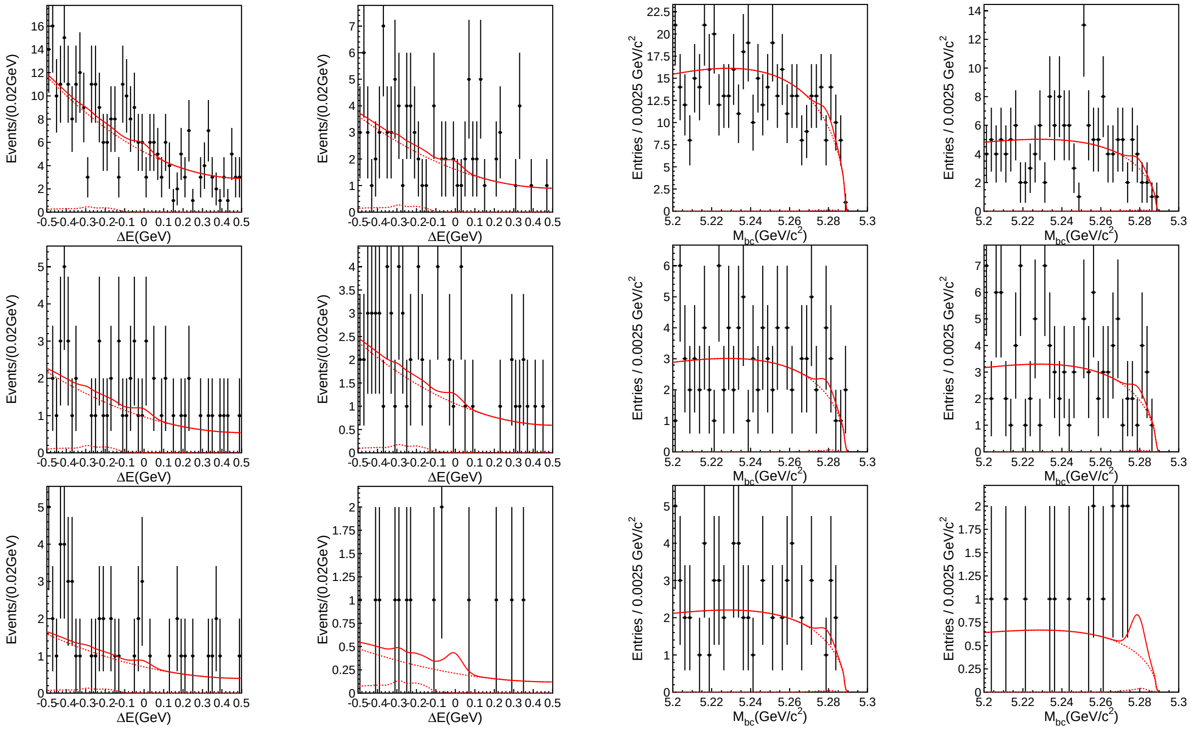

Figure D.3: ΔE and M_{bc} plots of LLR W/ Vertex in each r-bin

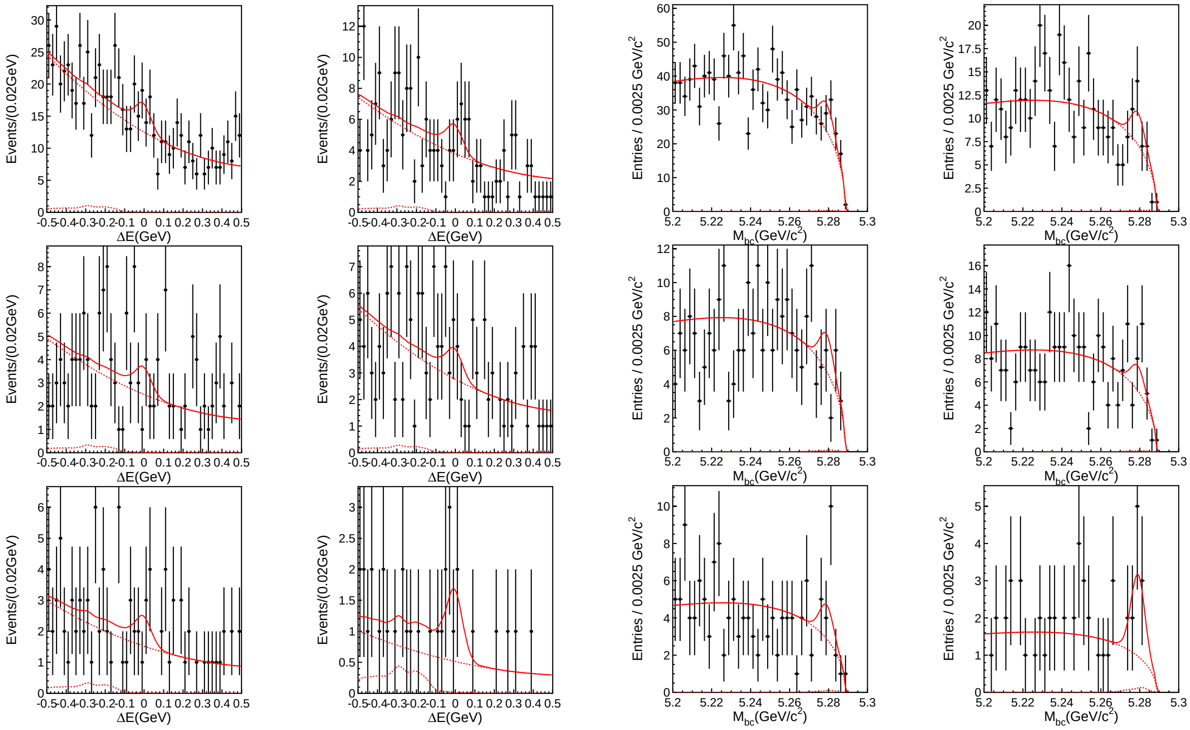

Figure D.4: ΔE and M_{bc} plots of LLR W/ Vertex in each r-bin

Appendix E

Measurement of Interaction Point Profile at Belle

E.1 Introduction

Interaction Point (IP) is collision point of positron and electron beam. IP profile is important, since it is used for IP constraint fit in Kfitter[87]. IP constraint fit is a powerful method for the vertex fit to the tracks that come from IP, because the beam size in the y direction is very small (The designed value is about 2μm.) and it is a strong constraint. To use this constraint fit, the mean position of IP distribution must be measured precisely.

It is also useful for checking the accelerator conditions to see the time dependence of IP profile. Because the current of HER and LER decrease as time passes. In this chapter we describe how IP profile is calculated.

E.2 Method of Calculation to IP Profile

This section describes how IP profile is calculated. First, IP is reconstructed using hadronic event sample,and in next step, IP distribution is fitted with the 3-dimensional Gaussian and calculated IP position, IP size and IP rotation angle. After that, IP profile is determined as error matrix from fit result and the information from KEKB accelerator group. Finally all IP profile information, IP position and Error matrix, are stored in the database.

E.2.1 IP Reconstruction with Hadronic Events

IP is calculated with hadronic data. At first, IP must be reconstructed from reproducted data. This subsection shows how IP is reconstructed.

Hadronic events are selected according to the Event Classification tools in BELLE. HadronC data sample is used in order to reject the beam-gas background events.[1]

After hadronic events are selected, the result of EvtVtx module is used as the preselection for the events and tracks. EvtVtx is a module for the primary vertex finding.[2] The events where EvtVtx module fails to find the primary vertex (i.e. the "quality" entry in the "Evtvtx_Primary_Vertex" Panther table is less than 2.) are rejected. Since the main aim of this module is the rejection of beam-wall or beam-gas events and its resolution is not as good as other vertexing tools such as Kfitter, IP is re-calculated using Kfitter. The tracks which are used for the IP reconstruction in the EvtVtx module are selected for the re-calculation. At least two hits are required in both SVD $r\phi$ and z strips to ensure good vertex resolution. Then IP is reconstructed using Kfitter using the selected tracks with pion hypothesis. If the vertex fit fails or the

---

[1] For the detail of the event classification, please see "Event Classification Task Force Home Page" (http://belle.kek.jp/~adachi/evtcls/) or "Selection Criteria in Classifying Beam Data" on the web.

[2] For the detail of the EvtVtx module, please refer to the "Belle Software Documentation Main Page" (http://www.hep.princeton.edu/~marlow/doc/).

reduced χ^2 (χ^2 devided by the number of degree of freedom(DOF)) is greater than or equals to 40.0, the event is rejected. The events where IP is reconstructed successfully are used for the IP distribution fit to obtain IP profile.

The selection criteria for the IP reconstruction are summarized in Table E.1.

Table E.1: Selection criteria for IP reconstruction.

Quantity		Criterion
for each track	Used in EvtVtx	true
	# of $r\phi$ SVD hits	≥ 2
	# of z SVD hits	≥ 2
for each event	Quality of EvtVtx	≥ 2
	χ^2/DOF	≤ 40.0

Example of reconstructed IP position distribution for a typical run is shown in Figure E.1.

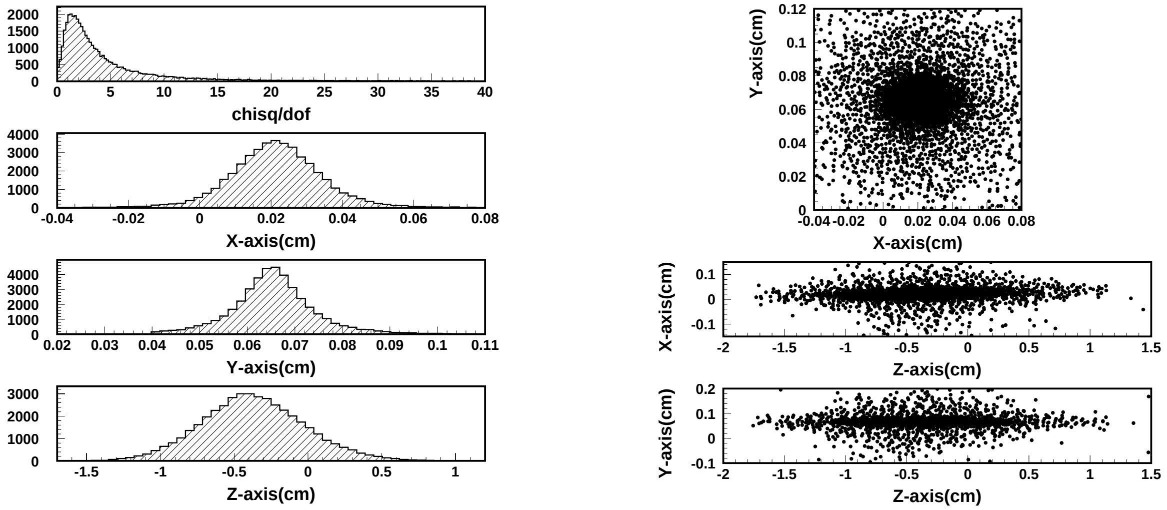

Figure E.1: Reconstructed IP distribution of Exp21 run 324.
In the left figure, the χ^2/DOF distribution (top figure) and IP distribution along x,y,z-axis(detector coordinate) are shown respectively. In the rigth figure, the scatter plot of IP distribution x_vs_y, z_vs_x and z_vs_y are shown.

E.2.2 IP Distribution Fitting

IP distribution is fitted with three-dimensional Gaussian using unbinned maximum likelihood method. As Figure E.1 shows, there still exist the beam-gas events in the tail of IP distribution even though HadronC cuts are applied. In order to reject these beam-gas tails, mean value and rms are calculated for the IP distribution along each axis x,y,z and events within 2.5 times rms around the mean for all axes are used for the fit.

The IP distribution of selected events is fitted with 3-dimensional Gaussian. The axes of the Gaussian are not necessarily parallel to the detector axes. Since the electron beam is tilted 22 mrad from z axis in the horizontal plane while the positron beam is parallel to z axis, IP distribution is rotated at least around y axis. And the detector coordinate may be tilted from the beam axis. Considering this rotation, IP profile coordinate (x', y', z') where the axes are parallel to the Gaussian axes and the origin is the mean point of the Gaussian is defined. The transformation between the detector coordinate (x, y, z) and the IP profile coordinate (x', y', z') is defined as follows :

$$\begin{pmatrix} x \\ y \\ z \end{pmatrix} = \mathbf{R}_z(\theta_z) \cdot \mathbf{R}_y(\theta_y) \cdot \mathbf{R}_x(\theta_x) \cdot \begin{pmatrix} x' \\ y' \\ z' \end{pmatrix} + \begin{pmatrix} \mu_x \\ \mu_y \\ \mu_z \end{pmatrix} \tag{E.1}$$

where (μ_x, μ_y, μ_z) is the mean position of the IP and $\mathbf{R}_i(\theta)$ is the rotation around i axis with angle θ :

$$\begin{aligned} \mathbf{R}_x(\theta_x) &= \begin{pmatrix} 1 & 0 & 0 \\ 0 & \cos\theta_x & -\sin\theta_x \\ 0 & \sin\theta_x & \cos\theta_x \end{pmatrix} \\ \mathbf{R}_y(\theta_y) &= \begin{pmatrix} \cos\theta_y & 0 & \sin\theta_y \\ 0 & 1 & 0 \\ -\sin\theta_y & 0 & \cos\theta_y \end{pmatrix} \\ \mathbf{R}_z(\theta_z) &= \begin{pmatrix} \cos\theta_z & -\sin\theta_z & 0 \\ \sin\theta_z & \cos\theta_z & 0 \\ 0 & 0 & 1 \end{pmatrix} . \end{aligned} \tag{E.2}$$

Since IP distribution has non-Gaussian tails in x and y directions while it seems to be a single Gaussian in z as Figure E.1 shows, a sum of two Gaussians with a same mean is used for the fit in x' and y' direction. The tail is considered to be due to mis-reconstructed events. A same value is used for the σ of a wider Gaussian in x' and y'. The likelihood function becomes

$$\begin{aligned} \mathcal{L} = \prod_i & \left\{ (1-f)\exp\left(-\frac{x'^2}{2\sigma_{x'}^2}\right) + f\exp\left(-\frac{x'^2}{2\sigma_{\text{wide}}^2}\right) \right\} \\ & \times \left\{ (1-f)\exp\left(-\frac{y'^2}{2\sigma_{y'}^2}\right) + f\exp\left(-\frac{y'^2}{2\sigma_{\text{wide}}^2}\right) \right\} \times \exp\left(-\frac{z'^2}{2\sigma_{z'}^2}\right) \end{aligned} \tag{E.3}$$

where $\sigma_{x'}$, $\sigma_{y'}$, $\sigma_{z'}$ is the size of IP distribution along x', y', z' axis respectively, f is the fraction of the wider Gaussian, and σ_{wide} is the width of the wider Gaussian. Thus the free parameters are μ_x, μ_y, μ_z, $\sigma_{x'}$, $\sigma_{y'}$, $\sigma_{z'}$, θ_x, θ_y, θ_z, f, σ_{wide}.

E.2.2.1 IP Distribution fitting fill by fill

If there are several runs in one fill, IP distributions in these runs are put together for the fit. Because there are some runs that do not have enough statistics and IP position seems stable within the resolution, the fit is applied fill by fill[3]. Fill by fill IP profile is used for physics analysis as discribe in next section. The results of the fit applied fill by fill for the IP distribution shown in Fig E.1 are listed in Table E.2. Since $\sigma_{x'}$ and $\sigma_{y'}$ are on the same order while $\sigma_{z'}$ is far larger than them as Table E.2 shows, it is difficult to determine the rotation around z axis while determination of rotation around x or y axis is just like a fit of a line and is easy. Therefore if the number of events used for the fit is less than 10000, the rotation around z axis is fixed to be 0.

All of fill results in Exp21 are shown in Fig E.2, E.3, E.4. In each figure, Horizontal axis is run number(not fill number) . Fig E.2 shows IP-Positions, Fig E.3 shows IP-size, and Fig E.4 shows Rotation angle.

E.2.2.2 IP Distribution fitting (Event dependent IP-profile)

IP distribution fitting with 3-dimension Gaussian is applied event dependent IP-profile.This IP profile is useally used for checking IP condition in a run, and we use it for physics analysis. In this case, the total events in one run is divided by 10,000 events[4] and fitted at each region. Each 10,000 events region has about from 300 to 500 hadronic events which are selected for IP reconstruction. In this fitting, only IP

---

[3] From exp25, IP-profile of fill-by-fill is changed to run-by-run completely. Because luminosity was high and we can obtain enough statistics in a run

[4] We used 60,000 events to calculate event dependent IP-profile and used farm ID from exp7 to exp13

Parameter	Value
μ_x	213.8 ± 0.6 μm
μ_y	652.4 ± 0.4 μm
μ_z	3.73 ± 0.02 mm
$\sigma_{x'}$	102.4 ± 0.5 μm
$\sigma_{y'}$	70.2 ± 0.4 μm
$\sigma_{z'}$	3.33 ± 0.01 mm
θ_x	0.40 ± 0.14 mrad
θ_y	7.29 ± 0.17 mrad
θ_z	5.40 ± 8.44 mrad
f	0.1635 ± 0.0003
σ_{wide}	266.7 ± 2.4 μm

Table E.2: Fit results for the IP distribution is shown in Fig.E.1. This result is Experiment 21 run 324

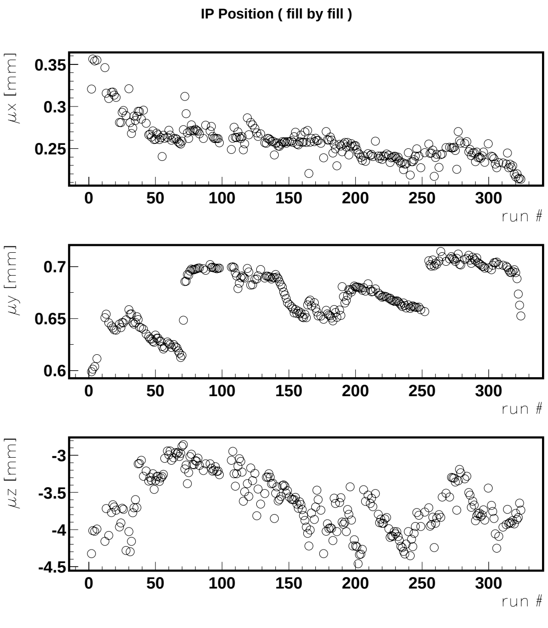

Figure E.2: IP Position fill by fill

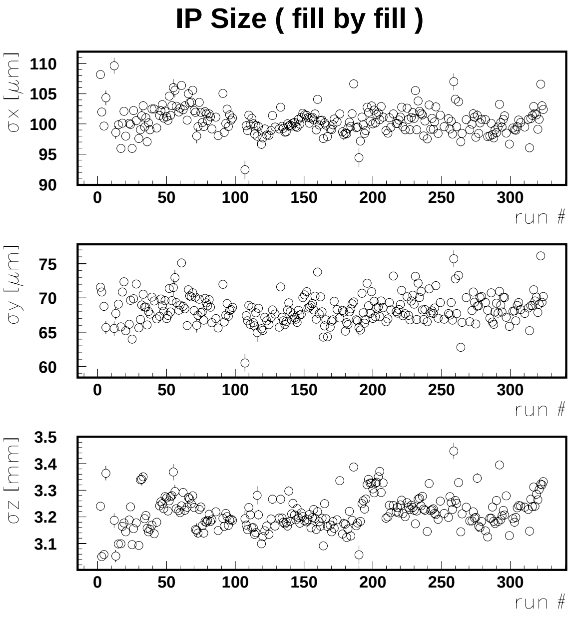

Figure E.3: IP Size fill by fill

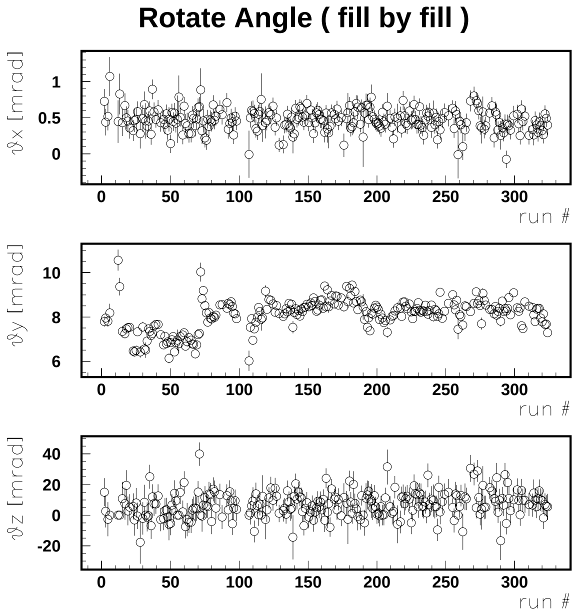

Figure E.4: IP Rotation Angle fill by fill

positions and those error are measured, and these information is used for calculation to error matrix with KEKB accelerator information as discribed in next subsection. In Fig E.5, the typical results of exp21 is shown.

E.2.3 Determination of IP Profile from KEKB information

The parameters of IP profile are determined from the previous fit results and the information from KEKB accelerator.

As Fig E.3 shows, the size of IP profile in x' and y' obtained from the fit are about $\sigma_{x'} \sim 100\,\mu$m and $\sigma_{y'} \sim 70\,\mu$m. But values expected from the designed parameters of the accelerator are $\sigma_{x'} \sim 80\,\mu$m and $\sigma_{y'} \sim 2\,\mu$m. This is due to the vertex resolution. In z or z' direction the vertex resolution $\sim 100\,\mu$m is negligible since the size of IP distribution is large ($O(1\,\mathrm{mm})$).

To obtain an actual size of IP profile in x' and y', the information from KEKB accelerator is used. The accelerator group measures beam size in x and y direction for HER and LER. The values at the time run starts and stops are recorded in a run summary. Mean of start and stop time values are taken as the beam size of that run for both HER and LER. If one of the start and stop time values is not measured correctly (i.e. the value is equal to 0.0), the other value is taken. If both values cannot be measured, then an average of previous and subsequent runs is taken. Run variation of mean value of beam sizes are shown in the Fig E.6.

Assuming they are crossing in the zx plane with angle $\pm\theta_{\rm cross}$(11mrad), the beam sizes of HER and LER are calculated as recalulated IP size, $\sigma_{x,y}^{acc}$:

$$\sigma_{x(y)}^{\rm HER(LER)} \equiv \frac{\sigma_{start}^{\rm HER(LER)} + \sigma_{stop}^{\rm HER(LER)}}{2} \tag{E.4}$$

$$\sigma_x^{acc} = \begin{cases} \frac{\sigma_x^{\rm HER}\sigma_x^{\rm LER}}{\sqrt{\sigma_x^{\rm HER\,2}+\sigma_x^{\rm LER\,2}}} \cdot \frac{1}{\cos\theta_{\rm cross}} & \sigma_x^{\rm HER} > 0 \cap \sigma_x^{\rm LER} > 0 \\ \frac{\sigma_x^{\rm HER}}{\sqrt{2}\cos\theta_{\rm cross}} & \sigma_x^{\rm HER} > 0 \cap \sigma_x^{\rm LER} < 0 \\ \frac{\sigma_x^{\rm LER}}{\sqrt{2}\cos\theta_{\rm cross}} & \sigma_x^{\rm HER} < 0 \cap \sigma_x^{\rm LER} > 0 \\ \frac{100\mu\mathrm{m}}{\sqrt{2}\cos\theta_{\rm cross}} & \sigma_x^{\rm HER} < 0 \cap \sigma_x^{\rm LER} < 0 \end{cases} \tag{E.5}$$

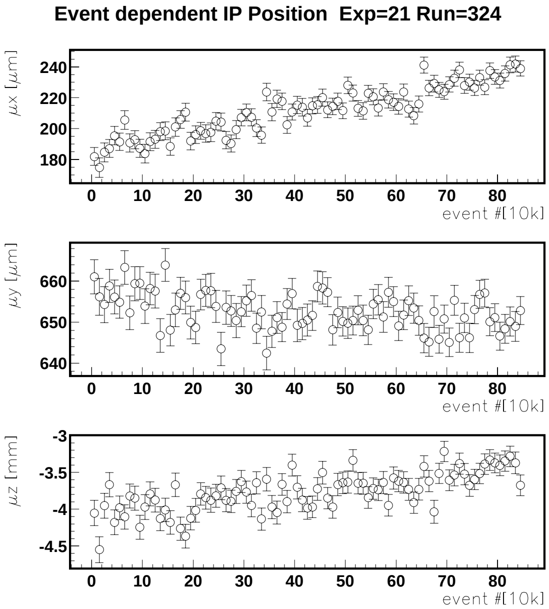

Figure E.5: Event dependent IP position in Exp=21 Run=324

$$\sigma_y^{acc} = \begin{cases} \frac{\sigma_y^{\mathrm{HER}}\sigma_y^{\mathrm{LER}}}{\sqrt{\sigma_y^{\mathrm{HER}\,2}+\sigma_y^{\mathrm{LER}\,2}}} & \sigma_y^{\mathrm{HER}} > 0 \cap \sigma_y^{\mathrm{LER}} < 0 \\ \frac{\sigma_y^{\mathrm{HER}}}{\sqrt{2}} & \sigma_y^{\mathrm{HER}} > 0 \cap \sigma_y^{\mathrm{LER}} < 0 \\ \frac{\sigma_y^{\mathrm{LER}}}{\sqrt{2}} & \sigma_y^{\mathrm{HER}} < 0 \cap \sigma_y^{\mathrm{LER}} > 0 \\ \frac{5\mu\mathrm{m}}{\sqrt{2}} & \sigma_y^{\mathrm{HER}} < 0 \cap \sigma_y^{\mathrm{LER}} < 0 \end{cases} \tag{E.6}$$

Since there is no information about beam size in z, the effect from z size on $\sigma_{x'}$ is ignored. For details of the space-time profile of the beam collision with finite crossing angle, please refer to [109].

For $\sigma_{x'}$ and $\sigma_{y'}$, the smaller value between the ones obtained from the fit and the accelerator information is taken as Eq E.7,E.8(Mostly the latter one is chosen.) Then the IP size is expressed as the error matrix in (x', y', z') system :

$$\sigma_{x'}^2 = \begin{cases} \sigma_{x'}^2 - \sigma_{y'}^2 & (\sigma_{x'} > \sigma_{y'}) \\ \sigma_x^{acc} & (\sigma_{x'} < \sigma_{y'}) \end{cases} \tag{E.7}$$

$$\sigma_{y'}^2 = \begin{cases} \sigma_y^{acc} & (\sigma_{y'} > \sigma_y^{acc}) \\ \sigma_{y'}^2 & (\sigma_{y'} < \sigma_y^{acc}) \end{cases} \tag{E.8}$$

$$\mathbf{E}' = \begin{pmatrix} \sigma_{x'}^2 & 0 & 0 \\ 0 & \sigma_{y'}^2 & 0 \\ 0 & 0 & \sigma_{z'}^2 \end{pmatrix} + \begin{pmatrix} \sigma_{posx}^2 & 0 & 0 \\ 0 & \sigma_{posy}^2 & 0 \\ 0 & 0 & \sigma_{posz}^2 \end{pmatrix}. \tag{E.9}$$

where σ_{posx}, σ_{posy} and σ_{posz} are error of μ_x, μ_y and μ_z which are calcuated in event-by-event, respectively. $\sigma_{x'}$, $\sigma_{y'}$ and $\sigma_{z'}$ are calcualted in fill-by-fill.

This error matrix is converted in (x, y, z) system (Lab. frame) as follows :

$$\mathbf{E} = \mathbf{R} \cdot \mathbf{E}' \cdot \mathbf{R}^{-1} \tag{E.10}$$

$$\mathbf{R} \equiv \mathbf{R}_z(\theta_z) \cdot \mathbf{R}_y(\theta_y) \cdot \mathbf{R}_x(\theta_x). \tag{E.11}$$

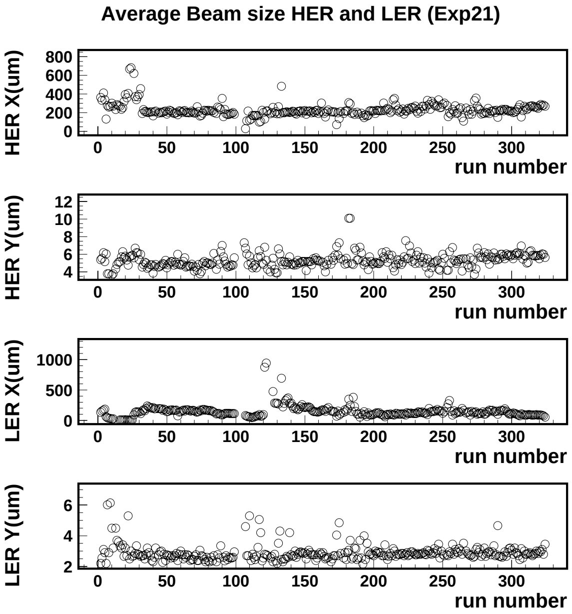

Figure E.6: Average Beam size HER and LER

Kfitter can apply an IP-constraint fit using IP mean position and this error matrix.

These information of IP position and its error matrix are stored in the database for general users. Beam size information from accelerator group are also stored in the database.

E.2.4 Average IP profile at one Experiment

In addition to these IP profile, one more IP profile is calculated. That is average of one experiment. The average IP profile information is used for MC production. Unlike previus IP profile, this profile is not stored in database. Averge IP profile is calculated from results of fill by fill IP profile. IP position along x,y and z are calculated as mean of IP position distributions, and IP size along y'-axis is calculated from Lumnosity, only z'-axis is calculated as sigma of fitted z(=z')-distributions. Basicaly, a luminosity of collision accelerator type is defined by frequency, number of bunch, number of particle in each bunch and beam size. Bunch size can be defined as IP-size. Then, IP-size along x-axis and y-axis are defined as follows if rotation angle is ignored.

$$\sigma_x^2 \simeq \sigma_{x'}^2 + \sigma_{resolution\_x}^2 \tag{E.12}$$

$$\sigma_y^2 \simeq \sigma_{y'}^2 + \sigma_{resolution\_y}^2 \tag{E.13}$$

$$\sigma_{resolution\_x}^2 \sim \sigma_{resolution\_y}^2 \tag{E.14}$$

$$\sigma_{resolution\_y}^2 \sim \sigma_y^2 \gg \sigma_{y'}^2 \tag{E.15}$$

σ_x and σ_y are IP size which are calculated with hadronic data. $\sigma_{x'}^2$ and $\sigma_{y'}^2$ are real IP size along x',y'-axis. $\sigma_{resolution\_x}^2$ and $\sigma_{resolution\_y}^2$ are detector resolution of vertex along x and y-axis. We explained that σ_y is much larger than $\sigma_{y'}^2$ as described in last sub-section. And we find that dector resolution along x and y-axis have same order. Above all, real IP size can be calculated from following equation.

$$\sigma_{x'} \sim \sqrt{\sigma_x^2 - \sigma_y^2} \tag{E.16}$$

$$L = fN_{bunch}\frac{n_{HER}n_{LER}}{4\pi\sigma_{x'}\sigma_{y'}} \tag{E.17}$$

$$\sigma_{y'} = \frac{I_{HER}I_{LER}}{4\pi f e^2 N_{bunch}\sigma_{x'}}\frac{1}{L} \tag{E.18}$$

IP-size along x'-axis can be calculated from Eq E.16. L is defined as ECL delivery luminosity divided by runtime, these value can be obtained from run summary, f is frequency(Hz), N_{bunch} is number of bunch, n_{HER} and n_{LER} are number of particles in one HER and LER beam bunch respectively. I_{HER} and I_{LER} are beam current of HER and LER. IP-size along y-axis can be calculated from Eq E.16 and E.18.[5] Example of average IP-profile of exp 21, is shown in the Fig E.7, Fig E.8,and Table E.3. [6]

Table E.3: Average IP profile in Exp21

	Mean value	Error(RMS)
$< \mu_x >$ (cm)	0.0258	0.0023
$< \mu_y >$ (cm)	0.0672	0.0027
$< \mu_z >$ (cm)	-0.364	0.038
$< \sigma_{x'} >$(μm)	73.6	1.9
$< \sigma_{y'} >$(μm)	5.5	0.9
$< \sigma_{z'} >$(cm)	0.322	0.006
$< \theta_x >$(mrad)	0.47	0.16
$< \theta_y >$(mrad)	8.09	0.70
$< \theta_z >$(mrad)	7.2	8.4

---

[5] Frequency is constant value in KEKB, $f = 3.0 \times 10^8$(m/sec)/3016.26(m) $\sim 10^5$(Hz), In exp21, HER and LER beam current is around 0.8(A) and 1.2(A) respectively. And number of bunch is 1131.

[6] Users can see the summary of average value of IP profile from exp9 to exp27 in web page(http://belle.kek.jp/group/software/mc/status/HowToDoMC_general.txt)

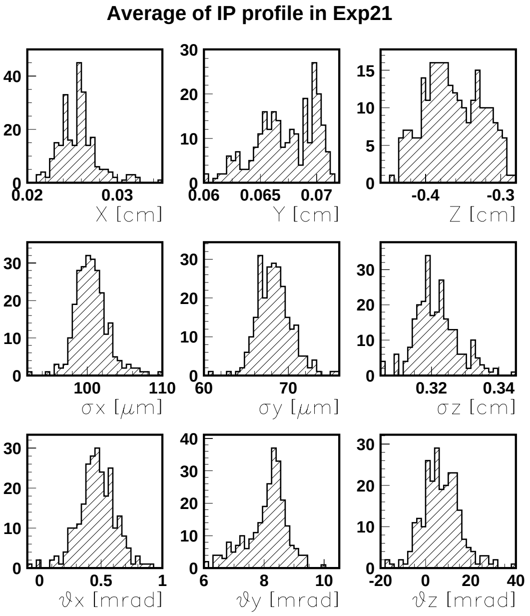

Figure E.7: IP position, IP size and IP rotation angle distribution of Exp21 Average IP profile is defined as mean of these distributions except σ_x and σ_y

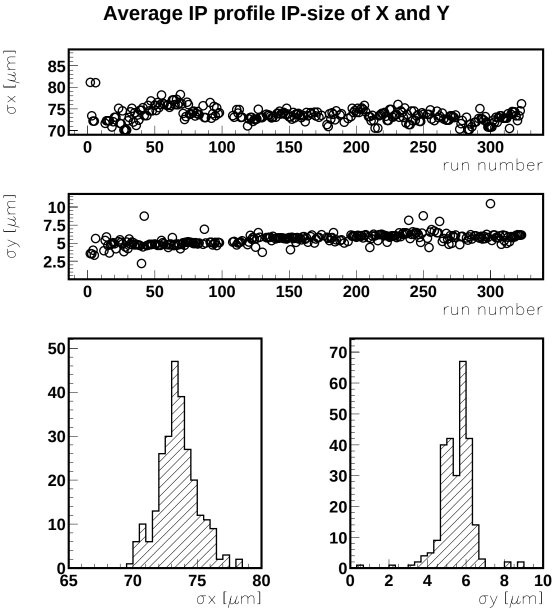

Figure E.8: Recalculated σ_x and σ_y distribution

Bibliography

[1] F.J.Hasert et.al.,Physics Letters B48B number1 (1973)121

[2] UA1, G.Arnison et.al., Physics Letters B122B(1983) 103

[3] UA1, G.Arnison et.al., Physics Letters B129(1983) 273

[4] UA2, M.Banner et.al., Physics Letters B126B(1983) 398

[5] UA2, M.Banner et.al., Physics Letters B129(1983) 130

[6] CHARM-II Collaboration, Physics Letters B232,number1 (1989)539

[7] CHARM-II Collaboration, Physics Letters B259,number4 (1991)499

[8] CDF Collaboration. Phys.Rev.Lett. 74 (1995) 2626-2631

[9] J.H.Christenson, J.Cronin. V.Fitch, R.Turlay. Phys.Rev.Lett 13(1964)138

[10] CERN-Dortmund-Edinburgh-Mainz-Orsay-PIsa-Siegen Collaboration. Physics Letters B206 (1988)169

[11] CPLEAR Collaboration. Physics Letters B286(1992)180-186

[12] Belle Collaboration. Physics Review Letters 87(2001)091802

[13] BaBar Collaboration. hep-ex/0205045

[14] Y.Fukuda et.al Super-Kamiokande Collaboration. Physics Review Letters 81(1998) 1562.

[15] Y.Ashie et.al Super-Kamiokande Collaboration. hep-ex/0404034

[16] Y.Fukuda et.al Super-Kamiokande Collaboration. Physics Review Letters 86(2001) 5651.

[17] Y.Fukuda et.al Super-Kamiokande Collaboration. Physics Letters 539(2002) 179-187

[18] Q.R.Ahmad SNO Collaboration. Physics Review Letters 89(2002) 011302-1

[19] K2K Collaboration. Physics Review Letters 90(2003) 041801-1

[20] KamLAND Collaboration Phys.Rev.Lett. 90 (2003) 021802

[21] T.Browder's Talk at Lepton Photon 2003

[22] Steven Weinberg. Phys.Rev.Lett. 19 (1967) 1264

[23] P.W.Higgs Physics Letters 12(1964) 132

[24] Physics Letters B Vol.592/1-4(2004)1-1110: Review of Particle Physics

[25] M.Kobayashi, T.Maskawa. Progress of Theoretical Physics, vol49(1973)652

[26] T.D.Lee,C.N.Yang. Physical review vol104(1956)254

[27] C.S.Wu. Letters To The Editor (1957)1413

[28] Goldhaber et.al. Phys.Rev 106(1958)1015

[29] Chau,L-L and Keung, W.-Y. Physical Review Letters 53(1984)1802

[30] L.Wolfstein. Physics Review Letters 51(1983)1945

[31] Particle Data Grou. Phys Review D50(1994) D54(1996) EPJ,3(1998)

[32] G.Altarelli and P.Franzini. Z Physics C37(1988) 271

[33] A.J.Buras et al. Nucl Phyiscs B245(1984) 369, B347(1990) 491

[34] F.Gliman and Y.Nir. Ann Review. Nucl. Part. Sci 40(1990) 213-238

[35] A.J.Buras, M.Jamin and P.Weisz. Nucl. Physics B347(1990) 491

[36] M.Neubert. Physics Review D51(1995) 5101

[37] I.I.Bigi and A.Sanda, Nucl.Phys. B193(1981)85, B281(1987)41

[38] Michael Gronau. Physics Review Letters 63(1989)1451

[39] M.Gronau, J.L.Rosner. Physics Review D65(2002)093012

[40] M.Gronau, J.L.Rosner. Physics Review D65(2002)013004

[41] M.Gronau, J.L.Rosner. Physics Review D65(2002)054027

[42] M.Beneke, G.Buchalla, M.Neubert and C.T.Sachrajda. Nucl. Phyiscs N606(2001)245

[43] 6th Workshop on a Higher Luminosity B Factory,
M. Hazumi (KEK) 'Overview of e+e- B-factory Result'

[44] K. Abe, et al., (Belle Collaboration), Physics Review Letters 86(2001)2509

[45] K. Abe, et al., (Belle Collaboration), Physics Review Letters 87(2001)091802

[46] K. Abe, et al., (Belle Collaboration), Physics Review D66(2002)071102

[47] K. Abe, et al., (Belle Collaboration), hep-ex/0408111

[48] Anders Ryd (for the BABAR Collaboration), Nucl.Instrum.Meth. A462 (2001) 57-65

[49] Philip J. Clark, for the BaBar collaboration, hep-ex/0110081

[50] C. Touramanis (for the BABAR Collaboration), hep-ex/0110064

[51] Gerhard Raven (for the BaBar collaboration), hep-ex/0205045

[52] B. Aubert, et al., BABAR Collaboration, Phys.Rev.Lett. 89 (2002) 201802

[53] 32nd ICHEP04 conference(Augst 16-22):Beijing, China. Talk; Augst 16, M.Bruinsma(UC Irvine) 'sin(2β)+cos(2β) at Babar'

[54] K.Abe, et al.(Belle Collaboration), Physics Review Letters 89(2002)071801

[55] K.Abe, et al.(Belle Collaboration), Physics Review D68(2003)012011

[56] K.Abe, et al.(Belle Collaboration), Physics Review Letters 93(2004)021601

[57] BaBar Collaboration, talk by K.Tabelsi at XXXVII th Reconstres de Moriond on
Electroweak Interactions and Unified Theories, Les Arcs, France, March 9-16, 2002

[58] The BABAR Collaboration: B. Aubert, et al. Phys.Rev.Lett. 89 (2002) 281802

[59] B. Aubert, et al, BABAR Collaboration, Contributed to ICHEP04, hep-ex/0408089

[60] D.London, A.Soni, Physics Letters B497(1997)61-65

[61] B. Aubert, et al, BABAR Collaboration, Phys.Rev.Lett. 93 (2004) 071801

[62] D.Atwood and A.Soni, Phys.Rev.Lett 78(1997)3257

[63] The Super-KEKB Physics Working Group. hep-ex/0406071

[64] Y.Grossman, M.P.Worah, Physics Letters B395(1997)241-249

[65] S.Baek, KIAS-P03090. hep-ph/0312101

[66] D.Chang, W.Y.Keung and A.Pilaftsis, Phys.Rev.Lett 82(1999)900

[67] T.Moroi, hep-ph/0007328. Physics Letters B493(2000)366-374

[68] J.Hisano, Y.Shimizu, ICRR-report-501-203-5 hep-ph/0308255

[69] Y.Wang. hep-ph/0309290

[70] M.Endo, S.Mishima, M.Yamaguchi. hep-ph/0409245

[71] KEKB B-factory, July 2003-July 2004 Annual Report 'A Continuous March on the Luminosity Frontier', http://www-kekb.kek.jp/Publication/KEK_Annual_Report/

[72] S.Mori(el) et al.'The Belle detector'. Nucl.Instrum.Meth.A479(2002)117-232

[73] G.Alimonti et.al Belle Collaboration, Nucl.Instrum.Meth. A453(2000)71

[74] H.Hirano et.al. Nucl.Instrum.Meth A455(2000)294

[75] T.Iijima, et.al. Nucl.Instrum.Meth A453(2000)321

[76] H.Kichimi et al., Nucl.Instrum.Meth A453(2000)315

[77] H.Ikeda et.al., Nucl.Instrum.Meth A441(2000)401

[78] A.Abashian et.al., Nucl.Instrum.Meth A449(2000)112

[79] The Belle Collaboration. 'BELLE Progress Report. April 1996-March 1997'. KEK Progress Report 97-1. KEK. 1997

[80] E.Niard et.al, Nucl.Instrum.Meth A301(1991)506

[81] O.Toker el.at, Nucl.Instrum.Meth A340(1994)572

[82] H.Ishino, A.Kibayashi, K.Takahashi, and H.Kawai. 'Alignment method of SVD2 and Its Peformance', Belle note #715

[83] Y.Ushoroda. Nucl.Instrum.Meth A511(2003)6

[84] Y.Harada. Master Thesis in Niigata-University 2003

[85] R.E.Kalman, Trans. ASME, J.Bas. Eng. 82D, 35(1960)

[86] R.E.Kalman and R.S.Bucy, Trans. ASME, J.Bas. Eng. 83D, 95(1961)

[87] J.Tanaka.'Kfitter Usage and Effect', Belle Note #193

[88] T.Iijima, et.al. Nucl.Instrum.Meth A387(1997)64

[89] Y.Ushiroda, A.Mohapatra, H.Sakamoto, Y.Sakai, M.Nakao, Q. An and Y.F.Wang, Nucl.Instrum.Meth A438(1999)460

[90] Y.Ushiroda. 'Development of the BELLE Central Trigger System. Global Decision Logic'. Feb 1998

[91] T.Higuchi 'Development of The Online Event Selection Program for The BELLE Experiment', Master thesis(1999)

[92] T.Hojo. M.Hazumi. and R.Itoh.'Level 3 trigger at Belle'. Belle note #421

[93] M.Nakao. Nucl.Instrum.Meth A379(1996)379

[94] M.Nakao, M.Yamaishi, S.U.Sukuki, R.Itoh, and H.Fuji. IEEE Trans.Nucl.Sci 47(2000)56

[95] Y.Fujita et.al. Nucl.Instrum.Meth A405(1998)105

[96] S.Y.Suzuki et.al IEEE Trans.Nucl.Sci 47(2000)61

[97] R.Itoh. 'BASF User's Manual' Belle note #161 (1996)

[98] R.Itoh and Ishozawa. 'Status of BELLE event processing framework based on SMP-server' Belle note #97 (1995)

[99] R.Brun and D.Lienart. 'Hbook User Guide: Cerm Computer Center Program Library Long Writeup Version 4' CERN-Y250

[100] T.Matsumoto, 'Measurement of$\sqrt{s}$ from full reconstructed B decays at $\Upsilon(4S)$ resonance' Belle Note #418

[101] H.Kakuno, 'Flavor tagging by Multidimensional likelihood method', Belle note #384(2001) H.Kakuno, 'Neutral B Flavor Tagging for the Measurement of Mixing-induced CP Violation at Belle', Nucl.Instrum.Meth A533(2994)516

[102] G.Fox and S.Wolfram, Phys.Rev.Lett 41(1978)1581

[103] N.Abe 'Measurement of CP Vioalting parameter ϕ_2 through B meson decay into $\pi^+\pi^-$' Ph.D thesis(2004) Tokyo Institute of Tecnology

[104] EvtGen A Monte Carlo Generator for B-physics

[105] H.Tajima et.al,'B-FactoryProper-time Resolution Function for Measurement of Time Evolution of B Mesons at the KEK B-Factory'. Nucl.Instrum.Meth A533(2004)370

[106] O.Long, M.Baak, R.N.Cahn and D.Kirkby. Physc.Revi D68(2003)034010

[107] 32nd ICHEP04 conference(Augst 16-22):Beijing, China. Talk; Augst 16, Andres Hoecker(LAL/Orsay) 'sin(2β) from penguin at Babar'

[108] 6th Workshop on a Higher Luminosity B Factory, Talk of T. Iijima(Nagoya),'Overview of Physics at Super B-Factory'

[109] H.Yamamoto.'Space-time Profile of e^+e^- Interaction With Crossing Angles', Belle note #269